

A NEW SEARCH FOR LOW-MASS DARK MATTER AND AN
EXAMINATION AND REDUCTION OF THE UNCERTAINTY DUE TO
THE PHOTOELECTRIC ABSORPTION CROSS SECTION USING A
CRYOGENIC SILICON DETECTOR WITH SINGLE-CHARGE
SENSITIVITY

by

Matthew James Wilson

A thesis submitted in conformity with the requirements
for the degree of Doctor of Philosophy
Graduate Department of Physics
University of Toronto

© Copyright 2022 by Matthew James Wilson

Abstract

A NEW SEARCH FOR LOW-MASS DARK MATTER AND AN EXAMINATION AND REDUCTION OF THE UNCERTAINTY DUE TO THE PHOTOELECTRIC ABSORPTION CROSS SECTION USING A CRYOGENIC SILICON DETECTOR WITH SINGLE-CHARGE SENSITIVITY

Matthew James Wilson
Doctor of Philosophy
Graduate Department of Physics
University of Toronto
2022

Many astrophysical observations point to the abundant existence of dark matter (DM) in the universe composed of particles beyond the Standard Model. However despite numerous experiments using different techniques, DM particles have yet to be directly observed. The Super Cryogenic Dark Matter Search (SuperCDMS) SNOLAB experiment will employ silicon and germanium crystal detectors operated at temperatures as low as 15 mK to probe DM interactions using phonon and ionization signals. Recently, R&D facilities have developed gram-sized high-voltage eV-scale (HVeV) silicon detectors that achieve single-electron-hole-pair resolution. By probing effective DM-electron interactions, these devices can be used for searches of low-mass DM candidates.

This dissertation presents a DM search experiment known as HVeV Run 2 that employs a second-generation HVeV detector operated in an above-ground laboratory at Northwestern University (IL, USA). Energy spectra are obtained from a blind analysis with 0.39 and 1.2 g-days of exposure with the detector biased at 60 and 100 V, respectively. The 0.93 gram detector achieves a 3 eV phonon energy resolution, corresponding to a world-leading charge resolution of 3% of a single electron-hole pair for a detector bias of 100 V. With charge carrier trapping and impact ionization effects incorporated into the DM signal models, the resulting exclusion limits are reported for inelastic DM-electron scattering for DM masses from $0.5\text{--}10^4 \text{ MeV}/c^2$; in the mass range from $1.2\text{--}50 \text{ eV}/c^2$ the limits for dark photon and axion-like particle absorption are reported.

Several DM search experiments, including HVeV Run 2, are sensitive to low-mass DM candidates that rely on the temperature-dependent photoelectric absorption cross section of silicon. However discrepancies in the underlying literature data result in dominating systematic uncertainties on the DM exclusion limits. In order to reduce these systematic uncertainties, this dissertation presents a novel method of making a direct, low-temperature measurement of the photoelectric absorption cross section of silicon at energies near the band gap (1.2–2.8 eV).

To my fiancée Aira, my parents Jamie and Marisa, my siblings Cole and Alanna, and my Nonna Franca, who continue to support and inspire me.

People are usually afraid of change because they fear the unknown. But the single greatest constant of history is that everything changes.

—Yuval Noah Harari, *Homo Deus: A History of Tomorrow*

Acknowledgements

First and foremost, I must thank my fiancée Aira for her unwavering support she has given me during my PhD studies. From the beginning, Aira has encouraged me to always pursue my educational and career goals. She has been a steady presence in my life and a reliable partner who has been there during the stressful and joyous times. Although we are currently living in two separate countries, I am glad we were both fortunate enough to have the incredible opportunity of working and living in Europe. And getting engaged next to the Swiss alps wasn't so bad either! Aira has also been incredibly understanding whenever I've needed to work late or on weekends (a habit that both of us unfortunately share sometimes). Especially of late, she has done everything to help me get past this finish line. I am forever grateful for the support and inspiration she has provided me over the past eight years.

Next I would like to thank my family, starting with my parents, Jamie and Marisa, my brother Cole and his fiancée Keenan, my sister Alanna and her partner Romahllo, my Nonna Franca, and my future in-laws Anthony, Gemma, and Giselle; all of whom have supported and encouraged me in their own way. I come from a strong educational background: my mom is a primary school teacher and my dad also has his PhD in physics. Both of them instilled in me the value of education and the meaning of hard work. They taught me to be open-minded and curious, and also provided me with an incredible amount of support and encouragement to pursue my PhD. I can't thank them enough for all the little things they did to help along the way, like picking me up late from the train station, and making sure there was always a meal for me when I came home. With my two siblings, I appreciate that we can talk about almost any subject, from physics to movies to politics. Both of them have traits that I really admire and try to learn from. For my brother it's his knowledge and creativity, and for my sister it's her thoughtfulness and confidence. Although we can be quite competitive sometimes, I know we are all rooting for each other. Lastly, I am very thankful that my entire family has been able to put up with all of my odd quirks and idiosyncrasies for all these years!

I would also like to thank my close friends for all of the wonderful (and sometimes crazy) adventures and experiences we've shared, which have made my time during the course of my PhD and throughout my university studies in general way more enjoyable and memorable, and which have given me the much needed relief from thinking about work all the time. Specifically I want to acknowledge my "DMM" friends Fatima, Neelan, and Diana, my "CR3W" friends Giselle and Eason, and my good friend and past roommate Chris. Going through university, and especially a PhD program, is often challenging and stressful, and these people have not only made it bearable for me, but a period of life that I will look back fondly upon.

Throughout my PhD studies there were many people who played a significant role in getting me to where I am today. I first need to thank my first supervisor Hirohisa (Hiro) Tanaka for taking me on as a grad student way back in 2016. I will always appreciate the way Hiro approaches topics with a high degree of insight and intelligence, as well as his ability to carefully listen to his students. Starting a PhD program can at times be intimidating, but Hiro made me feel comfortable and unafraid to share my thoughts and questions. Next I would like to thank my current supervisor Miriam Diamond, who guided me through my first major analysis as a lead analyzer and made sure I always kept on track to graduate. The lessons I learned from her throughout the latter half of my PhD studies have helped me become a better physicist. And thanks to Miriam, I have a new-found appreciation for guinea pigs! I am truly happy to see the SuperCDMS group at the University of Toronto grow by so much since I started, and I know it is in good hands with Miriam, Ziqing, and Pekka leading the way. I also must

give thanks to Scott Oser, who kept an eye out for me while I was between supervisors, and made sure I didn't become a grad student "lost at sea".

I owe a great deal of gratitude to my unofficial supervisor Belina von Krosigk, whom I've been working with since the start of my PhD studies, back when I was doing, shall I say, less interesting data acquisition software tasks. I always felt comfortable asking Belina all of my dumb questions (which I still ask to this day!). But more importantly, Belina instilled in me the feeling that my work had purpose and was valued. I am especially grateful that she offered me an opportunity to work with her in Germany. Not only was working abroad something I've always wanted to experience, but it also fortuitously coincided with my now-fiancée also moving to Europe. Although working in Germany so far has been marred by a certain global pandemic, I am most definitely looking forward to continuing working with Belina in Karlsruhe. I would also like to thank Noah Kurinsky for giving me a significant role in the HVeV Run 1 analysis. This was the first dark matter analysis I directly participated in, and much of what I learned from this analysis and from Noah I was able to apply to the HVeV Run 2 analysis. I always considered Noah to be a top-tier grad student, and was always (and still am) astounded by the depth of his knowledge. He also taught me that there really is no limit to what a grad student can accomplish during their studies.

It goes without saying that the work presented in this dissertation would not be possible without the combined efforts from many of my collaborators and supervisors within SuperCDMS, including those whom I've directly worked with and those whom I have not. The HVeV Run 2 dark matter search experiment that I present in Chapters 4 and Chapters 5 was a huge undertaking that led to a collaboration paper, and so I must acknowledge and thank my co-lead-analyzers Yen-Yung Chang and Valentina Novati for the incredible amount of time and effort put into making this experiment a success. The detector for this experiment was designed by Noah Kurinsky, Ziqing Hong, and Brian Nebolsky, and is also the result of previous designs and detector technologies that have been worked on and developed over many years by many other people. Furthermore, I want to thank Noah, Ziqing, Brian, Tom Ren and Doug Pinckney for doing the often overlooked task of getting this experiment up and running, which made it very easy for myself and fellow analyzers to come in and start collecting data. Apart from myself, Yen-Yung, and Valentina, the other key contributors to the HVeV Run 2 analysis include Noah, Ziqing, Tom, Belina von Krosigk, Miriam Diamond, and Enectali (Tali) Figueroa-Feliciano, with contributions made by Francisco Ponce and Elizabeth Wills.

The photoelectric absorption cross section measurement and analysis I present in Chapter 6 is a satisfying conclusion to many years of focusing on this one parameter and led to two publications. Again, this work would not have been possible without the combined efforts from my colleagues. Early concepts of this experiment were formulated by myself, Chris Stanford, and Noah Kurinsky, but I owe a great deal of gratitude to Chris for getting this experiment setup and collecting the data for this measurement. Apart from myself and Chris, the other key contributors to this experiment and analysis include Noah, Blas Cabrera, Miriam Diamond, Robert Moffatt, Francisco Ponce, Belina von Krosigk, Betty Young, and Steve Yellin. The work of examining how this new measurement affects dark matter exclusion limits also had helpful contributions from Rob Calkins, Dan Jardin, and Chih-Pan Wu.

Writing this dissertation was a long and sometimes tiring process, but one that I found to be ultimately beneficial. The first people I need to thank for helping me during this writing process are my official supervisor Miriam Diamond and my unofficial supervisor Belina von Krosigk. The guidance and suggestions that Miriam and Belina provided were invaluable, and they both enabled me to write the

best dissertation I am capable of. I would also like to especially thank Ziqing Hong for always allowing me to bug him whenever there was a topic I wanted to understand better. Ziqing was willing to spend much of his time (accumulating to many hours) discussing various concepts with me, and my dissertation is truly better because of it. Furthermore, I would like to thank Rouven Essig for helping me understand certain dark matter models, both while writing my dissertation and throughout my PhD studies.

Every person I have mentioned here has played a role in helping me become a better scientist and a more critical thinker. I want to end by acknowledging the role that the SuperCDMS collaboration had on my studies. At the start of my PhD, I would often worry about working for four to five years in a large collaboration, and by the end, have nothing of my own to write dissertation about. I soon found that my collaborators and colleagues within SuperCDMS actively encouraged the success of graduate students by involving them in meaningful and significant work. Indeed a grad student such as myself can play a leading role in a collaboration dark matter search experiment. The exposure and experience I obtained during my PhD studies will undoubtedly be beneficial for my future career, wherever it may go.

Contents

Abstract	ii
Acknowledgements	iv
List of Tables	ix
List of Figures	xi
Statement about Collaborative Work	xv
1 Dark Matter: The Missing Mass	1
1.1 A Brief History of Dark Matter	1
1.2 Evidence of Dark Matter	3
1.2.1 Galaxy Rotation Curves	3
1.2.2 Gravitational Lensing	5
1.2.3 Cosmic Microwave Background	7
1.3 Properties of Dark Matter	9
1.3.1 Local Dark Matter	10
1.4 Searching for Dark Matter	13
1.5 Dark Matter Candidates	14
1.5.1 WIMPs	14
1.5.2 Light Dark Matter	19
1.5.3 Bosonic Dark Matter	22
1.5.4 Other Candidates and Interaction Channels	25
1.6 The SuperCDMS Experiment	27
2 Detector Physics	30
2.1 Cryogenic Semiconductor Crystal Detectors	30
2.1.1 Phonon Energy	33
2.2 Detector Response Model	35
2.2.1 Ionization Production	35
2.2.2 Charge Trapping and Impact Ionization	36
2.2.3 Conversion to eV Scale	39
2.3 Photoelectric Absorption Cross Section	40
2.3.1 Temperature Correction	43

2.3.2	Other Considerations	45
2.3.3	Photoelectric Absorption Cross Section Curves	46
2.4	Detector Leakage	46
2.5	SuperCDMS Detectors	48
3	HVeV Phonon Sensors and Detector Design	51
3.1	Phonon Detection Concepts	51
3.1.1	Transition Edge Sensors	51
3.1.2	SQUID Circuits	51
3.1.3	Quasiparticle-trap-assisted Electrothermal-feedback TESs	54
3.1.4	Optimized Parameters	55
3.2	The Second-Generation HVeV Detector	56
3.2.1	Detector Design and Optimization	56
3.2.2	Improvements from the First-Generation HVeV Detector Design	57
3.3	Detector Characterization	58
4	HVeV Run 2 Dark Matter Search: Experiment, Calibration, and Data Selection	62
4.1	Motivation	62
4.2	Experimental Setup	65
4.2.1	Hardware and Refrigeration	65
4.2.2	Data Acquisition and Triggering	67
4.2.3	Data Processing	69
4.2.4	Blinding Scheme	73
4.3	Energy Corrections and Calibration	75
4.3.1	Relative Calibration	76
4.3.2	Temperature Correction	77
4.3.3	High-Voltage Correction	81
4.3.4	QET Photon Absorption	85
4.3.5	Non-Linearity Correction and Calibration	87
4.4	Analysis Selection Criteria	92
4.4.1	Livetime Selection Criteria	92
4.4.2	Data-Quality Selection Criteria	100
4.5	Livetime, Efficiency, and Experimental Parameters	110
4.5.1	Livetime	111
4.5.2	Efficiency Calculation	112
4.5.3	Detector Resolution	119
4.5.4	Charge Trapping and Impact Ionization Probabilities	121
5	HVeV Run 2 Dark Matter Search: Limit Setting, Unblinding, and Final Results	123
5.1	Limit Setting Methods	123
5.1.1	OI Limit Setting Method	124
5.1.2	Poisson Limit Setting Method	125
5.1.3	Comparison of Methods	126
5.2	Initial Limit Results	128

5.3	Unblinding	132
5.3.1	Stage-1 Unblinding	135
5.3.2	Stage-2 Unblinding	135
5.4	Final Results	139
5.4.1	Exposure and Energy Spectra	139
5.4.2	Exclusion Limits	141
5.4.3	Characterizing the Limit Uncertainty Estimates	144
5.5	Discussion	147
6	Photoelectric Absorption Cross Section Measurement in Silicon	152
6.1	Motivation	152
6.2	Experimental Setup	153
6.2.1	Experiment Design	153
6.2.2	Data Acquisition	155
6.3	Calibration	156
6.4	Analysis	161
6.5	Effect on Dark Matter Exclusion Limits	165
6.6	Discussion	169
7	Conclusions and Outlook	173
7.1	Unknown Backgrounds	173
7.2	Experimental and Model Uncertainties	176
7.3	Outlook	179
	Appendices	180
A	Inelastic Nuclear Scattering Models	181
A.1	Bremsstrahlung	181
A.2	Migdal Effect	186
B	Relationship between Complex Conductivity and Photoelectric Absorption	188
C	Derivation of Discrete Distributions of Electron-Hole Pair Probability	190
D	Charge Trapping and Impact Ionization Model	192
D.1	Description of the Model	192
D.2	Model Assumptions	194
E	Optical Parameters for Si and Ge	199
F	Photon Absorption Model for Si	203
	Acronyms and Abbreviations	206
	Bibliography	208

List of Tables

2.1	Properties of SuperCDMS SNOLAB detectors	49
3.1	Design and operating parameters of the second-generation HVeV detector	61
4.1	List and description of RQs computed during data processing	74
4.2	Best-fit results for the temperature correction	80
4.3	Summary of trigger and leakage burst quantities using ^{57}Co -calibration data	100
4.4	Best-fit results from the $\chi^2(f)$ and $\chi^2(t)$ DQ cuts	104
4.5	Summary of the livetime calculations for the stage-0 background data	113
4.6	Best-fit results for the trigger efficiency curves	114
4.7	Best-fit results for the detector efficiency curves	116
4.8	Summary of the event rejection rates from the DQ cuts	118
4.9	Summary of the energy resolutions at each e^-h^+ -pair peak for the laser-calibration data	120
5.1	Summary of passage fractions for the stage-1 unblinding	135
5.2	Summary of KS test statistics for the stage-1 unblinding	136
5.3	Summary of passage fractions for the stage-2 unblinding	136
5.4	Summary of KS test statistics for the stage-2 unblinding	137
5.5	Summary of the final livetime and exposure after unblinding	139
5.6	Summary of e^-h^+ -pair peak positions and widths	140
5.7	Summary of the experimental and model parameter inputs and probability distributions used to compute the final limit results	142
5.8	Comparison of the efficiency-correct event rate at each e^-h^+ -pair peak between HVeV Run 1 and HVeV Run 2	149
6.1	Summary of the monochromatic light sources used to measure $\sigma_{\text{p.e.}}$	154
E.1	List of references for the $\sigma_{\text{p.e.}}$ data obtained for Si and Ge	201
F.1	List of parameters and their corresponding values used for the photon absorption model	205

List of Figures

1.1	Composite image illustrating the history of astronomy	2
1.2	Superposition of the galactic rotation curves measured by Rubin <i>et. al.</i>	4
1.3	Images of the stellar and plasma components of the Bullet Cluster	7
1.4	Temperature map of the CMB	7
1.5	CMB power spectrum	9
1.6	Summary of the measurements of the local dark matter density made over time	12
1.7	Examples of the total and differential event rates for WIMP-nucleus scattering	18
1.8	Parameter space of the spin-independent WIMP-nuclear scattering cross section	18
1.9	Examples of the total and differential event rates for LDM-electron scattering	22
1.10	Examples of the total event rates for dark photon and ALP absorption	25
1.11	Schematic diagram of the SuperCDMS SNOLAB experiment	28
1.12	Projected limits on the spin-independent WIMP-nuclear scattering cross section for the SuperCDMS SNOLAB experiment	29
2.1	Illustration of the energy states in a semiconductor	31
2.2	Illustration of a DM-nucleus interaction in a semiconductor detector	32
2.3	Illustration of a quantized versus a continuous n_{eh} distribution	34
2.4	Illustration of the n_{eh} distributions for various Fano factors	36
2.5	Illustration of charge trapping and impact ionization	37
2.6	Examples of quantized distributions with charge trapping and impact ionization	38
2.7	Conversion of a continuous energy spectrum to a quantized signal spectrum	40
2.8	Comparison of quantized signal spectra for various applied voltages	41
2.9	Cross sections for absorption and scattering processes of light in Si and Ge	42
2.10	Photoelectric absorption cross section data for Si obtained from the literature	43
2.11	Illustration of direct and indirect photon absorption	44
2.12	Temperature-corrected photoelectric absorption cross section data	45
2.13	Photoelectric absorption cross section curves	47
2.14	Channel layout and photographs of the SuperCDMS SNOLAB detectors	49
3.1	Illustration of the resistance-temperature curve for a TES	52
3.2	Illustration of the voltage dependence on magnetic flux for a SQUID and the TES-SQUID circuit schematic	52
3.3	Overview of the energy transport and design geometry for a QET	54
3.4	Illustration of the NF-C mask design	58

3.5	NF-C HVeV detector performance and energy efficiency	59
3.6	Calibrated energy spectrum in second-generation HVeV detector	60
4.1	Comparison of the HVeV Run 1 energy spectrum with a detector leakage MC	63
4.2	Projected limits on DM-electron scattering using toy experiments	64
4.3	Projected limits on dark photon absorption using toy experiments	65
4.4	Images of the HVeV Run 2 detector inside the copper housing	66
4.5	Images of the HVeV Run 2 laboratory setup	66
4.6	Summary of the exposure obtained for HVeV Run 2	68
4.7	Example of event triggering	69
4.8	Noise PSDs measured during data acquisition	71
4.9	Overlay of the normalized pulses used to create the pulse templates	71
4.10	Overlay of the selected pulses used to create the pulse templates	72
4.11	Averaged normalized pulse used to create the pulse templates	72
4.12	Pulse templates in the time and frequency domain	73
4.13	Average of veto detector pulses compared with the pulse template	75
4.14	Relative gain in the inner and outer channels	77
4.15	Fridge temperature calibration and summary of fridge temperature data	78
4.16	Summary of laser-calibration datasets acquired for the temperature correction	79
4.17	Linear fits for the temperature correction	80
4.18	Slope parameter used to describe the temperature correction	81
4.19	Laser-calibration data before and after the temperature correction	82
4.20	Effect of the temperature correction on OF amplitudes	82
4.21	OF amplitude dependence on voltage measured for each day	83
4.22	Averaged HV bias measured for the laser-calibration data	84
4.23	Effect of the voltage corrections on OF amplitudes	85
4.24	Zeroth-peak offset versus λ for laser-calibration data	87
4.25	Non-linear energy correction and calibration	89
4.26	Best-fit results from the energy calibration	90
4.27	Energy-calibrated laser-calibration data spectra	91
4.28	Fridge temperature variation over time	93
4.29	Fridge temperature livetime cut	94
4.30	Δ Mean Base variation over time	95
4.31	Δ Mean Base livetime cut	96
4.32	Trigger burst livetime cut	97
4.33	Leakage burst livetime cut	98
4.34	Leakage burst cut applied to the ^{57}Co -calibration data before and after unblinding	99
4.35	Summary of the energy spectra after applying the livetime cuts	101
4.36	Trigger offset DQ cut	102
4.37	Mean Base DQ cut example	103
4.38	$\chi^2(f)$ and $\chi^2(t)$ DQ cuts	105
4.39	Comparison of events passing the $\chi^2(f)$ cut versus the $\chi^2(t)$ cut	106
4.40	Examples of events that pass the $\chi^2(f)$ cut but fail the $\chi^2(t)$ cut	106
4.41	Veto detector DQ cut	107

4.42	Partition DQ cut using the ^{57}Co -calibration data	109
4.43	Energy spectrum of the ^{57}Co -calibration data after applying the DQ cuts	110
4.44	Summary of the energy spectra after applying the DQ cuts	111
4.45	Trigger efficiency at 50 and 52 mK	114
4.46	Efficiency data and curve for the 60 V laser-calibration data	117
4.47	Efficiency data and curve for the 100 V laser-calibration data	117
4.48	Density map of events demonstrating the observed efficiency dips	119
4.49	Examples of traces from events that cause the observed efficiency dips	120
4.50	Example of the CT and II model fitted to laser-calibration data	122
4.51	Summary of the best-fit CT and II probabilities	122
5.1	Comparison of the OI and Poisson limit setting methods for various resolutions	127
5.2	Variation in the LDM-electron scattering cross section due to the uncertainty in the detector resolution using the OI or Poisson method	128
5.3	The OI limit-setting interval for DM signal models computed for various Fano factors	129
5.4	Examples of the DM limits computed for each e^-h^+ -pair peak	130
5.5	Results of the e^-h^+ -pair peak selection procedure for limit setting	132
5.6	Initial DM exclusion limit results	133
5.7	Comparison of the Δ Mean Base distributions and EDFs from the different stages of unblinding, all days combined	137
5.8	Comparison of the mean base distributions and EDFs from the different stages of un- blinding, day-by-day	138
5.9	The DM-search energy spectra after unblinding	139
5.10	Example of the limit distributions computed for each e^-h^+ -pair peak	143
5.11	The final exclusion limits on the LDM-electron scattering cross section for the 60 V and 100 V measurement	145
5.12	The final exclusion limits on the dark photon kinetic mixing parameter and axioelectric coupling constant for the 60 V and 100 V measurement	145
5.13	Distributions of parameter variates used to compute the limit distributions	146
5.14	Results of the linear regression analysis for each limit setting parameter	147
5.15	Comparison of the LDM-electron scattering limit at each e^-h^+ -pair peak between HVeV Run 1 and HVeV Run 2	149
6.1	Illustration of the experimental setup used to measure $\sigma_{\text{p.e.}}$	153
6.2	Illustration of the front and back filter mount design	154
6.3	Example of the voltage traces resulting from light pulses	156
6.4	Pulse amplitude linearity correction	157
6.5	2D scans of the averaged pulse amplitude through each empty transmission hole	158
6.6	Relative transmission through each empty hole for various wavelengths and temperatures	159
6.7	Hole correction factors used to adjust the 1028 nm transmission measurements	160
6.8	2D scans of the transmission measurements through each hole with the Si filters	161
6.9	Summary of the transmission results as a function of filter thickness at each temperature	163
6.10	Exponential fit of the A_1 proportionality constant and summary of the new $\sigma_{\text{p.e.}}$ results	165
6.11	Comparison of the nominal and fitted $\sigma_{\text{p.e.}}$ curves used for limit setting	166

6.12	Comparison of the Migdal and Bremsstrahlung inelastic scattering models generated using the nominal or fitted $\sigma_{p.e.}$ curve	167
6.13	Examples of quantized DM signal models generating using the nominal or fitted $\sigma_{p.e.}$ curve overlaid the HVeV Run 2 spectrum	168
6.14	Exclusion limits on dark photon and ALP absorption computed using the nominal or fitted $\sigma_{p.e.}$ curve	170
6.15	Exclusion limits on Migdal and Bremsstrahlung inelastic scattering computed using the nominal for fitted $\sigma_{p.e.}$ curve	170
7.1	Comparison of the event rate spectra from HVeV Run 1 and HVeV Run 2	174
7.2	Photoluminescence spectrum for various SiO ₂ materials and the resulting MC simulation compared to the HVeV Run 2 spectrum	175
7.3	Comparison of the event rate spectra from HVeV Run 2 and early data acquired at the NEXUS facility	176
7.4	Probability distributions of e^-h^+ pair creation in Si	177
7.5	Comparison of the current and an expanded CT and II model	178
A.1	Examples of the total and differential event rates for DM-nucleus inelastic scattering under the emission of a Bremsstrahlung photon	183
A.2	Examples of the kinematically allowed parameter space of the recoil and photon energies for Bremsstrahlung inelastic scattering for Si and Xe	185
A.3	Fraction of the kinematically allowed parameter space with negligibly small recoil energies as a function of DM mass	186
A.4	Examples of the total and differential event rates for DM-nucleus inelastic scattering under the emission of a Migdal electron	187
D.1	Example of a probability distribution from the CT and II model	193
E.1	Index of refraction data for Si and Ge	199
E.2	Amalgamation of the $\sigma_{p.e.}$ data obtained from the literature for Si and Ge	200
E.3	Data of the imaginary part of the complex conductivity for Si and Ge	202

Statement about Collaborative Work

The work that I present in this dissertation was done while I was a member of the SuperCDMS collaboration. Collaborative efforts, involving multiple participants, are responsible for the analysis and results of the HVeV Run 2 experiment presented in Chapters 4 and 5, as well as the photoelectric absorption cross section measurement presented in Chapter 6. The following statement clarifies and summarizes my individual contributions, and acknowledges the contributions of other key collaborators to these efforts. At the beginning of each of Chapters 4 through 6, I again include the names of the other key collaborators; furthermore, I appropriately give credit for any plot or figure I did not originally create.

The main contributors to the HVeV Run 2 analysis presented in Chapters 4 and 5 include myself, Yen-Yung Chang, and Valentina Novati. Other key contributors include Noah Kurinsky, Ziqing Hong, Tom Ren, Belina von Krosigk, Miriam Diamond, and Enectali (Tali) Figueroa-Feliciano, with additional contributions made by Francisco Ponce and Elizabeth Wills. The design and setup of this experiment was done by Noah, Ziqing, and Brian Nebolsky, including the detector design discussed in Chapter 3. I participated in the data acquisition throughout all of HVeV Run 2. I was involved in many stages throughout the analysis pipeline, including developing the temperature correction as part of the energy calibration, and developing the trigger and leakage burst cuts as part of the livetime selection procedure. My main contribution came at the limit-setting stage. This included choosing and validating the limit-setting method, implementing each of the dark matter signal models as well as the detector response model, incorporating the photoelectric absorption cross section, implementing the limit-setting procedure on both the pre-unblinded and unblinded datasets, producing the final results, and characterizing the uncertainty in the limit results. This analysis was also the first analysis within SuperCDMS to incorporate charge trapping and impact ionization into the detector response model (see Sec. 2.2.2). The results from this work appear in an article published by the entire collaboration [1], of which I was a main author, the main editor, and the article submitter. Most importantly, I shared the title of co-lead analyzer for the HVeV Run 2 analysis, meaning that I was heavily and directly involved with all of the decision making that occurred at all stages of this analysis.

The main contributors to the new photoelectric absorption cross section measurement and analysis presented in Chapter 6 are myself and Chris Stanford. Other contributors to this experiment and analysis include Noah Kurinsky, Blas Cabrera, Miriam Diamond, Robert Moffatt, Francisco Ponce, Belina von Krosigk, Betty Young, and Steve Yellin, with helpful contributions from Rob Calkins, Dan Jardin, and Chih-Pan Wu. The initial motivation for doing this measurement came from the work I did gathering photoelectric absorption cross section data and applying a temperature correction (see Sec. 2.3). I was therefore involved with this experiment from its conception. I helped with developing the design of the experiment, and procured some of the equipment needed to perform the experiment. The data for this experiment were acquired by Chris Stanford, and Chris conducted the initial parts of the analysis by

transforming the transmission measurements into the photoelectric absorption cross section values. I conducted the final parts of the analysis, including fitting the absorption model to the measurements in order to generate photoelectric absorption cross section curves over photon energy and temperature that can be used for dark matter limit setting. I also investigated the effect that this new measurement has on the exclusion limit for various dark matter models. The results from this work appear in two articles with limited author-lists [2, 3], both of which I wrote a significant portion of the text, and one of which I was a main editor.

Lastly, I want to state that some of the work that I did throughout my PhD as a member of the SuperCDMS collaboration is not included in this dissertation. Some examples include work on the data acquisition software for the SuperCDMS SNOLAB experiment, work on the data monitoring software for the SuperCDMS SNOLAB experiment, and work on the HVeV Run 1 analysis. However, the most significant work that I did throughout my PhD in terms of both time and importance are included in this dissertation.

Chapter 1

Dark Matter: The Missing Mass

1.1 A Brief History of Dark Matter

Throughout history, philosophers and astronomers alike looked up into the stars to ponder and study the universe in which we live. The first observations of the cosmos were made with just the human eye by tracking the motion of planets and stars. Yet scientific curiosity prevailed over technological limitations with each new breakthrough in astronomy, from Aristotle's model of the cosmos that placed Earth at the center of an immutable universe, to Ibn al-Shatir's use of experimental techniques and empirical observations to construct lunar and solar models, to the major paradigm shift caused by the Copernican revolution that reasoned the Sun to be at the center of the Solar System instead of the Earth.

Each new advancement in astronomical technology gave scientists a new window to view the cosmos (see Fig. 1.1). The development of the telescope in the early 1600's provided unprecedented observations of the Solar System, and in one of its first uses, Galileo concluded the Milky Way is composed of innumerable stars. It wasn't until 1924 when Hubble confirmed that the Milky Way is not the only galaxy in the universe. Eventually massive telescopes could be launched into space, and in 1995 the Hubble Space Telescope captured the famous Hubble Deep Field image that shows thousands of young galaxies [4], demonstrating plainly that to look far into space is to look back in time.

In the early 1900's, astrophysical experiments began to draw a strange yet similar conclusion: that systems of stars and galaxies behaved as if there were more mass than what was observed. Up to this point, the mass of stars and galaxies would be inferred by measuring the amount of light they emit (i.e. their luminosity). So these strange observations suggested that there exists some massive substance that isn't visible by light, or so-called dark matter (DM). At first, DM did not necessarily imply the existence of some new, mysterious substance, but rather just implied the presence of unseen matter that interacted with other objects through gravity. Perhaps DM is composed of just very dim stars, or some interstellar material that does not emit nor interact with light. The brief historical recounting of DM provided here follows the excellent summary given in Ref. [5].

Some of the first quantitative measurements of DM were made by Jacobus Kapteyn, Jan Oort, James Jeans, and Bertil Lindblad in the 1920's and 30's, whereby the local density of DM was inferred by observing the kinematics of stars in the solar neighbourhood. However one of the most significant watershed moments for DM came from observations made by Fritz Zwicky in 1933. Zwicky was studying

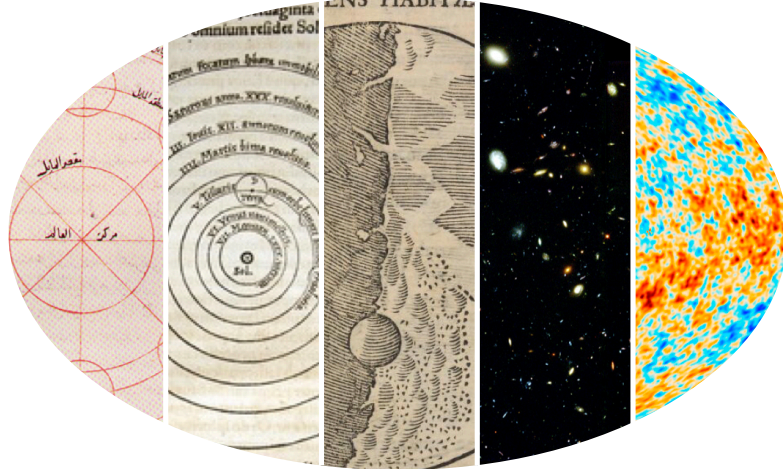


Figure 1.1: Composite image illustrating the history of astronomy. From left to right with citations for the respective images: Ibn al-Shatir uses experimental techniques and empirical observations to develop a lunar model [6]; the Copernican revolution puts the Earth at the center of the Solar System [7]; after the invention of the telescope, Galileo is able to make extremely detailed illustrations of the Moon [8]; in 1995, the Hubble Space Telescope captures the famous Hubble Deep Field image, showing a zoo of young galaxies [4]; recent temperature map of the Cosmic Microwave Background, the earliest state of the universe that can be observed by light [9].

the redshifts[†] of galaxies in the Coma Cluster in order to determine their apparent velocities. He then used the virial theorem to determine the mass of the entire cluster. For a system of N particles bound by potential forces, the time-averaged kinetic energy $\langle T \rangle$ of the entire system is given by:

$$\langle T \rangle = \frac{1}{2} \sum_{k=1}^N \langle \vec{F}_k \cdot \vec{r}_k \rangle, \quad (1.1)$$

where \vec{F}_k is the force acting on the k^{th} particle located at \vec{r}_k . If the forces acting on the particles result from a potential energy V dependent on the distance r between particles such that $V \propto r^n$, the virial theorem takes the form:

$$2\langle T \rangle = n\langle V \rangle, \quad (1.2)$$

where for a gravitational potential, $n = -1$. This relationship says that for a system with more potential energy (i.e. more mass in a gravitational potential), the average kinetic energy of the particles will be larger. Zwicky noticed that the high velocities of galaxies implied that the total mass of the Coma Cluster is much larger than the mass found by observing the total luminosity. In other words, the Coma Cluster must contain a significant amount of DM in order to explain the high velocities of the galaxies. In 1936, Sinclair Smith came to similar conclusions after observing the circular motion of galaxies in the Virgo Cluster.

As astronomers and astrophysicists deliberated about this missing mass, the field of particle physics was surging. The turn of the 19th century saw the discovery of the electron and proton, quantum

[†]A redshift is an increase in the wavelength of light that occurs to light emitted from distant objects due to both the relative motion of the object and the expansion of the universe. The relative velocities of galaxies in a cluster can be inferred by measuring each galaxy's redshift; galaxies travelling toward Earth will appear slightly bluer compared to galaxies travelling away from Earth.

mechanics was formalized in the 1920's and 30's, and later throughout the 20th century the Standard Model (SM) was developed, describing all of the known elementary particles (quarks, leptons, and bosons) and three of the four fundamental forces (electromagnetic, weak, and strong). Eventually, the nature of DM became just as much a question of particle physics as it was a question of cosmology. Perhaps DM is ordinary matter made up of SM particles. Or perhaps DM is made up of some yet unknown particle and/or force mediator. In 1985, Mark Goodman and Ed Witten suggested that if DM is composed of particles, then it might be detectable using techniques similar to neutrino detection. Thus began the era of DM direct detection search experiments, starting with an experiment carried out in 1986 at the Homestake Mine in South Dakota using a low-background germanium ionization detector [10].

More recently in 1998, the DAMA/LIBRA collaborations conducted a DM search experiment at the underground Gran Sasso Laboratory in Italy using scintillating sodium iodide detectors. In their first results they observed a signal consistent with DM scattering with an annual modulation (slight variations in the signal rate due to the Earth's rotation around the Sun), and have since observed the same signal with increasing statistical significance [11]. Unfortunately, other DM search experiments were unable to corroborate the signal observed by DAMA/LIBRA, and so it remains difficult to determine whether the signal was in fact DM. Yet as Ref. [5] says, no convincing alternative explanation for this signal has been identified. In more recent years, the CoGeNT and CRESST-II collaborations have reported similar signals as the DAMA/LIBRA experiments, but the observed amplitudes of the annual modulations are a few factors higher than what would be expected [12].

This dissertation is yet another step toward uncovering the true nature of DM. Chapter 1 summarizes the most pertinent evidence and properties related to DM, and describes the various DM models that are relevant to later chapters. Chapter 2 outlines the physics of detecting DM using cryogenic solid-state detectors, and Chapter 3 details the design of a second-generation high-voltage eV-scale (HVeV) detector. In Chapters 4 and 5, a DM search experiment and subsequent analysis using this HVeV detector is presented in its entirety. Chapter 6 presents a novel method for measuring the photoelectric absorption cross section in detector materials at cryogenic temperatures, and uses the results to evaluate the impact on DM exclusion limits. Lastly, Chapter 7 provides some concluding remarks and a brief outlook on future experiments. All of the work presented in this dissertation was conducted as part of the Super Cryogenic Dark Matter Search (SuperCDMS) collaboration.

1.2 Evidence of Dark Matter

Just as phenomena related to electricity were studied and characterized well before the discovery of the electron by J. J. Thomson in 1897, phenomena related to DM have been studied despite the true nature of the substance remaining unknown. This section summarizes several key observations relating to DM, which together provide extremely compelling evidence of the existence of this mysterious form of matter. For the sake of brevity, the following sub-sections that cover this topic are terse. Many other fascinating details and examples are omitted, and so the reader is encouraged to learn more about each topic by following the references provided.

1.2.1 Galaxy Rotation Curves

Galaxy rotation curves are studies of the circular velocity profiles of orbiting stars or gas as a function of their distance from the galactic center, and are an important chapter in the history of DM observations.

Galaxies are composed of millions or billions of stars and interstellar gas that all orbit around the galactic center. The motion of these object can be predicted using the virial theorem for a gravitational potential, as given by Eq. 1.2. For a star or object with mass m orbiting a mass M , the time-averaged potential energy is given by:

$$\langle V \rangle = -\frac{GmM(r)}{r}, \quad (1.3)$$

where G is the gravitational constant, r is the radius from the center and $M(r)$ is the mass enclosed within r . If the object has a circular orbit and a velocity v , its time-averaged kinetic energy is given by:

$$\langle T \rangle = \frac{1}{2}mv^2. \quad (1.4)$$

Using the virial theorem in Eq. 1.2, the object's velocity as a function of radius is given by:

$$v = \sqrt{\frac{GM(r)}{r}}. \quad (1.5)$$

Although Eq. 1.5 provides the velocity profile for the simplest example of an object in circular orbit, the general form remains consistent for more complicated cases, such as elliptical orbits and different (but symmetric) mass distributions. As the amount of stellar and gaseous matter at the edge of a galaxy is relatively small, the total enclosed mass should reach an asymptotic value for large radii. Therefore, Eq. 1.5 predicts that the velocities of objects near the edge of a galaxy should fall as $r^{-1/2}$.

This prediction was put to the test starting in the 1970's using astrophysical observations. Vera Rubin and Kent Ford used observed optical light from the Andromeda Galaxy to measure the velocity profile of ionized hydrogen, and soon after David Rogstad and Seth Shostak used 21-cm observations to measure the velocity profile of hydrogen gas in several galaxies [5]. These and other scientist all came to notice that the velocities of objects orbiting near the edges of galaxies do not fall as $r^{-1/2}$; instead, their velocities remain *constant*. Figure 1.2 shows a superposition of the rotation curves for several galaxies later measured by Rubin *et. al.*

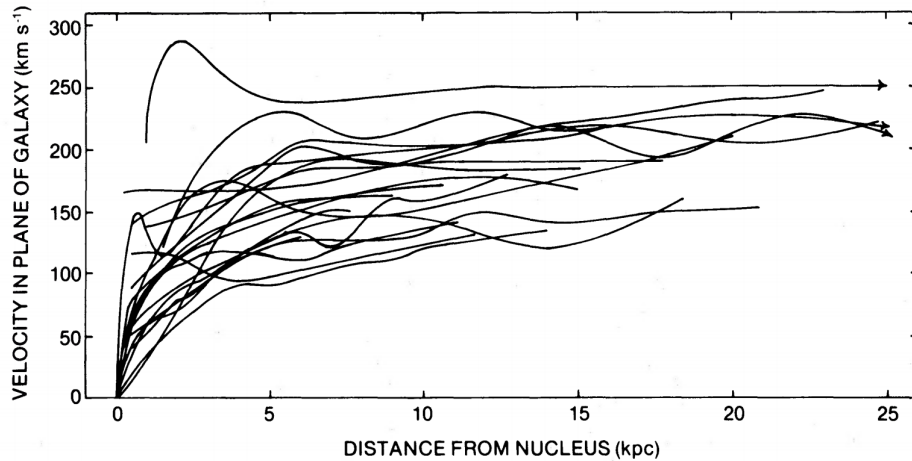


Figure 1.2: Superposition of the rotation curves for several galaxies. The velocity of objects far from the galactic core (nucleus) is relatively constant. Figure provided by Rubin *et. al.* [13].

Several hypotheses emerged to explain the observed rotation curves. One formally prevalent category of hypotheses assert that the theory of gravity is incorrect. The solution therefore is to introduce a

new theory of gravity, the most well-known being modified Newtonian dynamics (MOND). The basic premise of MOND is that Newton's second law can be modified to exhibit different behaviour at low accelerations [5]:

$$F = m \mu \left(\frac{a}{a_0} \right) a, \quad (1.6)$$

where $a_0 \sim 1.2 \times 10^{-10} \text{ m/s}^2$ and $\mu(a/a_0)$ is some unspecified function with the limits $\mu(a/a_0) \rightarrow 1$ for $(a/a_0) \gg 1$ and $\mu(a/a_0) \rightarrow (a/a_0)$ for $(a/a_0) \ll 1$. With this formulation, MOND can indeed explain the behaviour of galaxy rotation curves. The original formulation of MOND also presented problems with energy and momentum conservation, although more complex models have since been introduced to solve such issues [5]. More importantly to this discussion, theories of modified gravity are unable to explain other dark matter observations, such as the effects of gravitational lensing as outlined in Sec. 1.2.2. Despite these setbacks, MOND and modified theories of gravity continue to develop and evolve (see, for example, Ref. [14]).

Another hypothesis that can explain the observations made of galaxy rotation curves asserts that the mass distribution is incorrect. For a sphere with a radius-dependent mass density $\rho(r)$, the total enclosed mass at a distance r is given by:

$$M(r) = \int 4\pi r^2 \rho(r) dr. \quad (1.7)$$

Furthermore in the constant-velocity regime of Eq. 1.5, the mass distribution for objects with velocity v_{const} is $M(r) = v_{\text{const}}^2 r/G$. Equating this to Eq. 1.7 and taking the derivative in r , the mass density is given by:

$$\begin{aligned} 4\pi r^2 \rho(r) &= \frac{v_{\text{const}}^2}{G}, \\ \rho(r) &= \frac{v_{\text{const}}^2}{4\pi G r^2}. \end{aligned} \quad (1.8)$$

This demonstrates that the behaviour of rotation curves can be explained if the galactic mass is described by a density distribution that scales as r^{-2} . Not only does this suggest that most of the galactic mass is distributed further away from the galactic core, it also suggests that much of the mass is distributed far beyond any observable objects. The next question that naturally arises is what would cause such a mass distribution to exist in galaxies? With all of the combined evidence, it is now commonly thought that galaxies contain massive DM structures with a mass density that scales as r^{-2} . However the conclusion of DM is not necessarily apparent based on this evidence alone. Perhaps galaxies contain a significant amount of mass due to non-luminous but ordinary matter. Yet as Ref. [15] outlines, objects composed of ordinary matter such as stars with low luminosity and interstellar gas cannot account for the apparent mass distribution.

1.2.2 Gravitational Lensing

In Einstein's theory of general relativity (GR), light travels such that it follows the curvature of spacetime. As objects with mass cause spacetime to bend, GR predicts that light passing by a massive object can bend around it. This effect of gravitational lensing is similar to the effect caused by traditional optical lenses. With gravitational lenses, it is possible to view background objects that would otherwise be

obscured by a massive foreground object. In the simplest example, the angular deflection of light α due to a point-like lens with mass M is given by [16]:

$$\alpha = \frac{4GM}{rc^2} = \frac{2r_s}{r}, \quad (1.9)$$

where c is the speed of light, r is the distance between the light and the lens in the plane perpendicular to the observer, and $r_s = 2GM/c^2$ is the Schwarzschild radius. For massive lenses such as black holes where $r \gg r_s$, and in the limit of small angles, Eq. 1.9 provides a good approximation for angular deflection of light. If the background object, lens, and observer are all aligned, gravitational lensing can cause what are known as Einstein rings. Equation 1.9 also shows that by observing gravitational lensing, the mass of the lens can be inferred without knowing the contents of the lens itself.

In practice, observations of gravitational lensing are much more complex than the simple example described above. The most extreme (and stunning) examples of gravitational lensing fall under the category of strong lensing, where background objects are seen as multiple images and in giant arcs or rings around the lens. However most examples of gravitational lensing fall under the category of weak lensing, where background objects are only slightly sheared or distorted. In the weak lensing regime, the shear distortion of objects such as distant galaxies can alter their major-to-minor axis ratio by $\sim 2\%$, which is much smaller than the normal shape variation observed in galaxies [17]. Therefore weak lensing is not observed for individual objects, but rather for a collection of distant background objects along adjacent lines of sight where lensing effects are seen at a statistical level.

The most prominent example of gravitational lensing with respect to DM is the Bullet Cluster. The Bullet Cluster consists of two colliding clusters of galaxies^{††} and is composed of stars, X-ray emitting interstellar plasma, and, possibly, dark matter. During the collision of these clusters, the plasma and stellar components behave in different ways [18]. The stars, planets, and galaxies effectively act like collisionless particles. Conversely the colliding plasma, which accounts for most of the mass from ordinary matter in the Bullet Cluster, is significantly slowed by electromagnetic interactions. Therefore over the course of the collision, the stellar and plasma components are spatially decoupled [18], and can be separately observed with optical and X-ray telescopes sensitive to the emitted light. Independently, the mass distribution of the Bullet Cluster can be inferred through weak gravitational lensing, as shown by Fig. 1.3.

The result from Ref. [18] and shown in Fig. 1.3 is remarkable, and provides very strong evidence of the existence of DM. Specifically, the most simple theories of modified gravity would predict that the centers of mass determined from gravitational lensing should be aligned with the centers of mass of the ordinary matter (i.e. the more massive interstellar plasma). Yet this result shows with a high degree of certainty that the centers of the total mass do not align with the centers of the mass of ordinary matter. Therefore, the majority of the matter in the Bullet Cluster must come from some unknown and unseen substance. This result also provides evidence that DM is mostly collisionless, as the separate DM components from colliding clusters appear to have bypassed each other and the interstellar plasma unperturbed. More recent results have used similar observations to put constraints on the DM self-interacting cross section [19].

^{††}Strictly speaking, the Bullet Cluster is the smaller cluster that is moving away from the larger cluster. In practice, the name ‘‘Bullet Cluster’’ typically refers to the combined system of both clusters.

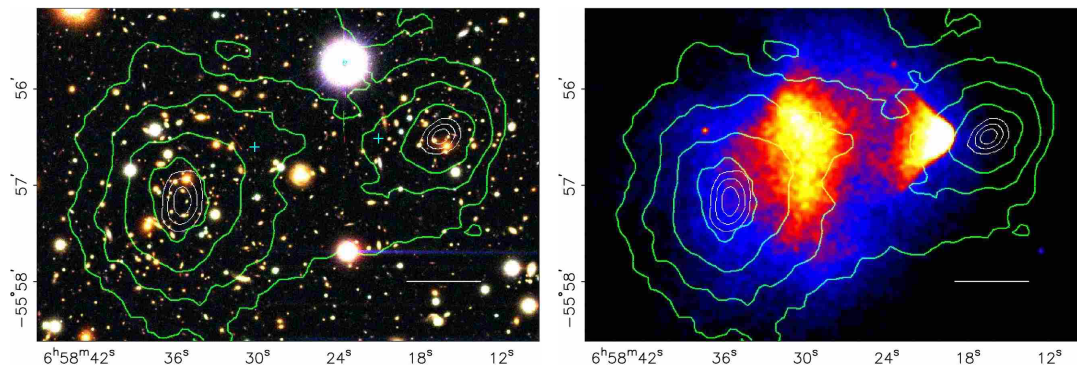


Figure 1.3: Images of the stellar (left) and X-ray emitting plasma (right) components of the Bullet Cluster. The green contour lines show the mass distribution determined by weak gravitational lensing. Note that the “peaks” of the contours do not align with the “peaks” of the colliding plasma. Figure provided by Ref. [18].

1.2.3 Cosmic Microwave Background

Perhaps the most compelling evidence for the existence of dark matter lies in the Cosmic Microwave Background (CMB). The CMB provides a snapshot of the early universe during the epoch of recombination. During recombination, the universe was an extremely hot and dense fluid of matter and radiation. At some point, this primordial fluid cooled enough that electrons and protons could combine to produce hydrogen atoms (i.e. recombination). With fewer charged particles to interact with, light was able to escape from the hot matter, leaving a faint radiation remnant that can be seen today. The temperature of this background radiation, however, is not *exactly* uniform. Rather there are tiny temperature fluctuations in the CMB, and it is in these anisotropies where the evidence of DM is hidden. Figure 1.4 shows the temperature fluctuations observed in the CMB.

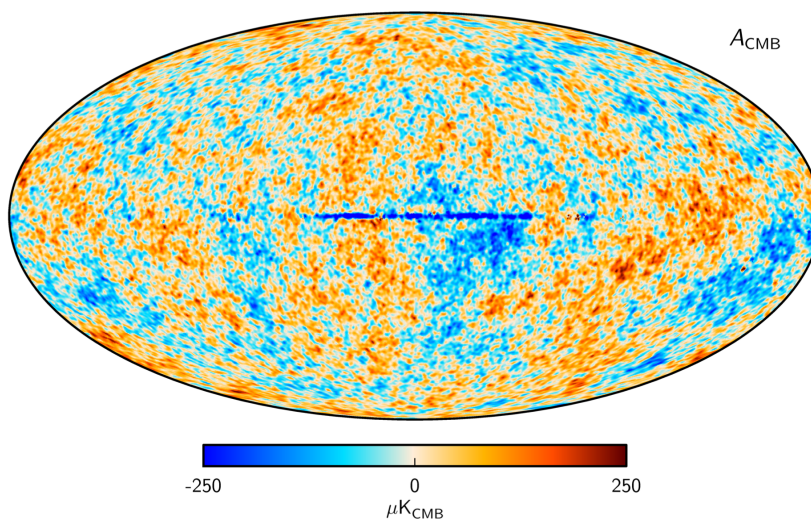


Figure 1.4: Temperature map of the Cosmic Microwave Background derived from *Planck*, WMAP, and 408 MHz observations. As is discussed in the text, these small temperature fluctuations are related to the composition of the universe. Figure provided by Ref. [9].

The composition of the universe is broken down into several components, including dark energy, matter (both dark and ordinary), and radiation. In cosmology, these components are parameterized by the dimensionless density parameter Ω_i , which is related to the energy density of each constituent. For a flat universe, the total density parameter of the universe Ω is [20]:

$$\Omega = \sum_i \Omega_i = \Omega_\Lambda + \Omega_M + \Omega_R = 1, \quad (1.10)$$

where Ω_Λ is the dark energy density, Ω_R is the radiation density, and $\Omega_M = \Omega_b + \Omega_{\text{DM}}$ is the combined density of baryonic (ordinary particles like protons and neutrons) and dark matter. As will become evident, the values of Ω_i have a large impact on the temperature fluctuations observed in the CMB.

An intuitive explanation of the CMB temperature fluctuations can be found in Ref. [21]. As previously mentioned, the recombination epoch consisted of an extremely hot and dense primordial fluid. This fluid was composed of baryonic matter and radiation, which were tightly coupled by scattering processes between charged particles and light. Moreover the fluid exerted an outward pressure due to the density of the radiation. Conversely dark matter at this time was largely decoupled from the baryonic-radiation fluid, yet still interacted with the fluid through gravity. The gravity of the DM caused the fluid to compress into pockets of over-dense regions, which by matter conservation also created under-dense regions. The force due to the fluid pressure acted to move the fluid out of the over-dense regions and into under-dense regions. These competing forces resulted in oscillating compressions and decompressions of the fluid, a process analogous to sound waves. At the end of recombination, the radiation escaped from the baryonic matter, and the density of the fluid ceased to oscillate. Meanwhile, the leftover baryonic matter was frozen into a pattern of low-density and high-density regions. The frozen-out high-density regions of matter are the seeds that would eventually evolve into the large-scale structure of the universe. Light that escaped from high-density regions has on average a higher temperature than light that escaped from low-density regions. This means that the temperature fluctuations observed in the CMB are also a measure of the density fluctuations of the primordial fluid at the end of recombination.

Using spherical harmonics, the temperature functions observed in the CMB can be transformed into the power spectrum seen in Fig. 1.5. Here, the x-axis is represented by ℓ , the multipole number of the spherical harmonics that is related to angular scale in the sky ($\ell = 1$ corresponds to an angle of 180° across the sky). The y-axis is a measure of the amount of temperature fluctuation observed at each ℓ . The multiple peaks that can be observed in Fig. 1.5 relate regions of the primordial fluid that were caught in either maximum density or minimum density at the end of recombination. For example, the first peak corresponds to regions that only had time to collapse once before the end of recombination. The second peak corresponds to regions that only had time to collapse and fully expand again, and so on. Importantly, the relative heights of these peaks are influenced by the composition of the universe, with the abundance of DM having a significant impact on the higher multipole peaks. This relationship can be modelled numerically, and by fitting the models to the CMB power spectrum the relative abundances of each constituent can be found.

The latest constraints on the relative abundances come from the *Planck* satellite [22], with the best-fit result shown by the red curve in Fig. 1.5. Specifically for baryonic and dark matter, the density parameters are found to be $\Omega_b = 0.0491 \pm 0.00035$ and $\Omega_{\text{DM}} = 0.264 \pm 0.0033$, respectively. The ratio of

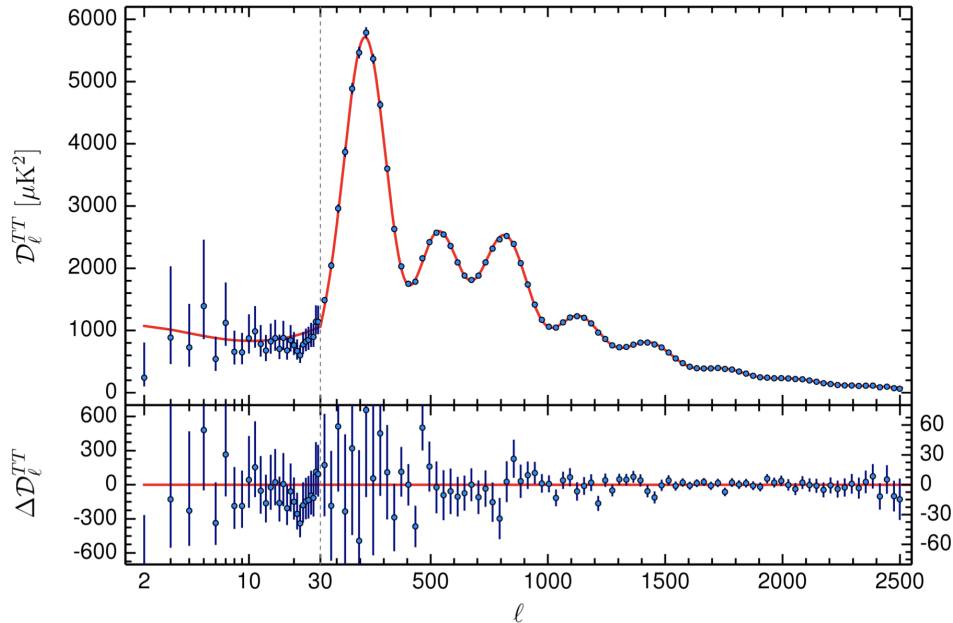


Figure 1.5: CMB power spectrum that is a measure of the amount of temperature fluctuation as a function of the multipole number ℓ . The relative heights and positions of the peaks are related to the density composition of the universe and help determine the relative abundance of dark energy, dark matter, baryonic matter, and radiation. The data points are found from observations of the CMB, and the red curve is the best-fit result of numerical models. Figure provided by Ref. [22].

dark matter to baryonic matter is therefore given by:

$$\frac{\Omega_{\text{DM}}}{\Omega_b} = \frac{0.264}{0.0491} \approx 5. \quad (1.11)$$

This result is not only evidence that non-baryonic dark matter exists, but also leads to the often quoted figure that $\sim 85\%$ of all matter in the universe is dark! It is hard to understate the impressiveness of this CMB measurement and the results that are concluded from it. There are many more interesting details and observations that are not discussed here, and the reader is encouraged to see Refs. [20, 22] and references therein.

1.3 Properties of Dark Matter

Many properties of DM have been argued based on astrophysical and cosmological observations and studies. It is these properties that form the basis of some of the most commonly proposed DM models. The following list provides a brief description of the main properties attributed to DM. The reader should keep in mind that these properties are not certain, and various DM models assume properties that differ from the ones listed here.

- *Dark Matter is Neutral:* It is generally accepted that DM is electrically neutral. If DM particles did carry a charge, they would interact with light and would therefore be visible. However some models have abandoned this assumption to place an upper bound on the charge of DM particles [23].

- *Dark Matter is Non-baryonic*: There is very strong evidence to suggest that DM is not comprised of ordinary (baryonic) matter. Both the CMB observations outlined in Sec. 1.2.3 and studies of Big Bang nucleosynthesis conclude that baryonic matter does not account for the missing dark matter mass. Regarding Big Bang nucleosynthesis, a larger abundance of baryonic matter in the early universe would result in a drastically different abundance of isotopes than what is observed. Before such evidence was found, several models of baryonic DM were proposed (one example is given in Sec. 1.5.4).
- *Dark Matter is Thermal*: The arguments for thermal or non-thermal DM attempt to explain how the present abundance of DM came to be. In the case of thermal dark matter, the DM particles in the early universe are in thermal equilibrium with the primordial plasma. During this time the DM particles are created and destroyed at equal rates. The creation of DM particles is expected to occur from Standard Model particles through some unknown mechanism, whereas the particles are destroyed through a presumptive self-annihilation process. As the universe cools, the number density of DM particles decreases until the particles are so far spread out that the rate of self-annihilation tends to zero. The DM is then “frozen out”, leaving behind a relic abundance that is observed today. Several models do not require DM to be thermal, and hypothesize other processes to explain the current abundance of DM. For example in a “freeze-in” scenario, there may be little or no DM in the early universe, and Standard Model particles can instead annihilate to produce the current abundance of DM.
- *Dark Matter is Cold*: Dark matter that is “cold” means that DM particles travel slowly compared to the speed of light (i.e. non-relativistically). In contrast, “hot” DM models predict that particles travel at relativistic speeds. This property is important to explain structure formation in the universe. Cold DM is expected to aggregate (i.e. clump) around smaller-scale objects like galaxies, whereas hot DM would clump around larger-scale objects like galaxy clusters or superclusters. Observations of the large-scale structure of the universe favour the cold DM paradigm, although some discrepancies exist [24]. Other models propose intermediate solutions such as “warm” DM.
- *Dark Matter is Long-lived*: The evidence of dark matter’s impact on the CMB and the structure formation of the universe suggests that DM has been present since the early universe. It is therefore quite reasonable to conclude that DM has a very long lifetime. Many models predict that DM particles are stable, meaning that they are the lightest particle in some unknown “dark sector”. However stable DM is not a requirement; models that predict very weak couplings may propose that DM is unstable but has a lifetime longer than the age of the universe.

1.3.1 Local Dark Matter

Observations like galaxy rotation curves (Sec. 1.2.1) and gravitational lensing (Sec. 1.2.2), as well as the paradigm of cold DM, imply the existence of structures of DM that form around galaxies known as DM halos. DM halos are predicted to envelop the entire galactic disc and extend far beyond the edge of the visible matter of a galaxy. Indeed the Earth itself is constantly drifting through a dark matter halo (or equivalently dark matter particles are constantly drifting through the Earth). As will become evident in Sec. 1.5, predictive models for observing DM from Earth depend greatly on the properties of DM in Earth’s local vicinity. One such parameter is the local dark matter density ρ_{DM} . The importance of

having an independent measurement of ρ_{DM} should not be ignored; without this value, it would not be possible to set constraints on potential DM interactions.

The first estimates of ρ_{DM} were made in the 1920's and 1930's by Jacobus Kapteyn, Jan Oort, and James Jeans by observing stellar kinematics [5], and since then numerous more measurements have been made. Reference [25] provides a detailed summary and analysis of the measurements made of ρ_{DM} . As was done by Kapteyn, Oort, and Jeans, estimates of ρ_{DM} are typically found by observing the position and velocity of “tracer” stars moving in a gravitational potential. Following Ref. [25], a population of these tracer stars will obey the collisionless Boltzmann equation:

$$\frac{df}{dt} = \frac{\partial f}{\partial t} + \nabla_x f \cdot \vec{v} - \nabla_v f \cdot \nabla_x \Phi = 0, \quad (1.12)$$

where $f(\vec{x}, \vec{v})$ is the distribution function of stars with positions \vec{x} and velocities \vec{v} , and Φ is the gravitational potential. In the case of Newtonian weak field gravity, the force $\nabla_x \Phi$ is related to the total mass density ρ through Poisson's equation:

$$\nabla_x \nabla_x \Phi = \nabla_x^2 \Phi = 4\pi G \rho, \quad (1.13)$$

where G is the gravitational constant. Here, ρ is the total mass density from all the stars, gas, and dark matter in the system. Therefore solving Eq. 1.12 for a set of tracer stars can provide an estimate of ρ_{DM} . However in practice, solving for Eq. 1.12 outright is very difficult. Reference [25] describes several methods for solving Eq. 1.12, each with their own advantages and disadvantages. A summary of ρ_{DM} measurements that have been made over time is shown in Fig. 1.6.

The currently accepted value of the local DM density is $\rho_{\text{DM}} \sim 0.3 \text{ GeV}/\text{cm}^{3\ddagger}$, and is the value that is used for the DM models computed in Sec. 1.5. Lastly, Ref. [25] argues that the DM density as measured for the local stellar vicinity of the Sun is a reasonable approximation for the DM density around the very tiny volume occupied by a detector on Earth, assuming that baryonic matter does not significantly alter the DM distribution. For example, even if 10% of the DM mass fraction exists in DM subhalos with densities larger than ρ_{DM} , the most likely DM density around a detector on Earth is shifted only to $\sim 0.9\rho_{\text{DM}}$, with a very small probability that the density is larger than ρ_{DM} .

Another important property of local DM is its velocity distribution, as DM particles travelling at different speeds can deposit different amounts of energy if they collide with an Earth-bound detector. DM particle velocities are typically modelled using the Standard Halo Model (SHM), where the DM halo is assumed to be an isotropic and isothermal sphere with a density that scales as $\rho \propto r^{-2}$, where r is the distance from the galactic core. Under these assumptions, the DM particles with velocities \vec{v} are expected to obey a Maxwellian distribution in the galactic rest frame [26]:

$$f_{\text{gal}}(\vec{v}) = \begin{cases} \frac{N}{(2\pi\sigma_v)^{2/3}} e^{-\frac{|\vec{v}|^2}{2\sigma_v^2}} & |\vec{v}| < v_{\text{esc}}, \\ 0 & |\vec{v}| \geq v_{\text{esc}}, \end{cases} \quad (1.14)$$

where N is a normalization constant, and σ_v is the one-dimensional velocity dispersion that is related to the local circular velocity v_c by $\sigma_v = v_c/\sqrt{2}$. In principle, the distribution function can extend to infinity. However in the SHM, $f_{\text{gal}}(\vec{v})$ is artificially truncated at the escape velocity of the galaxy, v_{esc} .

[‡]Despite what the units suggest, ρ_{DM} is indeed a mass density rather than an energy density. Although the correct units of ρ_{DM} are $\text{GeV c}^{-2}\text{cm}^{-3}$, it is common to report it in units of GeV/cm^3 .

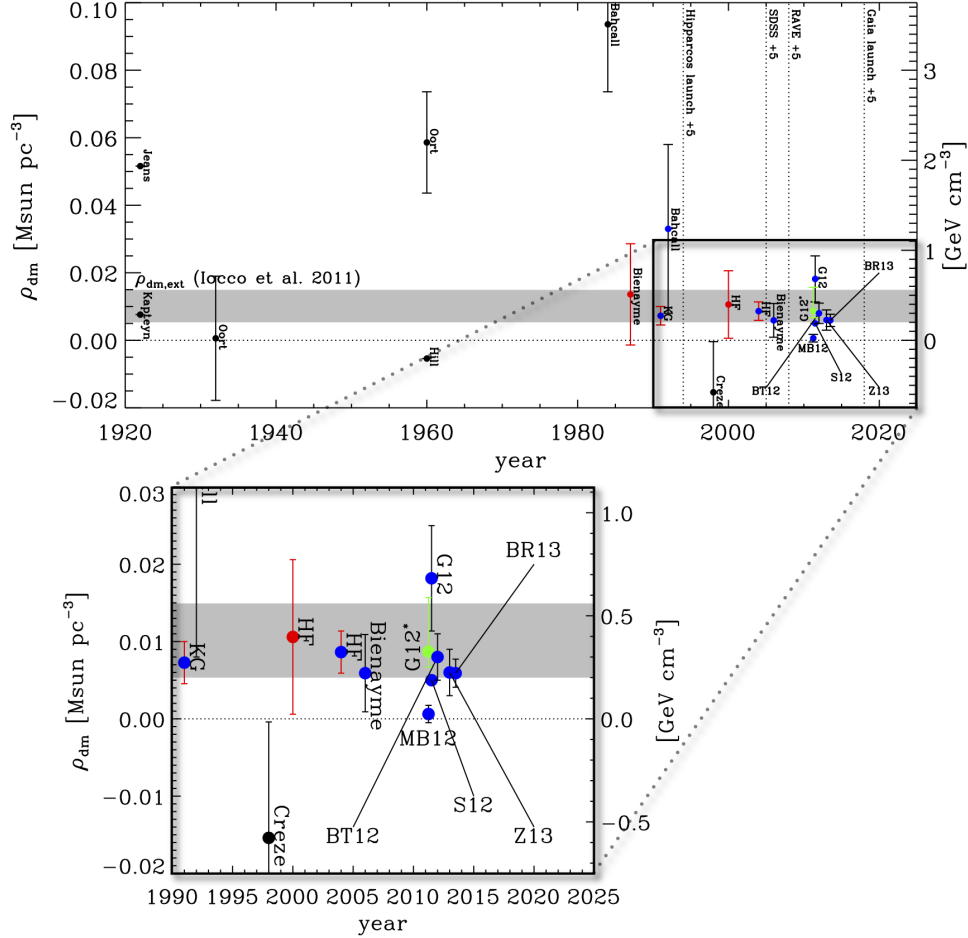


Figure 1.6: Summary of the measurements of the local dark matter density ρ_{DM} made over time. The currently accepted value of ρ_{DM} is $\sim 0.3 \text{ GeV/cm}^3$. The grey band is the DM density extrapolated to the entire DM halo. Figure provided by Ref. [25].

Typical values for v_c and v_{esc} are $\sim 220 \text{ km/s}$ and $\sim 550 \text{ km/s}$, respectively [26]. For DM experiments that take place on Earth, it is additionally important to account for the Earth's motion relative to the DM halo. This can be done with the simple transformation $\vec{v} \rightarrow \vec{v} + \vec{v}_E$, where \vec{v}_E is the velocity of the Earth. The velocity distribution of DM particles can then be written as:

$$f(\vec{v}) = f_{\text{gal}}(\vec{v} + \vec{v}_E). \quad (1.15)$$

\vec{v}_E accounts for the Sun's motion around the galaxy, as well as the Earth's motion around the Sun. It can therefore vary by about $\pm 15 \text{ km/s}$ based on the time of year. This slight velocity variation can lead to an annual modulation of the expected rate of DM interactions that some DM experiments may be sensitive to. Some other models propose that a fraction of the local DM may also be comprised of non-galactic DM particles that not gravitationally bound to the Milky Way and have velocities greater than the galactic escape velocity [27]. However this dissertation only considers the SHM to describe the local dark matter.

1.4 Searching for Dark Matter

Section 1.2 outlined the strong evidence that points to the existence of DM, and Sec. 1.3 described some of its inferred properties. Yet the most elusive question remains unanswered: What *is* dark matter? The most effective way to answer this question is to *find* dark matter. A confirmed detection of dark matter particles would start to reveal key information about this missing mass, such as its particle mass, the forces that mediate its interactions, the method and rate at which it interacts with Standard Model particles, and if it is comprised of more than one type of particle. In general there are three methods of dark matter particle detection: direct detection, indirect detection, and production.

- *Direct Detection:* Direct detection experiments aim to directly observe the interactions of DM particles with some target medium as they pass through the Earth. The most common interaction mechanism hypothesized has been DM-nucleus scattering, which would induce low-energy recoils in the target medium that can be measured. This category encompasses a broad range of detection techniques. Experiments performed by the SuperCDMS [28], EDELWEISS [29], and CRESST [30] collaborations use cryogenically-cooled crystal detectors to measure ionization or heat energy produced by particle interactions. Noble gas detectors measure scintillation produced by particle interactions with liquid xenon or argon, and are used by collaborations such as XENON [31], DEAP [32], DarkSide [33], PandaX [34], and LUX [35]. The SENSEI [36] and DAMIC [37] collaborations use charge-coupled devices to detect ionization over an array of pixels. Other detector technologies include bubble chambers used by the PICO collaboration [38], time projection chambers used by the DRIFT and XENON collaborations [39, 31], and resonant detectors used to probe extremely low-mass DM candidates [40].
- *Indirect Detection:* Indirect detection experiments search for the products produced by the self-annihilation of DM particles or, if dark matter is unstable, by the decay of DM particles. These products are primarily expected to be either high-energy gamma-rays or Standard Model particle-antiparticle pairs. Experiments often look for an excess of decay products around massive objects such as stars or black holes, where the clumping of DM near these objects would significantly increase the probability of self-annihilation. For example, the Fermi Gamma-ray Space Telescope has searched for gamma-ray excesses around the supermassive black hole at the center of the Milky Way, and has performed dwarf spheroidal galaxies searches to set constraints on the self-annihilation cross section for various annihilation channels [41]. Furthermore, measurements of the cosmic ray excess of positrons obtained by PAMELA and AMS-02 have been used to constrain DM annihilation [42, 43].
- *Production:* Dark matter particles may also be found by producing them in collider and beam dump experiments. For example, DM is searched for with the Large Hadron Collider by examining the particles produced from the collision of proton beams [44], as well as with the Belle II detector using the SuperKEKB electron-positron collider [45]. Because DM rarely interacts with Standard Model particles, it can only be detected as missing mass or momentum among the collision products. Therefore a discovery of DM through production mechanisms would need to be confirmed using other detection methods.

The vast amount of DM search experiments provides a landscape that is both competitive and complementary. Different detection designs and techniques are better suited to search for certain DM

models and interaction channels. Additionally any potential discovery can be corroborated by other experiments that are also sensitive to the proposed DM interaction. The experiments and analyses presented in this dissertation are for direct dark matter searches. The following section describes various models of DM that are relevant for this method of detection.

1.5 Dark Matter Candidates

Since the observance of DM through astrophysical studies, many DM candidates have been proposed. Candidates are derived as plausible particles predicted by various particle theories that can explain the observed abundance of DM in the universe. In general, DM particles exist in an unknown “dark sector”, and interact with known SM particles through some mediating force. This unknown dark sector may be comprised of several types of DM particles, or rather just a single type of DM particle. One of the earliest proposed DM candidates is known as the Weakly Interacting Massive Particle (WIMP).

The argument for WIMP dark matter stems from determining the velocity-averaged self-annihilation cross section $\langle\sigma v\rangle$ that results in the current DM density seen today. As described in detail in Ref. [46], the observed relic abundance of stable DM particles remaining after the freeze-out period corresponds with $\langle\sigma v\rangle \approx 3 \times 10^{-27} \text{ cm}^3/\text{s}$. This value also happens to be roughly similar to the self-annihilation cross section for a new particle with weak-scale interactions and a mass of $\sim 100 \text{ GeV}/c^2$ [46]. Amazingly, theories that extend beyond the SM independently predict a new particle in this mass range [47]. Specifically, versions of the Supersymmetry (SUSY) model [46, 20, 48] predict a new particle with a mass between $\sim 20\text{--}300 \text{ GeV}/c^2$ (see Fig. [44] in Ref. [46]). This remarkable coincidence between astrophysical observation and particle theory has been dubbed the “WIMP miracle”, and as a result WIMPs have been the primary search candidate of direct-detection experiments over the past several decades.

Although WIMP searches are still ongoing, as will be discussed later in this section, the favoured parameter space of the proposed DM-SM interaction for WIMPs has almost entirely been excluded. As a result, several other DM candidates that rely on different DM-SM interactions have emerged over the past few decades. This section summarizes the WIMP model, as well as various other models of low-mass DM candidates. The particular models for low-mass candidates are the focus of the DM search analyses presented in Chapters 5 and 6.

1.5.1 WIMPs

The summary of the WIMP model presented here follows the derivations provided in Refs. [47, 49, 50]. For this model, the interaction considered is a WIMP χ with mass m_χ scattering off of a nucleus inside a target material and depositing some amount of recoil energy E_R . For a target material with a total mass of m_T and nucleus mass m_N , the total number of target nuclei is m_T/m_N . If the cross section of WIMP-nucleus scattering is σ , the effective area of the target is $\sigma \cdot m_T/m_N$. The flux of DM particles passing through the detector is $n_\chi \cdot \langle v \rangle$, where $n_\chi = \rho_{\text{DM}}/m_\chi$ is the number density of WIMPs and $\langle v \rangle$ is the average WIMP velocity. Putting this all together, the number of expected interactions N detected over some time t is given by:

$$N = t \cdot \sigma \cdot \frac{m_T}{m_N} \cdot \frac{\rho_{\text{DM}}}{m_\chi} \cdot \langle v \rangle. \quad (1.16)$$

More typically, interactions are expressed as an event rate R , which is measured as the number of events per unit time per unit mass of the detector. Expressing Eq. 1.16 in terms of R gives:

$$\begin{aligned} R &= \frac{\rho_{\text{DM}}}{m_N m_\chi} \sigma \cdot \langle v \rangle \\ &= \frac{\rho_{\text{DM}}}{m_N m_\chi} \int \sigma \cdot v f(\vec{v}) d^3 \vec{v}, \end{aligned} \quad (1.17)$$

where $\langle v \rangle$ has been substituted by an integral over the velocity distribution $f(\vec{v})$ of DM particles, as described by Eq. 1.15. Equation 1.17 can further be expressed as a differential rate over the possible recoil energies E_R :

$$\frac{dR}{dE_R} = \frac{\rho_{\text{DM}}}{m_N m_\chi} \int \frac{d\sigma}{dE_R} \cdot v f(\vec{v}) d^3 \vec{v}. \quad (1.18)$$

The relative speed of WIMPs and nuclei is on the order of $\mathcal{O}(100)$ km/s, which means that scattering interactions occur in the non-relativistic limit. For a 2-body elastic scattering collision, the final velocity of a nucleus in the lab frame, v_N , assuming it is initially at rest, is given by:

$$\begin{aligned} v_N &= v \frac{2m_\chi}{m_\chi + m_N} \sin\left(\frac{\theta^*}{2}\right) \\ &= v \frac{2\mu_N}{m_N} \sin\left(\frac{\theta^*}{2}\right) \end{aligned} \quad (1.19)$$

where v still denotes the initial WIMP velocity in the lab frame, θ^* is the scattering angle in the center of mass frame, and

$$\mu_N \equiv \frac{m_\chi m_N}{m_\chi + m_N} \quad (1.20)$$

is the WIMP-nucleus reduced mass. The recoil energy deposited by the WIMP to the nucleus is therefore given by:

$$\begin{aligned} E_R &= \frac{1}{2} m_N v_N^2 \\ &= \frac{1}{2} m_N v^2 \frac{4\mu_N^2}{m_N^2} \sin^2\left(\frac{\theta^*}{2}\right) \\ &= v^2 \frac{2\mu_N^2}{m_N} \frac{1}{2} (1 - \cos\theta^*) \\ &= \frac{\mu_N^2 v^2}{m_N} (1 - \cos\theta^*). \end{aligned} \quad (1.21)$$

Equation 1.21 can further be used to determine the minimum WIMP speed v_{\min} that can result in a recoil energy of E_R :

$$v_{\min} = \sqrt{\frac{m_N E_R}{2\mu_N^2}}. \quad (1.22)$$

Equation 1.22 provides an important relationship between v_{\min} and the mass of the target nuclei. In the region where $m_\chi < m_N$, v_{\min} increases with m_N . This means that a target with heavier nuclei requires a larger minimum WIMP velocity to produce a recoil energy of E_R compared to a target with lighter nuclei. For scattering events in the non-relativistic limit, the scattering cross section is approximately isotropic. This means that the cross section over all scattering angles θ^* in the center of mass frame is constant between $\cos\theta^* = -1$ and $\cos\theta^* = 1$, and therefore $d\sigma/d\cos\theta^* = \sigma/2$. The differential cross

section $d\sigma/dE_R$ can be found simply by using the chain rule:

$$\begin{aligned}\frac{d\sigma}{dE_R} &= \frac{d\sigma}{d\cos\theta^*} \frac{d\cos\theta^*}{dE_R} \\ &= \frac{\sigma}{2} \frac{m_N}{\mu_N^2 v^2} \\ &= \frac{m_N}{2\mu_N^2 v^2} \sigma.\end{aligned}\tag{1.23}$$

The cross section term σ and the corresponding differential term $d\sigma/dE_R$ that have been used up to this point have hidden a lot of details relating to WIMP-nucleus scattering. To start, it is important to note the momentum transfer $q = \sqrt{2m_N E_R}$ that occurs from WIMP scattering. The differential cross section can be decoupled into a momentum-independent term $(d\sigma/dE_R)_0$ and a form factor term $F(E_R)$:

$$\begin{aligned}\frac{d\sigma}{dE_R} &= \left(\frac{d\sigma}{dE_R} \right)_0 (F(E_R))^2 \\ &= \frac{m_N}{2\mu_N^2 v^2} \sigma_0 F^2(E_R),\end{aligned}\tag{1.24}$$

where σ_0 is the cross section at zero momentum transfer. The $(d\sigma/dE_R)_0$ term is the differential cross section obtained if the nucleus is treated as a point-like target. $F(E_R)$ encodes the dependence on the momentum transfer and accounts for the suppression that occurs when the substructures within the target nuclei are considered. Furthermore, the total WIMP-nucleus cross section $\sigma_{N,0}$ can be separated into a spin-dependent (SD) and spin-independent (SI) contribution:

$$\sigma_{N,0} = \sigma_{N,0}^{\text{SD}} + \sigma_{N,0}^{\text{SI}}.\tag{1.25}$$

The distinction between these contributions relates to the particular coupling of the WIMP to the quarks inside the nucleus. Spin-dependent and spin-independent refers to whether the coupling depends on the net spin of the target nucleus. The SD term arises from a axial-vector coupling, with the cross section given by:

$$\sigma_{N,0}^{\text{SD}} = \frac{32G_F^2 \mu_N^2}{\pi} \frac{J+1}{J} (a_p \langle S_p \rangle a_n \langle S_n \rangle)^2,\tag{1.26}$$

where G_F is Fermi's constant, J is the total nuclear spin, $\langle S_{p,n} \rangle$ are the expectations values of the proton and neutron spins, and $a_{p,n}$ are the couplings of the WIMP to protons and neutrons. This contribution, however, can only be explored using target materials with a non-zero total nuclear spin, such as fluorine. Other materials, including germanium (Ge) and silicon (Si), are unable to probe this type of interaction for this reason*. The SI term primarily arises from a scalar coupling, with the cross section given by:

$$\sigma_{N,0}^{\text{SI}} = \frac{4\mu_N^2}{\pi} (Zf_p + (A-Z)f_n)^2,\tag{1.27}$$

where A is the number of nucleons, Z is the number of protons, and $f_{p,n}$ are the couplings of the WIMP to protons and neutrons. In most cases, the coupling to protons and neutrons are taken to be similar, so $f_p \approx f_n = f$ and

$$\sigma_{N,0}^{\text{SI}} = \frac{4\mu_N^2}{\pi} A^2 f^2.\tag{1.28}$$

*For material like Si and Ge, the most naturally abundant isotope has no nuclear spin. However spin-dependent interactions can still be probed by considering less common yet stable isotopes, such as ^{73}Ge [51].

In order to compare and combine results from experiments that use different target materials, the WIMP-*nucleon* cross section $\sigma_{n,0}$ must be decoupled from the WIMP-*nucleus* cross section $\sigma_{N,0}$. For the SI interaction, this is done by defining $\sigma_{n,0}$ as:

$$\sigma_{n,0}^{\text{SI}} \equiv \frac{4\mu_n^2}{\pi} f^2, \quad (1.29)$$

where μ_n^2 is the WIMP-nucleon reduced mass. Thus the SI cross section for any target nucleus containing A nucleons is simply:

$$\sigma_{N,0}^{\text{SI}} = \sigma_{n,0}^{\text{SI}} \frac{\mu_N^2}{\mu_n^2} A^2. \quad (1.30)$$

Putting this all together, the expected differential event rate for spin-independent WIMP scattering can be written as:

$$\begin{aligned} \frac{dR}{dE_R} &= \frac{\rho_{\text{DM}}}{m_N m_\chi} \int_{v_{\text{min}}}^{\infty} \left(\frac{d\sigma}{dE_R} \right)^{\text{SI}} \cdot v f(\vec{v}) d^3\vec{v} \\ &= \frac{\rho_{\text{DM}}}{m_N m_\chi} \int_{v_{\text{min}}}^{\infty} \frac{m_N}{2\mu_N^2 v^2} \sigma_{N,0}^{\text{SI}} F^2(E_R) \cdot v f(\vec{v}) d^3\vec{v} \\ &= \frac{\rho_{\text{DM}}}{2\mu_N^2 m_\chi} \sigma_{N,0}^{\text{SI}} F^2(E_R) \int_{v_{\text{min}}}^{\infty} \frac{1}{v} f(\vec{v}) d^3\vec{v} \\ &= \frac{\rho_{\text{DM}}}{2\mu_N^2 m_\chi} \sigma_{n,0}^{\text{SI}} \left(\frac{\mu_N}{\mu_n} \right)^2 A^2 F^2(E_R) \int_{v_{\text{min}}}^{\infty} \frac{1}{v} f(\vec{v}) d^3\vec{v}. \end{aligned} \quad (1.31)$$

The bounds of integration of the velocity term in Eq. 1.31 are from the previously defined v_{min} to infinity. However there is an implicit maximum velocity set by the escape velocity of the galaxy, normally taken as $v_{\text{esc}} \approx 550$ km/s [26]. Lastly, the form factor term $F(E_R)$ is typically found experimentally for various elements, as shown in Refs. [46, 49]. For lighter nuclei, it can often be approximated by unity, $F(E_R) \approx 1$, and thus $\sigma_N^{\text{SI}} \approx \sigma_n^{\text{SI}}$. Figure 1.7 shows the total event rate (found by integrating Eq. 1.31 over E_R) as a function of WIMP mass for Si and Ge, assuming a SI WIMP-nucleon cross section of $\sigma_n^{\text{SI}} = 10^{-41}$ cm². Also shown are the differential event rates at various WIMP masses for a Si target.

Figure 1.8 shows the SI WIMP-nucleon cross section parameter space and the exclusion limits of various recent experiments. Many experiments using different techniques and different target materials have been able to further exclude smaller values of σ_n^{SI} and push the sensitivity to smaller WIMP masses. The type of target material that is used determines which mass range a given experiment is sensitive to. Take, for instance, the number density of DM particles ρ_{DM}/m_χ found in Eq. 1.31. Large WIMP masses are expected to result in a lower interaction rate because there is a smaller abundance of WIMPs to interact with the detector. For this reason, heavier target materials are better suited for WIMP searches above ~ 10 GeV/ c^2 (note the A^2 dependence in Eq. 1.31). Experiments such as XENON1T [52] and PandaX [53] use liquid xenon as the target material, which also benefits from easy scalability to obtain large fiducial volumes and exposures. Conversely, lighter target materials have better sensitivity to WIMP masses $\lesssim 10$ GeV/ c^2 due to the kinematics of WIMP-nucleus scattering. This includes the germanium and silicon targets used by the SuperCDMS experiment. These lighter target materials typically come in the form of solid-state detectors which are much harder to scale. However the lack of scalability is less important due to the expected increased abundance of WIMPs in this mass range.

Despite the progress made by many scientists and collaborations to improve the mass range of and sensitivity to potential WIMP interactions, it is hard not to notice in Fig. 1.8 that the exclusion limits

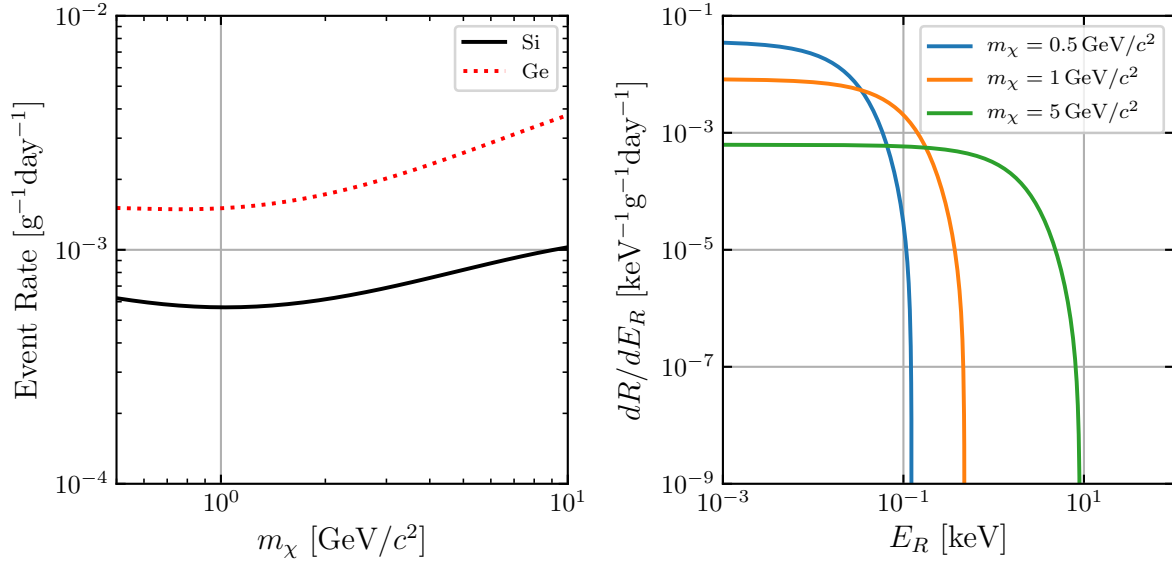


Figure 1.7: Left: expected event rate for WIMP-nucleus scattering as a function of WIMP mass m_χ for Si and Ge, assuming a spin-independent (SI) WIMP-nucleon cross section of $\sigma_n^{\text{SI}} = 10^{-41} \text{ cm}^2$. Right: differential event rate as a function of the nuclear recoil energy E_R at various WIMP masses for Si.

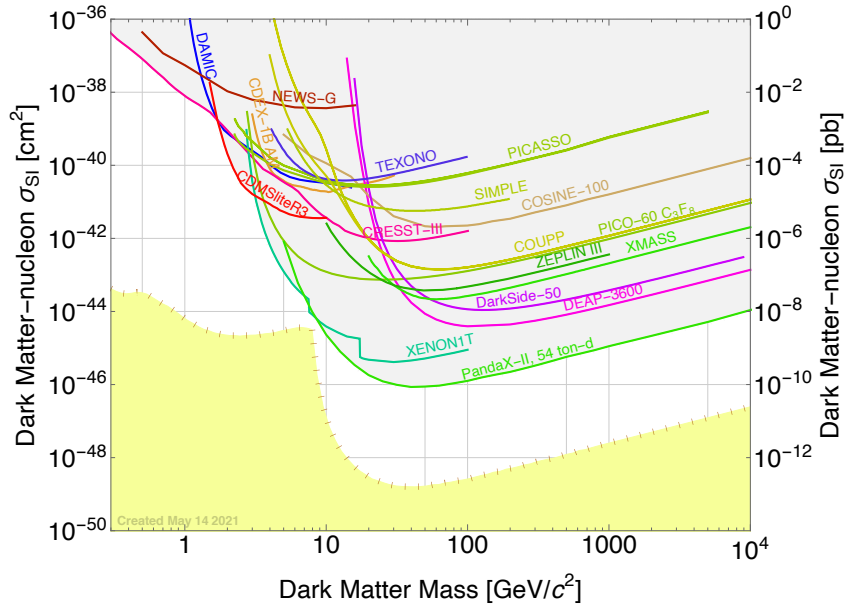


Figure 1.8: Parameter space of the spin-independent (SI) WIMP-nucleon scattering cross section σ_n^{SI} over WIMP mass. The curves shown are the exclusion limits on σ_n^{SI} obtained by various DM search experiments over recent years [54, 55, 56, 57, 58, 59, 60, 61, 62, 53, 63, 64, 65, 66, 52, 67, 68]. The yellow-shaded region is the neutrino floor for a Si target [69], as described in the text. This plot was produced using the SuperCDMS Limit Plotter v5.16.

are all nearing what is called the neutrino floor. The neutrino floor arises from coherent neutrino-nucleus scattering from neutrinos that originate from several astrophysical sources such as the Sun, the atmosphere, and diffuse supernovae [69]. As detectors become more sensitive, there is a greater ability

to detect these neutrino interactions. At some point the neutrino background becomes dominant over the expected WIMP signal and, at some masses, can even mimic the shape of the expected WIMP signal. Not being able to distinguish the WIMP signal from the neutrino background is what limits the discovery potential. To summarize Ref. [69], the neutrino floor at each WIMP mass is defined as the value of σ_n^{SI} such that if the true value of σ_n^{SI} was larger, there would be a 90% chance of detecting the WIMP signal over the neutrino background with at least a 3σ confidence level. The neutrino floor differs depending on the target material, and assumes no directional-detection capability. Overall, the lack of discovery of the ‘‘WIMP miracle’’ SUSY particle, as well as the ongoing approach to the neutrino floor, has led experiments and collaborations to extend the WIMP search to lower masses (such as the SuperCDMS experiment), as well as to consider other DM candidates.

1.5.2 Light Dark Matter

As mentioned in the previous sub-section, there has been growing interest in considering other DM candidates than span different mass ranges. One such class of candidates are DM particles lighter than the WIMP, with masses in range of keV–GeV/ c^2 , known as light dark matter (LDM). The distinction between LDM and WIMPs may at first seem superficial, but there are several significant differences between these models. If low mass DM were linked to the same weak-scale mediators as the WIMP, the relic abundance of DM would be much larger than what is observed. This puts a lower bound of $\sim 2\text{ GeV}/c^2$ on the mass of the WIMP, known as the Lee-Weinberg bound [70]. Thus for LDM, the relic abundance is explained by introducing a new force mediator that enables interactions between LDM and the SM. Furthermore, LDM interacts with the target material primarily via electron scattering, in contrast to WIMPs that undergo nuclear scattering. The LDM model explained here follows the work presented in Ref. [71]. As will become evident, electron scattering introduces a lot more complexities compared to the WIMP model, so the reader is encouraged to refer to Refs. [71, 72, 73, 74] and references therein for more details.

Consider LDM particles χ with mass m_χ that interact with SM particles via a new force mediator. This new force mediator can take the form of a gauge boson A' with mass $m_{A'}$ in some dark sector that includes a $U(1)_D$ gauge group that can kinetically mix with the SM hypercharge $U(1)_Y$ gauge group. A' can therefore mediate interactions between DM particles and charged particles, including electrons. Following Refs. [71, 75], the underlying LDM-electron scattering cross section $\bar{\sigma}_e$ can be parameterized as:

$$\bar{\sigma}_e \equiv \frac{\mu_{\chi e}^2 \overline{|\mathcal{M}_{\chi e}(\vec{q} = \alpha m_e)|^2}}{16\pi m_\chi^2 m_e^2}, \quad (1.32)$$

where $\alpha \approx 1/137$ is the fine structure constant, m_e is the electron mass (with αm_e being the momentum of an electron with speed αc), and $\mu_{\chi e}^2$ is the LDM-electron reduced mass. Here $\overline{|\mathcal{M}_{\chi e}(\vec{q} = \alpha m_e)|^2}$ is the squared matrix element for LDM-electron scattering averaged over the initial and summed over the final particle spins given a momentum transfer of αm_e . This term can be generalized to find the matrix element for any momentum transfer:

$$\overline{|\mathcal{M}_{\chi e}(\vec{q})|^2} = \overline{|\mathcal{M}_{\chi e}(\vec{q} = \alpha m_e)|^2} \times F_{\text{DM}}(q), \quad (1.33)$$

where $F_{\text{DM}}(q)$ is the DM form factor that provides the momentum-transfer dependence of the interaction and is given by:

$$F_{\text{DM}}(q) = \frac{m_{A'}^2 + \alpha^2 m_e^2}{m_{A'}^2 + q^2}. \quad (1.34)$$

Equation 1.34 can further be simplified depending on the mass of the gauge boson:

$$F_{\text{DM}}(q) \simeq \begin{cases} 1 & m_{A'} \gg \alpha m_e, \\ \frac{\alpha^2 m_e^2}{q^2} & m_{A'} \ll \alpha m_e. \end{cases} \quad (1.35)$$

$F_{\text{DM}}(q) = 1$ results from a point-like interaction caused by the exchange of a heavy mediator, whereas $F_{\text{DM}}(q) \propto 1/q^2$ results from the exchange of an ultra-light or massless mediator. Using a separate derivation of the DM form factor, the momentum-transfer dependence can be in the form of $F_{\text{DM}}(q) = (\alpha m_e/q)$ when considering an electric dipole moment coupling [71]. The abundance of relic DM can be explained through different scenarios depending on the mass hierarchy of m_χ , $m_{A'}$, and m_e :

- *Secluded Freeze-out*: In this scenario, $m_\chi > m_{A'}$, and DM particles can annihilate into pairs of mediators. DM particles are frozen out to the mediator, which is later expected to decay or interact with SM particles. DM particles are therefore “secluded” from the SM. The velocity-averaged self-annihilation cross section for this case goes as $\langle \sigma v \rangle \propto g_D^4/m_\chi^2$, where g_D^4 is the DM-mediator coupling. As this scenario involves a heavy mediator, it corresponds to $F_{\text{DM}}(q) = 1$.
- *Direct Freeze-out*: Here, $m_\chi < m_{A'}$, and thus DM is the lightest particle in the dark sector. DM particles in this case are frozen out directly from the SM through the exchange of a heavy mediator, where the velocity-averaged self-annihilation cross section goes as $\langle \sigma v \rangle \propto g_D^2 g_{\text{SM}}^2 m_\chi^2/m_{A'}^4$ with g_{SM}^2 being the SM-mediator coupling. Again this scenario involves a heavy mediator, and thus corresponds to $F_{\text{DM}}(q) = 1$.
- *Freeze-in*: In this last scenario, $m_{A'} \ll \alpha m_e$, and the DM is very weakly coupled to the SM; the weak coupling means that the DM would not have thermalized with the SM sector. Therefore the normal paradigm of DM as a thermal relic does not apply. Instead the DM abundance is explained by a freeze-in scenario, where SM particles annihilate into DM sector particles. As this scenario involves an ultra-light mediator, it corresponds to $F_{\text{DM}}(q) \propto 1/q^2$.

LDM particles can in principle scatter off of a target nucleus or a target electron. However, these two types of interactions significantly differ in the amount of energy that can be deposited. Referring to Eq. 1.21, the energy deposition for nuclear recoils, E_R , is bounded by:

$$E_R \leq \frac{2\mu_N^2 v^2}{m_N}. \quad (1.36)$$

In the regime where $m_\chi \ll m_N$, $\mu_N \approx m_\chi$. For a light target and a DM particle moving with a speed of $v = 550$ km/s near the escape velocity of the galaxy, Eq. 1.36 can be described in terms of numerical bounds:

$$E_R \lesssim 3 \text{ eV} \left(\frac{m_\chi}{100 \text{ MeV}} \right)^2 \left(\frac{m_N}{20 \text{ GeV}} \right)^{-1}. \quad (1.37)$$

For a heavy target material like xenon, nuclear recoil energies on this scale are well below the detection threshold. Even for lighter targets such as Si and Ge, only the recoil energies near the upper bound rise

above the detection threshold. In contrast, the energies deposited by inelastic DM-electron scattering are much more accessible to DM experiments. The kinematics of DM-electron scattering is, however, much more complicated than DM-nucleus scattering. Because the electron is in a bound state, it does not have a definite momentum, and can therefore have an arbitrarily high momentum with non-zero probability. Normally this would make a direct calculation of the electron recoil energy E_r quite complicated. Instead, E_r can be related to the energy loss of the DM particle and the energy gain of the nucleus through energy conservation. When the nuclear recoil energy is negligible, E_r is exactly equal to the energy loss of the DM particle. In this scenario, E_r is bounded by:

$$E_r \leq \frac{1}{2} \mu_N v^2. \quad (1.38)$$

Using the same conditions as before ($m_\chi \ll m_N$ and $v = 550$ km/s), the numerical bound on the electron recoil energy is given by:

$$E_r \lesssim 170 \text{ eV} \frac{m_\chi}{100 \text{ MeV}}. \quad (1.39)$$

By comparing Eq. 1.39 and 1.37, it is clear the electron scattering provides a much larger energy scale for detection compared to nuclear scattering. For this reason, only energy depositions from electron recoils are considered, and the event rate is concerned only with the DM-electron scattering cross section. Following Ref. [71], the differential event rate for this process in a crystal target is given by:

$$\frac{dR}{d \ln E_r} = \frac{\rho_{\text{DM}}}{m_\chi} N_{\text{cell}} \bar{\sigma}_e \alpha \frac{m_e^2}{\mu_{\chi e}^2} \int d \ln q \left(\frac{E_r}{q} \eta(v_{\min}(q, E_r)) \right) F_{\text{DM}}(q)^2 |f_{\text{crystal}}(q, E_r)|^2, \quad (1.40)$$

where $N_{\text{cell}} = m_T/m_{\text{cell}}$ is the number of unit cells in the target with total mass m_T ($m_{\text{cell}} = 2m_N$ for Si and Ge), and the DM velocity distribution is contained in $\eta(v_{\min}(q, E_r))$, defined as:

$$\eta(v_{\min}) = \int_{v_{\min}}^{\infty} \frac{1}{v} f(\vec{v}) d^3 \vec{v} \quad (1.41)$$

with

$$v_{\min}(q, E_r) = \frac{E_r}{q} + \frac{q}{2m_\chi}. \quad (1.42)$$

As with the WIMP model, there is an implicit maximum velocity set by the escape velocity of the galaxy. The term $|f_{\text{crystal}}(q, E_r)|$ in Eq. 1.40 is referred to as the crystal form factor, and contains all of the details of the target's electronic structure and electron momentum states. Unlike with DM-nucleus scattering, there is not a direct relation between the recoil energy and momentum transfer for DM-electron scattering. The total event rate is therefore found by integrating over E_r and q separately, and is why an integral over q is seen in Eq. 1.40.

The analysis presented in Chapter 5 uses the publicly available electron recoil spectra provided by Ref. [76] which have been numerically calculated using a program called ‘‘QEdark’’. Electron recoil spectra are provided for LDM masses between $0.1 \text{ MeV}/c^2$ to $10 \text{ GeV}/c^2$ as well as for the various forms of F_{DM} . The recoil spectra themselves are binned across E_r using a bin size of 0.1 eV . Figure 1.9 shows the total event rate as a function of LDM mass for a Si target with $F_{\text{DM}} = 1$ and $F_{\text{DM}} \propto 1/q^2$, assuming a DM-electron cross section of $\bar{\sigma}_e = 10^{-37} \text{ cm}^2$. Also shown are the binned electron recoil spectra for various LDM masses for a Si target. The fluctuations observed in these signal spectra are not due to statistics, but rather a direct consequence of the band structure of the target material. What is

interesting to note in Fig. 1.9 is that for even (relatively) large LDM masses, the most probable electron recoil energy is eV-scale. This arises because the most likely momentum transfer is the electron’s Bohr momentum, which happens to correspond to recoil energies at this scale. Low-threshold DM experiments are thus particularly suited to probe the DM-electron scattering parameter space.

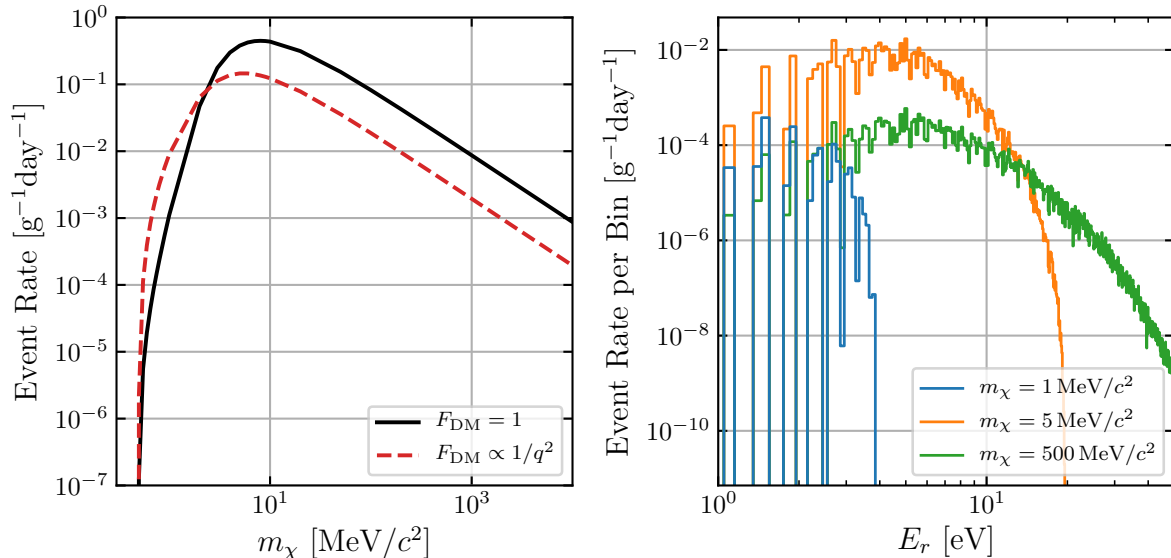


Figure 1.9: Left: expected event rate for LDM-electron scattering as a function of LDM mass m_χ for a Si target assuming a DM-electron cross section of $\bar{\sigma}_e = 10^{-37} \text{ cm}^2$. The event rate is shown separately for different assumptions of the DM form factor F_{DM} . Right: binned spectra of the electron recoil energy E_r at various LDM masses for $F_{\text{DM}} = 1$. The data in these plots are provided by the publicly available “QEdark” outputs [76].

1.5.3 Bosonic Dark Matter

The mass of fermionic DM, such as WIMPs and LDM, are constrained to masses above the keV/c^2 level due to the Lyman-alpha forest astrophysical observations made of substructure formation [77]. Specifically, the number density of sub- keV/c^2 fermionic DM would be large enough that its Fermi degeneracy pressure in the early universe would affect the formation of galactic substructure [72]. This constraint has led to a class of “Ultralight Dark Matter” comprised of bosonic DM candidates; bosonic DM would not produce Fermi degeneracy pressure and thus avoids the issue with galactic substructure formation. Two prominent bosonic DM candidates that are described in this sub-section are dark photons and axion-like particles (ALPs).

Dark Photons

The dark photon A' is hypothesized to be the massive vector boson of a dark sector $U(1)_D$ gauge group with mass $m_{A'}$ that can kinetically mix with the SM hypercharge $U(1)_Y$ gauge group, with the dominant mixing channel between dark photons and the SM photon [78]. This mixing is characterized by the DM-SM kinetic mixing parameter, ε . For sufficiently small ε and with $m_{A'}$ less than twice the electron mass, the decay lifetime of dark photons can be longer than the age of the Universe; dark photons therefore

may constitute all of the relic DM [78]. An interaction mechanism for dark photons is an absorption process akin to photoelectric absorption of SM photons. The model for dark photon absorption described here follows the work presented in Refs. [79, 78].

The basic construction of the interaction rate for dark photon absorption is similar to that of the WIMP in Eqs. 1.16 and 1.17. Yet instead of considering the number of target nuclei, dark photon absorption considers the number of target electrons. For a target material with a total mass of m_T and density ρ , the number of target electrons is $m_T \cdot n_e / \rho$, where n_e is the number density of electrons. The expected event rate is therefore given by [79]:

$$R = \frac{1}{\rho} \frac{\rho_{\text{DM}}}{m_{A'}} \langle n_e \sigma_{\text{abs}} v_{\text{rel}} \rangle_{A'}, \quad (1.43)$$

where σ_{abs} is the absorption cross section and $\langle n_e \sigma_{\text{abs}} v_{\text{rel}} \rangle_{A'}$ is the cross section averaged over the dark photon velocities v_{rel} that also defines a DM-electron absorption rate. As Ref. [79] shows, the equivalent rate for photon absorption, $\langle n_e \sigma_{\text{abs}} v_{\text{rel}} \rangle_{\gamma}$, is equal to the real part of the complex conductivity σ_1 of the target material. Furthermore, σ_1 is related to the SM photoelectric absorption cross section $\sigma_{\text{p.e.}}$ by $\sigma_1 = n \cdot \sigma_{\text{p.e.}}$, where n is the index of refraction of the target material (see Appendix B).

Dark photon absorption is modelled as the absorption of a massive particle that deposits an absorption energy of $E_{A'}$ with an effective coupling of εe to electrons. The matrix elements for dark and SM photons are related by $|\mathcal{M}|_{A'}^2 = \varepsilon_{\text{eff}}^2 |\mathcal{M}|_{\gamma}^2$, which leads to the relation:

$$\begin{aligned} \langle n_e \sigma_{\text{abs}}(E_{A'}) v_{\text{rel}} \rangle_{A'} &= \varepsilon_{\text{eff}}^2 \langle n_e \sigma_{\text{abs}}(E_{A'}) v_{\text{rel}} \rangle_{\gamma} \\ &= \varepsilon_{\text{eff}}^2 \frac{\sigma_1(E_{A'})}{\hbar} \\ &= \varepsilon_{\text{eff}}^2 \frac{n \cdot \sigma_{\text{p.e.}}(E_{A'})}{\hbar}, \end{aligned} \quad (1.44)$$

where $\sigma_{\text{p.e.}}$ is taken to be in units of eV and \hbar is the reduced Planck constant. Here, $\varepsilon_{\text{eff}}^2$ is the effective kinetic mixing parameter that accounts for in-medium effects that can significantly alter ε if the kinetic mixing does not occur in vacuum. $\varepsilon_{\text{eff}}^2$ depends on the dark photon mass, as well as both the real and imaginary parts of the complex conductivity, σ_1 and σ_2 :

$$\varepsilon_{\text{eff}}^2 = \frac{\varepsilon^2 m_{A'}^2}{(m_{A'}^2 - 2m_{A'}\sigma_2 + \sigma_2^2 + \sigma_1^2)}. \quad (1.45)$$

For dark photon masses $\gtrsim 100 \text{ eV}/c^2$, ε_{eff} is well approximated by ε for most target materials, and so $\varepsilon_{\text{eff}} \sim \varepsilon$. Below $100 \text{ eV}/c^2$, ε_{eff} and ε can differ by over an order of magnitude for target materials such as Si and Ge.

Lastly, for non-relativistic, cold DM, the absorption energy is well approximated by the mass energy of the dark photon (i.e. $E_{A'} \sim m_{A'} c^2$). This means that the mass range accessible for a given experiment performing a dark photon search is simply the energy range that experiment is sensitive to. For semiconductor detectors such as Si and Ge, this puts a lower bound on the accessible dark photon masses at the band gap energy of the target material. Putting all of these components together, Eq. 1.43 can be rewritten as:

$$R = \frac{1}{\rho \hbar} \frac{\rho_{\text{DM}}}{m_{A'}} \varepsilon_{\text{eff}}^2 \cdot n \cdot \sigma_{\text{p.e.}}(m_{A'} c^2). \quad (1.46)$$

The expected signal for dark photon absorption is a delta function at $m_{A'}$ with an event rate given by Eq. 1.46, where the signal will only deviate from a delta function due to the detector resolution or other detector-related effects. The left plot in Fig. 1.10 shows the expected rate of dark photon absorption in Si assuming $\varepsilon = 5 \times 10^{-13}$ for dark photon masses below $1 \text{ keV}/c^2$. For comparison, the expected rate is shown with and without accounting for the in-medium effects.

Axion-like Particles

The axion is a hypothetical particle that solves the strong Charge-Parity problem [80] in quantum chromodynamics. Axions are proposed as bosons that arise from spontaneous breaking of a $U(1)$ symmetry, and are constrained to masses between $\sim 10^{-5}$ – $10^{-3} \text{ eV}/c^2$ [81]. Although the axion itself may explain the abundance of DM, the parameter space for axion searches is limited by a fixed relationship between the axion mass and its coupling strength to SM particles. A broader category of particles called axion-like particles (ALPs), where the relationship between the ALP mass and coupling strength is independent, allows experiments to explore a much wider and more general parameter space [82].

This model considers the case where ALPs with mass m_a constitute all of the relic abundance of DM and interact with the SM through what is known as the axioelectric effect [83, 84]. The axioelectric effect is a process akin to photoelectric absorption of a SM photon, whereby an ALP is absorbed by a bound electron in an atom, producing a liberated electron. This process is characterized by the axioelectric coupling constant g_{ae} of the ALP to the electron. As with the previous models discussed, the expected event rate is found by determining the effective area of the target material and the flux of DM particles:

$$R = \frac{\rho_{\text{DM}}}{m_N m_a} \sigma_a(E_a) \langle v_a \rangle = \frac{\rho_{\text{DM}}}{m_N m_a} \sigma_a(E_a) \beta_a \cdot c, \quad (1.47)$$

where m_N is the mass of a nucleus in the target material, $\sigma_a(E_a)$ is the absorption cross section for an axion with an absorption energy E_a , v_a is the axion velocity, c is the speed of light, and $\beta_a = \langle v_a \rangle / c$ is the relativistic beta factor. The axioelectric absorption cross section is proportional to the SM photoelectric absorption cross section $\sigma_{\text{p.e.}}$ of the target material, and is given by [84, 85]:

$$\sigma_a(E_a) = \sigma_{\text{p.e.}}(E_a) \frac{g_{ae}^2}{\beta_a} \frac{3E_a^2}{16\pi\alpha m_e^2 c^4} \left(1 - \frac{\beta_a^{2/3}}{3}\right), \quad (1.48)$$

where m_e is the electron mass and α is the fine structure constant. For non-relativistic, cold DM, the energy of the ALP is well approximated by its mass energy (i.e. $E_a \sim m_a c^2$), and $\beta_a \ll 1$. Equation 1.48 therefore reduces to:

$$\sigma_a(m_a c^2) = \sigma_{\text{p.e.}}(m_a c^2) \frac{g_{ae}^2}{\beta_a} \frac{3m_a^2}{16\pi\alpha m_e^2}. \quad (1.49)$$

Substituting Eq. 1.49 into Eq. 1.47, the expected rate for ALP absorption is written as:

$$R = \frac{\rho_{\text{DM}}}{m_N} \sigma_{\text{p.e.}}(m_a c^2) \frac{3g_{ae}^2}{16\pi\alpha} \frac{m_a}{m_e^2} c. \quad (1.50)$$

It should be noted that Eq. 1.50 is often written in literature without the explicit dependence on m_N ; usually m_N is just absorbed by the $\sigma_{\text{p.e.}}$ term. There are many similarities between the DM model for ALPs and the model for dark photons. Mainly, both models involve absorption processes that liberate bound electrons in the target material with an energy equal to the mass energy of the DM candidate.

Like with the dark photon model, the expected signal for ALP absorption is a delta function at m_a with an event rate given by Eq. 1.50. Therefore experiments are able to explore the parameter space of both ALPs and dark photons over the same mass range (and as a consequence, a potential discovery may not be able to distinguish between these two signals). The right plot of Fig. 1.10 shows the expected event rate of ALP absorption in Si assuming $g_{ae} = 5 \times 10^{-11}$ for ALP masses below $1 \text{ keV}/c^2$.

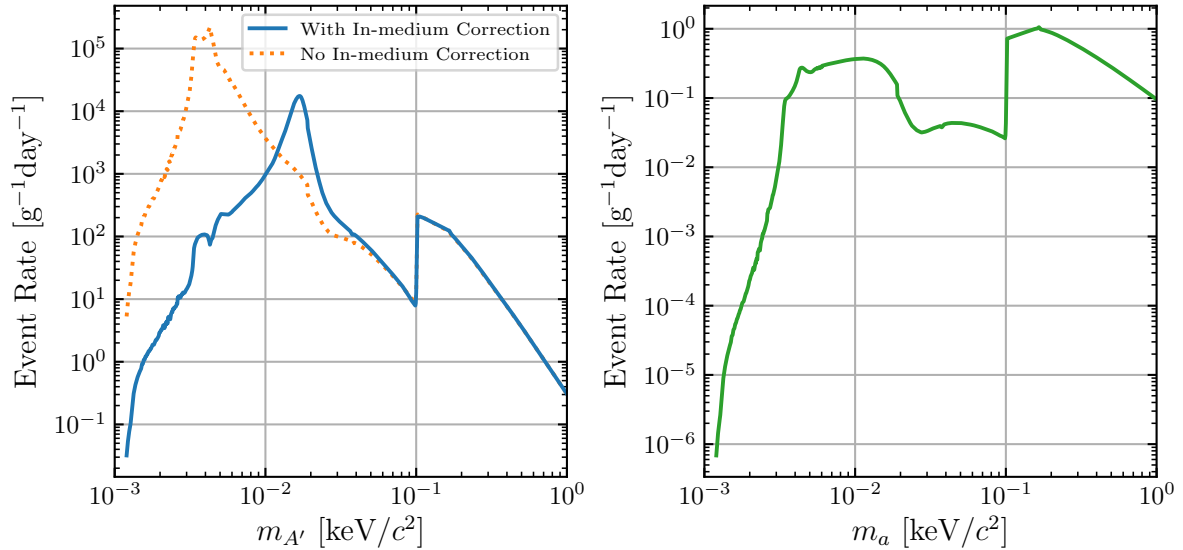


Figure 1.10: Left: expected event rate of dark photon absorption in Si over the dark photon mass $m_{A'}$ assuming a dark photon kinetic mixing parameter of $\varepsilon = 5 \times 10^{-13}$. The event rate is computed with (blue, solid) and without (orange, dotted) accounting for the in-medium correction. Right: expected event rate of axion-like particle (ALP) absorption in Si over the ALP mass m_a assuming an axioelectric coupling constant of $g_{ae} = 5 \times 10^{-11}$.

1.5.4 Other Candidates and Interaction Channels

The DM candidates outlined in the previous sub-sections are only a subset of models that exist, and are the ones primarily relevant to the analyses presented in Chapters 5 and 6. There is, however, a vast array of interesting models that are currently or have previously been explored. Furthermore, existing DM candidates can be investigated in different ways by probing alternative channels of the DM-SM interaction. The following list is meant to provide a sense of the various different types of DM candidates that exist. It is important to remember that DM models and candidates are constantly being developed and modified. Constraints from precise astrophysical measurements and unexplained phenomena in particle physics can motivate some models while disfavouring others. The most strongly supported explanations of DM remain models that introduce a new, massive particle or force mediator.

- *Inelastic Nuclear Scattering of WIMPs or LDM*: This is an example of existing DM candidates that may be probed by investigating different interaction channels. Section 1.5.1 discusses the model for the elastic scattering of WIMPs with the nucleus of an atom in a target material. However WIMPs, and even LDM, can also provide an inelastic scattering contribution that can be separately detectable. Inelastic nuclear scattering may result in the emission of an observable

photon, known as Bremsstrahlung, or may result in a dislodged electron through the so-called Migdal effect [86]. These models are relevant to the analysis presented in Chapter 6, and are summarized in Appendix A.

- *WIMPZillas*: The standard WIMP has an upper bound on its mass at $\sim 30\text{--}300\text{ TeV}/c^2$ due to constraints on the self-annihilation cross section [20]. However by considering non-thermal DM (i.e. DM that was not in thermal equilibrium during freeze-out), a new supermassive DM candidate called the “WIMPzilla” emerges. Such a candidate can have mass ranging from $10^{12}\text{--}10^{16}\text{ GeV}c^2$. Rather than a freeze-out scenario, the current abundance of WIMPZillas as DM is explained by a freeze-in scenario and some production mechanism. Models for WIMPZillas are motivated by unexplained, ultra-high energy cosmic rays that could be produced by the decay of supermassive DM [20].
- *Asymmetric Dark Matter*: Models of asymmetric DM assert that the present abundance of DM is due to an asymmetry between DM particles and antiparticles. Furthermore, the asymmetry in the DM sector is specifically related to the observed baryon asymmetry (i.e. the imbalance of matter and antimatter in the observable universe). Comparing the observed densities of baryons and DM constrains the mass of DM between $5\text{--}15\text{ GeV}/c^2$, depending on the specifics of the model [87, 88]. Asymmetric DM may be directly detected via nuclear scattering, or indirectly detected via DM particle-antiparticle annihilation [87].
- *Massive Astrophysical Compact Halo Objects (MACHOs)*: Models of MACHOs depart from the models of the DM candidates discussed so far that introduce a new dark sector of one or more particles. Instead, MACHO models assert that the abundance of DM is explained by non-luminous baryonic matter. The term MACHO represents a broad category of completely or nearly non-luminous astronomical objects, including planets, brown dwarfs, red dwarfs, white dwarfs, and black holes [5]. However over the past several decades, the evidence for baryonic MACHOs has become increasingly slim and cosmological and astrophysical measurements become more precise. Specifically, precise measurements of the baryonic abundance largely rule out models for MACHOs as DM [5].
- *Primordial Black Holes*: The model for primordial black holes is another example of a non-particle DM candidate. Here, the abundance of DM is due to black holes that were formed in the early universe before the epoch of Big Bang nucleosynthesis [5]. Various scenarios of formation under this model offer a very wide range of the potential black hole mass. Although several masses have been excluded due to cosmological and astrophysical measurements [89], recent observations made by the LIGO/Virgo collaborations have fueled new interest in this DM candidate [90].
- *Sterile Neutrinos*: Sterile neutrinos are hypothesized massive fermions that are thought to only interact with gravity. They are distinct from standard neutrinos in that they have right-handed chirality (as opposed to the left-handed chirality observed for standard neutrinos) and do not interact with other SM particles. However, sterile neutrinos can mix with standard neutrino via the Higgs mechanism [91]. As sterile neutrinos are massive and have no electromagnetic charge, they naturally also serve as a potential DM candidate. To produce the current abundance of DM, sterile neutrinos would need to have a mass on the keV/c^2 scale. While these particles are not stable, they can have a lifetime longer than the age of the Universe [91]. Sterile neutrinos may be

indirectly detected from the emission of X-rays from their electroweak decay, or directly detected by mixing with a standard neutrino and subsequently scattering off of an electron [92].

1.6 The SuperCDMS Experiment

The Super Cryogenic Dark Matter Search (SuperCDMS) is one of many collaborations performing direct dark matter search experiments. Experiments conducted by SuperCDMS employ cryogenically-cooled Si and Ge crystal detectors that are designed to measure extremely small nuclear recoil energies. The SuperCDMS SNOLAB experiment is the successor to previous generations of CDMS experiments that is currently under construction. As the name suggests, SuperCDMS SNOLAB will be operated in the underground SNOLAB facility in Sudbury, Ontario, Canada.

The primary science goal of SuperCDMS SNOLAB is to search for WIMPs with masses below $10 \text{ GeV}/c^2$ via spin-independent DM-nucleus elastic scattering using complementary target nuclei (Si and Ge) as well as complementary detection techniques. Secondary science goals include searches for other low-mass DM candidates (including those discussed in Sec. 1.5), as well as searches for other particles such as solar neutrinos, solar axions, and lightly ionizing particles. The detectors to be employed for this experiment have a lower energy threshold compared to previous CDMS detectors, allowing for improved sensitivity to lower DM masses. Furthermore, the SNOLAB facility provides an extremely low-background environment for SuperCDMS SNOLAB, which will improve the overall sensitivity to potential DM interactions. The facility, which operates as a class-2000 clean room, is located 2 km underground and is the home of several particle physics experiments. SNOLAB’s 2 km of rock overburden provides $\sim 6000 \text{ m}$ of water equivalent shielding, and reduces the amount of background radiation from cosmic rays by a factor of 50 million compared to the Earth’s surface with only one cosmic ray per 4 m^2 per day [93].

Figure 1.11 shows a schematic diagram of the SuperCDMS SNOLAB experiment. The SuperCDMS SNOLAB detectors will be arranged in tower configurations and placed inside a vacuum-sealed container called the “Snobox” that is made of copper. A dilution refrigeration system will be able to cool the Snobox and the detectors inside to temperatures of $\sim 15\text{--}30 \text{ mK}$. The Snobox is surrounded by several layers of shielding to protect against various sources of background. The outer water tanks provide protections from cavern neutrons, the gamma shield protects against external gamma-rays, and the inner polyethylene layers are used to absorb radiogenic neutrons that are emitted from the Snobox and gamma shield. Lastly, the entire assembly is mounted on top of a seismic platform to provide isolation from seismic events. More information about the SuperCDMS SNOLAB experiment setup is found in Ref. [94].

Despite the low-background environment provided by the SNOLAB facility, the experiment is still concerned with several sources of background. Reference [94] goes into great detail about each source of background that may be observed by the DM detectors. The background sources are generally categorized by those that induce electron-recoil (ER) events and those that induce nuclear-recoil (NR) events. Some of the largest contributors to ER-type backgrounds include: β -decay products from cosmogenically-produced tritium (^3H) contamination in the detectors; gamma-rays and β particles from the decay of contaminant radioisotopes in non-detector materials; and the decay products from radioisotopes in non-detector materials that are activated by high-energy cosmic-ray secondaries. For Si detectors, *the* largest source of background events is the β -decay of the unstable ^{32}Si isotope that is naturally occurring in

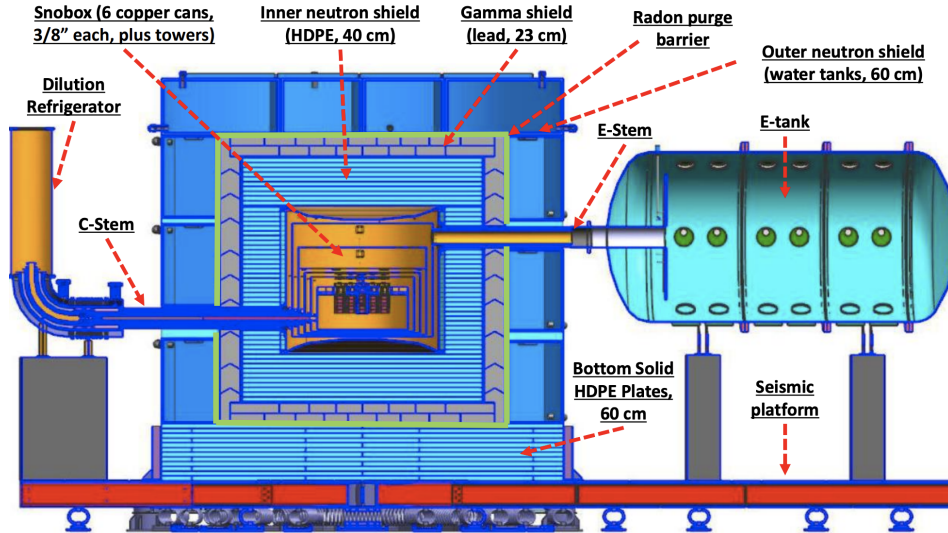


Figure 1.11: Schematic diagram of the SuperCDMS SNOLAB experiment. The dark matter detectors are arranged in tower configurations inside the Snobox. A dilution refrigeration system is able to cool the Snobox and the contents therein to temperatures as low as 15 mK. The Snobox is also surrounded by several shielding layers to protect against various background sources. The entire assembly is mounted on top of a seismic platform to provide isolation from seismic events. Figure provided by Ref. [94].

Si. Another source of background for Ge detectors are the activation lines produced by long-lived radioisotopes that decay by electron capture. The event rate from NR-type background sources is expected to be significantly smaller compared to ER-type sources. Some of the largest contributors to the NR background rate include: coherent neutrino-nucleus scattering; α -decay products from contaminant radioisotopes in non-detector materials; and neutrons induced cosmogenically or in the cavern environment.

The SuperCDMS SNOLAB experiment will employ four types of detectors: interleaved Z-sensitive ionization phonon (iZIP) detectors comprised of either a Si or Ge crystal, and high voltage (HV) detectors comprised of either a Si or Ge crystal. As will be discussed in Sec. 2.5, iZIP and HV detectors utilize different yet complementary detection techniques to probe the WIMP-nucleus scattering parameter space. The initial payload of SuperCDMS SNOLAB will use four detector towers that together contain ten Ge iZIP, two Si iZIP, eight Ge HV, and four Si HV detectors; all of the detectors combine for a total exposure of 144.4 kg-years [94]. In anticipation of future experiments, the Snobox is designed to add more detector towers in order to achieve larger exposures. Figure 1.12 shows the projected limits on the spin-independent (SI) WIMP-nucleon cross section for the initial payload of the SuperCDMS SNOLAB experiment. The projected limits are shown separately for each type of detector that will be used. The differences in the projected limits for each detector type is better understood after knowing how the detectors operate, as is discussed in Sec. 2.5.

Apart from the SNOLAB experiment, the SuperCDMS collaboration encompasses many other smaller-scale experiments at various R&D test facilities. The purpose of these smaller-scale experiments can range from hardware or software detector development to studies of background sources. In some cases, an experiment at a test facility is able to perform a dark matter search, as is the case with the experiment presented in Chapters 4 and 5.

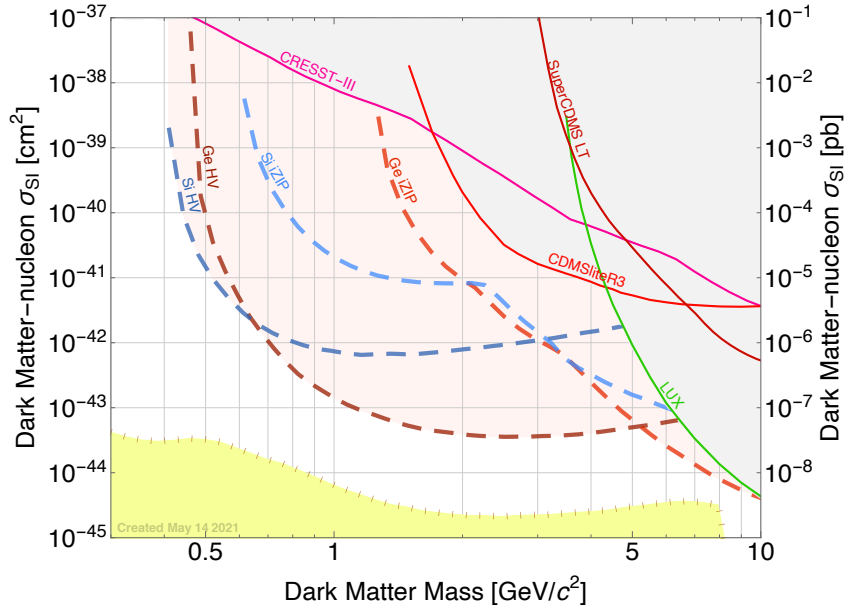


Figure 1.12: Projected limits on the spin-independent (SI) WIMP-nucleon scattering cross section σ_n^{SI} over WIMP mass for the initial payload of the SuperCDMS SNOLAB experiment. The projected limits are shown separately for the four types of detectors that will be used. Other exclusion limits on σ_n^{SI} in this low-mass region obtained by recent DM search experiments are also shown [55, 95, 58, 96]. The yellow-shaded region is the neutrino floor for a Si target [69]. This plot was produced using the SuperCDMS Limit Plotter v5.16.

This introductory chapter provided a brief history of DM, and described how galaxy rotation curves, weak gravitational lensing, and the CMB provide some of the most compelling evidence of the existence of DM. These observations combined with other experiments and studies further suggest that DM is composed of neutral, non-baryonic DM particles, and observations of the large-scale structure of the universe favour the cold DM paradigm. This chapter also outlined the models for the direct detection of WIMPs, LDM, dark photons, and ALPs, where the latter three are the DM candidates most relevant to this dissertation. Finally, the SuperCDMS SNOLAB experiment was introduced, along with its projected sensitivity to WIMP-nucleus scattering at low DM masses. The following chapter will describe how potential DM interactions could be directly detected using cryogenic semiconductor crystal detectors.

Chapter 2

Detector Physics

This chapter will provide an overview of the mechanics and concepts of how cryogenic semiconductor crystal detectors, like the ones employed by SuperCDMS, are used for particle detection. Section 2.1 discusses the primary interaction mechanisms for such solid-state detectors, and Sec. 2.2 introduces the detector response model that is used for various analyses in later chapters. Other important concepts and parameters for dark matter (DM) search analyses, including the photoelectric absorption cross section and detector leakage, are outlined in Secs. 2.3 and 2.4, respectively. Lastly, some of the detector types that are used for SuperCDMS experiments are shown in Sec. 2.5.

2.1 Cryogenic Semiconductor Crystal Detectors

Solid-state detectors are operated by many DM search experiments, but they also define a broad category of detectors that encompasses many different compositions and technologies. The specific type of solid-state detectors described here are semiconductor crystals operated at cryogenic temperatures (< 1 K). Other types of solid-state detectors can be found in Refs. [30, 37, 36]. Cryogenic semiconductor crystal detectors are comprised of two main components: a semiconductor crystal that is used as the target material for DM interactions, and sensors situated around the semiconductor to measure energy depositions. Specifically the SuperCDMS collaboration uses detectors made of crystal silicon (Si) and germanium (Ge). Semiconductors are useful materials for particle detection because of how they conduct electrons. Electrons in a semiconductor can occupy energy states inside the valence band where they remain orbiting crystal nuclei, or in higher energy states inside the conduction band where electrons are able to drift throughout the crystal. The energy difference between the conduction and valence is known as the band gap energy E_g . No energy states exist inside the band gap, so materials with a larger band gap are less able to carry an electric current. Electrons will occupy energy states with energy E according to the Fermi-Dirac distribution $f(E)$:

$$f(E) = \frac{1}{e^{(E-E_F)/k_b T} + 1}, \quad (2.1)$$

where k_b is the Boltzmann constant, T is the temperature of the system, and E_F is the Fermi constant. E_F specifies the energy state at which there is a 50% probability that the state is occupied by an electron. For intrinsic semiconductors, E_F lies midway between the valence and conduction bands. For

this reason, electrons in semiconductors mostly occupy states in the valence band. However at high temperatures some electrons occupy energy states above E_F and, if the temperature is high enough, can occupy states inside the conduction band. The distribution of electrons occupying energy states in a semiconductor is illustrated in Fig. 2.1.

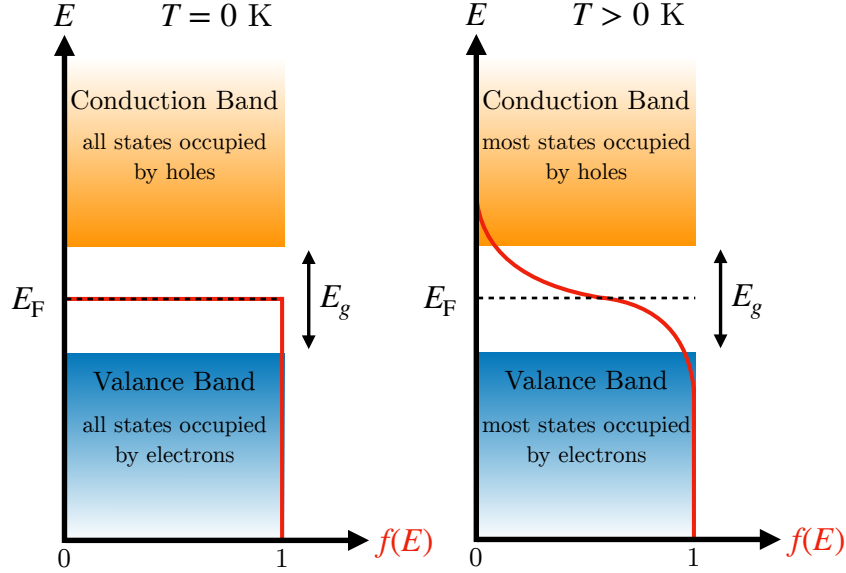


Figure 2.1: Illustration of how electrons and holes occupy energy states in a semiconductor with a temperature of $T = 0$ K (left) and $T > 0$ K (right). Electrons and holes can occupy energy states inside the valence or conduction band which are separated by the band gap energy E_g . Electrons will occupy states according to the Fermi-Dirac distribution $f(E)$. For semiconductors, the Fermi energy E_F lies between the valence and conduction bands. At $T = 0$ K, all energy states in the valence band are occupied by electrons. As the temperature increases, more electrons are able to occupy energy states above E_F and, if the temperature is high enough, can occupy states inside the conduction band.

Because these semiconductor detectors are operated at cryogenic temperatures, nearly all of the electrons occupy states in the valence band. This means that electrons will only move into the conduction band if there is an external energy deposition larger than the band gap energy. Methods such as doping can change the value of E_F to make it harder or easier for a semiconductor to carry a current. However only intrinsic (undoped) semiconductors are used for DM detectors to date.

The crystal structure of solid-state detectors means that the absence of an electron in an atomic lattice creates a quasiparticle with a net positive charge known as a hole. Although holes are not real particles, they behave as such by “occupying” energy states as Fig. 2.1 illustrates. If all energy states inside the valence band of a semiconductor are occupied by electrons, then all energy states inside the conduction band are “occupied” by holes. Every electron inside a semiconductor can therefore be associated with a corresponding hole. When an electron moves from the valence band to the conduction band, there is a corresponding hole that moves from the conduction band to the valence band. This pairing of an electron and a corresponding hole is referred to as an electron-hole pair (e^-h^+). Furthermore, just as electrons inside the conduction band can move freely in the semiconductor material, holes inside the valence band are also able to move. However the motion of holes is only apparent; a nearby electron that moves to fill the hole makes a new hole that is filled by another electron, and so on, creating the illusion of motion for the quasiparticle hole.

Particle interactions with a solid-state detector, whether from potential DM candidates, background sources, or calibration sources, will excite e^-h^+ pairs inside the cryogenic semiconductor by depositing energy to either an atomic nucleus or directly to a valance electron. If a uniform electric field is applied across the detector, the liberated electrons and holes will drift to opposite sides of the detector. Although the drifting e^-h^+ pairs can be directly measured, the primary mechanism for measuring energy in SuperCDMS detectors is measuring the heat energy from lattice vibrations in the crystal (i.e. phonons). Figure 2.2 illustrates the interaction of a DM particle with a solid-state detector.

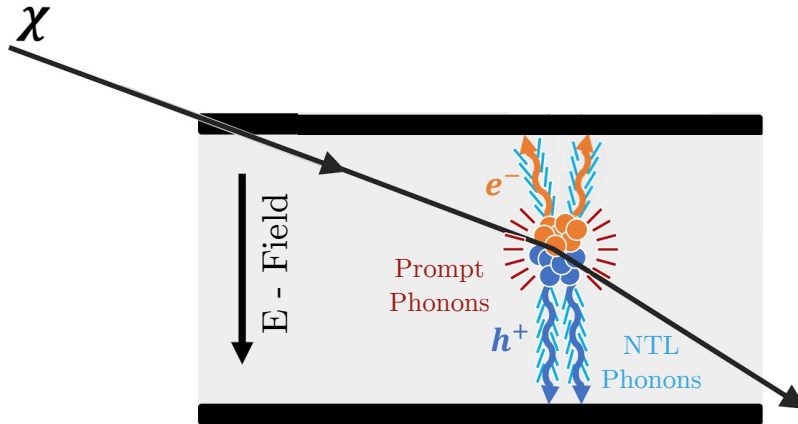


Figure 2.2: Illustration of the interaction of a DM particle χ scattering off of an atomic nucleus in a semiconductor detector. The interaction liberates some number of e^-h^+ pairs, and an electric field applied across the detector allows the electrons and holes to drift to opposite sides of the detector. The energy of the interaction is found by measuring lattice vibrations in the crystal (i.e. phonons). Phonons are generated either from the initial DM-nucleus recoil (prompt phonons), or by the Neganov-Trofimov-Luke effect that occurs when charges are accelerated in an electric field (NTL phonons). The phonons are then absorbed by sensors on the surface of the detector, producing a signal.

Phonons that are measured by solid-state detectors generally fall into two categories. The first are prompt phonons, which are the initial lattice vibrations generated when a particle scatters off of an atomic nucleus or electron and deposits some recoil energy. Interactions with a larger recoil energy will produce more prompt phonons. The second are phonons generated when electrons and holes are drifted across the detector under an applied electric field, known as the Neganov-Trofimov-Luke (NTL) effect [97, 98]. The electric field applied across the detector will act to accelerate the free charges. However the drifting charges quickly reach a terminal velocity due to the crystal lattice obstructing the motion of the charges. Any energy gained by a charge due to the electric field is dissipated as heat energy in the form of phonons. The excess amount of energy dissipated by a charge is equal to the change in potential over the distance it travelled [98]. Because an e^-h^+ pair together travels the full length of the detector, the energy produced as NTL phonons for a single e^-h^+ pair is equal to $e \cdot V_{\text{bias}}$, where e is the electron charge and V_{bias} is the voltage bias applied across the detector.

Prompt and NTL phonons are categorized as athermal phonons, and are distinct from thermal phonons that naturally arise due to the temperature of the semiconductor target. If the semiconductor is operated at cryogenic temperatures, athermal and thermal phonons will also have distinct energies. While thermal phonons will have energies of ~ 1 μeV for a detector operated at 10 mK [99], the average energy of athermal phonons produced in Si or Ge semiconductor targets is $\gtrsim 0.4$ meV [100]. In contrast to

the low-energy thermal phonons, athermal phonons have enough energy to be absorbed by sensors placed along the surface of the detector, where they produce an observable signal. Chapter 3 provides more details about how phonon signals are measured. A detailed review of phonon and electron excitation and propagation from a condensed matter perspective is found in Ref. [101].

2.1.1 Phonon Energy

The total amount of phonon energy measured by the detector for a single particle interaction, E_{ph} , is the sum of the recoil energy E_{recoil} of the interaction and the energy produced from the drifting e^-h^+ pairs:

$$E_{\text{ph}} = E_{\text{recoil}} + n_{eh} \cdot e \cdot V_{\text{bias}}, \quad (2.2)$$

where n_{eh} is the number of e^-h^+ produced in the event. Although some of the recoil energy is required to excite the n_{eh} e^-h^+ pairs, that energy is recovered as the charges recombine with the semiconductor crystal at the surface. Moreover, Eq. 2.2 makes it apparent how the NTL effect is able to amplify phonon signals. The signals from small recoil energies can be amplified by applying a strong voltage bias and increasing the amount of NTL phonons produced.

The number of e^-h^+ pairs produced in an interaction is proportional to the recoil energy. Although an initial ionized electron may be given a surplus of energy above the band gap, a cascading process occurs that distributes the energy of the initial electron to create additional e^-h^+ pairs [102]. The *mean* number of e^-h^+ pairs produced for a given energy deposition of E_{recoil} is:

$$\langle n_{eh} \rangle = Y(E_{\text{recoil}}) \frac{E_{\text{recoil}}}{\epsilon_{eh}}, \quad (2.3)$$

where ϵ_{eh} is the average energy to produce a single e^-h^+ pair (taken to be ~ 3.0 eV in Ge and ~ 3.8 eV in Si [94]). $Y(E_{\text{recoil}})$ is the ionization yield that describes how much of the recoil energy is converted to produce e^-h^+ pairs. For electron-recoil (ER) interactions, $Y(E_{\text{recoil}}) = 1$. For nuclear-recoil (NR) interactions, $Y(E_{\text{recoil}}) < 1$ and is described by Lindhard theory [103, 104, 105], as well as empirical fits to data for recoil energies below 15 keV [94] where Lindhard theory is known to become inaccurate. Using E_R and E_r to differentiate between the recoil energy from NR and ER interactions, respectively, Eq. 2.2 can be written as:

$$E_{\text{ph}} = \begin{cases} E_R + Y(E_R) \frac{E_R}{\epsilon_{eh}} \cdot e \cdot V_{\text{bias}} & \text{NR events,} \\ E_r + \frac{E_r}{\epsilon_{eh}} \cdot e \cdot V_{\text{bias}} & \text{ER events.} \end{cases} \quad (2.4)$$

Equation 2.3 indicates that n_{eh} is not constant for a given E_r . Indeed n_{eh} is a distribution with a mean of $\langle n_{eh} \rangle$ and a width described by the Fano factor parameter F . The n_{eh} distribution can either be *continuous* or *quantized*, depending on the energy resolution of the detector. For detectors with a high enough resolution that individual e^-h^+ pairs can be observed (such as the detector used in the DM search experiment presented in Chapters 4 and 5), the n_{eh} distribution appears as quantized e^-h^+ -pair peaks. Figure 2.3 illustrates the difference between detectors that observe quantized and continuous n_{eh} distributions.

The total phonon energy for ER events given by Eq. 2.4 describes the energy produced when a particle scatters off of an electron in the detector. It can equally be used to describe photoelectric absorption interactions, whereby an electron in the valance band absorbs a photon and excites into the conduction

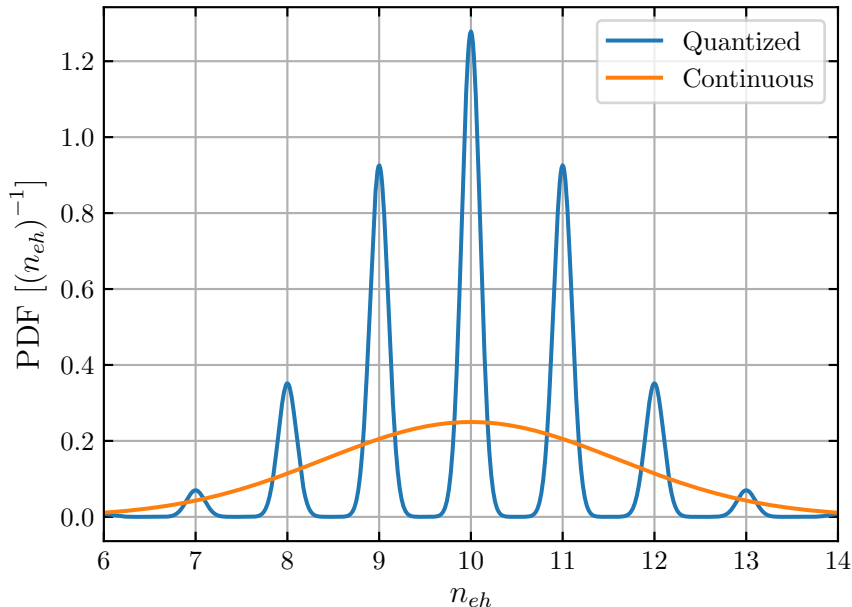


Figure 2.3: Illustration of the probability distribution functions (PDFs) for the number of e^-h^+ pairs n_{eh} observed by detectors with different energy resolutions. The blue curve demonstrates a detector that can resolve individual e^-h^+ pairs, and thus observes quantized e^-h^+ -pair peaks. Conversely the orange curve demonstrates a detector that cannot resolve individual e^-h^+ pairs, and only observes a continuous n_{eh} distribution. The underlying n_{eh} distribution is the same in both cases, with a mean of $\langle n_{eh} \rangle = 10$ and a Fano factor $F = 0.155$.

band. For absorption interactions, E_r in Eq. 2.4 can be simply replaced by the energy of the absorbed photon, E_γ . Furthermore, Eq. 2.4 assumes that interactions are individually resolved within the timing resolution of the detector (i.e. coincident particle interactions are not measured). This assumption is valid for all of the proposed DM models discussed in Sec. 1.5. However it is purposefully not valid for certain calibration sources. Specifically the DM search experiment presented in Chapters 4 and 5 uses a laser to calibrate the energy of the detector. Although the energy of photons used for this calibration are such that $n_{eh} = 1$, multiple photons may be absorbed at the same time. The total phonon energy measured when n_γ photons are simultaneously absorbed is given by:

$$E_{\text{ph}} = n_\gamma (E_\gamma + e \cdot V_{\text{bias}}). \quad (2.5)$$

Section 1.5 discussed the models of various DM candidates. However these models and their expected interaction rates are independent of the detector that would be used to measure them. A detector response model is therefore required to bridge the gap between the DM models and the expected signal that would be observed by a detector. Section 2.2 details the detector response model that describes the signal response of the single- e^-h^+ -sensitive Si detector used in the DM search experiment presented in Chapters 4 and 5.

2.2 Detector Response Model

The analyses presented in Chapters 5 and 6 perform DM searches using a detector with single- e^-h^+ -pair sensitivity, and are primarily concerned with DM interactions with electrons in the crystal. In order to conduct such analyses, the energy spectrum of events measured with the detector is compared with the expected spectrum from the signal of a given DM model. To obtain an expected signal spectrum, a model is used to describe how the detector will respond to an interaction with a proposed DM particle. Specifically, this detector response model describes how much ionization is produced for a given amount of energy absorbed by a crystal electron, and accounts for charge propagation effects like charge trapping (CT) and impact ionization (II). The ionization production part of the model is the same model that has been used in previous SuperCDMS analyses [106]. However the analyses presented in Chapters 5 and 6 are the first SuperCDMS DM search analyses to include the effects of CT and II in the detector response model.

2.2.1 Ionization Production

When a particle, DM or otherwise, interacts with an electron in the crystal (either through a scattering or absorption process), the electron will ionize and create e^-h^+ pairs if the amount of recoil/absorption energy E_r deposited to the electron is above the band gap energy E_g of the crystal material. Referring to Eq. 2.3, the mean number of e^-h^+ pairs n_{eh} produced in the high energy limit ($E_r \gg E_g$) for electron interactions is given by:

$$\langle n_{eh} \rangle = \frac{E_r}{\epsilon_{eh}}. \quad (2.6)$$

However this relationship breaks down as E_r approaches E_g . Near the band gap energy, the mean number of e^-h^+ pairs produced given an energy deposition of E_r can be described by a piece-wise function:

$$\langle n_{eh}(E_r) \rangle = \begin{cases} 0 & E_r < E_g, \\ 1 & E_g < E_r < \epsilon_{eh}, \\ E_r/\epsilon_{eh} & \epsilon_{eh} < E_r. \end{cases} \quad (2.7)$$

Equation 2.7 describes the mean number of e^-h^+ pairs because the actual number of e^-h^+ pairs is determined from a probability distribution. A detector with single- e^-h^+ -pair sensitivity detecting a mono-energetic source without coincident interactions would measure a distribution of e^-h^+ -pair peaks, as illustrated in Fig. 2.3. The probability distributions in the first two cases of Eq. 2.7 are delta functions, necessary in order to conserve energy. In the third case, discrete distributions of n_{eh} are generated with an arbitrary Fano factor F defined as:

$$F = \frac{\sigma^2}{\mu} \quad (2.8)$$

where $\mu = \langle n_{eh} \rangle$ is the mean of the distribution, and σ^2 is the variance. The value of F therefore relates to the probability of an interaction producing a given number of e^-h^+ pairs, and hence the relative heights of the e^-h^+ -pair peaks in the energy spectrum. The discrete distributions of n_{eh} for when $E_r > \epsilon_{eh}$ are determined from binomial distributions using selected values of F ; the full derivation is provided in Appendix C.

The analyses presented in Chapters 5 and 6 use $\epsilon_{eh} = 3.8 \text{ eV}$ [107] and $F = 0.155$ in the detector response model to produce the nominal results, where the latter parameter is chosen because it is the

value of Fano factor measured at energies $\gtrsim 50$ eV [108]. In order to estimate the uncertainty in the dark matter exclusion limit results, the analysis presented in Chapter 5 also uses the values of $F = 10^{-4}$ and $F = 0.3$ assumed to cover the systematic uncertainty of the Fano factor at energies below 50 eV. Figure 2.4 illustrates the effect the selected value of F has on a quantized energy distribution with $E_r = 12$ eV.

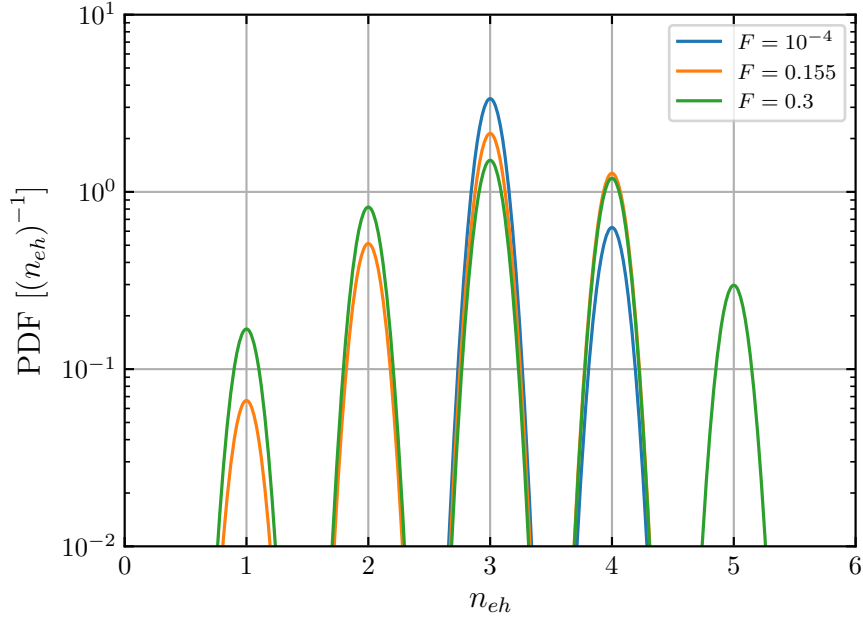


Figure 2.4: Illustration of the quantized probability distribution function (PDF) for the number of e^-h^+ pairs n_{eh} produced given a selected value of Fano factor F . Each PDF is produced for a deposited energy of $E_r = 12$ eV.

This ionization production model does not consider any processes that result in sub-gap ionization and therefore incidentally produces a low-energy limit of $E_r \geq E_g$ for electron interactions. Since the completion of the analyses Chapters 5 and 6, a more sophisticated ionization model has been developed to determine the temperature-dependent n_{eh} probability distributions for energy depositions near the band gap [102].

2.2.2 Charge Trapping and Impact Ionization

The detector response model additionally accounts for the charge propagating effects of charge trapping (CT) and impact ionization (II). These two effects largely account for the distribution of events observed between quantized e^-h^+ -pair peaks [109]. Charge trapping occurs when a propagating electron or hole falls into a charge vacancy in the crystal, thereby reducing the number of electrons or holes that traverse the detector. Impact ionization occurs when a propagating charge liberates an additional loosely bound charge in the crystal, thereby increasing the number of electrons or holes that traverse the detector. Therefore the measured energy of events that undergo charge trapping is decreased, whereas the measured energy of events that undergo impact ionization is increased. A likely source of CT and II effects are impurities within the crystal, which can introduce sites of charge vacancies or loosely bound charges. Figure 2.5 illustrates the effects of CT and II inside the crystal for a single e^-h^+ pair.

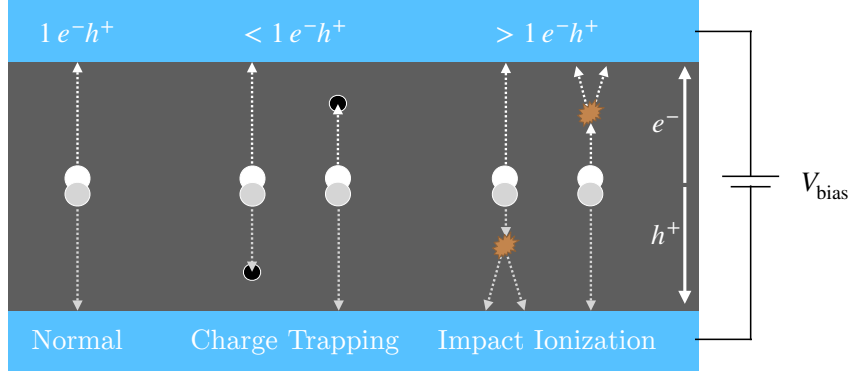


Figure 2.5: Illustration of the effects of charge trapping (CT) and impact ionization (II) for a single e^-h^+ pair. When an event generates e^-h^+ pairs inside the detector, the applied voltage bias V_{bias} will cause the electrons and holes to drift to either side of the detector. For normal events, the electrons and holes will reach the surface unimpeded. However in some cases, an electron or hole may become trapped inside a charge vacancy, or liberate an additional loosely bound charge. Note that these illustrates do not comprise all possible situations. For example, it is possible that both the electron and hole from a single e^-h^+ pair will undergo CT or II.

The detector response model used for the analyses presented in Chapters 5 and 6 incorporate the first-order CT and II model described in Ref. [110]. The details of this model are found in Appendix D. The model describes CT and II in the detector using two new parameters, whose inputs are the fractional probabilities f_{CT} and f_{II} that describe the probability of a single e^-h^+ pair to undergo CT or II, respectively. The output of the model is an energy spectrum in units of n_{eh} that contains the quantized e^-h^+ -pair peaks, but that also contains tails on either side of the e^-h^+ -pair peaks depending on the values of f_{CT} and f_{II} . Furthermore, the relative heights of the e^-h^+ -pair peaks and their tails are determined by the assumed source of events. For instance, events generated by a laser source generally have the heights of the e^-h^+ -pair peaks follow a Poisson distribution to describe the probability of absorbing n_γ number of photons at once (see Eq. 2.5 and Sec. 4.2), whereas the e^-h^+ -pair peak heights for a DM model would follow the ionization production model and Fano statistics described in Sec. 2.2.1. Figure 2.6 illustrates the effect the values of f_{CT} and f_{II} have on a n_{eh} distribution. The example in Fig. 2.6 is shown for a laser source with a mean of one photon absorbed per laser event; the e^-h^+ -peak heights therefore follow a Poisson distribution with $\lambda = 1$. Generally speaking, higher values of f_{CT} and f_{II} lead to a greater proportion of the signal in the between-peak, or tail, regions, and a lesser proportional of the signal in the e^-h^+ -pair peak regions.

The values of f_{CT} and f_{II} can differ for each detector, and are measured by fitting the model described in Appendix D.1 to data captured using a laser source (see Sec. 4.5.4). Although this CT and II model is able to fit well to laser data as shown in Chapter 4 and Ref. [109], it is important to note the limitations of the model. First, the model only considers first-order processes, meaning that it does not consider secondary CT or II occurrences for a charge after a prior II occurred. However because the probability of II measured in the detectors are typically found to be $\mathcal{O}(1\%)$, second-order processes are considered to be negligible. Secondly, the model assumes that the probability of a CT or II process occurring for a single charge is a flat distribution across the thicknesses of the detector. A more realistic model may assume an exponential decay akin to an absorption process. For such a model, the probability $P(x)$ of

a CT or II process occurring at a location x in the detector is given by:

$$P(x) = \frac{e^{-x/\tau}}{\tau}, \quad (2.9)$$

where τ is a characteristic length for either the CT or II process. Appendix D.2 demonstrates how a probability distribution described by an exponential decay approximates a flat probability distribution for small values of f_{CT} and f_{II} . The CT and II model described in Appendix D.1 also assumes that values of f_{CT} and f_{II} are the same for electrons and holes. Although this assumption made a priori, measurements of f_{CT} and f_{II} have found similar values for electrons and holes [109]. Furthermore, the model assumes that the rates of impact ionization with an opposite charge ($e^- \rightarrow h^+$ or $h^+ \rightarrow e^-$) and a same charge ($e^- \rightarrow e^-$ or $h^+ \rightarrow h^+$) are the same.

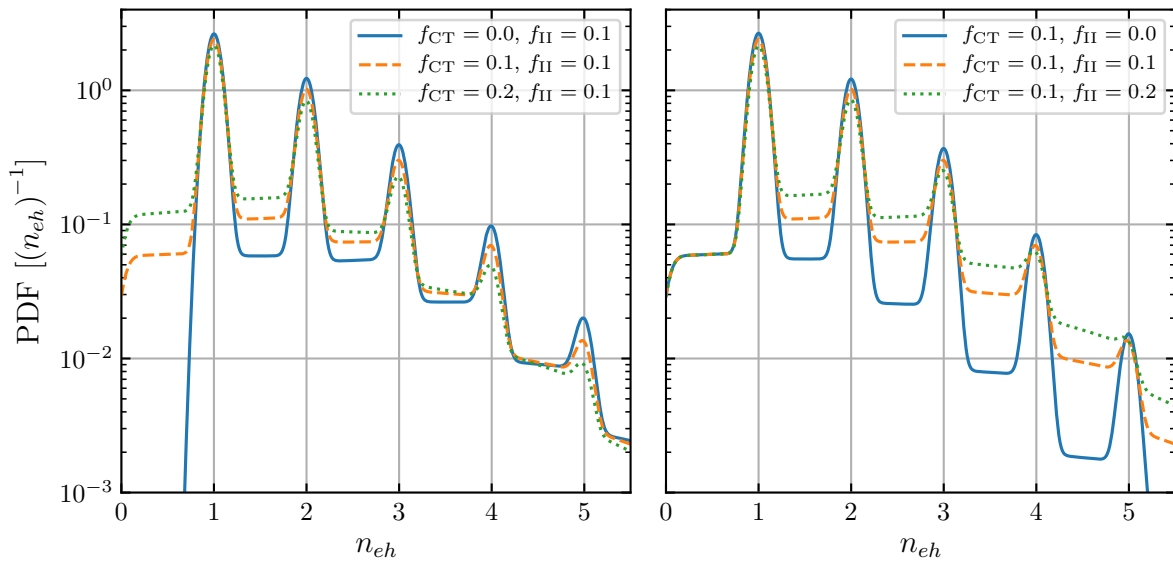


Figure 2.6: Probability distribution functions (PDFs) of signal spectra generated using the charge trapping (CT) and impact ionization (II) model with varying probabilities of each process. The model inputs f_{CT} and f_{II} described the probability of CT or II occurring for a single e^-h^+ pair, respectively. The left (right) plot shows how the PDF changes with varying f_{CT} (f_{II}) while fixing f_{II} (f_{CT}). For all of the PDFs shown, the e^-h^+ -peak heights follow a Poisson distribution with $\lambda = 1$.

The CT and II model is also assumed to be equally valid for events generated at the detector surface and events generated in the bulk of the detector. This assumption is especially important because the values of f_{CT} and f_{II} are measured using laser data which, as discussed in Chapter 4, generates e^-h^+ pairs at the surface of the detector. Therefore depending on the sign of the voltage bias applied across the detector, the values of f_{CT} and f_{II} are only measured for a single electron or hole travelling the length of the detector. In contrast, other sources of events, such as DM candidates, are expected to generate e^-h^+ pairs randomly throughout the bulk of the detector. However as long as the values of f_{CT} and f_{II} are the same for electrons and holes, the probabilities of a CT or II occurrence for a surface event or a bulk event are the same. This verification is shown in Appendix D.2.

Lastly, it is important to note that CT and II processes may not account for all of the events observed between e^-h^+ -pair peaks. For example, events whose charges hit the sidewall of a detector

before reaching the detector surface would have a measured energy between e^-h^+ -pair peaks. Despite the limitations of the CT and II model described in this section, it can sufficiently be used to explain the between- e^-h^+ -pair-peak events observed from laser sources. Along with more precise measurements of f_{CT} and f_{II} , a more robust model would be required to describe second-order CT and II processes, differences in probabilities for electrons and holes, and nuanced differences between surface- and bulk-generated events.

2.2.3 Conversion to eV Scale

The last step of the detector response model is to convert signal spectra into the expected phonon energy in units of eV. The ionization production model together with the CT and II model produce signal spectra as a function of the number of e^-h^+ pairs, n_{eh} . However as discussed in Sec. 2.1, the total phonon energy measured by the detector, E_{ph} , is the sum of the initial recoil/absorption energy of the scattered/absorbed particle, E_r , plus the energy gained via ionization production and NTL phonon amplification. Therefore the final signal spectra are dependent on both the voltage bias applied across the detector, V_{bias} , and E_r . As both the analyses in Chapters 5 and 6 are focused on particle interactions with electrons, the detector response model uses the ER case in Eq. 2.4 to convert signals in n_{eh} to signals in E_{ph} ; particle interactions with crystal nuclei would instead use the NR case in Eq. 2.4 to convert the signal spectra.

The final signal spectra are determined by scaling the energies of the pre-converted signal spectra by $e \cdot V_{\text{bias}}$ (thereby converting them to an eV energy scale) and then adding the E_r energy component to them. To keep the proper normalization of the signals, the signal spectra heights are subsequently scaled by $1/(e \cdot V_{\text{bias}})$. Although this final step of the detector response model is relatively straightforward, it has important consequences. The signal spectra produced for a detector operated at different voltage biases will have e^-h^+ -pair peaks positioned at different energies. Moreover even if a detector is operated at a constant voltage bias, the position of e^-h^+ -pair peaks can differ for two sources with different values of E_r . For example, for a detector operated at $V_{\text{bias}} = 100 \text{ V}$ measuring mono-energetic photons with energy $E_r = 2 \text{ eV}$, the first e^-h^+ -pair peak would be positioned at 102 eV. If that same detector were instead to measure 10 eV photons, the first e^-h^+ -pair peak would be positioned at 110 eV.

Lastly, the detector response model also considers cases where a given signal model consists of a spectrum of E_r values. In such cases, the signal spectrum for a *continuous*, differential event rate, $dR/dE_r(E_r)$, is first divided in to discrete values of E_r , where each $E_{r,i}$ is associated with a weight w_i that corresponds to the probability of $E_{r,i}$ occurring and $\sum_i w_i = \int dR/dE_r(E_r) dE_r$. Next, the entire detector response model (from the ionization production model to the conversion to eV scale) is performed separately for each $E_{r,i}$ to produce a corresponding *quantized* PDF, $\text{PDF}_i(E_{\text{ph}})$. The final quantized signal spectrum $dR/dE_{\text{ph}}(E_{\text{ph}})$ is the sum of the $\text{PDF}_i(E_{\text{ph}})$ functions weighted by w_i :

$$\frac{dR}{dE_{\text{ph}}}(E_{\text{ph}}) = \sum_i w_i \cdot \text{PDF}_i(E_{\text{ph}}) = \sum_i \frac{dR}{dE_{\text{ph}}}(E_{\text{ph}}, E_{r,i}), \quad (2.10)$$

where $dR/dE_{\text{ph}}(E_{\text{ph}}, E_{r,i}) = w_i \cdot \text{PDF}_i(E_{\text{ph}})$ is the quantized, differential event rate corresponding to $E_{r,i}$. An example of converting a signal model with a continuous E_r spectrum to a final quantized spectrum is shown in Fig. 2.7. Here, the continuous signal spectrum for DM-electron scattering with dark matter particles of mass $m_\chi = 5 \text{ MeV}/c^2$ and a DM-electron scattering cross section of $\bar{\sigma}_e = 10^{-37} \text{ cm}^2$

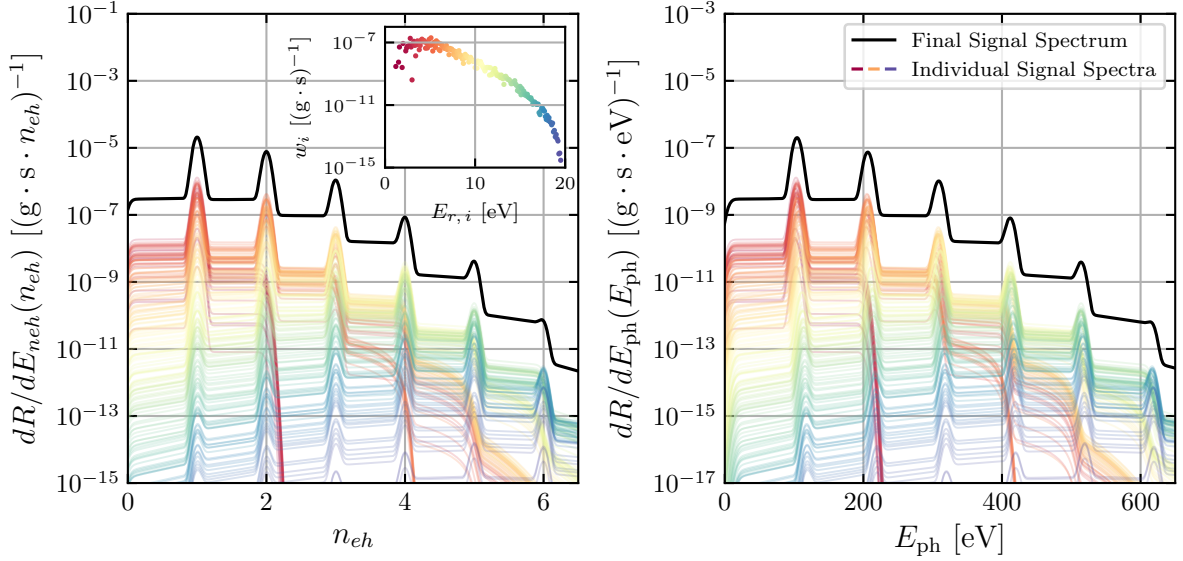


Figure 2.7: Example of a signal model with a continuous spectrum of recoil energies E_r converted to a quantized signal spectrum using the detector response model. In this example, the continuous signal spectrum for DM-electron scattering with dark matter particles of mass $m_\chi = 5 \text{ MeV}/c^2$ and a DM-electron scattering cross section of $\bar{\sigma}_e = 10^{-37} \text{ cm}^2$ is divided into discrete values of $E_{r,i}$, each with a weight of w_i in units of $(g \cdot s)^{-1}$. The inset plot on the left shows the discrete $(E_{r,i}, w_i)$ pairings. For each $E_{r,i}$, a quantized signal spectrum is produced in the n_{eh} energy space (left) and subsequently converted to the total phonon energy E_{ph} space (right) assuming an applied voltage bias of $V_{\text{bias}} = 100 \text{ V}$. The colour of each quantized signal spectrum corresponds to the $(E_{r,i}, w_i)$ pair of matching colour in the inset plot. The final quantized signal spectrum (black curve) is a differential event rate and is the sum of the individual quantized spectra.

is broken down into the individual quantized signal spectra in the n_{eh} energy space (left) and then the converted E_{ph} energy space (right). The detector response model in this example assumes an applied voltage bias of $V_{\text{bias}} = 100 \text{ V}$, a detector energy resolution of 5 eV , a Fano factor values of $F = 0.155$, and charge trapping and impact ionization probabilities of $f_{\text{CT}} = 0.1$ and $f_{\text{II}} = 0.02$, respectively. Figure 2.8 shows how the final signal spectrum from the example in Fig. 2.7 changes for different voltage biases applied to the detector. What is interesting to note in Fig. 2.8 is that the maximum dR/dE_{ph} values of the same e^-h^+ -pair peaks are equal for the different signal models. This is because, despite different voltage biases being used, the n_{eh} probabilities, as well as the energy resolution, are the same for each model. In contrast, the heights of the between-peak regions changes depending on V_{bias} . For higher values of V_{bias} , the same number of events is spread over a larger energy space, and therefore the height decreases.

2.3 Photoelectric Absorption Cross Section

The event rate of several DM candidates discussed in Sec. 1.5.3, including that of dark photons and axion-like particles (ALPs), depend on the photoelectric absorption cross section $\sigma_{\text{p.e.}}$ of the detector's target material. An accurate DM search experiment therefore requires precise determinations of $\sigma_{\text{p.e.}}$ in the energy region of interest for that experiment. When light travels through a medium, photoelectric

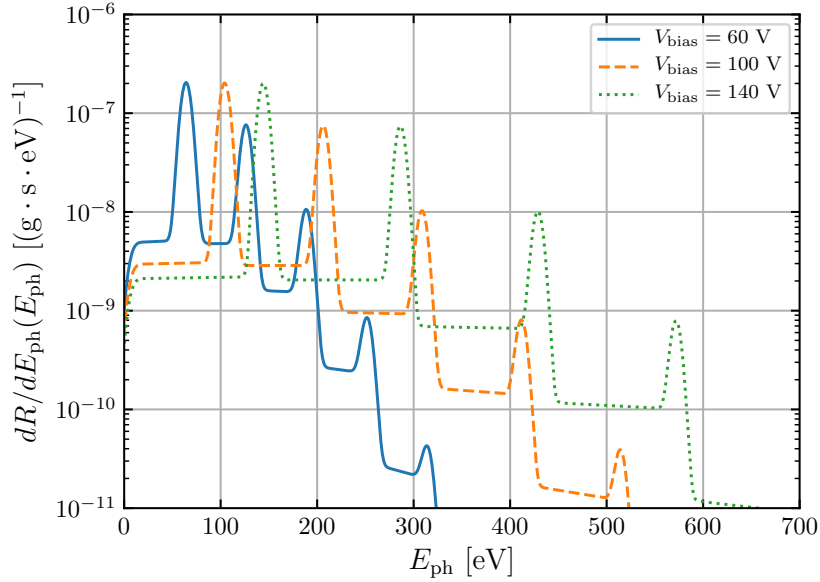


Figure 2.8: Final quantized signal spectra produced using the detector response model assuming different values of the applied voltage bias V_{bias} . The final spectra are the differential event rates across the total phonon energy measured by the detector, $dR/dE_{\text{ph}}(E_{\text{ph}})$, from the example shown in Fig. 2.7.

absorption is not the only process that can occur. Depending on the energy of the photons, coherent (Rayleigh) and incoherent (Compton) scattering may also occur. The total cross section σ_{total} of a photon travelling through a medium is the sum of the cross sections for each process:

$$\sigma_{\text{total}} = \sigma_{\text{p.e.}} + \sigma_{\text{R}} + \sigma_{\text{C}}, \quad (2.11)$$

where σ_{R} and σ_{C} are the cross sections for Rayleigh and Compton scattering, respectively. Figure 2.9 shows the breakdown of σ_{total} for both Si and Ge, the two target materials used for SuperCDMS detectors. In both Si and Ge, $\sigma_{\text{p.e.}}$ is the dominant interaction process that occurs for photons that are $\lesssim 100$ keV in energy. Because the absorption energy region of interest for the DM search experiment presented in Chapters 4 and 5 is < 100 eV, only $\sigma_{\text{p.e.}}$ needs to be considered, while σ_{R} and σ_{C} can be neglected.

The photoelectric cross section is related to other similar parameters through simple unit conversions. The analyses presented in Chapters 5 and 6 use $\sigma_{\text{p.e.}}$ in the units of cm^2/g . $\sigma_{\text{p.e.}}$ in these units is also referred to as the mass absorption coefficient or mass attenuation coefficient. Converting $\sigma_{\text{p.e.}}$ to units of cm^2 is found by:

$$\sigma_{\text{p.e.}} [\text{cm}^2] = \frac{m_A}{N_A} \sigma_{\text{p.e.}} [\text{cm}^2/\text{g}], \quad (2.12)$$

where m_A is the atomic mass of the target material, and $N_A = 6.022 \times 10^{23} \text{ mol}^{-1}$ is Avogadro's number. $\sigma_{\text{p.e.}}$ is also related to the linear absorption coefficient α :

$$\alpha = \sigma_{\text{p.e.}} \cdot \rho, \quad (2.13)$$

where ρ is the density of the target material, with $\rho = 2.33 \text{ g/cm}^3$ and $\rho = 5.32 \text{ g/cm}^3$ for Si and Ge, respectively.

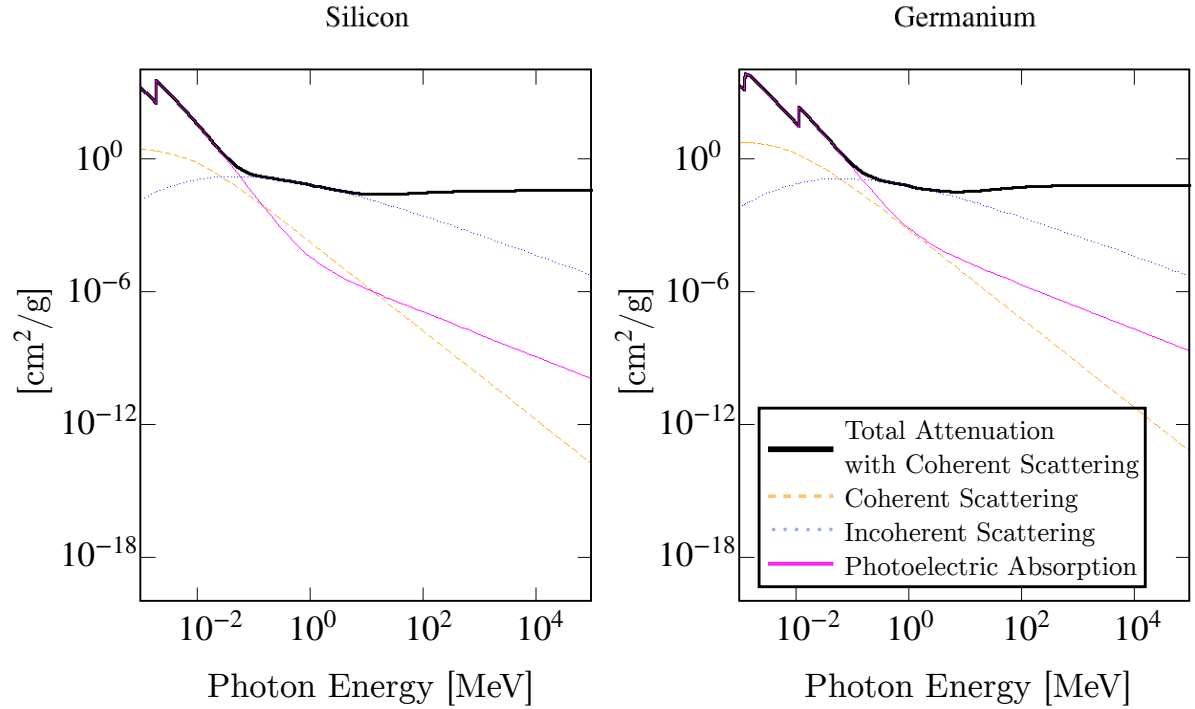


Figure 2.9: Breakdown of the cross sections for photoelectric absorption, Rayleigh scattering, and Compton scattering for photons interacting with Si (left) and Ge (right). These plots have been generated using the NIST XCOM database [111].

A broad and extensive literature search was conducted in order to obtain the $\sigma_{\text{p.e.}}$ data available for Si and Ge; Table E.1 in Appendix E contains a lists of the various references obtained through the literature search with relevant information about the data collected from each reference. The analyses presented in Chapters 5 and 6 use data that was captured with a Si detector with single- e^-h^+ -pair sensitivity. For these analyses, $\sigma_{\text{p.e.}}$ information is primarily required for photon energies up to ~ 50 eV and for energies as low as the Si band gap energy $E_g \sim 1.1$ eV. The $\sigma_{\text{p.e.}}$ data obtained through the literature search within this energy range is shown in Fig. 2.10. Other experiments and analyses may require a different range of $\sigma_{\text{p.e.}}$ data, which can also be found in Tab. E.1.

The $\sigma_{\text{p.e.}}$ data shown in Fig. 2.10 cannot be used as-is for DM search analyses for two main reasons. First, there are discrepancies of up to an order of magnitude in the available data for photon energies nearing the Si band gap. These discrepancies need to be treated as a systematic uncertainty on any DM search results that use this $\sigma_{\text{p.e.}}$ data. Second, the available data do not take into account the operating conditions that exist during DM search experiments. Specifically, the experiment described in Chapter 4 operated the Si detector at 50 mK. While some of the data in Fig. 2.10 were measured at low temperatures (see Macfarlane *et al.* [112]), none of the data were measured at temperatures as low as 50 mK over the entire energy region of interest. Therefore, a correction is applied to the $\sigma_{\text{p.e.}}$ data to account for the temperature discrepancies.

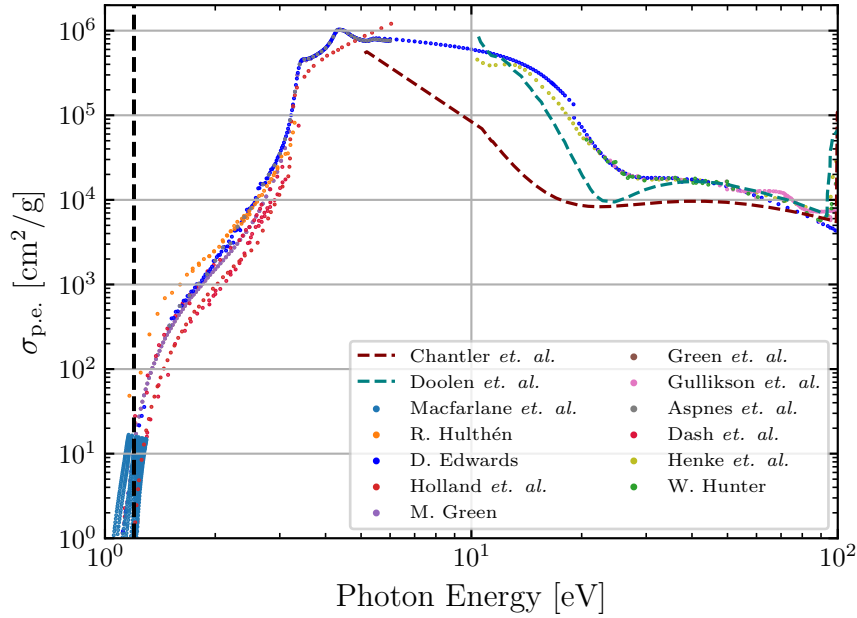


Figure 2.10: Photoelectric absorption cross section $\sigma_{\text{p.e.}}$ data for Si obtained through the literature search for photon energies $\lesssim 50$ eV [112, 113, 114, 115, 116, 117, 118, 119, 120, 121, 122, 123, 124]. See Tab. E.1 for more information about these data sources. The data points correspond to experimental or semi-empirical measurements of $\sigma_{\text{p.e.}}$, whereas the dashed lines indicate theoretical calculations of $\sigma_{\text{p.e.}}$. The dashed, vertical line is the Si band gap.

2.3.1 Temperature Correction

The dependence that $\sigma_{\text{p.e.}}$ has on temperature is predominantly due to *direct* versus *indirect* photon absorption. For photons with energies well above the band gap of the target material, electrons can absorb enough energy to be excited from the valance band directly into the conduction band. Viewing this in terms of the band structure of a semiconductor material, a direct absorption happens when an electron is excited into the conduction band without a change in its momentum k . The energy difference between the conduction and valance bands at the same momentum value is known as the *direct* band gap energy. Photons with energies less than the direct band gap energy cannot be absorbed via direct absorption.

For some materials, the highest-energy state in the valance band and the lowest-energy state in the conduction band align at the same momentum. Such materials are called direct band gap materials. In other materials, including crystalline Si and Ge, the highest-energy state in the valance band and the lowest-energy state in the conduction band exist at different momenta. The difference between the lowest-energy state in conduction band and the highest-energy state in the valance band at differing momenta is known as the *indirect* band gap energy. Materials with indirect band gaps are evidently called indirect band gap materials. For indirect band gap materials, photons with energies less than the direct band gap energy can still be absorbed by means of indirect photon absorption. To undergo indirect absorption, a photon must have an energy at least as large as the indirect band gap, and the electron will have to experience a change in its momentum when excited into the conduction band. In order to conserve momentum, the process must involve either the absorption or emission of a phonon,

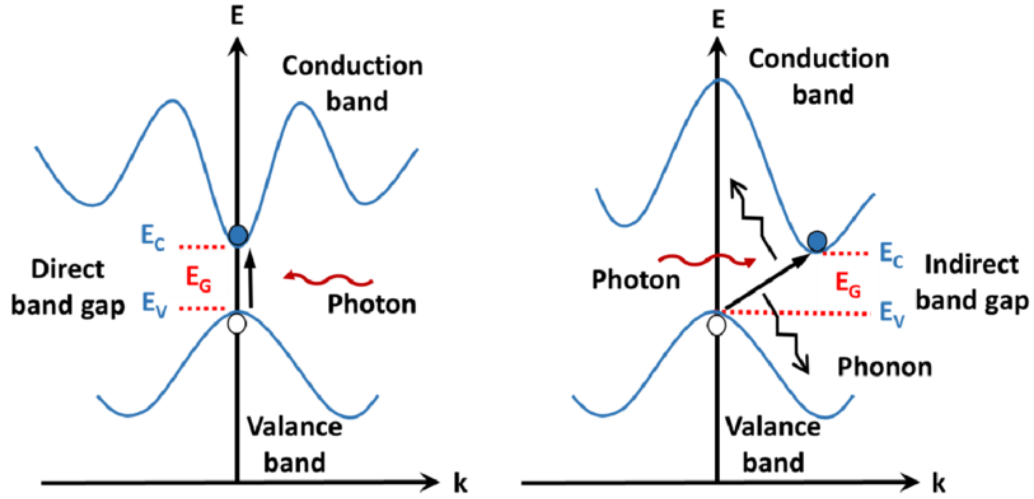


Figure 2.11: Illustration of direct (left) and indirect (right) photon absorption for band structures with energy E and momentum k . Indirect band gap materials, including crystalline Si and Ge, can undergo indirect photon absorption that involves either the absorption or emission of a phonon. E_V , E_C , and E_G denote the valence band, conduction band, and band gap, respectively. Illustration provided by Ref. [125].

where the momentum of the phonon is equal to the change in momentum of the electron. Fig. 2.11 illustrates both direct and indirect photon absorption.

A temperature dependence arises in the linear absorption coefficient for indirect absorption, $\alpha_n(T)$, due to the probability distribution of phonon absorption or emission. As the temperature decreases, the probability that a phonon can be simultaneously absorbed or emitted along with a photon being absorbed decreases. More specifically, the linear absorption coefficient for indirect absorption via phonon absorption, $\alpha_{n,a}(T)$, is proportional to the probability of finding phonons in a given state with energy E_p : $\alpha_{n,a}(T) \propto (e^{E_p/k_b T} - 1)^{-1}$. Similarly, the linear absorption coefficient for indirect absorption via phonon emission, $\alpha_{n,e}(T)$, is proportional to the probability of emitting phonons in a given state with energy E_p : $\alpha_{n,e}(T) \propto (1 - e^{-E_p/k_b T})^{-1}$. As $T \rightarrow 0$, $\alpha_{n,a}(T) \rightarrow 0$ and there are no available phonon states that can be absorbed. Although indirect absorption via phonon emission is still possible at $T = 0$, $\alpha_{n,e}(T)$ is minimized at low temperatures given that $(1 - e^{-E_p/k_b T})^{-1} \rightarrow 1$ as $T \rightarrow 0$. This temperature dependence is only relevant for photon energies near or below the direct band gap energy. For photons with energies well above the direct band gap, indirect absorption is a highly subdominant process and thus temperature considerations are not required.

The $\sigma_{p.e.}$ data shown in Fig. 2.10 is corrected for temperature by utilizing the photon absorption model for Si described in Appendix F. Equation F.5 provides a formula for calculating $\alpha(T, E_\gamma)$, the total linear absorption coefficient at a given temperature and photon energy E_γ . This absorption model is valid for energies as low as the lowest indirect band gap energy for Si (~ 1.1 eV) and up to 4 eV, slightly above the direct band gap energy for Si (~ 3.2 eV). The value of every $\sigma_{p.e.}$ data point within this range that was measured at a temperature $T = T_{\text{meas}}$ is corrected to a temperature $T = T_{\text{corr}}$ by

finding the ratio of $\alpha(T, E_\gamma)$ computed at T_{corr} and T_{meas} (see Appendix F):

$$\sigma_{\text{p.e.}}(T_{\text{corr}}, E_\gamma) = f \cdot \frac{\alpha(T_{\text{corr}}, E_\gamma)}{\alpha(T_{\text{meas}}, E_\gamma)} \cdot \sigma_{\text{p.e.}}(T_{\text{meas}}, E_\gamma), \quad (2.14)$$

where f is an additional factor that ensures $\alpha(T_{\text{meas}}, E_\gamma)/\alpha(T_{\text{corr}}, E_\gamma) = 1$ at $E_\gamma = 4 \text{ eV}$, the boundary of where the model is valid. Figure 2.12 shows the $\sigma_{\text{p.e.}}$ data before and after applying the temperature correction with $T_{\text{corr}} = 50 \text{ mK}$.

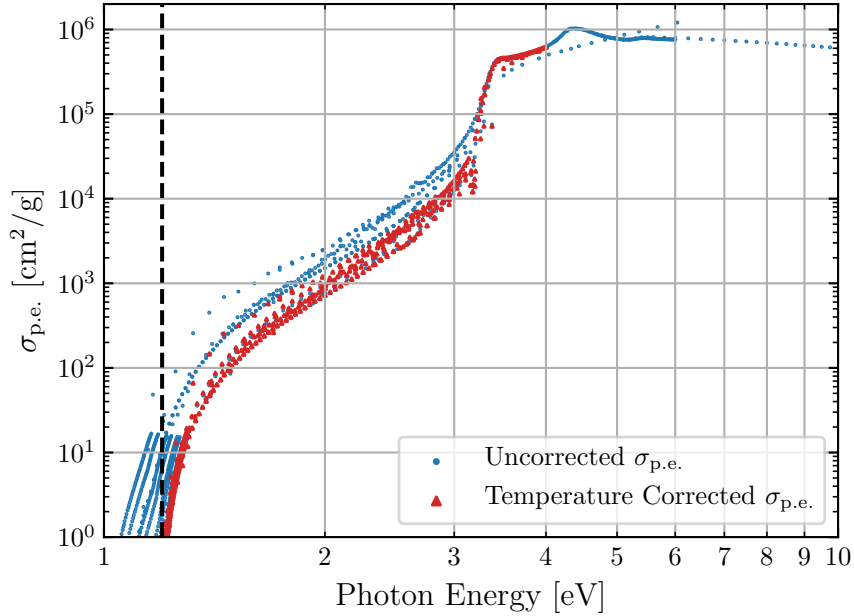


Figure 2.12: Photoelectric absorption cross section $\sigma_{\text{p.e.}}$ data before and after applying the temperature correction. The blue data points are the uncorrected $\sigma_{\text{p.e.}}$ data seen in Fig. 2.10. The red data points are the $\sigma_{\text{p.e.}}$ data corrected to 50 mK using Eq. 2.14, and the dashed, vertical line is the Si band gap.

2.3.2 Other Considerations

A few more effects are considered to assess whether they have an impact on $\sigma_{\text{p.e.}}$. One such effect is how $\sigma_{\text{p.e.}}$ depends on an external electric field. As mentioned in Sec. 2.1, cryogenic semiconductor crystal detectors are operated with an applied voltage bias across the detector. However the externally applied electric field can induce what is known as the Franz-Keldysh effect [126]. The Franz-Keldysh effect occurs when a strong electric field applied to a semiconductor material alters the wavefunctions of electrons and holes, resulting in changes to the shape of the absorption edge of the semiconductor. This effect can alter $\sigma_{\text{p.e.}}$ at energies near the band gaps, but only for strong electric fields. Using a model that computes the change in $\sigma_{\text{p.e.}}$ due to an applied electric field [126], it is determined that the typical field strengths used for SuperCDMS detectors ($< 400 \text{ V/cm}$) are not strong enough to produce significant changes to the absorption edge of Si. Therefore voltage-induced effects on $\sigma_{\text{p.e.}}$ are neglected.

Another effect considered is the effect of free carrier absorption. Free carrier absorption occurs when a carrier (electron or hole) in an already excited state absorbs a photon and moves to another exciting state in the same band. The total absorption cross section is comprised of both interband

absorption (transitions from the valance to conduction band) and intraband (free carrier) absorption. Like with indirect absorption, free carrier absorption also exhibits a temperature dependence due to the temperature dependence of the concentration of free carriers. As the temperature approaches zero, the concentration of free carrier electrons and holes also approach zero and the electrons fill all the available states in the valance band. Yet models for free carrier absorption demonstrate that even for free carrier concentrations of undoped Si at room temperature, this process is highly subdominant compared to interband absorption [127]. Therefore free carrier effects on the $\sigma_{p.e.}$ data also neglected. Free carrier absorption does become significant when considering sub-gap absorption in highly-doped semiconductor materials [127].

2.3.3 Photoelectric Absorption Cross Section Curves

Figure 2.12 shows that even after correcting for temperature, there are still discrepancies in the $\sigma_{p.e.}$ data at energies near the Si band gap. For DM search experiments that depend on $\sigma_{p.e.}$ in this low energy region, the discrepancies in the data are a source of systematic uncertainty in the DM search results. Two questions naturally arise: which $\sigma_{p.e.}$ data should be used to produce DM search results, and how can the uncertainty in the $\sigma_{p.e.}$ data be characterized? Both questions are answered by generating three separate $\sigma_{p.e.}$ curves defined as the *nominal*, *lower*, and *upper* $\sigma_{p.e.}$ curves.

The nominal $\sigma_{p.e.}$ curve is comprised of $\sigma_{p.e.}$ data that is commonly used in DM search experiments. Its definition roughly follows the approach taken in Ref. [79], with data from D. Edwards [114] for energies below 1 keV and Henke *et. al.* [123] for energies between 1–20 keV. Additionally for energies above 20 keV, $\sigma_{p.e.}$ data is obtained from the NIST XCOM database [114]. The upper and lower curves are derived by tracing upper and lower bounds of the experimental and semi-empirical $\sigma_{p.e.}$ data after the temperature correction is applied, along with the nominal curve data that does not have the temperature correction applied. Including the nominal curve data ensures that the upper and lower curves always produce the highest and lowest values of $\sigma_{p.e.}$ at a given energy. The upper and lower $\sigma_{p.e.}$ curves thus represent the highest and lowest reasonable values of $\sigma_{p.e.}$ while accounting for discrepancies in the data and temperature dependencies. In the context of DM search experiments, analyses can be repeated by interchanging these three curves in order to assess the systematic uncertainty on the DM search results. A similar procedure is used for the analysis presented in Chapter 5; in Chapter 6, a new measurement of $\sigma_{p.e.}$ in Si is presented. Figure 2.13 shows the nominal, lower, and upper $\sigma_{p.e.}$ curves generated using the Si $\sigma_{p.e.}$ data for photon energies below 100 eV.

2.4 Detector Leakage

Every DM search experiment is concerned with the sources that cause background events that are measured by the detector. Some sources of background events are generated from external particle interactions with the detector. For a semiconductor-type DM detector, that can include muons, cosmic rays, or infrared photons that undergo sub-gap absorption with impurities in the crystal. However for those same detectors there is another significant type of background events referred to as detector leakage. Detector leakage, sometimes called charge leakage, is a loosely defined term to mean any source of events that are not generated by external particle interactions with the detector. Sources of detector leakage are likely induced by the voltage bias applied across the detector. The large electric fields that are used for signal amplification can also cause spontaneous ionization at sites of impurities

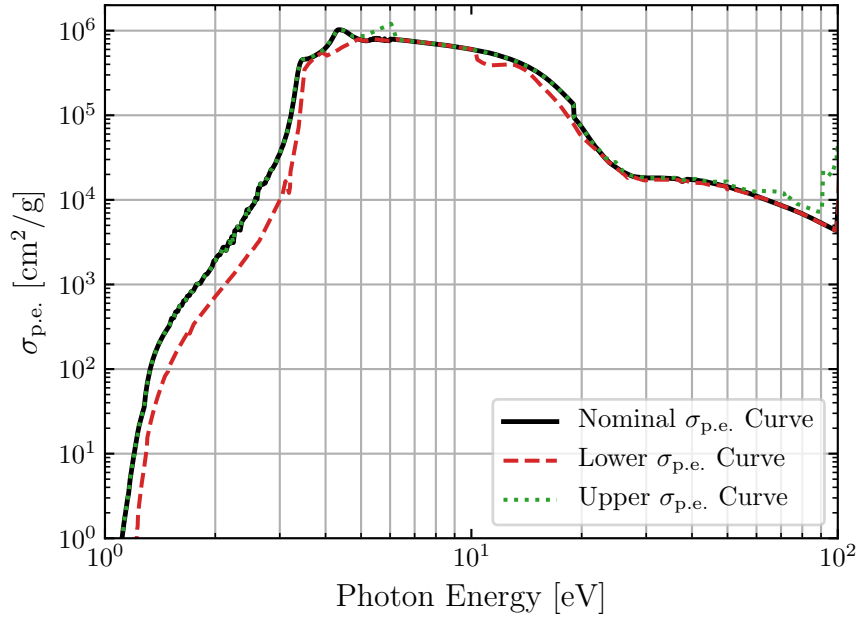


Figure 2.13: Photoelectric absorption cross section $\sigma_{p.e.}$ curves generated from the Si $\sigma_{p.e.}$ data. The solid, black curve is the nominal $\sigma_{p.e.}$ curve comprised of commonly used data. The dashed, red and dotted, green curves are the lower and upper $\sigma_{p.e.}$ curves, respectively, determined by tracing upper and lower bounds of the published data from the literature search after applying the temperature correction. For energies below ~ 5 eV, the nominal and upper $\sigma_{p.e.}$ curves are overlapping.

in the bulk of the detector or at sites of imperfections (e.g. chips or rough edges) along the surfaces of the detector. The electric fields may also induce tunneling of charge carries at interfaces between the detector crystal and other semiconductor materials, such as electrodes. Each of these sources of detector leakage produce single- e^-h^+ -pair events that are measured by the detector. The significance of detector leakage is therefore dependent on the energy resolution and threshold of the detector. For detectors that have single- e^-h^+ -pair sensitivity, including the ones used in Ref. [106] and Chapters 4 and 5, detector leakage is hypothesized to be a leading source of events observed in the first e^-h^+ -pair peak.

Detector leakage can be difficult to quantify, predict, or distinguish between the various sources. A study using the Si, 4 mm thick detector in Ref. [106] found that the rate of leakage events increases with the applied voltage bias for voltages above ~ 120 – 140 V and that a breakdown occurs at around 180 V. Despite the challenges with characterizing detector leakage, there are ways to lower the leakage rate. One obvious solution is to use a detector made with extremely high-purity semiconductor material and to use precise fabrication techniques to avoid damages along the surfaces of the detector. Another solution is to pre-bias the detector by holding it at a high voltage prior to data acquisition to release any loose charges. Lastly, one could minimize the surface area of semiconductor-semiconductor interfaces in the detector to reduce charge tunneling effects. However the significance of this source of detector leakage is presently unclear, and, as Chapter 3 discusses, these interfaces are important for phonon collection and the overall performance of the detector.

2.5 SuperCDMS Detectors

The SuperCDMS collaboration employs various types of solid-state detectors for DM search experiments. Four types of detectors will be used for the SuperCDMS experiment at SNOLAB as mentioned in Sec. 1.6: interleaved Z-sensitive ionization phonon (iZIP) detectors made of either Si or Ge, and high voltage (HV) detectors made of either Si or Ge. Information about these detectors is obtained from Ref. [94] and references therein. Each of these detectors consist of a cylindrical crystal that is 100 mm in diameter and 33.3 mm thick. Si and Ge detectors have a mass of 0.61 and 1.39 kg, respectively. iZIP and HV detectors are fabricated identically, but utilize a different combination and layout of either ionization (charge) sensing channels or phonon sensing channels in order to optimize the detectors for separate purposes. The charge channels consist of high-electron-mobility transistors (HEMTs) that measure the amount of charge energy produced by an event. The phonon channels use aluminum fins to absorb phonons and tungsten transition edge sensors (TESs) to measure the amount of phonon energy (see Chapter 3).

iZIP detectors operate using a combination of phonon and charge channels. Both the top and bottom surfaces of the detector are fitted with six phonon channels interleaved with two charge channels. A small voltage bias of $\sim 5\text{--}10\text{ V}$ is applied to allow e^-h^+ pairs to drift to either surface. The top image in Fig. 2.14 shows the channel layout for iZIP detectors. By separately measuring phonon and charge signals, iZIP detectors are able to discriminate between nuclear recoil (NR) and electron recoil (ER) interactions with the detector. The measured charge signal E_{ch} is equal to the amount of energy from ionization produced for a given event:

$$E_{\text{ch}} = n_{eh} \cdot \epsilon_{eh} = Y(E_{\text{recoil}}) \cdot E_{\text{recoil}}. \quad (2.15)$$

This charge energy can be compared to the measured phonon energy E_{ph} described by Eq. 2.4. Isolating for E_{recoil} and substituting in Eq. 2.15, the measured charge and phonon signals are related by:

$$\begin{aligned} E_{\text{ch}} &= E_{\text{ph}} \cdot Y(E_{\text{recoil}}) \left(1 + \frac{Y(E_{\text{recoil}}) \cdot e \cdot V_{\text{bias}}}{\epsilon_{eh}} \right)^{-1} \\ &= E_{\text{ph}} \left(\frac{1}{Y(E_{\text{recoil}})} + \frac{e \cdot V_{\text{bias}}}{\epsilon_{eh}} \right)^{-1}. \end{aligned} \quad (2.16)$$

Equation 2.16 shows that the relationship between E_{ch} and E_{ph} can be approximated as a line with a slope of $\left(\frac{1}{Y(E_{\text{recoil}})} + \frac{e \cdot V_{\text{bias}}}{\epsilon_{eh}} \right)^{-1}$. For ER events with $Y(E_{\text{recoil}}) = 1$, the slope of E_{ch} versus E_{ph} is larger than that of NR events with $Y(E_{\text{recoil}}) < 1$. By plotting the E_{ch} and E_{ph} data of events, ER and NR interactions can easily be distinguished based on which slope they follow. This remains true as long as the resolution is high enough and the applied voltage bias remains relatively small; if $e \cdot V_{\text{bias}}/\epsilon_{eh} \gg 1/Y(E_{\text{recoil}})$ in Eq. 2.16, the distinction between ER and NR events becomes less apparent. iZIP detectors are able to utilize this ER/NR discrimination to identify events resulting from ER interactions. From the perspective of NR DM searches, this discrimination can be used to remove ER backgrounds that interact with the bulk of the detector.

HV detectors consist of only phonon channels, with six channels arranged on both the top and bottom surfaces. The bottom image in Fig. 2.14 shows the channel layout for HV detectors. HV detectors have more phonon sensors compared to iZIP detectors, which allows for better phonon collection and therefore better phonon energy resolution and a lower energy threshold. Furthermore, HV detectors

will be operated with a bias voltage up to ~ 100 V. The high operating voltage allows for a greater amplification of the phonon signal due to NTL production, and allows the HV detectors to be sensitive to much lower recoil energies. Table 2.1 summarizes the properties for each detector type for the SuperCDMS SNOLAB experiment obtained from Ref. [94]. The listed values for the phonon and charge energy resolution depend on properties of the sensor designs that are not discussed here.

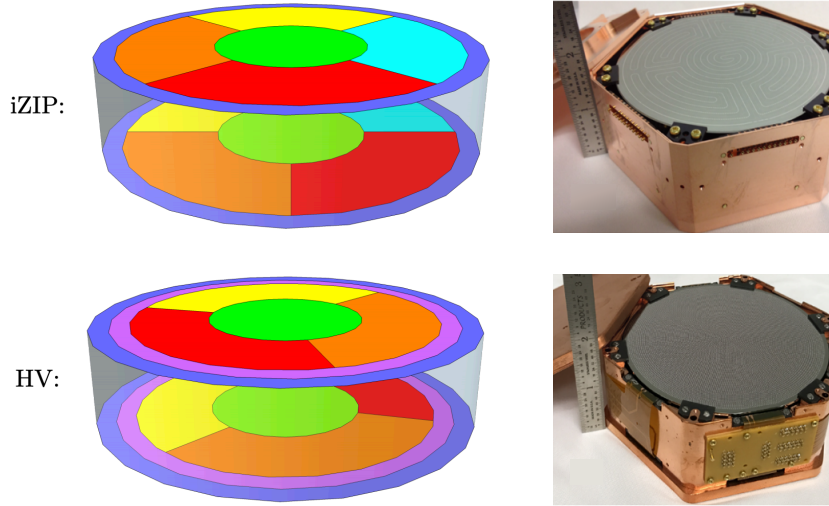


Figure 2.14: Channel layout for the interleaved Z-sensitive ionization phonon (iZIP) (top) and high-voltage (HV) (bottom) detectors. iZIP detectors consist of six phonon channels interleaved with two charge channels on each side. The 12 phonon channels are outlined in the diagram above by separate colours. On each side, one charge channel shares the same area as the outer most ring phonon channel, and the other charge channel is interleaved with the remaining phonon channels. HV detectors consist of six phonon channels arranged on each side. Beside each channel layout is a photograph of the detector inside the detector housing. The channel layouts are obtained from Ref. [94], and the photographs are provided by the SuperCDMS collaboration.

Table 2.1: Summary of the properties for interleaved Z-sensitive ionization phonon (iZIP) and high-voltage (HV) detectors expected for the SuperCDMS SNOLAB experiment. All of the values in this table are obtained from Ref. [94]. The expected phonon energy thresholds are converted to nuclear recoil energy thresholds by inverting Eq. 2.4. The number of each type of detector and corresponding exposure are based on the initial payload for the SNOLAB experiment.

	iZIP		HV	
	Ge	Si	Ge	Si
Phonon energy resolution [eV]	50	25	10	5
Charge energy resolution [eV]	100	110	–	–
Phonon energy threshold [eV]	350	175	100	100
Nuclear recoil energy threshold [eV]	272	166	40	78
Voltage bias [V]	6	8	100	100
Number of detectors	10	2	8	4
Exposure [kg-yr]	56	4.8	44	9.6

The differences between the detectors can be used to explain the differences in the projected sensitivities for WIMP-nucleon scattering observed in Fig. 1.12 for each detector type. The iZIP detectors have a better projected sensitivity for WIMP masses $\gtrsim 5 \text{ GeV}/c^2$ because of the ability of iZIP detectors to remove the vast majority of expected background events [94] due to ER/NR discrimination. This means that iZIP detectors are expected to operate in a nearly background-free mode where the sensitivity is only limited by the amount of exposure. The projected sensitivity for Ge iZIP detectors is better than Si because of the greater exposure of Ge iZIPs expected in the initial payload for the SNOLAB experiment. Conversely, HV detectors have better sensitivity for WIMP masses below $\sim 5 \text{ GeV}/c^2$ because they are sensitive to lower nuclear recoil energies. However because HV detectors cannot distinguish between ER and NR events, the projected sensitivities are limited by the background rate. The projected sensitivity for Si HV detectors is worse than Ge due to the additional background rate from beta particles caused by the decay of ^{32}Si . However Si HV detectors are sensitive to slightly lower WIMP masses compared to Ge. This is due to the kinematics of NR interactions and the fact that Si detectors contain lighter isotopes compared to Ge detectors (see Eq. 1.21).

The detectors described for the SNOLAB experiment are not the only detectors employed by the SuperCDMS collaboration. Other detectors with similar technologies have been developed at test facilities for the purposes of R&D and, in some cases, are used to perform DM search experiments. This includes a class of detectors known as high-voltage eV-scale (HVeV) detectors that are small, 0.93 g devices made of Si that utilize the same concepts as the SNOLAB HV detectors but have extremely high energy resolution. Chapter 3 discusses the second-generation HVeV detector that is used for the DM search experiment presented in Chapters 4 and 5.

Chapter 3

HVeV Phonon Sensors and Detector Design

This chapter provides an overview of the sensor technology and design that is used in SuperCDMS high-voltage eV-scale (HVeV) detectors that have single-charge sensitivity. These detectors measure interactions of dark matter (DM) or background particles with the target material using cryogenic athermal phonon sensor technology [128, 129, 130], and over recent years have demonstrated single- e^-h^+ -pair sensitivity and \sim eV-scale resolution [106, 131, 132]. After outlining the detector concepts, this chapter will discuss the design and optimization of the second-generation HVeV detector that was used for the HVeV Run 2 experiment in Chapters 4 and 5, including how it differs and improves from the first-generation detector used in the HVeV Run 1 experiment [106]. Lastly, some basic characterization metrics of the HVeV Run 2 detector are shown. Much of the information in this chapter is reported in Ref. [99] and references therein.

3.1 Phonon Detection Concepts

3.1.1 Transition Edge Sensors

As discussed in Chapter 2, the energy from an interaction of a particle with a SuperCDMS detector (including HVeV detectors) is measured as heat energy through athermal phonons. When the prompt and Neganov-Trofimov-Luke (NTL) phonons reach the surface of the detector, the heat energy is eventually measured using transition edge sensors (TESs). The TESs in HVeV-type detectors are made of tungsten (W), and have a critical temperature of $T_c \sim 65$ mK. T_c indicates the temperature where the TES transitions between its superconducting and normal modes, as illustrated in Fig. 3.1. To measure heat depositions, the TES is held at a temperature near T_c . If a heat deposition occurs, the temperature and thus the resistance of the TES will rise. The increased resistance results in a change in current that is later observed as a measurement signal.

3.1.2 SQUID Circuits

Resistance changes in the TES are converted to a measurement signal using superconducting quantum interference devices (SQUIDs). SQUIDs operate using superconducting loops containing Josephson

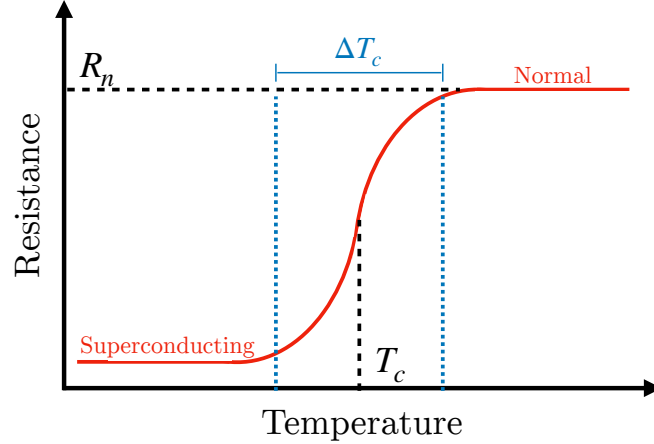


Figure 3.1: Illustration of a resistance-temperature curve for a transition edge sensor (TES). To measure heat depositions, TESs are operated near the critical temperature T_c between the superconducting the normal modes. R_n is the normal-mode resistance of the TES and ΔT_c is the transition width.

junctions to measure extremely small magnetic fields. If the current through a SQUID exceeds a critical current, a voltage will appear across the SQUID with a periodic dependence on the magnetic flux through the SQUID. This voltage dependence on magnetic flux is illustrated in the left plot of Fig. 3.2, with the period of oscillation equal to one flux quantum Φ_0 . The right image of Fig. 3.2 shows a simplified schematic of the TES-SQUID readout circuit.

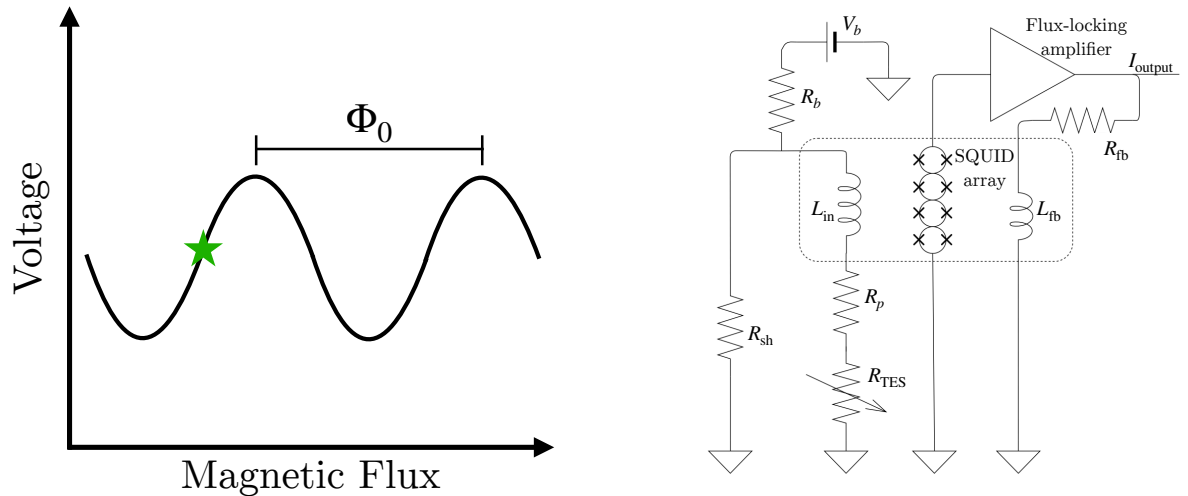


Figure 3.2: Left: illustration of the periodic voltage dependence on the magnetic flux through a SQUID. The period of oscillation is equal to one flux quantum Φ_0 , and the green star is an example of a SQUID lock point. Right: simplified schematic of the TES-SQUID circuit used for HVEV detectors replicated from Ref. [99]. The parameters shown in this schematic include: voltage bias V_b , bias resistance R_b , shunt resistor R_{sh} , parasitic resistance R_p , TES resistance R_{TES} , feedback resistor R_{fb} , input inductance L_{in} , feedback inductance L_{fb} , and output current I_{output} .

For the sake of brevity, only a brief summary of the TES-SQUID circuit will be provided; more details on this topic can be found in Refs. [133, 134, 135]. An array of TESs in parallel are held at a temperature T_0 near the critical temperature by providing a voltage bias V_b with a bias resistance R_b

that keeps a constant current I_s through the TESs. Because the TESs are thermally coupled with the detector substrate that has a bath temperature of T_b , the TESs exhibit thermal power loss described by:

$$P = K (T_0^5 - T_b^5), \quad (3.1)$$

where K is the thermal conductivity between the TESs and the thermal bath of the detector substrate and $T_b < T_0$. When there is no heat deposition in the TESs, this thermal power loss is equal to the Joule power provided by the bias voltage and current through the TESs, described by:

$$P = I_s^2 R_{\text{TES}} = \frac{V_b^2}{R_{\text{TES}}}, \quad (3.2)$$

where R_{TES} is the TES resistance. The shunt resistor R_{sh} in the TES-SQUID circuit ensures that the voltage across the TESs remains relatively constant. Therefore the Joule power can be expressed solely as $P = V_b^2/R_{\text{TES}}$, which provides the necessary negative-feedback system referred to as electrothermal feedback. As the resistance of the TESs increases, the Joule power provided to the TESs will decrease and become less than the thermal power loss. This power inequality returns the TESs to their original operating temperature and resistance.

The array of TESs are also in series with a coil that provides an input inductance L_{in} to an array of SQUIDS in series, as seen in the circuit diagram in Fig. 3.2. The SQUIDS are connected to a flux-locking amplifier, which serves multiple purposes. One such purpose is to provide a bias current through the SQUIDS to “lock” them at some point on the periodic voltage-magnetic flux curve. The left plot of Fig. 3.2 shows an example of a lock point. The magnetic flux from L_{in} induces a voltage across each of the SQUIDS, and the total voltage signal across the SQUID array is amplified by the flux-locking amplifier. Let the amplified output voltage signal from the SQUID array be denoted as V_{SQ} . A feedback voltage V_{fb} is provided to supply a current through a feedback resistor R_{fb} and an additional coil that provides a feedback inductance L_{fb} to the array of SQUIDS.

The purpose of this feedback inductance is to continuously counteract the magnetic flux through the SQUIDS supplied by L_{in} by supplying an opposing magnetic flux. Through a negative-feedback loop gain circuit, V_{fb} provides the voltage required to keep the net magnetic flux through the SQUIDS, and thus V_{SQ} , constant at all times. This remains true when the TES-SQUID circuit is in a steady state and there is no heat deposition in the TESs. When a heat deposition does occur, the current through the input coil will decrease, and V_{fb} will adjust to the necessary voltage to keep V_{SQ} constant. The actual signal that is taken as a measurement is V_{fb} recorded over time and later converted to the current through the TESs and digitized.

The flux-locking feedback system is a critical component to measure heat depositions in the TESs. Keeping the SQUIDS locked at one point on the periodic voltage-magnetic flux curve ensures a linear relationship between the current through the input coil and V_{fb} . Additionally, the lock point determines the amount of direct current (DC) offset that signals are subject to; the baseline current of signals measured at different lock points will be offset by different amounts. Setting a lock point is mentioned as part of the experimental procedure for the HVEV Run 2 experiment in Sec. 4.2. Although this flux-locking mechanism is very robust, there are rare instances, as described in Chapter 4, where the lock point can spontaneously and unintentionally jump to a new position during data acquisition.

3.1.3 Quasiparticle-trap-assisted Electrothermal-feedback TESs

For SuperCDMS detectors, TESs themselves are not used as the primary means to collect or absorb athermal phonons. Although increasing the area that the TESs cover on the substrate surface would increase the amount of phonons that can be collected, it would also increase the thermal conductance of the TESs and degrade the energy resolution of the detector. Instead, HVEV-style detectors employ quasiparticle-trap-assisted Electrothermal-feedback TESs (QETs) [136] to interface with the detector substrate. A QET consists of a superconducting thin film (or fin) made of Al coupled to a TES, as shown in Fig. 3.3.

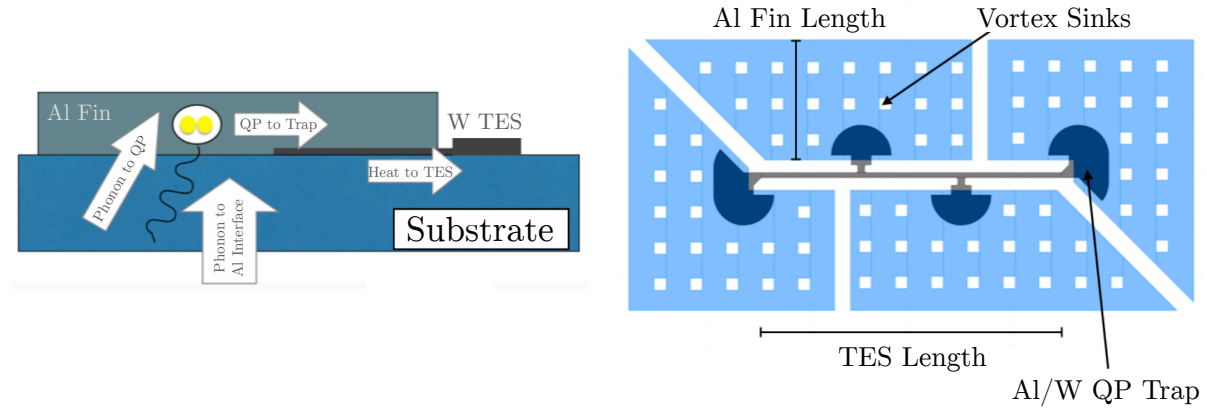


Figure 3.3: Overview of the energy transport (left) and design geometry (right) for a QET sensor. Athermal phonons generated by interactions within the detector substrate propagate to the Al/substrate interface, where they are either reflected or transmitted. The transmitted phonons break Cooper pairs in the Al fin, creating quasiparticles (QPs) that diffuse throughout the fin. The QPs that reach the lower-gap energy region of the Al/W quasiparticle trap will convert most of their energy to phonons that subsequently heat the TES. The vortex sinks are holes placed in the Al fins to prevent magnetic vortices from forming in the superconducting material. Replicated from Ref. [99].

The Al fins interface with the detector substrate and collect phonons from a preceding interaction. As a phonon reaches an Al fin, it may either be transmitted into the Al fin or reflected back into the detector substrate. A phonon may be reflected several times (by both absorbing and non-absorbing surfaces) before it is transmitted into an Al fin, while others may never be transmitted. The probability that a phonon will eventually be absorbed by an Al fin is characterized by the phonon collection efficiency. The transmitted phonons will break Cooper pairs and create quasiparticles (QPs) that diffuse throughout the fins. Some of those QPs will reach an overlapping region of a fin and a TES that forms a QP trap. QPs that diffuse into the trap will release most of their energy via phonon emission into the overlapping TES. The combined heat deposition experienced by an array of TESs connected in parallel is then measured by the readout SQUID readout circuit illustrated in Fig. 3.2.

The Al fins have a critical temperature of $\sim 1.2\text{K}$ that is well above the critical temperature of $\sim 65\text{mK}$ of the W TESs, meaning that the fins will remain in a superconducting mode when the TESs are held near their critical temperature. Furthermore, the energy to break a Cooper pair in Al ($\sim 350\mu\text{eV}$) is much larger than the energy of residual thermal phonons at low temperature ($\sim 1\mu\text{eV}$ at 10mK). The Al fins are thus able to separate thermal phonons from the athermal phonons produced by an interaction in the detector. Because the superconducting Al fins do not contribute to the heat

capacity of the TESs, they can be designed to cover a large proportion of the substrate surface without degrading the energy resolution.

3.1.4 Optimized Parameters

One of the goals of the detector design optimization is to minimize the phonon energy resolution σ_{ph} . Following Refs. [133, 135, 15], σ_{ph} can be expressed as:

$$\sigma_{\text{ph}} = \frac{1}{\epsilon} \sqrt{2Gk_b T_0^2 \tau_{\text{BW}}}, \quad (3.3)$$

where T_0 is the operating temperature of the TESs, G is the thermal conductance between the TESs and the detector substrate, ϵ is the efficiency of phonon energy collection, and τ_{BW} is the time constant of the detector bandwidth. For a TES with a narrow transition width, T_0 can reasonably be approximated by T_c . The energy resolution in Eq. 3.3 uses the fact that the noise power in the detectors are dominated by the intrinsic TES thermal fluctuation noise that is characterized by the white noise power $N_G \approx 2Gk_b T_0^2$, where G is proportional to the total TES volume v_{TES} . The detector bandwidth can further be expressed as $\tau_{\text{BW}} = \tau_{\text{ph}} + \tau_-$, where τ_{ph} is the phonon collection time of the detector, and τ_- is the effective TES response time that characterizes the timescale of the electrothermal feedback process. These two time constants determine the shape of the readout pulses and affect the signal-to-noise ratio of the measurements.

Equation 3.3 also shows that σ_{ph} is dependent on ϵ . This dependency arises from the calibration of the collected energy to the true energy of an interaction. For example, if a TES has a resolution of 1 eV and collects 20% of the total phonon energy, the measured energy resolution would be 5 eV. However if the same TES collects only 10% of the total phonon energy, the measured energy resolution would be 10 eV. As outlined in Ref. [99], ϵ is comprised of four main components: (i) the phonon collection efficiency ϵ_{ph} that describes the probability that an initial phonon is absorbed by the Al fin; (ii) the phonon to QP conversion efficiency ϵ_{qp} for a phonon absorbed in the Al fin; (iii) the QP collection efficiency ϵ_{coll} for the QPs to drift into the trapping regions; and (iv) the trapped QP to TES thermal energy conversion efficiency ϵ_{trap} . The total efficiency is the product of these four individual efficiencies: $\epsilon = \epsilon_{\text{ph}} \epsilon_{\text{qp}} \epsilon_{\text{coll}} \epsilon_{\text{trap}}$.

Two of these efficiencies, ϵ_{ph} and ϵ_{coll} , can be tuned through design optimization. ϵ_{ph} can be increased by increasing the fraction of the substrate surface that is covered by the Al fins. Furthermore, the dimensions of the detector substrate can be tuned to minimize the amount of detector side-wall area, which is a more dominant source of phonon energy loss [137]. ϵ_{coll} can also be highly optimized by tuning the Al fin length, fin thickness, and trap geometry [138, 139]. Because QPs diffuse throughout the Al fins and have no preferred direction, the design of the fins and the Al/W trap regions impact the probability of QPs that can be collected. The optimization of the QP collection efficiency from the Al fin geometry is discussed in detail in Ref. [15]. For fin lengths shorter than 100 μm , the expected collection efficiency for all geometries is $\epsilon_{\text{coll}} \geq 75\%$.

The other two efficiencies, ϵ_{qp} and ϵ_{trap} , cannot be tuned by design optimization. ϵ_{qp} is the fixed efficiency of phonon to QP conversion in the Al fins, known as Kaplan down-conversion [140], and is the largest source of efficiency reduction. Detailed studies have found that for energies well above the superconducting band gap, this process is limited to an efficiency around 50–60%; the efficiency increases for energies close to the band gap [140, 141]. The HVEV detectors are designed by taking $\epsilon_{\text{qp}} \sim 50\%$

as the upper limit. Lastly, ϵ_{trap} concerns the efficiency of the down-conversion of QPs to phonons plus normal electrons in the TESs. Experiments comparing the efficiency between events absorbed in the Al fin and events absorbed directly into the TES have found that $\epsilon_{\text{trap}} \sim 62\%$ [15].

Apart from the phonon energy resolution, the other parameter that is considered when designing the detector is the dynamic range DR . Increasing the dynamic range increases the upper limit of energies that can be measured by the detector. DR is related to the saturation energy E_{sat} of the TESs. As seen in Fig. 3.1, a large enough energy deposition will put the TESs into the normal mode where the TES response to energy depositions is non-linear. E_{sat} describes the energy required to put the TESs in the normal mode. For TESs with a transition width ΔT_c , heat capacity C , and specific heat c_w , the saturation energy is described by:

$$E_{\text{sat}} \approx \frac{1}{\epsilon} C (\Delta T_c) \propto \frac{1}{\epsilon} c_w v_{\text{TES}} T_c (\Delta T_c). \quad (3.4)$$

While the TESs are in the linear response region, the dynamic range is roughly the ratio of the saturation energy to the energy resolution, expressed as:

$$DR \sim \frac{E_{\text{sat}}}{\sigma_{\text{ph}}} \propto \frac{\sqrt{v_{\text{TES}}}}{T_c^2 \sqrt{\tau_{\text{BW}}}} (\Delta T_c). \quad (3.5)$$

More information about the dynamic range model are found in Ref. [99]. Equations 3.3 and 3.5 detail the two main parameters that are optimized in the design of HVeV detectors. Reducing the detector bandwidth both decreases the energy resolution and increases the dynamic range. The TES volume, however, acts in opposing directions; reducing the TES volume will decrease the energy resolution, but it will also decrease the dynamic range.

3.2 The Second-Generation HVeV Detector

The dark matter search experiment presented in Chapters 4 and 5 uses a second-generation HVeV detector. This sub-section provides an overview of how the design of this detector is optimized, as well as other major design choices. Furthermore, the design of this detector is compared with the design of the first-generation HVeV detector in order to highlight the main areas of improvement.

3.2.1 Detector Design and Optimization

The second-generation HVeV detector substrate is a 0.93 g Si crystal with dimensions of $1 \times 1 \times 0.4 \text{ cm}^3$. As with previous versions of HVeV detectors, the QETs are arranged on one face of the detector substrate and are held at ground potential, while the opposing face contains an Al grid that is biased in order to induce an electric field of 0–625 V/cm across the detector. The layout and geometry of the QETs on the detector substrate is referred to as the mask design. For the second-generation HVeV detector, the mask design is called NF-C.

As discussed in Sec. 3.1.4, the goal of the detector design is to minimize the phonon energy resolution σ_{ph} while at the same time maximize the dynamic range DR . This optimization is simplified by fixing the overall normal resistance of the QET array, R_n , as well as other TES properties including T_c and the TES thickness t_{TES} . Here, an array of QETs is defined as a QET channel. By fixing R_n , T_c , and t_{TES} , only adjustable parameters in the models are TES length l_{TES} and Al fin length l_{fin} . Following

Ref. [99], the number of QETs per channel N_{QET} is set as a function of l_{TES} by keeping R_n constant:

$$R_n = \frac{R_{\text{TES, QET}}}{N_{\text{QET}}} = \frac{\rho_{\text{TES}} \cdot l_{\text{TES}}}{w_{\text{TES}} \cdot t_{\text{TES}} \cdot N_{\text{QET}}}, \quad (3.6)$$

where $R_{\text{TES, QET}}$ is the normal resistance of each QET cell, ρ_{TES} is the W resistivity, and w_{TES} is the TES width. Because the TES volume per QET cell $v_{\text{TES, QET}}$ is $l_{\text{TES}} \cdot w_{\text{TES}} \cdot t_{\text{TES}}$, the volume of TES per channel $v_{\text{TES, ch}}$ scales as:

$$v_{\text{TES, ch}} = v_{\text{TES, QET}} \cdot N_{\text{QET}} = \frac{\rho_{\text{TES}}}{R_n} j_{\text{TES}}^2. \quad (3.7)$$

Equations 3.3– 3.7 provide a simplified overview of how the detector design is optimized. For the sake of brevity, the full complexities of these models are not discussed in this work (see Ref. [99] and references therein), but the broad relationships between the parameters of interest can still be understood. Increasing the TES length increases the TES volume and thus the dynamic range, but it also worsens the energy resolution. Although these relationships oppose one another, Eq. 3.3 shows that $\sigma_{\text{ph}} \propto \frac{\sqrt{v_{\text{TES}}}}{\epsilon}$ whereas Eq. 3.5 shows that $DR \propto \sqrt{v_{\text{TES}}}$. Therefore the dynamic range can be increased without worsening the energy resolution by keeping the ratio $\frac{\sqrt{v_{\text{TES}}}}{\epsilon}$ constant.

Furthermore, both the fin length and TES length determine the QET geometry as well as the overall Al coverage fraction, thereby impacting the QP collection and phonon collection efficiencies. The total energy efficiency is thus also set by l_{TES} and l_{fin} . Increasing the Al coverage fraction also leads to a shorter phonon collection timescale, which improves the energy resolution. Using these relationships, the two-dimensional space of $(l_{\text{TES}}, l_{\text{fin}})$ is used to parameterize the energy resolution, saturation energy, energy efficiency, and Al coverage fraction.

The chosen parameters for the NF-C design are $l_{\text{TES}} = 150 \mu\text{m}$ and $l_{\text{fin}} = 60 \mu\text{m}$. In order to obtain positional information about events, the NF-C mask design implements two separate channels of QET arrays. Figure 3.4 shows the QET pattern used in the NF-C design. The inner channel is a square centered on the detector face, and the outer channel is a surrounding frame of equal area. Based on the chosen values of l_{TES} and l_{fin} , the number of QETs in each channel are 536 and 504 for the inner and outer channel, respectively. Each channel is connected to separate TES-SQUID circuit, and thus energy depositions in each channel are measured separately.

The vales of l_{TES} and N_{QET} independently set the normal resistance R_n . Based on the chosen values for the NF-C design, the expected normal resistance in each channel is 350 m Ω . Furthermore, the chosen values of l_{TES} and l_{fin} set the Al coverage fraction at $\sim 50\%$ and predict a phonon collection efficiency of $\epsilon_{\text{ph}} \gtrsim 95\%$. Combined with the other efficiencies discussed in Sec. 3.1, the overall efficiency expected for the NF-C design is $\epsilon = 27\%$ [99]. Other important parameters chosen for the NF-C are listed in Tab. 3.1.

3.2.2 Improvements from the First-Generation HVEV Detector Design

The first-generation HVEV detector was used in the HVEV Run 1 experiment, which produced the first dark matter constraints using an HVEV-style detector [106]. Details about this detector design are found in Ref. [131]. This detector is able to measure individual e^-h^+ pairs, and has a resolution of $\sim 0.09 e^-h^+$ pairs when operated with a 160 V voltage bias. The first- and second-generation detectors both contain a Si crystal substrate of the same dimensions, and both detectors use QET sensors to measure phonon

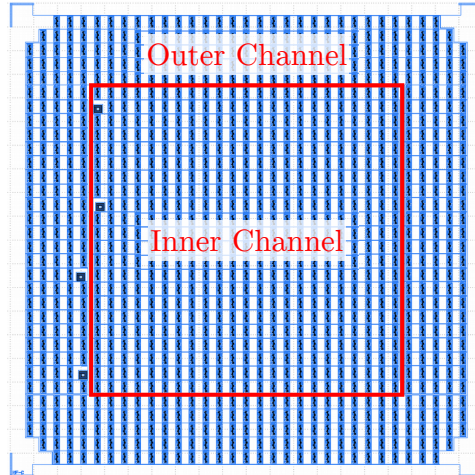


Figure 3.4: Illustration of the QET pattern used in the NF-C mask design. The red line divides the inner and outer channel of this design, where each channel is comprised of an array of QETs connected in parallel. The four filled squares on the left side are contacts used for wire bonding to the readout electronics. Illustration provided by Ref. [99]

energy depositions. However, there are a few notable differences between the first-generation detector design and the second-generation NF-C design that improve the detector performance.

One notable difference is that the first-generation detector has a 40 nm thick amorphous Si layer that sits between the detector substrate and QET array [131]. This amorphous layer was added as an attempt to insulate the detector substrate from potential leakage at the metal-substrate interfaces. However since operating the first-generation detector, various tests have concluded that the inclusion of an amorphous Si layer makes no significant impact on the amount of detector leakage. Therefore the second-generation detector has no such amorphous layer. It is presently unclear whether or not the amorphous layer impedes phonon collection into the Al fins.

Several other design choices were made in order to improve the energy resolution for the second-generation detector. This was accomplished largely by significantly increasing the energy efficiency. The NF-C design has a Al coverage fraction of $\sim 50\%$ compared to only 13% in the first-generation design, and an expected energy efficiency of 27% compared to the measured efficiency of 5% in the first-generation detector. This corresponds to an efficiency improvement by a factor of ~ 4.4 , which coincides well with the improved energy resolution measured with the second-generation detector (see Tab. 3.1).

The last notable difference between these two detectors is the number of channels used. The first-generation detector operates with only one channel [106], whereas the second-generation detector operates with an inner and outer channel. With the additional channel, the positional information of events can be analyzed by comparing the energy deposition measured in each channel. This feature is studied in the HVEV Run 2 analysis presented in Chapters 4 and 5.

3.3 Detector Characterization

The second-generation HVEV detector with the NF-C design was operated in a surface-level facility at Northwestern University (Evanston, IL, USA) in order to characterize the detector parameters as well as to perform the dark matter search experiment presented in Chapters 4 and 5. The detector was placed

inside of an adiabatic demagnetization refrigerator (ADR) that cooled the detector to a temperature of ~ 50 mK. The setup also provided mechanisms for calibration purposes via optical and soft X-ray photons. More information about the ADR system and the experimental setup is provided in Sec. 4.2.

A scan over the TES bias voltage V_b was performed simultaneously for each channel in order to evaluate basic TES parameters of the detector. The top plot in Fig. 3.5 (left) shows the variation of the measured signal current I_s with V_b for each channel. The middle and bottom plots show the variation of the inferred channel resistance R and the Joule power produced $P = I_s^2 R$ with V_b , respectively. Measurements were made by setting V_b at a value such that the TESs operated around 45% of R_n , as shown by the dashed, vertical line in the left plots of Fig. 3.5.

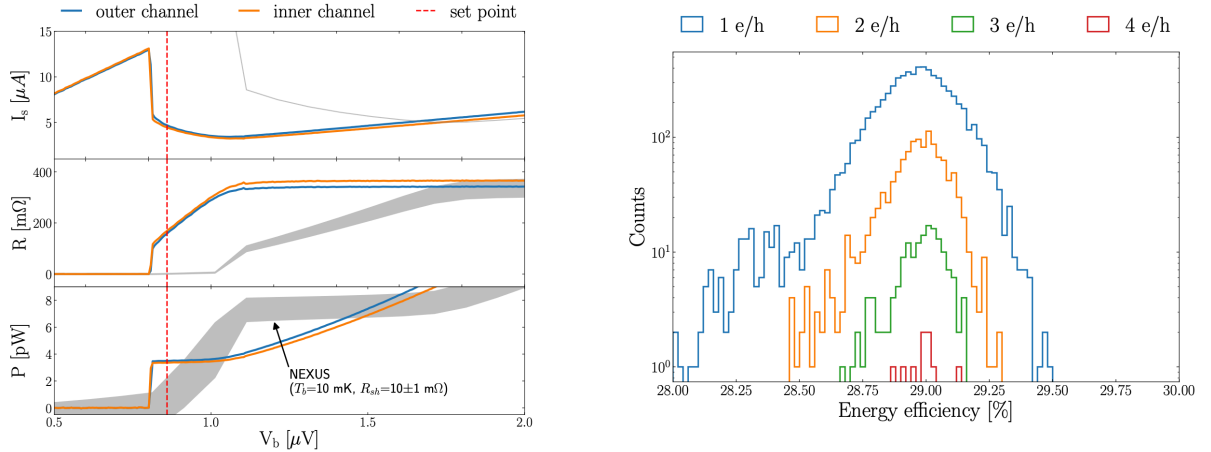


Figure 3.5: Left: TES signal current I_s (top), resistance R (middle), and power P (bottom) as a function of the voltage bias V_b applied to the TES circuit measured using the NF-C HVeV detector operated at 50 mK in the ADR with a voltage bias of 100 V applied across the detector. The blue and orange curves are the measurements on the outer and inner channel, respectively. The grey bands show the measurements taken using the NF-C HVeV detector operated at a different facility (NEXUS Facility [72]) with a lower bath temperature ($T_b = 10$ mK) and a lower shunt resistance ($R_{sh} \approx 10$ m Ω). Finally, the dashed, vertical line indicates the operating point of V_b . Right: reconstructed energy efficiency for the first four e^-h^+ -pair peaks of the NF-C HVeV detector, determined by comparing the inferred absorption energy (Eq. 3.8) with the calibrated energy of laser events. Figure provided by Ref. [99].

The detector energy efficiency can be evaluated by inferring true absorption energy E_{abs} from the change in the signal current and other circuit parameters. Following Refs. [99] and [136], E_{abs} is given as:

$$E_{abs} \approx \left(1 - 2 \frac{R_l}{R_l + R_0}\right) I_b R_{sh} \int \delta I_s(t) dt + R_l \int \delta I_s^2 dt, \quad (3.8)$$

where $R_l = R_{sh} + R_p$ is the combined shunt and parasitic resistance in the TES bias loop [136], R_0 is the TES operating resistance, $I_b = V_b/R_{sh}$, and $\delta I_s(t) = I_0 - I_s(t) > 0$ is the change in the signal current relative to the nominal value I_0 . The energy efficiency is determined by comparing the E_{abs} of events with their corresponding calibrated energy E_{ph} . A dedicated dataset was captured by exposing the detector to laser pulses of 1.95 eV photons with a mean number of photons per pulse $\lambda \sim 0.3$ while the detector was operated at 50 mK with a bias voltage of 100 V. The e^-h^+ -pair peaks resulting from this laser-calibration dataset were then calibrated to their expected energies; the energy calibration is discussed in detail in Sec. 4.3. Using this information, the energy efficiency of the detector is measured as $\epsilon = E_{abs}/E_{ph}$. The right plot in Fig. 3.5 shows the measured energy collection efficiency, separated

by each of the first four e^-h^+ -pair peaks. A lower bound of $\epsilon \gtrsim 29\%$ is obtained by selecting the most conservative set of assumptions to evaluate ϵ . This measurement is dominated by the systematic uncertainties in TES circuit parameters (e.g. R_0 and R_p), but the lower bound is comparable to the expected value of 27% that is determined from the design choices.

For the purposes of the HVeV Run 2 experiment, the second-generation detector is used to measure small signal responses (< 1 keV). Chapter 4 demonstrates sufficient energy calibration of the detector up to 700 eV only using 1.95 eV optical photons. Figure 3.6 shows a calibrated energy distribution from a laser-calibration dataset measured with an applied voltage bias of 100 V. While this example shows events only up to four e^-h^+ pairs, higher e^-h^+ -pair peaks are reached by increasing the mean number of incident photons per laser pulse. The events seen between the e^-h^+ -pair peaks are explained by charge trapping and impact ionization effects, as discussed in Sec. 2.2.2. Apart from the HVeV Run 2 experiment, this detector is also used to measured large signal responses, and is capable of energy calibration up to 120 keV using high-intensity laser, ^{57}Co , and ^{55}Fe sources [99]. For these large signal responses, the detector is often operated with a detector voltage bias of 0 V.

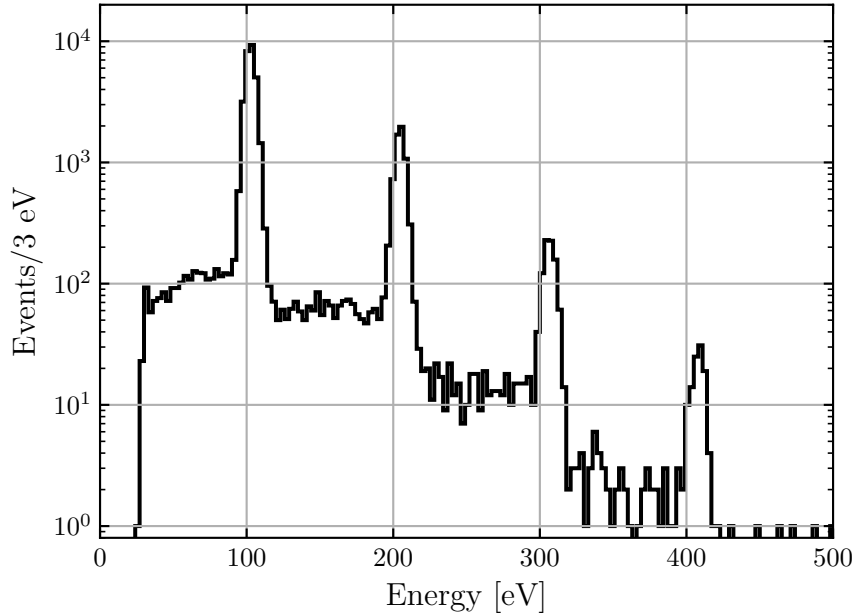


Figure 3.6: Example of the calibrated energy spectrum for a laser-calibration dataset measured with the second-generation HVeV detector. These data were measured while the detector was operated inside the ADR at 50 mK with an applied voltage bias of 100 V. Each peak corresponds to a quantized e^-h^+ pair.

The design of the NF-C detector operated inside the ADR has an expected phonon energy resolution σ_{ph} between 2.3 and 2.4 eV [99]. This parameter is characterized by measuring the baseline resolution of the detector. The baseline resolution is defined the energy resolution of the detector when no event pulses are recorded, and is measured to be 2.65 ± 0.02 eV for the second-generation HVeV detector operated inside the ADR. Although this value is fairly close to the expected value, there is a discrepancy between the baseline resolution and the energy resolution of ~ 3.3 eV measured at the first e^-h^+ -pair peak using laser-calibration data. This discrepancy is likely due to surface absorption of laser photons directly into the QETs; this effect is accounted for in the energy calibration outlined in Sec. 4.3. Furthermore, it is

found that the energy resolution is independent of the voltage bias applied across the detector for the range of voltage biases used in the HVEV Run 2 experiment.

Lastly, the resolution model used for the detector design assumes that the QET noise is dominated by thermal fluctuations across the thermal conductance between the TES and the detector substrate. Although noise characterization measurements were not made with the second-generation detector inside the ADR, such measurements have since been made while operating the detector at a different facility with a different fridge setup (NEXUS Facility [72]); these measurements demonstrate that the QET noise is dominated by thermal fluctuations [99]. All of the main design and characterization parameters for the second-generation, NF-C HVEV detector discussed in this chapter are listed in Tab. 3.1.

Table 3.1: List of the main design, characterization, and operation parameters for the second-generation, NF-C HVEV detector. The measured parameters are for the detector operated in an adiabatic demagnetization refrigerator (ADR) at Northwestern University (Evanston, IL, USA). More parameters can be found in Ref. [99].

Parameter	Description	Design	
A_{det}	Detector Area	1 cm ²	
η	Detector Thickness	4 mm	
m_{det}	Detector Mass	0.93 g	
T_c	TES Critical Temperature	~ 65 mK	
l_{TES}	TES Length	150 μm	
l_{fin}	Al Fin Length	60 μm	
N_{QET}	QETs Per Channel (Inner)	536	
	QETs Per Channel (Outer)	504	
v_{TES}	TES Volume (Per Channel)	~ $7.39 \times 10^3 \mu\text{m}^2$	
f_{Al}	Al Coverage Fraction	~ 50 %	
Parameter	Description	Expected	Measured in ADR
R_n	Normal Resistance (Inner)	350 m Ω	332–396 m Ω
	Normal Resistance (Outer)	350 m Ω	311–371 m Ω
σ_{ph}	Phonon Energy Resolution	2.3–2.4 eV	2.65 ± 0.02 eV
ϵ	Energy Efficiency	27 %	$\gtrsim 29$ %
τ_{BW}	Detector Bandwidth (Pulse Fall Time)	70–160 μs	~ 80 μs
E_{sat}	Saturation Energy (Linear Response)	~ 1 keV	$\gtrsim 700$ eV
Parameter	Description	Operated in ADR	
T_b	Bath Temperature	50–52 mK	
V_{bias}	Bias Voltage Across Detector	0–150 V	
V_b	TES Bias Voltage	~ 0.8 μV	
R_{sh}	Shunt Resistor	~ 50 m Ω	
R_b	Bias Resistance	8 k Ω	

Chapter 4

HVeV Run 2 Dark Matter Search: Experiment, Calibration, and Data Selection

This chapter is the first of two chapters presenting the dark matter (DM) search experiment and blinded analysis denoted as high-voltage eV-scale (HVeV) Run 2. HVeV Run 2 uses the second-generation HVeV detector described in Chapter 3 to set exclusion limits on DM-electron inelastic scattering, as well as dark photon and axion-like particle (ALP) absorption. Section 4.1 outlines the motivation for the HVeV Run 2 experiment, and the experimental setup and data collection are described in Sec. 4.2. The energy calibration and analysis selection criteria are detailed in Sec. 4.3 and 4.4, respectively, and finally Sec. 4.5 provides an overview of important experimental parameters. The limit setting method, unblinding procedure, and final results are presented in Chapter 5. A summary of the experiment and analysis presented in these two chapters is found in Ref. [1], along with the results from the 100 V measurement. Furthermore, the work presented here was made by a collaborative effort, with the other leading contributors being Yen-Yung Chang and Valentina Novati.

4.1 Motivation

The first scientific run using a first-generation Si HVeV detector, denoted as HVeV Run 1, was successfully able to achieve sub- e^-h^+ -pair detector resolution and demonstrated the DM search potential of a phonon-mediated semiconductor detector with sensitivity to single electron excitations [106]. The second-generation HVeV detector described in Chapter 3 demonstrated an energy resolution of 3 eV at the first e^-h^+ -pair peak, which is an improvement of roughly 3 times lower compared to the resolution of the first-generation HVeV detector. Furthermore, the second-generation detector utilized two channels compared the single channel of the first-generation detector. The goal of the scientific run using the second-generation HVeV detector was to improve on the DM exclusion limits set in HVeV Run 1 by increasing the scientific exposure and by taking advantage of the improved detector design to use positional dependence to reject background events.

The result from HVeV Run 1 featured an unexpected excess of events at low numbers of e^-h^+ pairs. Although the exact source or sources that caused these events are unknown, a leading hypothesis is that most or all of the events are caused by detector leakage (see Sec. 2.4). This hypothesis is motivated in Fig. 4.1 by comparing the DM-search data spectrum of the first scientific run with a Monte Carlo (MC) simulation characterizing detector leakage. This MC simulation generated individually-resolved leakage events that originate either in the detector bulk or at the detector surface. The rates of bulk and surface leakage events were fitted to the HVeV Run 1 energy spectrum.

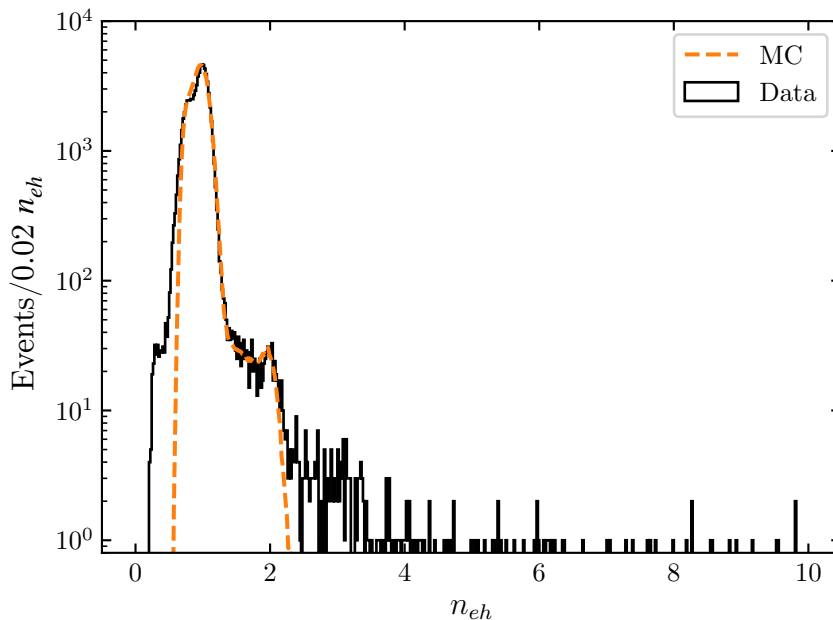


Figure 4.1: Comparison of the HVeV Run 1 DM-search energy spectrum (black) measured with the first-generation HVeV detector and 0.49 g-days of exposure [106] with an impact-ionization Monte Carlo (MC) model (orange) characterizing detector leakage. The events are measured in terms of the number of e^-h^+ pairs n_{eh} . Courtesy of Chris Stanford.

Figure 4.1 illustrates that the source of many of the events at low numbers of e^-h^+ pairs may be explained by detector leakage. However these events may also be explained by external particle interactions. It remains unknown what proportion of these events are generated by detector leakage versus external particle interactions. The goal of the second-generation HVeV detector was to use the improved detector design to obtain a higher rejection rate of events like those seen in the first and second quantization peaks of Fig. 4.1. A second scientific run was further motivated by using toy experiments to explore the potential reach that a second run may achieve.

The toy experiments assume that the DM-search spectrum of a future science run (after all analysis cuts are applied) contains events only in the first e^-h^+ -pair peak. The number of events in first e^-h^+ -pair peak is determined by various hypothesised background event rates and exposures: (i) 3 Hz/g with 1 g-days exposure; (ii) 0.1 Hz/g with 1 g-days exposure; (iii) 0.1 Hz/g with 30 g-days exposure; and (iv) 0 Hz/g with 1 g-days exposure. As in the HVeV Run 1 analysis, the DM limits were calculated using the optimum interval (OI) method [142, 143] and constrain ε for dark photons via absorption and $\bar{\sigma}_e$ for light dark matter (LDM) via electron scattering (see Sec. 1.5). The 90% confidence level (C.L.) limits

are shown in Figs. 4.2 and 4.3 and are compared to the HVeV Run 1 results [106], which had an exposure of 0.49 g-days and ~ 2 Hz/g event rate in the first e^-h^+ -pair peak.

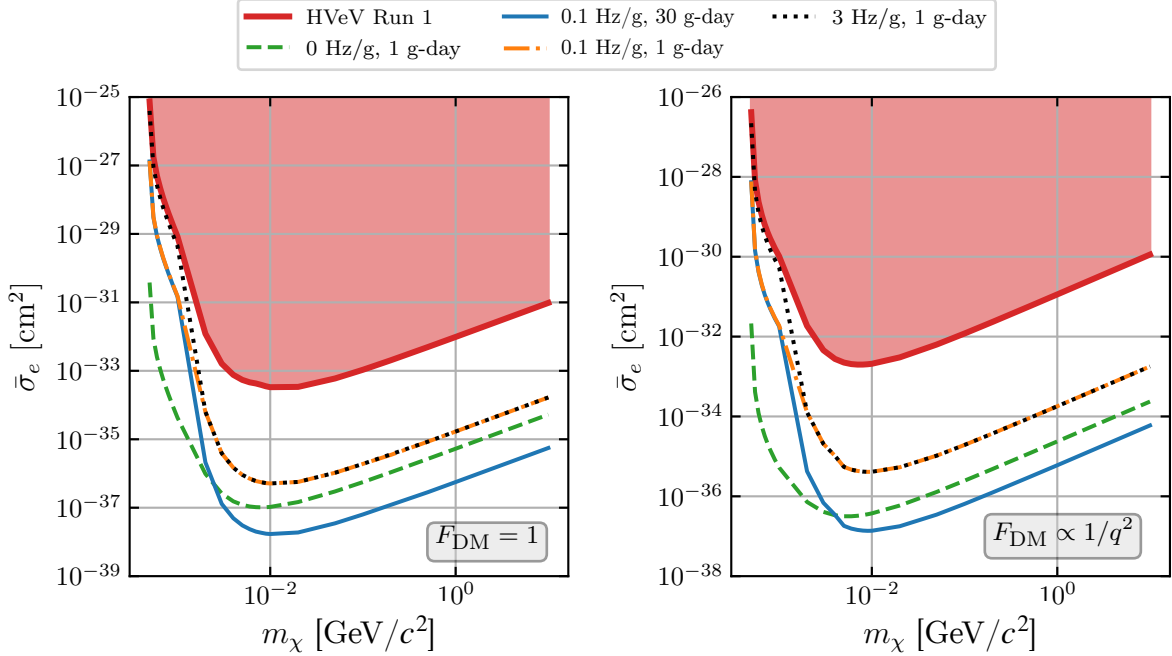


Figure 4.2: 90% C.L. projected limits on the effective DM-electron scattering cross section $\bar{\sigma}_e$ with form factor $F_{\text{DM}} = 1$ (left) and $F_{\text{DM}} \propto 1/q^2$ (right). The projected limits are computed from toy experiments using various assumptions of the event rate in the first e^-h^+ -pair peak and total exposure. The projected limits are compared to the parameter space excluded by the HVeV Run 1 experiment [106] (red). Courtesy of Belina von Krosigk.

Figures 4.2 and 4.3 demonstrate the potential parameter reach using an HVeV device if the observed events are predominately measured in the first e^-h^+ -pair peak. For the LDM electron scattering process, the projected limits on $\bar{\sigma}_e$ at low DM masses ($\lesssim 5 \times 10^{-3} \text{ GeV}/c^2$) are background limited. Conversely at higher DM masses, there is less of a dependence on the number of events in the first e^-h^+ -pair peak; the limits thus transition to become more, but not completely, exposure limited. The limits on ε for dark photon absorption tell a similar story. At low dark photon masses ($\lesssim 4 \text{ eV}/c^2$), the limits are *only* dependent on the number of events in the first e^-h^+ -pair peak and thus are completely background limited. As the dark photon mass increases, the dark photon signal model “walks-out” of the first e^-h^+ -pair peak therefore enter in the regime of zero background events presented in these toy experiments. As a result, the projected limits for dark photon absorption at higher masses are completely exposure limited. Overall, the subsequent scientific run using the second-generation HVeV detector showed the potential of several orders of magnitude improvement in the various DM parameter spaces assuming the observed events are predominately measured in the first e^-h^+ -pair peak.

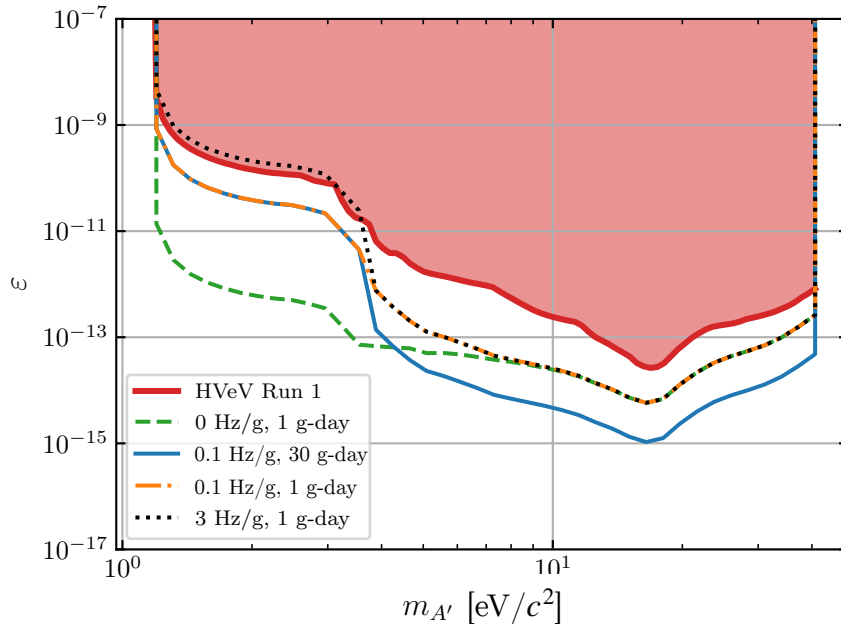


Figure 4.3: 90% C.L. projected limits on the kinetic mixing parameter ϵ for dark photon absorption. The projected limits are computed from toy experiments using various assumptions of the event rate in the first e^-h^+ -pair peak and total exposure. The projected limits are compared to the parameter space excluded by the HVeV Run 1 experiment [106] (red). Courtesy of Belina von Krosigk.

4.2 Experimental Setup

4.2.1 Hardware and Refrigeration

This experiment was performed in a Vericold adiabatic demagnetization refrigerator (ADR) at Northwestern University (Evanston, IL, USA) from April 29th to May 16th 2019. The ADR was hosted in a surface laboratory with negligible overburden, and was operated between 50–52 mK.

Two detectors were used for the measurement: the main second-generation Si HVeV detector described in detail in Chapter 3 with dimensions $1 \times 1 \times 0.4 \text{ cm}^3$ and a weight of 0.93 g (often referred to just as “the detector”), and an anti-coincidence (veto) Si detector of similar dimensions containing a single transition edge sensor (TES) with a critical temperature T_c of 52 mK. The HVeV detector contains an inner and outer quasiparticle-trap-assisted Electrothermal-feedback TES (QET) channel on the top surface, each with a T_c of 65 mK (see Chapter 3 for more details). The bottom surface of the HVeV detector is covered with an aluminum grid with 5% coverage used to induce the voltage bias across the detector. The applied voltage bias was in reference to the top surface of the detector that was kept at 0 V. Furthermore, the detector was kept between two printed circuit boards (PCBs): one that hosted the electrical readout contacts for the QET channels and a grounded copper plate around the detector, and another that served as the high-voltage electrode [132].

The veto detector was placed adjacent to the HVeV detector in the same orientation. Its purpose was to measure events coincident with the HVeV detector that are caused by radio-frequency (RF) sources. Both detectors were placed within a light-tight copper housing that was fixed to the coldest stage of the ADR. All of the conductive surfaces were explicitly tied to 0 V, except for the components of the

PCBs and the bottom-side of the HVeV detector that provided the HV bias. Both detectors are shown in Fig. 4.4 within the copper housing.



Figure 4.4: Left: top view of the second-generation Si HVeV detector and the adjacent veto detector inside the copper housing. The HVeV detector is at the center of the housing surrounded by the black frame, and the veto detector is to the right. Right: Lateral view of the HVeV detector mounted in the holder.

The ADR operated in multiple stages to cool the detectors to sub-Kelvin temperatures. First, liquid nitrogen and liquid helium baths were used to cool the fridge to 77 K and 4.2 K, respectively. Next, a vacuum pump was used to reduce the liquid helium bath temperature to ~ 1.4 K. Within the ADR was a Ferric Ammonium Alum (FAA) and a Gadolinium Gallium Garnet (GGG) paramagnetic salt pill that were surrounded by a 4 T superconducting magnet. The FAA salt pill provided the coldest stage of the ADR at 50 mK, and was in thermal contact with the detector housing via a cold finger. The GGG salt pill has a cold stage of ~ 300 mK and was used as an additional heat load. As long as the demagnetization process could be maintained, the detectors were held and regulated at the operating temperature of 50–52 mK for data acquisition. A hold time of 10–12 hours/day was obtained, and daily cycling of the ADR cooling was required to replenish the liquid helium bath. To avoid any effects on the detectors from the 4 T magnets, the copper detector housing was placed inside a superconducting Niobium enclosure that served as a magnetic shield [132]. The left image in Fig. 4.5 shows a photograph of the ADR in the laboratory.

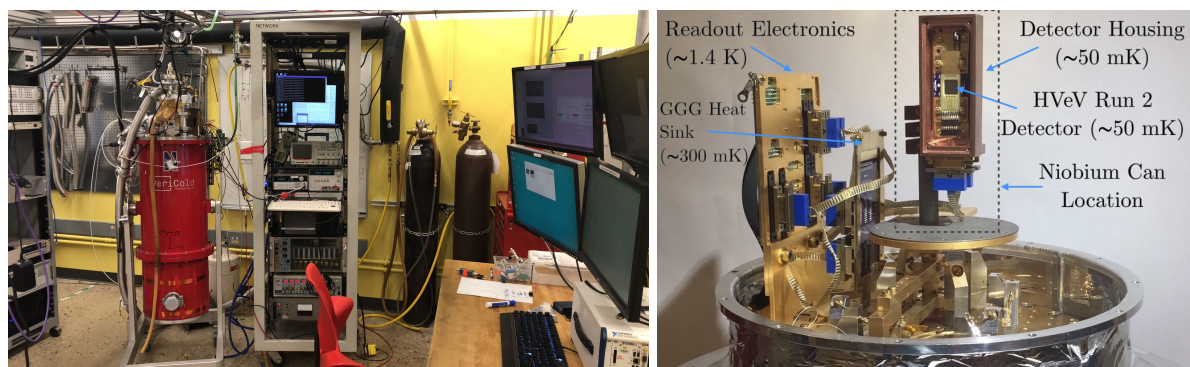


Figure 4.5: Left: the laboratory setup for the second-generation HVeV experiment. The red dewar is the Vericold ADR, with the equipment to control the ADR shown on the rack to the left of the ADR. The equipment on the rack to the right of the ADR hosted the data acquisition systems. Right: the copper detector housing shown inside of the ADR.

The required daily cycling of the ADR also meant daily recalibration of the bias points of the two QET channels in the HVeV detector, as well as the single TES in the veto detector. This led to small

differences in the bias points seen day to day, as well as in the direct current (DC) offset that varied each day depending on the SQUID lock point found in the electronics. See Sec. 3.1 for further details about the QET and TES electronics.

Two calibration systems for optical photons and soft X-rays were built into the ADR [132]. The first was a 635 nm laser diode (corresponding to 1.95 eV photons) connected with a single-mode fiber inside the ADR via a vacuum feed-through at room temperature. The other end of the single-mode fiber was coupled to a plastic optical fiber with a core diameter of 1 mm through two pieces of KG-3 glass at 1.4 K. The KG-3 glass pieces were used to attenuate infrared light from ambient and black-body radiation from the higher temperature stages in the ADR. Finally, the plastic optical fiber was fed through the copper detector housing allowing photons to be emitted onto the top surface of the HVEV detector. For the second calibration system for soft X-rays, a 1 cm² window was cut on the lid of the detector housing and resealed with a 0.17 mm thick piece of aluminum. This opening aligned with a Beryllium window in the ADR, allowing the passage of X-rays. Between the detector housing and the Beryllium window were multiple layers of aluminized mylar sheets at the various thermal stages in order to block black-body radiation. The right image in Fig. 4.5 shows a photograph of the detector housing inside the ADR.

During data acquisition of the HVEV Run 2 experiment, the detectors inside the ADR were operated at two different temperatures: 50 mK from April 29th to May 7th, and 52 mK from May 8th to May 16th. The increase in the operating temperature was due to a decrease of the cooling power of the ADR and ultimately the hold time per day that could be achieved. Residual magnetization of the salt pills and of the magnetic shield from continuous operation was hypothesized to be the reason for the decrease in cooling power. The increase in operating temperature maximized the daily exposure by holding the temperature for an additional 2-4 hours per day compared to before the temperature increase was made. Consequently because the veto detector had $T_c = 52$ mK, identical to the increased operating temperature, it became impractical to operate during this time and therefore did not provide veto rejection of measured events after May 7th. The data acquisition spanned a total of 18 days, and various forms of data were captured: background DM-search data at detector biases of 100 V, 60 V, and 0 V, as well as calibration data with a ⁵⁷Co source at 60 V and 0 V. A summary of the exposure is seen in Fig. 4.6.

Lastly, detector characterization measurements were taken each day prior to the start of data acquisition. The measurements include: (i) detector noise in superconducting and normal modes to characterize electronic noise; (ii) a set of current versus TES voltage bias curves to establish and set the QET bias point for each channel; (iii) background noise to determine the power noise present in the detector; and (iv) laser-calibration data for calibrating the gain of the TESs at their respective bias points. The daily laser calibration data was measured using low- λ laser pulses to achieve a mean of 1–4 photons per pulse. On a few occasions, laser data with high- λ laser pulses were measured to improve the calibration at higher energies. Finally, a dedicated laser dataset was taken in which the crystal temperature was intentionally varied while the QET bias points were held constant; this dataset was used to reconstruct the temperature dependence of the QET responsivity.

4.2.2 Data Acquisition and Triggering

All data measured during this experiment were recorded as a current in Ampere units and were taken with a continuous streaming data acquisition (DAQ) system on an analog-to-digital converter (ADC) card. The ADC digitized the analog traces at a rate of 1.515 MHz for each QET channel separately. The

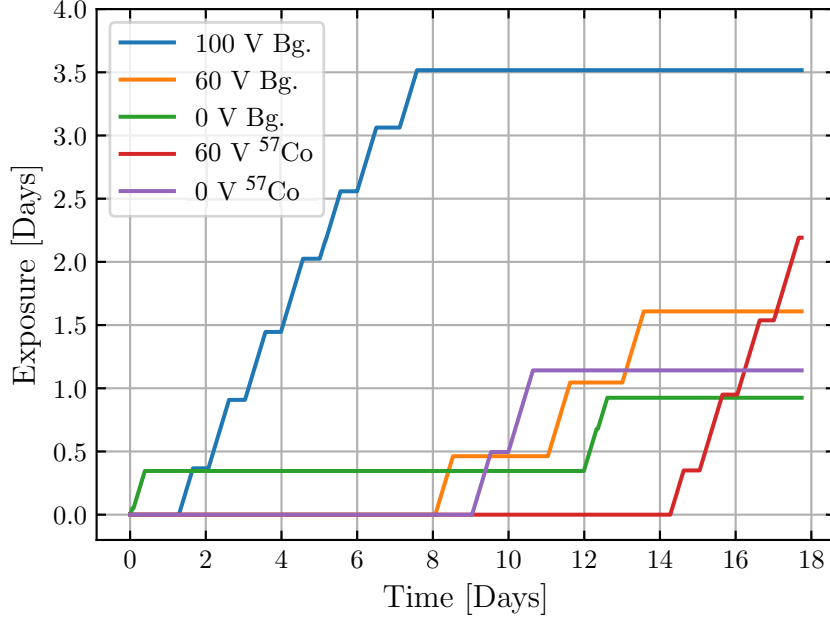


Figure 4.6: Summary of the exposure obtained during the 18 days of data acquisition for the HVEV Run 2 experiment. Background (Bg.) data was acquired at detector biases of 100 V, 60 V, and 0 V, and calibration data with a ^{57}Co source was acquired at detector biases of 60 V and 0 V. Courtesy of Yen-Yung Chang.

data were segregated into 1 hour-long series, and each second of data was saved in a separate file. This method of data storage was ideal to implement the blinding scheme as discussed in Sec. 4.2.4. Event triggering and data processing were performed in sequential steps offline.

The ADR temperature was measured using a resistance temperature detector (RTD) mounted on the FAA salt pill stage inside the ADR. The RTD was measured with a resistance bridge, and the analog voltage output from the bridge was read out once per second using a multi-channel digital voltmeter and recorded in the raw data. During the offline processing a series of static conversion tables were used to convert the voltage output to first a resistance measurement and then a temperature measurement. The HV bias applied across the detector was read out once per second and subsequently recorded in the raw data using the same digital voltmeter as the ADR temperature measurement; the digital voltmeter mapped input voltages of 0–3.5 kV to 0–5 V for readout. A separate measurement of the HV electronics circuit was taken prior to the start of the science run in order to calibrate the readout voltage to the actual voltage applied to the detector.

Event triggering in this analysis was done by passing the raw digitized traces through a shaping filter. First, the summed trace of the inner and outer QET channels was down-sampled by a factor of four in order to reduce the computational load. Next, the entire 1 s-long trace was convolved with an idealized pulse shape. The idealized pulse used for triggering shown by the right plot in Fig. 4.7 is a double exponential function with a rise time of 20 μs and a fall time of 80 μs and was determined based on prior studies of the pulse shape. The left plot in Fig. 4.7 shows an example of the triggering procedure using a toy down-sampled trace (blue) and the resulting filtered trace (orange) after convolving the down-sampled trace with the idealized pulse.

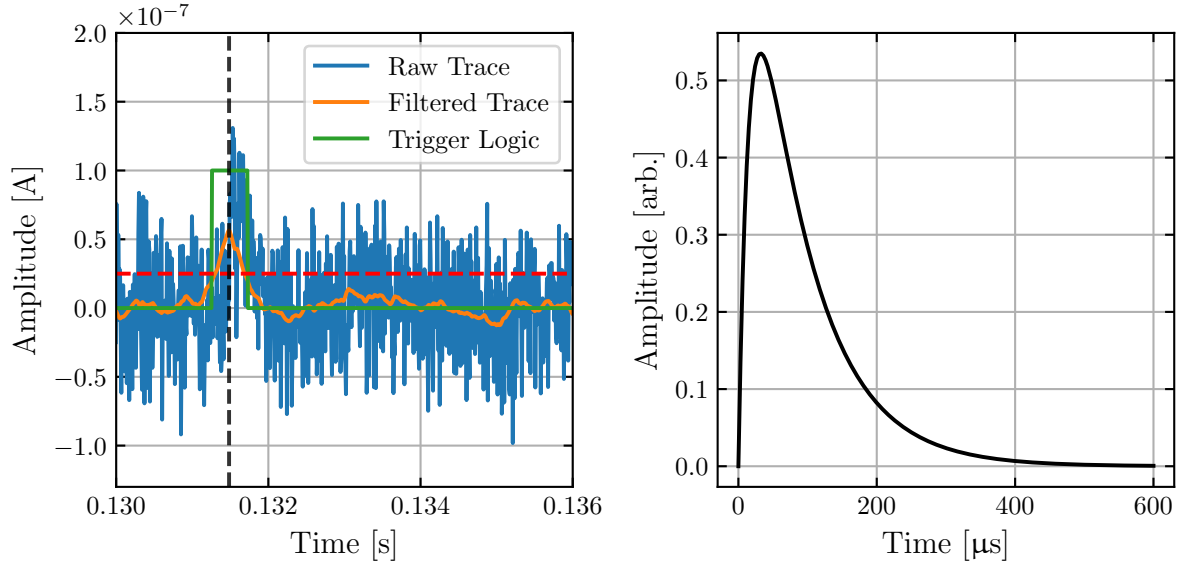


Figure 4.7: Left: example of the trigger procedure using a toy down-sampled raw trace (blue). The filtered trace (orange) is determined by convolving the raw trace with the ideal pulse shape, producing the trigger logic (green) for this event. The vertical dashed line corresponds to the trigger time determined in this example, and the horizontal dashed line is the trigger threshold. Right: idealized pulse shape used for triggering. Courtesy of Noah Kurinsky.

A fixed threshold of $0.025 \mu\text{A}$, corresponding to an energy of $\sim 0.4 e^-h^+$ pairs, was applied to each filtered trace for event identification. The threshold value was chosen to be slightly above the baseline resolution to avoid noise-triggered events while also being well below the first e^-h^+ -pair peak. Once part of a filtered trace crosses the threshold, a trigger time is defined as the time when the maximum amplitude of the filter trace occurs within a trigger window of 700 time bins. The trigger logic is shown by the green curve in Fig. 4.7. A window of 1024 time bins before and 3072 time bins after the trigger time, corresponding to a pre-trigger time of $675 \mu\text{s}$ and a post-trigger time of $2034 \mu\text{s}$, respectively, define the event window for an issued trigger. There is then a trigger hold-off until 4096 time bins after the trigger time in order to exclude any additional pulses either in the saved trace or in the pre-trigger region of the next trace from issuing a trigger. This trigger procedure allows for a maximum trigger rate of $\sim 370 \text{Hz}$. With the event window defined, the raw, continuous traces from each of the two QET channels, as well as the summed trace from both channels (denoted as the “total channel”), are extracted and saved for further processing discussed in Sec. 4.2.3. For laser calibration data, events are also identified by triggering on a transistor-to-transistor logic (TTL) signal that is coincident with the generated laser pulses.

4.2.3 Data Processing

For every event captured in the offline data triggering procedure, further processing was required in order to reconstruct the pulse and determine the energy information of each event. This was done using the optimal filter (OF) method [144, 15]. The OF algorithm requires a pulse template, $s(t)$ in the time domain or $s(f)$ in the frequency domain, and a noise power spectral density (PSD) function $J(f)$. A PSD function decomposes a series of data points measured over time into its frequency components, and

describes the amount of power at each frequency. In the most basic OF application, an event trace $v(t)$ is transformed to the frequency domain, $v(f)$, and the pulse amplitude A is found by minimizing the goodness of fit χ^2 according to:

$$\chi^2(A) = \int_{-\infty}^{\infty} \frac{|v(f) - As(f)|^2}{J(f)} df. \quad (4.1)$$

Equation 4.1 assumes that the reconstructed event pulse is fixed at the time in which the event issued a trigger. A slightly more complex version of the OF algorithm relaxes the assumption of a fixed pulse time and allows for a time offset. A time offset t_0 is implemented into the filtering by allowing the pulse template to move in time:

$$s(f) \rightarrow s(f, t_0) = e^{-i\omega t_0} s(f) \quad (4.2)$$

where $\omega = 2\pi f$. This version of the OF algorithm determines the values of A and t_0 by minimizing χ^2 according to:

$$\chi^2(A, t_0) = \int_{-\infty}^{\infty} \frac{|v(f) - Ae^{-i\omega t_0} s(f)|^2}{J(f)} df. \quad (4.3)$$

Equations 4.1 and 4.3 provide only the framework of the OF algorithms used in this analysis represented in the continuous limit. More details about the OF algorithms, including derivations of the functions in the discrete case (transitioning from an integral to a sum) and time-domain OF algorithms, are found in Ref. [15].

The pulse amplitude of each event, which is a measure of the event energy, was determined using both the basic OF and time-offset OF algorithms. At the expense of requiring more computing power, the OF algorithms provide more accurate determinations of the pulse amplitudes compared to the triggering scheme. Moreover, the filters were applied separately to each QET channels' trace, as well as the summed trace from both channels (i.e. the total channel). Therefore this method provided an estimation of the event energy in the inner, outer, and total channels with and without a time offset. Calibrating the OF amplitude to an energy is detailed in Sec. 4.3.

Noise PSD templates were determined separately for each data series (representing an hour of data acquisition) in order to account for variations in the noise from the environment or electronic sources that can occur throughout the run. For every second of data acquired within a series, ten non-overlapping traces with random start times were extracted, and the traces containing a pulse were rejected. The remaining traces were used to compute an averaged noise PSD for the series. A summary of all of the averaged noise PSDs during the course of data acquisition are shown overlaid in Fig. 4.8. Although the noise level was fairly stable between most series, some variation was observed. The disappearance of some high-frequency noise lines after the first few days of data acquisition, shown by the black noise PSD curves in Fig. 4.8, is attributed to replacing a noisy high-voltage power supply. The averaged noise PSD for each series was used for the OF filtering of the events identified within the respective series.

The pulse templates were derived from the traces of triggered events from the laser-calibration data averaged over each series. Because there was little variation in the pulse shape over time, it was sufficient to compute a single template to be used for the entire experiment run. Different templates were however determined for the inner, outer, and total channels. This process is demonstrated in Figs. 4.9 to 4.12. Figure 4.9 shows an overlay of normalized pulses from laser events averaged over each series in both the time and frequency domain.

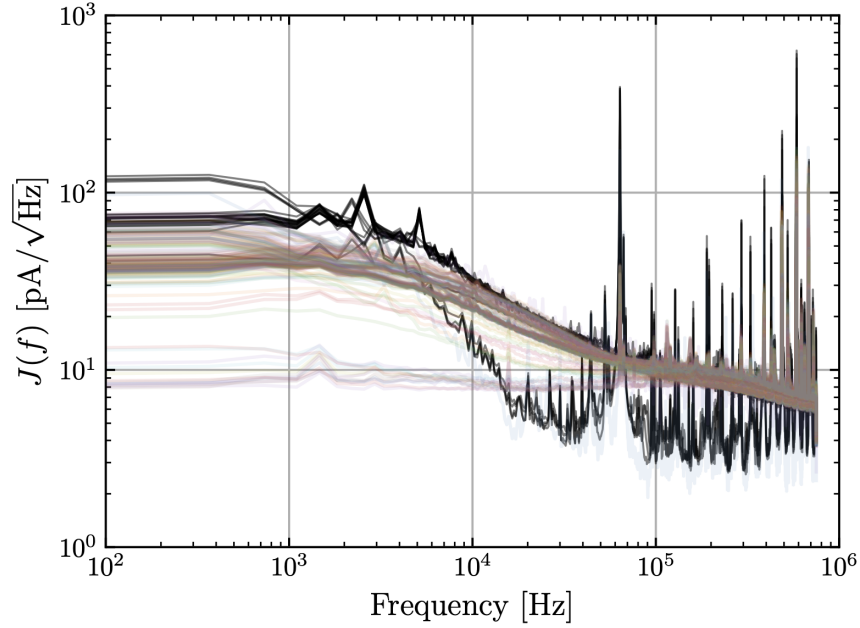


Figure 4.8: Overlay of the averaged noise PSD $J(f)$ for each series of data acquisition. The black curves correspond to noise PSDs measured during the first two days of data acquisition during which a noisy high-voltage power supply was used. The remaining, coloured curves are the noise PSDs measured from the third day of data acquisition until the end. Courtesy of Noah Kurinsky.

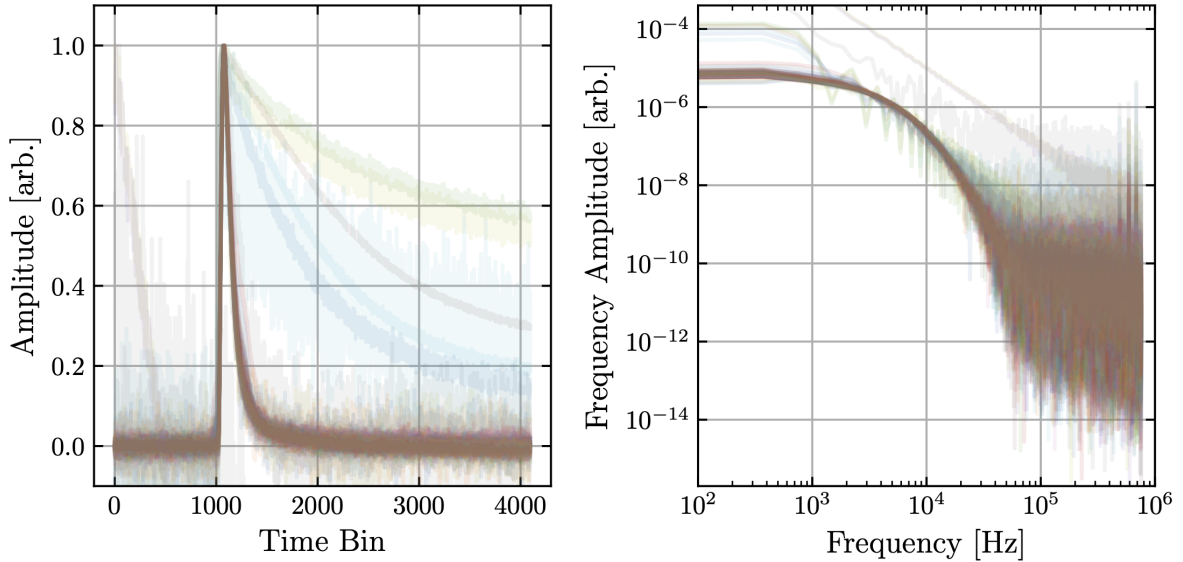


Figure 4.9: Overlay of the normalized pulses from laser events in the time domain (left) and frequency domain (right) used to create the pulse templates. Each trace displayed represents an average of pulses for a series in which laser-calibration data was captured. The length of each time bin is $\sim 0.6 \mu\text{s}$. Courtesy of Noah Kurinsky.

The pulses in Fig. 4.9 show some variation in the baseline noise level between series and a few averaged traces with extreme deviations from the expected pulse shape that were measured while the

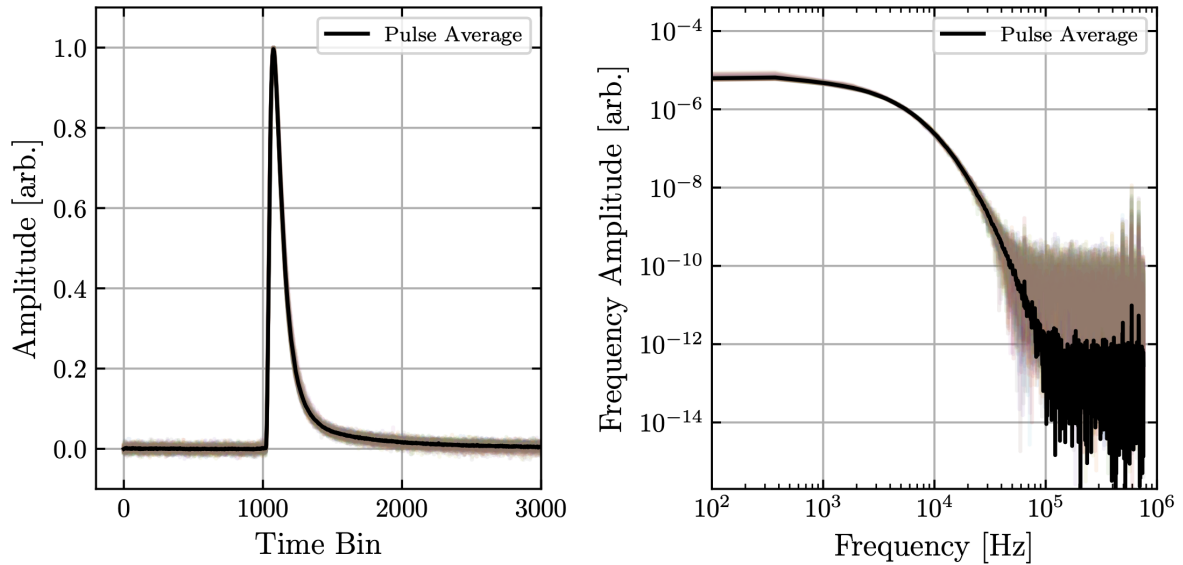


Figure 4.10: Overlay of the normalized pulses from laser events in the time domain (left) and frequency domain (right) after rejecting pulses with a high variance in either the pre- or post-pulse mean of the pulse. The black curve in both plots is the average of the accepted pulses. The length of each time bin is $\sim 0.6 \mu\text{s}$. Courtesy of Noah Kurinsky.

ADR, and thus the detector, was warming. In order to improve the selection of pulses to generate the template, a cut is performed to reject pulses with a high-variance mean pre-pulse or post-pulse value. The remaining pulses are used to compute an averaged pulse and is shown in Fig. 4.10.

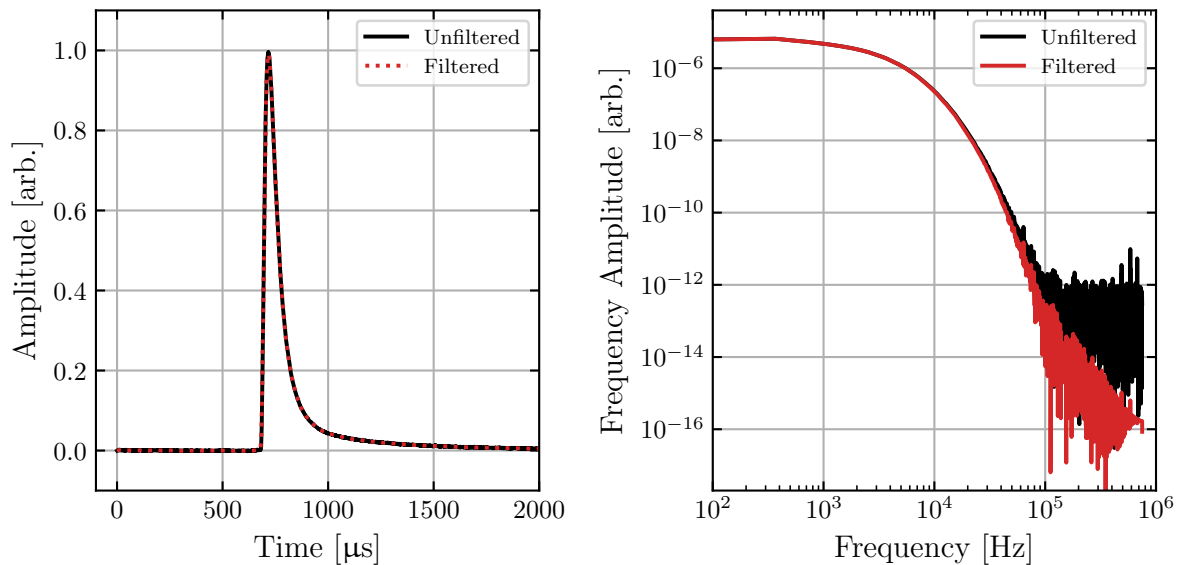


Figure 4.11: Averaged normalized pulse in the time domain (left) and frequency domain (right). The black and red curves in both plots show the pulse before and after applying a low-pass filter, respectively, to reduce the noise variance. The filtered pulse is what is used to create the pulse template. Courtesy of Noah Kurinsky.

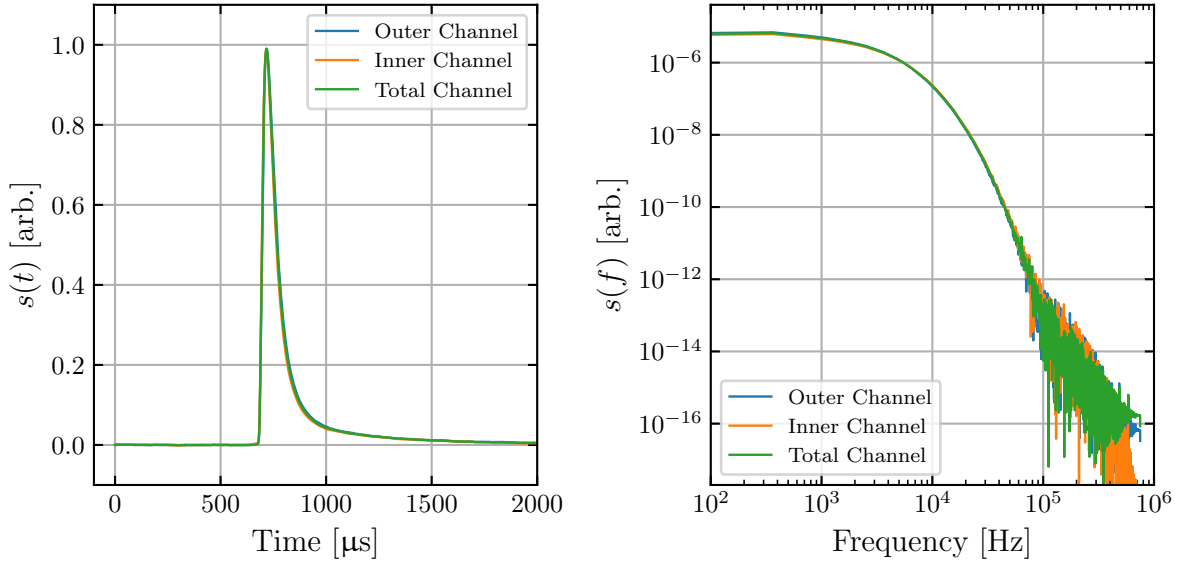


Figure 4.12: The pulse templates $s(t)$ and $s(f)$ in the time domain (left) and frequency domain (right), respectively, used for data processing. A separate template is used for the outer (blue), inner (orange), and total (green) channels. Courtesy of Noah Kurinsky.

Lastly, in order to further reduce the noise in the template, a low-pass filter is applied to the averaged pulse from the previous step. As seen in Fig. 4.11, the filtering produces very little difference in the pulse in the time domain, but is quite noticeable in the frequency domain. The result is a pulse template that is approximately noise-free, thus removing the need for an analytic fit.

Figure 4.12 shows the pulse template in the time and frequency domains for the inner, outer, and total channels. Only minor differences are observed between the templates. Due to the scarcity of events in the veto detector, its traces were processed using the same OF algorithm and pulse template as the traces from the HVEV detector. As Fig. 4.13 shows, the pulse template visually appears to match the shape of good pulses in the veto detector.

During the processing of the identified event traces a number of reduced quantities (RQs) were computed to provide relevant information about each event, including the reconstructed pulse amplitude and goodness of fit values. A description of the most relevant RQs used for this analysis are listed in Tab. 4.1.

4.2.4 Blinding Scheme

Unlike the HVEV Run 1 analysis, the HVEV Run 2 analysis implemented a three-stage blinding scheme based on the temporal segregation of the data in order to minimize bias. The blinding scheme and the procedure for unblinding the data were decided before data acquisition commenced. This blinding strategy was applied only to the science data that produced the final results and not to the laser-calibration data nor the ^{57}Co -calibration data that were used for developing the analysis.

For the purposes of the blinding scheme, the continuous data streams were partitioned into 10-s-long intervals and, as outlined in Sec. 4.2.2, were stored in one-second increments. This allowed for a simple classification of datasets that are defined as: (i) stage-0, which consists of the first second of each interval;

Table 4.1: List and description of reduced quantities (RQs) that were computed during the data processing of event traces. This list does not represent the entire set of RQs computed, but rather those which were most important to this analysis. The quantities A_0 , A , t_0 , $\chi_0^2(t)$, $\chi_0^2(f)$, $\chi^2(t)$, $\chi^2(f)$, and Mean Base were computed separately for the inner, outer, and total channels.

RQ	Description
A_0 [μA]	Amplitude determined from the OF algorithm with no time offset.
A [μA]	Amplitude determined from the OF algorithm with allowing a time offset.
t_0 [s]	Time offset determined from the OF algorithms allowing a time offset.
$\chi_0^2(t)$	Goodness of fit of the reconstructed pulse with amplitude A_0 in the time domain. A value of ~ 1 represents a good fit.
$\chi_0^2(f)$	Goodness of fit of the reconstructed pulse with amplitude A_0 in the frequency domain. A value of ~ 1 represents a good fit.
$\chi^2(t)$	Goodness of fit of the reconstructed pulse with amplitude A and time offset t_0 in the time domain. A value of ~ 1 represents a good fit.
$\chi^2(f)$	Goodness of fit of the reconstructed pulse with amplitude A and time offset t_0 in the frequency domain. A value of ~ 1 represents a good fit.
Mean Base [A]	Mean baseline value of the trace before the expected trigger time.
Laser Trig.	Boolean specifying whether or not an event coincides with a trigger issued by the laser TTL and therefore can be tagged as a laser event.
Laser Trig. Time [s]	Time where the laser TTL was found in the trace relative to the trigger time.
Crystal Voltage [V]	Calibrated voltage bias through the crystal when an event occurred.
Fridge Temp. [V]	Temperature of the detector housing inside the ADR, in units of V. This parameter is converted into units of K during analysis.

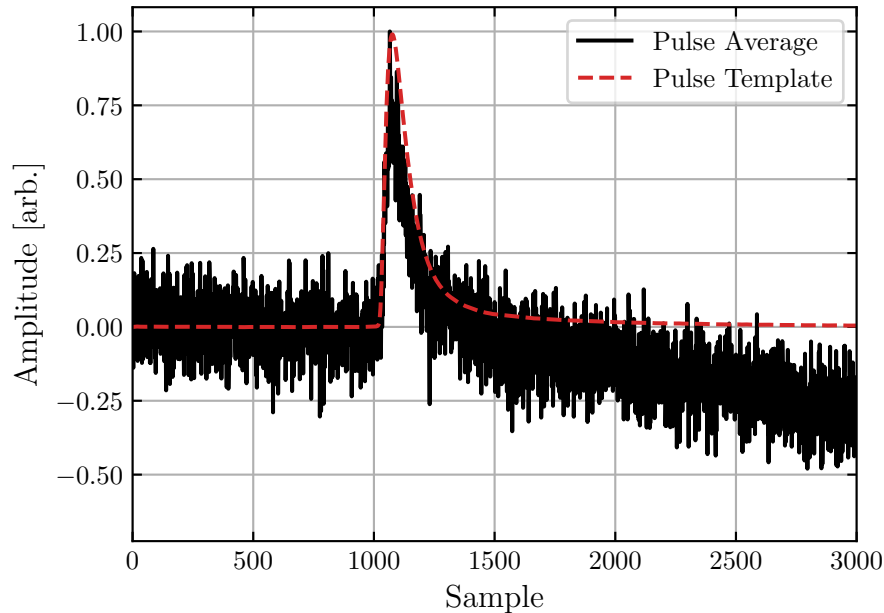


Figure 4.13: Average of traces from the veto detector with the pulse template determined using the HVEV detector. Although there were not enough events to determine a separate pulse template for the veto detector, the pulse shape is in good agreement with the pulse template from the HVEV detector.

(ii) stage-1, which consists of the second and third seconds of each 10 s interval; and (iii) stage-2, which consists of the remaining fourth–tenth seconds of each interval.

The stage-0 dataset, which accounts for 10 % of the entire dataset, was used to assist the development of the analysis pipeline as well as to produce preliminary DM results. The stage-1 dataset is used as part of the unblinding procedure. Its purpose is to verify that the analysis pipeline developed with the stage-0 dataset is invariant under a larger statistical sample. The consistency checks include a validation of the livetime calculations and a validation of the data distributions after data-quality cuts; DM limit results are not produced during this stage. As will be outlined in Sec. 5.3, the results from the consistency checks determine which datasets are used to produce the final results.

4.3 Energy Corrections and Calibration

This section describes the corrections to and calibration of the energy that are applied to the data collected during this analysis. The corrections and calibration are developed using the daily laser-calibration data, which provide a statistically large sample of good events across all energies within the analysis range and produce known-energy e^-h^+ -pair peaks; the procedure is subsequently applied to the background science (DM-search) data. The laser-calibration datasets were measured at 50 and 52 mK for the first and second half of data acquisition, respectively, with a detector bias voltage of either 60 or 100 V, depending on operating conditions of each day.

This section describes how the OF amplitude A for each identified event is mapped to a measured phonon energy. Section 4.3.1 verifies that the inner and outer QET channels have the same relative gain, as expected from the detector design; a differing gain in the two channels would result in degradation of

the resolution. Operating conditions, such as the detector bias voltage and the fridge temperature, affect the gain in the QET channels and thus needs to be corrected for. The temperature and HV corrections are described in Secs. 4.3.2 and 4.3.3, respectively. Because the calibration laser sent photon pulses from the top surface of the detector, some of its energy is directly absorbed in the QETs instead of in the crystal and slightly shifted the energy scale of the calibration. This effect, which is relevant only to the laser-calibration data and not the background data, is corrected for as outlined in Sec. 4.3.4. Lastly, Sec. 4.3.5 addresses non-linearities observed in the QET gain, and describes the calibration to phonon energy.

4.3.1 Relative Calibration

The detector design, as outlined in Chapter 3, implements an inner and outer QET channel in order to achieve good event position information and energy resolution. Because each channel was designed to have roughly equal surface area coverage, the total deposited energy for an event is the energy determined by the summed trace of both channels. This summation of the traces can be done using a relative ratio of 1 between the two traces as long as each QET channel is biased at the same operating point and therefore is expected to experience the same power-to-current gain. Although the QETs were biased daily during data acquisition, imperfections such as parasitic resistance in the readout electronics can potentially cause uneven gain in the channels. Therefore it is necessary to verify that the two channels do indeed experience the same gain in order to negate the need for a relative gain correction and to have optimal position information and energy resolution.

This verification requires a dataset that has a known fixed energy and has events sufficiently populated throughout the detector. The laser-calibration data is not ideal for this exercise because the laser was focused on the inner QET channel, resulting in event populations that are strongly biased to have a higher measured energy in the inner channel. Instead this exercise is performed using the first and second e^-h^+ -pair-peak events from the stage-0 background data. The relative gain is investigated for each day separately, and a set of data-quality cuts are applied to clean the data. The data quality cuts include a 3σ cut on the fridge temperature, one-sided cut on $\chi_0^2(t)$, and a two-sided cut on t_0 . Figure 4.14 shows a scatter plot of the measured OF amplitudes from the inner and outer channels, A_I and A_O respectively, from the stage-0 background dataset from one day.

Points along the diagonal line in Fig. 4.14 indicate events that have the same amplitude in each channel. The anti-diagonal lines are placed at the expected locations of the first and second e^-h^+ -pair peaks and have a slope of -1 . The events measured in the peak regions align with the anti-diagonal lines, which indicates that the summed amplitude of the two channels is constant along these or any anti-diagonal lines. Although Fig. 4.14 shows the comparison for only one day of data acquisition, similar results are observed for all other days. Because the inner and outer channels experience equal relative gain (as expected from the detector design), the total amplitude is calculated simply as the sum of the amplitudes from each channel without the need for relative scaling between the channels. Using the same logic, the main energy estimator used in this analysis is the computed amplitude from the sum of the *traces* from each channel (i.e. the “total channel”), rather than the sum of the OF amplitudes from each channel.

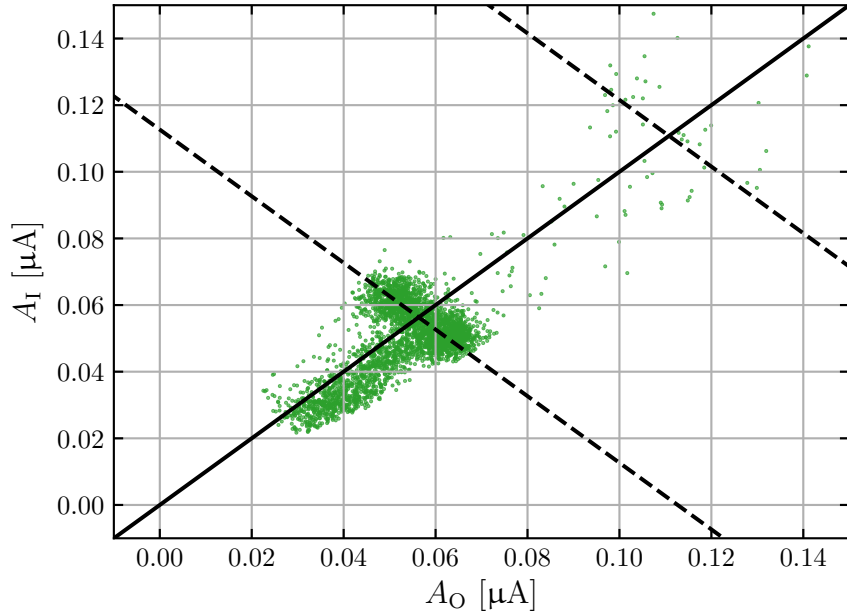


Figure 4.14: Scatter plot of the measured OF amplitudes from the inner and outer channels, A_I and A_O respectively, from the stage-0 background events measured on the ninth day of data acquisition after some data-quality cuts are applied. The solid diagonal line which has a slope of 1 indicates points that have the same amplitude in both channels. The dashed anti-diagonal lines have a slope of -1 and are placed at the expected locations of the first and second e^-h^+ -pair peaks. Courtesy of Valentina Novati.

4.3.2 Temperature Correction

Temperature fluctuations are the largest source of gain and amplitude variation of events measured in the detector. Correcting for this parameter is therefore important to achieve the best energy resolution and critical to ensure the final energy spectrum from this analysis is independent of temperature. The detector was thermally coupled to the coldest stage of the ADR, and thus is characterized by the fridge temperature parameter. As outlined in Sec. 4.2.2, the fridge temperature is a readout parameter measured in units of volts. The conversion between this readout parameter and the actual fridge temperature is displayed in the left plot of Fig. 4.15. Due to unknown noise sources and ADR behaviour that is not fully understood, the detector temperature experienced both small- and large-scale fluctuations. Additionally, the detector temperature would increase as a result of the ADR warm-up that occurred at the end of each day. A summary of the fridge temperature during data acquisition is shown in the right plot of Fig. 4.15. For some days of data acquisition, data were not recorded during the ADR warm-up.

The relationship between the fridge temperature and the detector gain variation can be understood by considering the basic operation of the TESs. The TES gain depends on the TES bias resistance R_{TES} , which is the resistance of the TES at its steady operating position while the TES is at its operating temperature T_0 . For a given energy deposition, a lower value of R_{TES} corresponds to a larger gain seen by the TES [15]. The Si crystal in the detector is held at the bath temperature T_b , that is lower than T_0 . The difference between T_b and T_0 is maintained by balancing the Joule heating applied on the TES with the small thermal conductance between the TES and the crystal. The power loss due to thermal

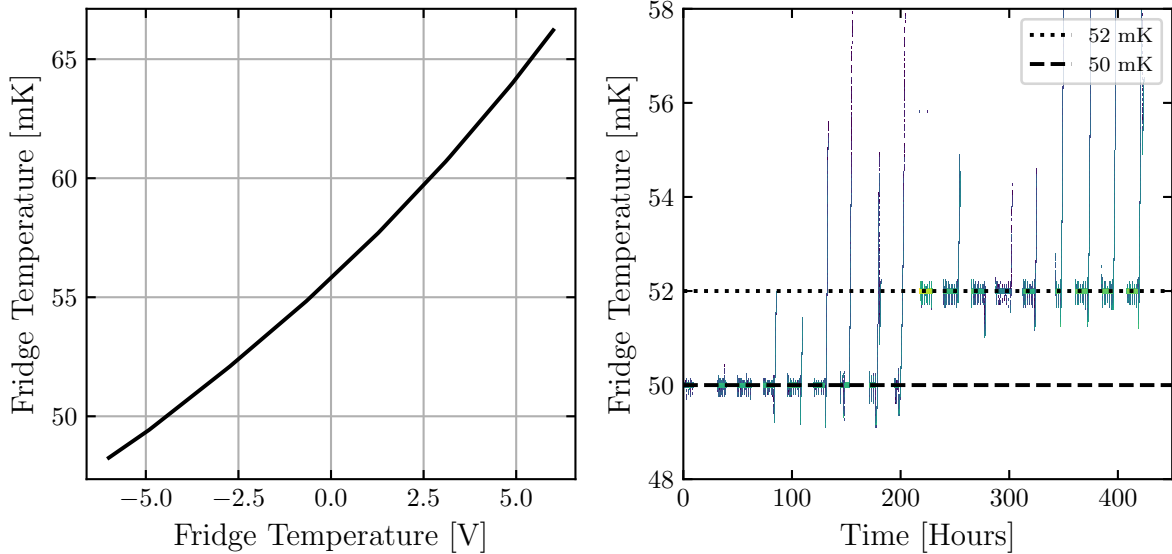


Figure 4.15: Left: Conversion between the fridge temperature readout parameter measured in volts and the actual fridge temperature in milli-Kelvin. Right: Summary of the fridge temperature during data acquisition. Fluctuations can be seen around the operating temperatures of 50 and 52 mK, with the long tails corresponding to the daily ADR warm-up. Courtesy of Yen-Yung Chang.

conductance and the biasing power for Joule heating are given by Eq. 3.1 and 3.2, respectively. By equating the power loss and power gain, R_{TES} can be expressed as:

$$R_{\text{TES}} = \frac{V_b^2}{K(T_0^5 - T_b^5)}. \quad (4.4)$$

During normal operation, V_b is held approximately at a constant. Therefore, a decrease in the fridge temperature and thus in T_b results in a decrease in R_{TES} and an increase in the gain for a given energy deposition. Because this reasoning is independent of the detector bias voltage, it negates the need for separate temperature corrections for the differing HV biases applied to the detector each day.

The temperature correction is developed using a dedicated laser-calibration dataset in which the QET channels were held at their normal operating point but the fridge temperature was intentionally varied. This dataset was measured with a 60 V bias voltage applied to the detector. Two temperature sweeps were conducted in order to develop a separate temperature correction for data captured at each of the two operating temperatures during data acquisition. The temperature varied from 49.9–51.0 mK and 51.9–53.0 mK for the 50 and 52 mK corrections, respectively, using 100 μK steps. Lastly, the laser-calibration dataset was measured using two different laser powers in order to investigate if there is any dependence on the mean number of photons per pulse λ . Ultimately no λ dependence is observed and the two datasets, denoted as high- λ and low- λ , are combined to develop the temperature correction. The data are first cleaned by applying some data-quality cuts: a cut on the OF amplitudes A from the inner, outer, and total channels using a constant cut-off value, and a 3σ cut on both the fridge temperature and mean base distributions. Furthermore, only events coincident with the last TTL trigger are selected. Figure 4.16 shows the OF amplitude A of the total channel versus fridge temperature from the low- λ laser-calibration datasets after data-quality cuts for the 50 and 52 mK corrections.

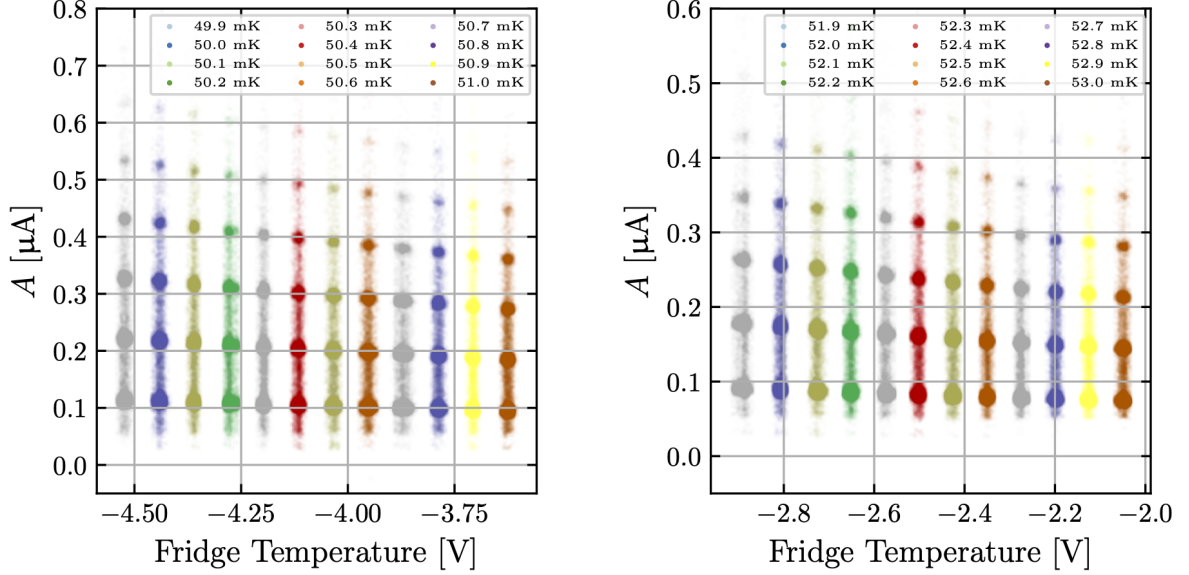


Figure 4.16: Summary of the low- λ laser-calibration datasets acquired for the 50 mK (left) and 52 mK (right) corrections. The data are plotted as the OF amplitude A of the total channel versus the readout fridge temperature; a more negative voltage in the fridge temperature parameter corresponds to a lower actual fridge temperature.

Each cluster of events in Fig. 4.16 corresponds to a quantized e^-h^+ -pair peak n_{eh} , starting with $n_{eh} = 1$ at the bottom. By following the locations of equal n_{eh} clusters, there is a clear relationship between the fridge temperature and A ; a lower fridge temperature results in a higher TES gain and thus a larger measured A for the same energy deposition. To quantify this trend, each n_{eh} cluster is fit to with a Gaussian function; the fit results from the 50 and 52 mK correction datasets are shown in Fig. 4.17.

The results of the Gaussian fits show a linear relationship between the Gaussian peak location and the fridge temperature T for equivalent e^-h^+ -pair peaks. The temperature dependence is parameterized by assuming each equal-energy line in the A - T plane is a straight line, verified by the linear fits shown in Fig. 4.17. Each equal-energy line has a slope A' that is parameterized as a function A at some reference temperature T_{ref} . The chosen values for the 50 and 52 mK corrections are $T_{\text{ref}} = -4.44$ and $T_{\text{ref}} = -2.81$, respectively, which correspond to 50 mK and 52 mK after the voltage-to-temperature conversion. Although the choices of T_{ref} are arbitrary and do not affect the performance of the correction, they are chosen so that the correction would have the smallest impact at the temperatures where most of data were acquired.

The goal of this parameterization is to rotate equal-energy lines, like the ones shown in Fig. 4.17, around the lines' intersection at T_{ref} until they are horizontal. In other words, the corrected OF amplitude A_{corr} given a measured OF amplitude A_{obs} and temperature T_{obs} should be equivalent to A_{corr} at T_{ref} following the equal-energy line with slope $A'(A_{\text{corr}})$ that connects A_{obs} at T_{obs} with A_{corr} at T_{ref} . This is written in the form:

$$A_{\text{obs}} = A'(A_{\text{corr}}|T = T_{\text{ref}}) \cdot (T_{\text{obs}} - T_{\text{ref}}) + A_{\text{corr}}. \quad (4.5)$$

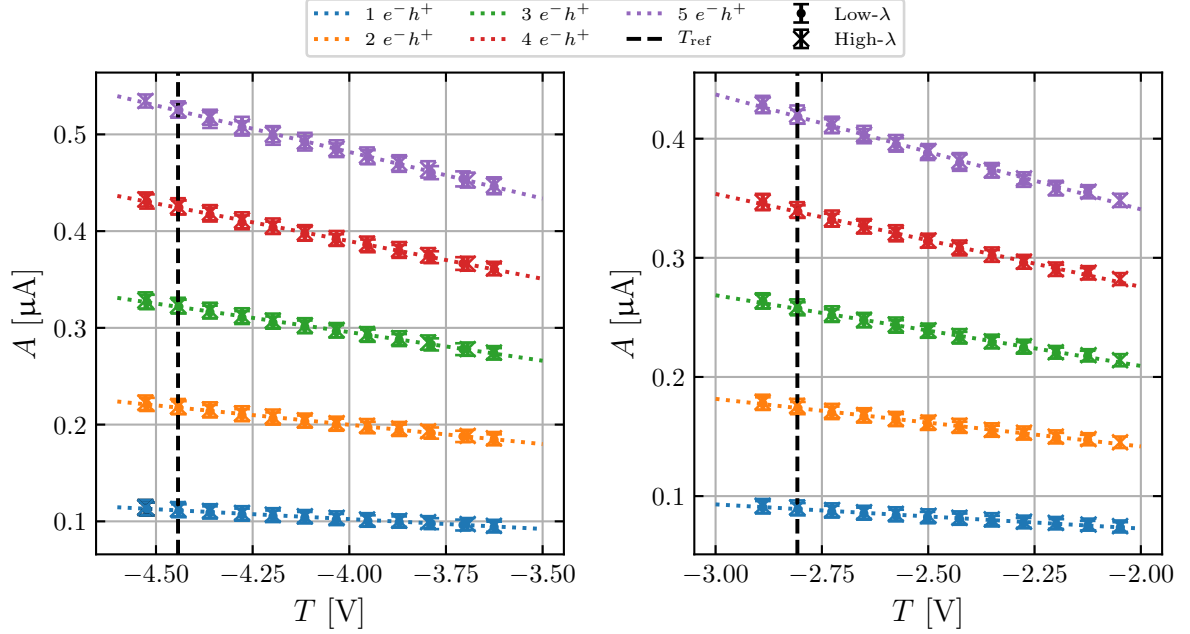


Figure 4.17: Results after fitting a Gaussian function to each n_{eh} cluster from the 50 mK (left) and 52 mK (right) temperature-correction datasets. The dotted lines are the linear fits of the Gaussian peak location versus temperature T for each e^-h^+ -pair quantization starting from $n_{eh} = 1$ at the bottom to $n_{eh} = 5$ at the top. The data points from the low- and high- λ datasets are combined to compute the linear fits. The vertical dashed lines correspond to the chosen reference temperatures $T_{\text{ref}} = 50$ mK (left) and $T_{\text{ref}} = 52$ mK (right) required to perform the temperature correction.

Equation 4.5 ensures that $A_{\text{corr}} = A_{\text{obs}}$ if $T_{\text{obs}} = T_{\text{ref}}$. $A'(A_{\text{corr}}|T = T_{\text{ref}})$ and the corresponding values of A_{corr} at $T = T_{\text{ref}}$ are extracted from the five linear fits in Fig. 4.17 separately for the 50 and 52 mK corrections, and are shown below in Fig. 4.18.

Figure 4.18 shows a linear dependence of A' with A_{corr} at $T = T_{\text{ref}}$, and therefore can be written simply as:

$$A'(A_{\text{corr}}|T = T_{\text{ref}}) = \frac{dA'}{dA_{\text{corr}}} \cdot A_{\text{corr}} + b, \quad (4.6)$$

where $\frac{dA'}{dA_{\text{corr}}}$ is the slope of A' versus A_{corr} , and b is a y-intercept parameter. The results from fitting Eq. 4.6 to the A' data points are shown by the orange curves in Fig. 4.18, with the fitted $\frac{dA'}{dA_{\text{corr}}}$ and b values listed in Tab. 4.2.

Table 4.2: Best-fit results from fitting the linear function in Eq. 4.6 to the A' data points in Fig. 4.18 for the 50 and 52 mK temperature corrections. T_{ref} is the chosen reference temperature for each correction in the readout units of volts.

	50 mK Correction	52 mK Correction
Parameter	Value	
T_{ref} [V]	-4.44	-2.81
$\frac{dA'}{dA_{\text{corr}}}$ [V^{-1}]	-0.1838 ± 0.0003	-0.236 ± 0.001
b [$\mu\text{A V}^{-1}$]	$(4 \pm 9) \times 10^{-4}$	$(7 \pm 1) \times 10^{-3}$

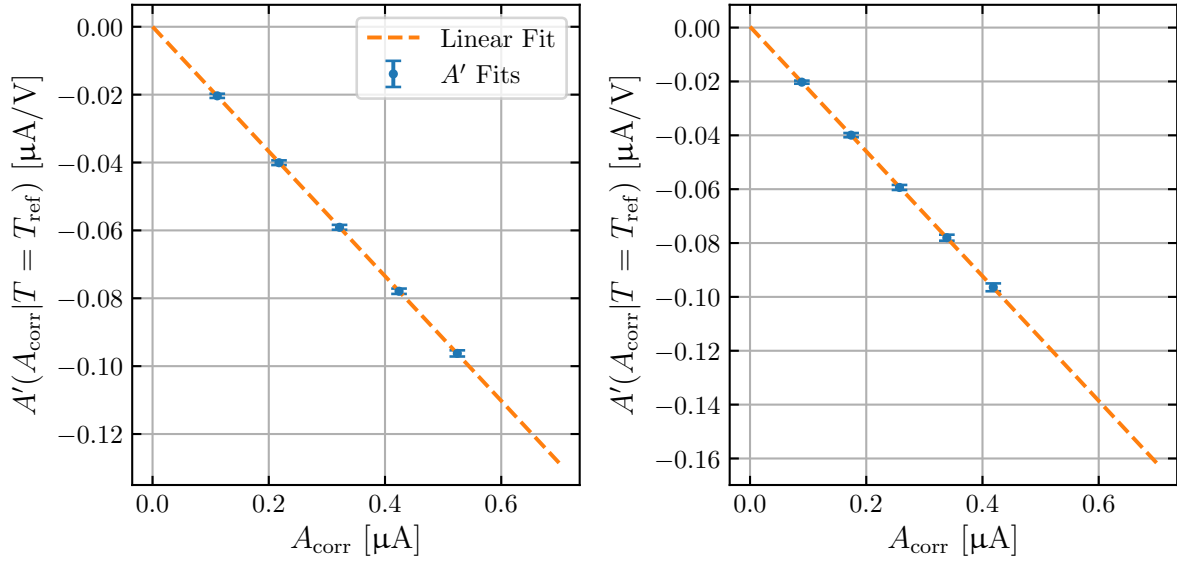


Figure 4.18: The slope parameter A' versus the corrected amplitude parameter A_{corr} at the reference temperature T_{ref} for the 50 mK (left) and 52 mK (right) temperature corrections. The data points are extracted from the linear fits shown in Fig. 4.17. The orange curves are the linear fits to the data points.

Equations 4.5 and 4.6 are combined and rearranged to solve for the corrected amplitude A_{corr} as a function of the observed amplitude A_{obs} , observed temperature T_{obs} , reference temperature T_{ref} , and the parameters $\frac{dA'}{dA_{\text{corr}}}$ and b :

$$A_{\text{corr}} = \frac{A_{\text{obs}} - b \cdot (T_{\text{obs}} - T_{\text{ref}})}{1 + \frac{dA'}{dA_{\text{corr}}} \cdot (T_{\text{obs}} - T_{\text{ref}})}. \quad (4.7)$$

For a hypothetical event with zero energy deposition, A_{obs} and A_{corr} must be zero for any arbitrary T_{obs} . This is only true if the fit parameter $b = 0$. Although Tab. 4.2 shows that b is not consistent with zero for the 52 mK correction, it was verified that setting b to zero would cause only a $\ll 1\%$ difference in the corrected amplitudes. Equation 4.7 can therefore be simplified to:

$$A_{\text{corr}} = \frac{A_{\text{obs}}}{1 + \frac{dA'}{dA_{\text{corr}}} \cdot (T_{\text{obs}} - T_{\text{ref}})}. \quad (4.8)$$

Figure 4.19 shows the temperature correction in Eq. 4.8 with the parameters in Tab. 4.2 applied to the 50 and 52 mK laser-calibration datasets. The equal-energy e^-h^+ -pair clusters after the correction is applied become horizontal over the temperature range.

Although the temperature correction described in this section is valid over a wide range of fridge temperatures, most of the data captured during data acquisition was measured when the fridge temperature was stable. Therefore most events have only a small, $\mathcal{O}(1\%)$ correction applied to the measured OF amplitude due to temperature, as shown in Fig. 4.20.

4.3.3 High-Voltage Correction

As described in Chapter 2, the energy measured for an event is amplified by Neganov-Trofimov-Luke (NTL) phonons induced by liberated e^-h^+ -pairs, where the amount of NTL amplification depends on

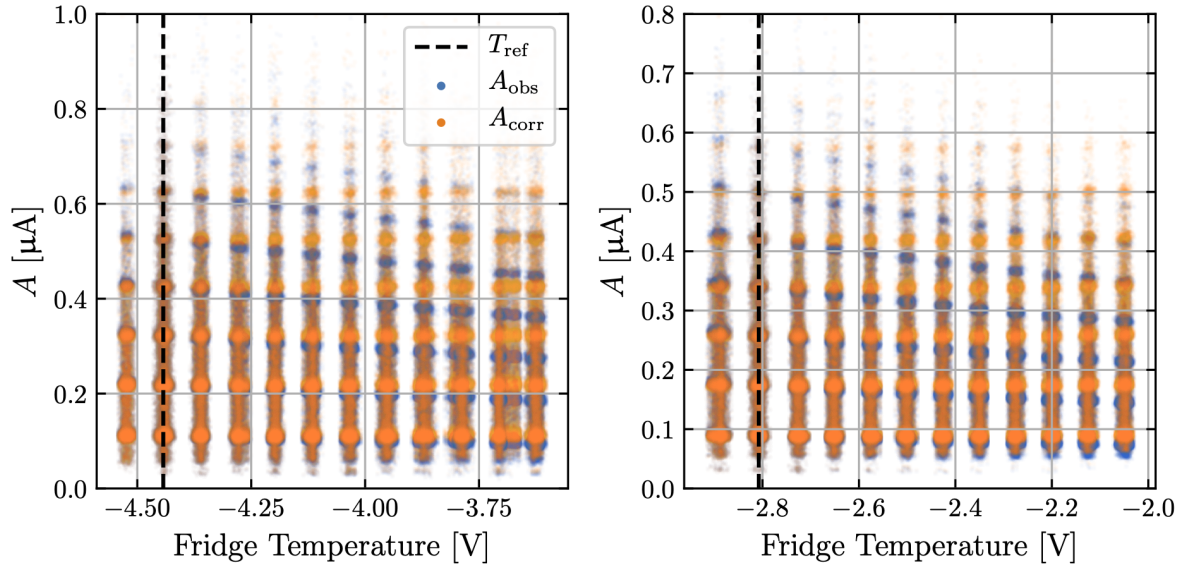


Figure 4.19: The combined low- and high- λ laser-calibration datasets acquired for the 50 mK (left) and 52 mK (right) corrections. The data are plotted as the OF amplitude A of the total channel versus the readout fridge temperature before (blue) and after (orange) the temperature correction. The dashed, vertical lines are the reference temperatures chosen for each correction.

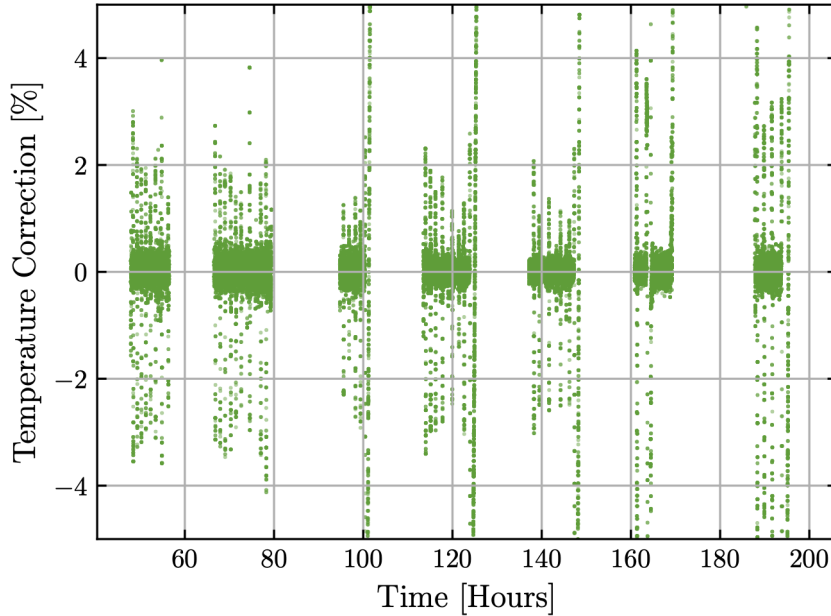


Figure 4.20: Temperature-corrected OF amplitude as a percentage of the measured OF amplitude versus event time for the 100 V, stage-0 background dataset.

the voltage bias applied across the detector. Therefore, variation in the HV bias over time directly leads to variation in the measured energy for equal-energy events. This section describes the procedure used to correct the OF amplitudes due to variations in HV bias. First, the event amplitudes are corrected for variations in the HV bias that occurred within each day of data acquisition. Second, the event amplitudes

are corrected for the day-to-day variations in the HV bias. The HV corrections were developed using the daily laser-calibration data with the *temperature-corrected* OF amplitude A_{TC} of the total channel. Due to the faulty HV power supply, the first two days of data acquisition did not properly record the HV bias data. Therefore for these days, the data is not corrected for same-day HV variations. Ultimately, these variations result in very small corrections, as will be shown by Figure 4.23. The data are first cleaned up by applying a 3σ cut on the fridge temperature and cut on $\chi^2(t)$ using a constant cut-off value, and only events coincident with the laser TTL trigger are selected.

Same-Day HV Correction

The same-day HV correction is formulated by first fitting a Gaussian function to the second e^-h^+ -pair peak in the laser-calibration spectrum from each day. The second e^-h^+ -pair peaks are chosen because they have a large enough statistical sample to produce a good fit and show relatively fewer non-laser, background events compared to the first e^-h^+ -pair peak. Next, events within the second e^-h^+ -pair peak are selected by using a $\pm 3\sigma$ cut around the mean value from the Gaussian fits. The remaining data are then binned by the measured HV bias V_{bias} ; the bin size is determined by the resolution of the HV readout measurement. A Gaussian function is then fit to the events within each HV bin, extracting the mean A_{TC} value for each HV bin. The left plot in Fig. 4.21 shows the A_{TC} versus V_{bias} data points from one day of laser-calibration data.

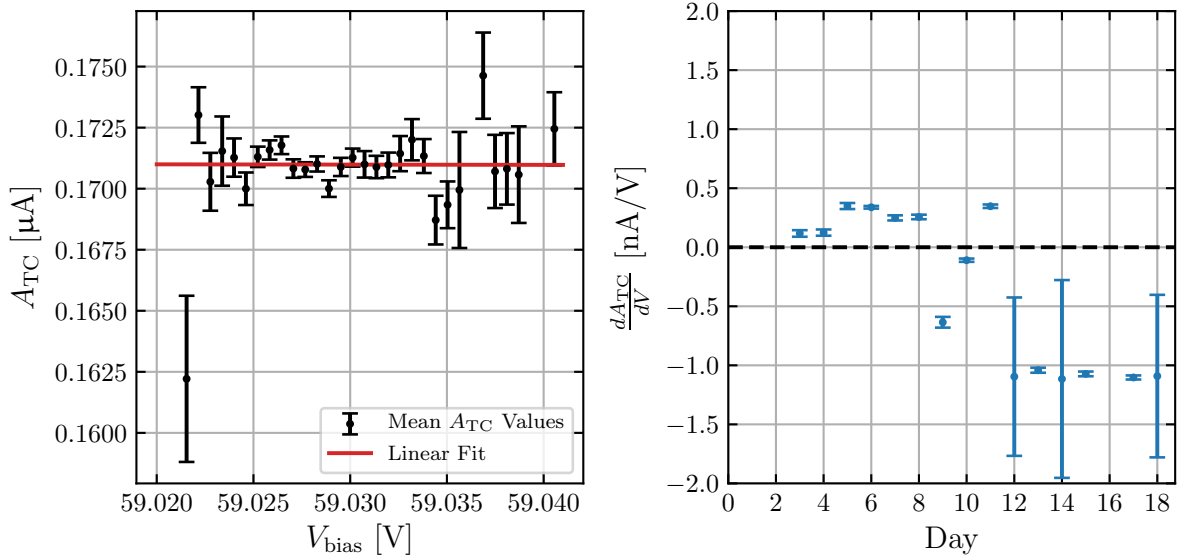


Figure 4.21: Left: Mean temperature-corrected OF amplitude A_{TC} from each HV bin from one day of laser-calibration data. A linear function described by Eq. 4.9 is fit to the data points and is shown by the red curve. Right: Summary of the slope values $\frac{dA_{TC}}{dV}$ from each laser-calibration dataset. The values for the first two days are not shown because of the faulty HV power supply that did not properly record the V_{bias} data. The 16th day has an unexpectedly larger value of $\frac{dA_{TC}}{dV}$ compared to the other days, and is thus not shown. However, the data acquired for this day was ^{57}Co -calibration data and was therefore not used for the main DM analysis. Courtesy of Valentina Novati.

The A_{TC} versus V_{bias} data points are subsequently fit to with a linear function to extract a slope value $\frac{dA_{TC}}{dV}$, as shown by the red curve in the left plot of Fig. 4.21. The right plot of Fig. 4.21 summarizes

the fitted $\frac{dA_{\text{TC}}}{dV}$ values computed from each day of laser-calibration data. Due to the linear relationship between the HV bias and NTL amplification, the $\frac{dA_{\text{TC}}}{dV}$ values are expected to be positive. However as Fig. 4.21 clearly shows, this is not always observed. It is suspected that the typical HV bias variation within a day is too small to measure significantly positive slope value. Nonetheless, the data within each day are corrected by doing a rotation about the averaged HV bias measured each day according to:

$$A_{\text{corr}}^i = \frac{dA_{\text{TC}}}{dV} \cdot (V_{\text{avg}} - V_{\text{obs}}) + A_{\text{TC}}, \quad (4.9)$$

where A_{corr}^i is the corrected OF amplitudes after the same-day HV correction, V_{avg} is the averaged measured HV bias for each day, and V_{obs} is the HV bias measured for each event. This correction that accounts for HV drifting is found to be relatively small compared to the day-to-day HV correction.

Day-to-Day HV Correction

The HV bias of each day was set by hand using a potentiometer operated by a dial, leading to day-to-day HV bias variation. Figure 4.22 summarizes this day-to-day variation in the HV bias that occurred during data acquisition. It is evident that the day-to-day variation in the HV bias is much larger than the same-day variation.

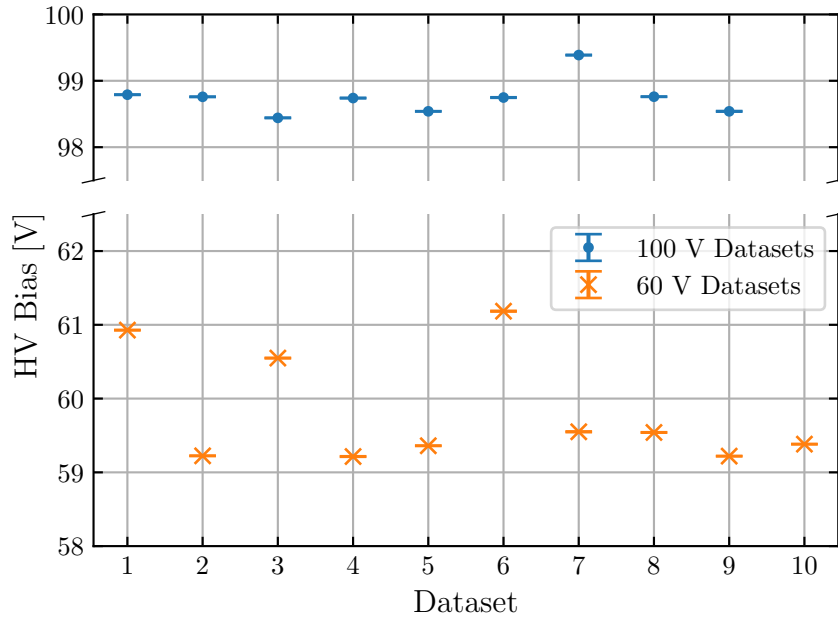


Figure 4.22: Summary of the averaged HV bias measured for the laser-calibration data acquired for the 100 V datasets (blue) and 60 V datasets (orange). The spreads in the measured HV bias of each day are represented by the y-direction error bars, and are small (and hard to see) compared to the day-to-day variation in the HV bias. Courtesy of Valentina Novati.

The day-to-day variation in the HV bias are corrected for by scaling the amplitudes according to:

$$A_{\text{corr}}^{ii} = A_{\text{corr}}^i \cdot \frac{V_{\text{corr}}}{V_{\text{avg}}}, \quad (4.10)$$

where A_{corr}^{ii} is the OF amplitude after the day-to-day HV correction, A_{corr}^i is the OF amplitude after the same-day HV correction from Eq. 4.9, V_{avg} is the averaged HV bias for each day, and V_{corr} is the HV bias to correct all the data to. For the 100 V and 60 V datasets, $V_{\text{corr}} = 100$ V and $V_{\text{corr}} = 60$ V, respectively. Although the HV scaling in Eq. 4.10 is consistent with the NTL phonon energy scaling with voltage, it is *not* consistent with the total energy scaling with voltage. This is because the total energy measured for an event is partially comprised of the voltage-independent recoil or absorption energy (see Sec. 2.1.1). However this analysis is concerned with events with recoil or absorption energies < 50 eV, and the HV corrections result in $< 1\%$ changes in the amplitudes. Therefore the systematic error produced by this HV correction is at most 0.5 eV and small enough to be neglected. Figure 4.23 shows the results of both the same-day and day-to-day HV corrections applied to the temperature-corrected OF amplitudes of the 100 V, stage-0 background dataset.

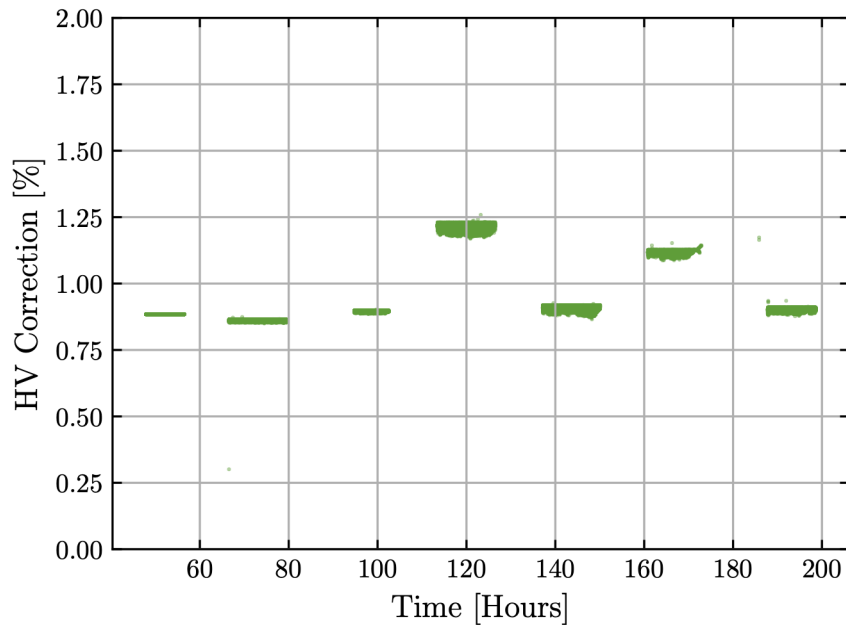


Figure 4.23: HV- and temperature-corrected OF amplitude as a percentage of the temperature-corrected OF amplitude versus event time for the 100 V, stage-0 background dataset.

4.3.4 QET Photon Absorption

The laser-calibration data was measured using a laser that shone on the top surface of the detector where the two QET channels are positioned. Because the Al fins of the QET channels cover roughly 50% of the surface area, a non-negligible fraction of photons emitted from the laser could be absorbed directly into the Al fins instead of being absorbed by the Si crystal. These type of events are distinct from the expected laser events whereby the photons are absorbed by the Si crystal, exciting e^-h^+ pairs which generate phonons through NTL amplification that are subsequently absorbed by the Al fins. A photon that is directly absorbed by the Al fins deposits all of its energy inside the Al fins which is then measured by the TESs. The QET-absorbed photons do not generate e^-h^+ pairs and therefore do not generate additional phonons through NTL amplification. As the W TESs have a small surface area

coverage, events produced via direct absorption in the TESs are ignored. Direct absorption of photons by the Al fins is known and has been previously observed in a HVEV detector [145].

The laser power, parameterized by the mean number of photons per pulse λ , was not stabilized, and therefore produced a Poisson distribution of the number of photons. For larger values of λ , individual events could be generated by photons absorbed by the Si crystal and photons absorbed by the QETs at the same time. Due to the voltage bias applied across the detector, the Si-absorbed photons produce a dominant fraction of the total measured energy and give rise to the quantized e^-h^+ -pair peaks. In contrast, the QET-absorbed photons account for a small fraction of the total measured energy and appear as offsets in the energy spectra. The effect of QET-absorbed photons has on the laser-calibration data is estimated by analyzing the energy offset in the zeroth e^-h^+ -pair peak. Events offset from the zeroth e^-h^+ -pair peak correspond to single photons that were absorbed by a QET. This correction was developed with the daily laser-calibration data using A_0 of the total channel after temperature and HV corrections applied, $A_{0, \text{THC}}$. A_0 , the OF amplitude with no time offset, is used instead of A as the energy estimator because A_0 is better at evaluating the energy of events below the energy threshold (i.e. events in the zeroth e^-h^+ -pair peak) that aligned with the laser TTL trigger. Due to the low signal-to-noise ratio below the energy threshold, A can often overestimate the energy by finding a nearby noise peak with a larger amplitude. The data are first cleaned with a cut on $\chi_0^2(t)$ using a constant cut-off value, and events coincident with the laser TTL trigger are selected.

A Gaussian function is fit to the quantized e^-h^+ -pair peaks, including the zeroth peak, from the $A_{0, \text{THC}}$ spectrum of each laser-calibration dataset. The amplitude of each e^-h^+ -pair peak, as well as the position of the zeroth e^-h^+ -pair peak, are extracted from the fits. The left plot in Fig. 4.24 shows the e^-h^+ -pair peak amplitudes as a function of peak number n_{eh} from one day of laser-calibration data. A Poisson function is then fit to these data points in order to extract the laser power λ for each laser-calibration dataset:

$$y = p_0 \frac{\lambda^x \cdot e^{-\lambda}}{\Gamma(x+1)}, \quad (4.11)$$

where y is the fitted amplitude of each e^-h^+ -pair peak, x is the number of each peak, $\Gamma(x+1)$ is the Gamma distribution, and p_0 is an overall scaling parameter. The result of fitting Eq. 4.11 to the data points in the left plot of Fig. 4.24 is shown by the red curve; the laser power for this laser-calibration dataset is found to be $\lambda = 1.842$.

The offsets of the zeroth e^-h^+ -pair peak, in units of n_{eh} , were converted to an energy offset in units of eV by multiplying the values by the HV bias applied to the detector, V_{bias} . The right plot of Fig. 4.24 shows the zeroth e^-h^+ -pair peak energy offset versus the fitted λ value for each laser-calibration dataset. The green curve shows the fitted linear function to these data points.

As Fig. 4.24 shows, there is a clear trend between the laser power and the zeroth e^-h^+ -pair peak energy offset in the laser-calibration data, demonstrating that photon absorption by the QETs is a real effect. However, the dispersion of the data points in the right plot of Fig. 4.24 is large relative to their uncertainty, and therefore the fitted linear function to these points cannot be trusted nor used in this analysis. One possibility for the underestimation of the uncertainty of the data points is that λ may not be constant over time. The 1σ spread of the residuals from the data points with respect to the fitted linear function is found to be 0.37(6) eV, and is considered when assessing the uncertainty in the final limit results.

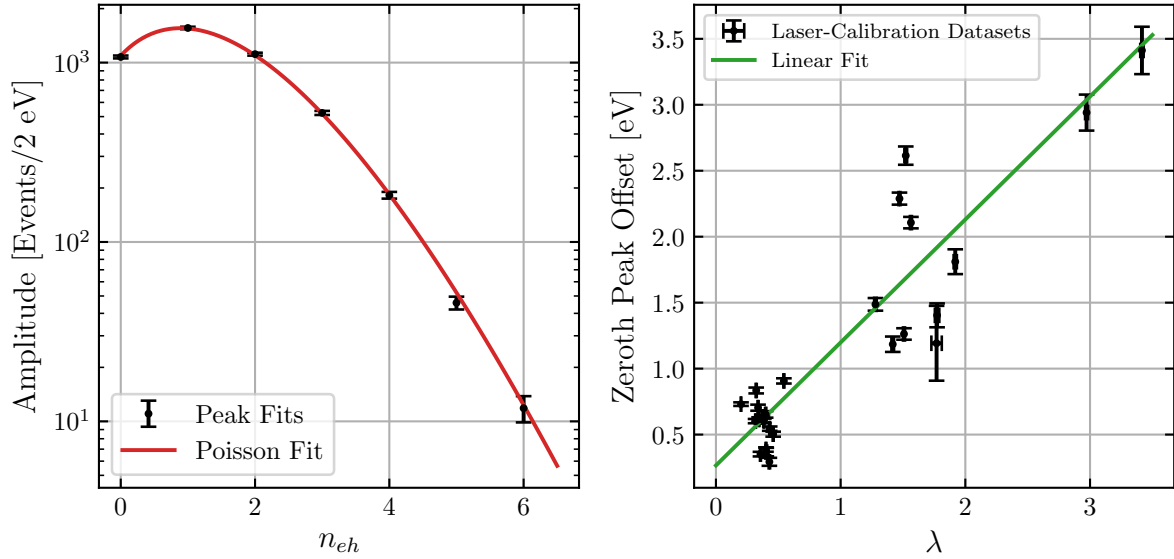


Figure 4.24: Left: Fitted peak amplitudes versus number of e^-h^+ pairs n_{eh} from the temperature- and HV-corrected $A_{0, \text{THC}}$ spectrum from one day of laser-calibration data. A Poisson function described by Eq. 4.11 is fitted to the data points to extract λ and is shown by the red curve. Right: Summary of the zeroth e^-h^+ -pair peak offset versus the fitted λ value from each laser-calibration dataset. A linear function, shown by the green curve, is fit to these data points. Courtesy of Valentina Novati.

In lieu of being able to adjust the energy of each event individually, the effect due to QET absorption is accounted for by adjusting the “true” energy points in the calibration phase described by Eq. 4.14 in Sec. 4.3.5. The value of the energy offset E_{offset} is determined by relating the ratio of the zeroth e^-h^+ -pair peak position in energy and OF amplitude space with the ratio of the difference between the first and zeroth e^-h^+ -pair peak in energy and OF amplitude space:

$$\frac{E_{\text{offset}}}{A_{0, \text{THC}}^0} = \frac{E_\gamma + e \cdot V_{\text{bias}}}{A_{0, \text{THC}}^1 - A_{0, \text{THC}}^0}, \quad (4.12)$$

where $E_\gamma = 1.95 \text{ eV}$ is the photon energy, e is the absolute value of the electron charge, and $A_{0, \text{THC}}^0$ and $A_{0, \text{THC}}^1$ are the positions of the zeroth and first peak, respectively, from the temperature- and HV-corrected A_0 amplitudes. The correction factor is evaluated separately for each laser-calibration dataset. Importantly, this effect is applicable for only the laser-calibration data and not for the background data, as DM particles are not expected to interact with the Al fins in the QETs and the Si crystal within the same event due to the small cross sections of the DM candidates. In order to combine the laser-calibration data from different days, and to calibrate the background data, the offset value from each laser-calibration dataset is corrected for during energy calibration.

4.3.5 Non-Linearity Correction and Calibration

This last step of energy calibration for this analysis involves correcting for non-linearities in the energy gain and to convert the OF amplitude measurements to the true energy values in units of eV. As with the energy corrections described in the previous sub-sections, the energy calibration was developed and applied separately each day using the daily laser-calibration datasets. This procedure calibrates the

temperature- and HV-corrected OF amplitudes A_{THC} of the total channel from each event, although the temperature- and HV-correction OF amplitudes with no time offset $A_{0, \text{THC}}$ are also required. The calibration uses only events coincident with the laser TTL trigger, and the data are cleaned by removing events above a constant cut-off value in the $\chi^2(t)$ and $\chi_0^2(t)$ parameters.

A Gaussian function is fit to the quantized peaks in the A_{THC} spectrum from each laser-calibration dataset, and the peak positions A_{THC}^n for $n \geq 1$ peaks were extracted. The number of fitted peaks differs for each laser-calibration dataset due to the daily variation in the laser power. To improve the quality of the calibration, particularly at low energies, the position of the zeroth quantized peaks are also included. However, as outlined in Sec. 4.3.4, the A amplitudes (with a time offset) are a poor energy estimator for events below the energy threshold and thus events can only be assessed with A_0 . To account for the subtle difference between A and A_0 , the positions of the zeroth peaks in A_{THC} are estimated using the positions of the zeroth and first peaks in $A_{0, \text{THC}}$, $A_{0, \text{THC}}^0$ and $A_{0, \text{THC}}^1$, by using the following proportion:

$$\frac{A_{\text{THC}}^0}{A_{\text{THC}}^1} = \frac{A_{0, \text{THC}}^0}{A_{0, \text{THC}}^1}. \quad (4.13)$$

The A_{THC}^n positions are then related to the expected energy at the n^{th} e^-h^+ -pair peak, E_n :

$$E_n = n \cdot (E_\gamma + e \cdot V_{\text{bias}}) + E_{\text{offset}}, \quad (4.14)$$

where $E_\gamma = 1.95 \text{ eV}$ is the photon energy. E_{offset} differs for each laser-calibration dataset, and the background datasets are expected to have no such offset. Therefore in order to combine the laser-calibration datasets and calibrate the background data, the energy calibration is performed with the E_{offset} subtracted; instead of the A_{THC}^n positions being calibrated to E_n energies, the $A_{\text{THC}}^n - A_{\text{THC}}^0$ positions are calibrated to $E_n - E_{\text{offset}}$ energies. Figure 4.25 shows the $E_n - E_{\text{offset}}$ versus $A_{\text{THC}}^n - A_{\text{THC}}^0$ calibration data points from one day of laser-calibration data.

The measured versus expected energy data points are subsequently fit to a calibration curve described by a quadratic polynomial function with the form:

$$y = a \cdot x (1 + b \cdot x), \quad (4.15)$$

where y is the expected e^-h^+ -pair peak energy less the QET energy offset, $E_n - E_{\text{offset}}$, x is the measured peak position less the QET energy offset, $A_{\text{THC}}^n - A_{\text{THC}}^0$, and a and b are fit parameters. The quadratic term in Eq. 4.15 corrects for non-linearities in the calibration. Equation 4.15 also ensures that $y(0) = 0$, meaning a measured OF amplitude of zero corresponds to zero energy. The fitted calibration curve is shown for one day of laser-calibration data in Fig. 4.25, which happens to have only five e^-h^+ -pair peaks to calibrate to. The calibration curve to each dataset is valid up to six e^-h^+ -pair peaks. Figure 4.26 summarizes the results of the fitted a and b values from the laser-calibration datasets.

After the energy calibration is applied to each laser-calibration dataset, the datasets are combined to produce the full calibrated laser-calibration data. Figure 4.27 shows the full calibrated datasets for the 100 V (left) and 60 V (right) measurement. To assess the accuracy of the energy corrections and calibration, the first six e^-h^+ -pair peaks in the combined energy spectra, where the calibration is valid, are fit to with a Gaussian function, and the peak positions are extracted.

The extracted e^-h^+ -pair peak locations are compared to the corresponding expected calibration energy E_{cal} , where $E_{\text{cal}} = E_n - E_{\text{offset}}$. The difference between the measured peak locations and E_{cal}

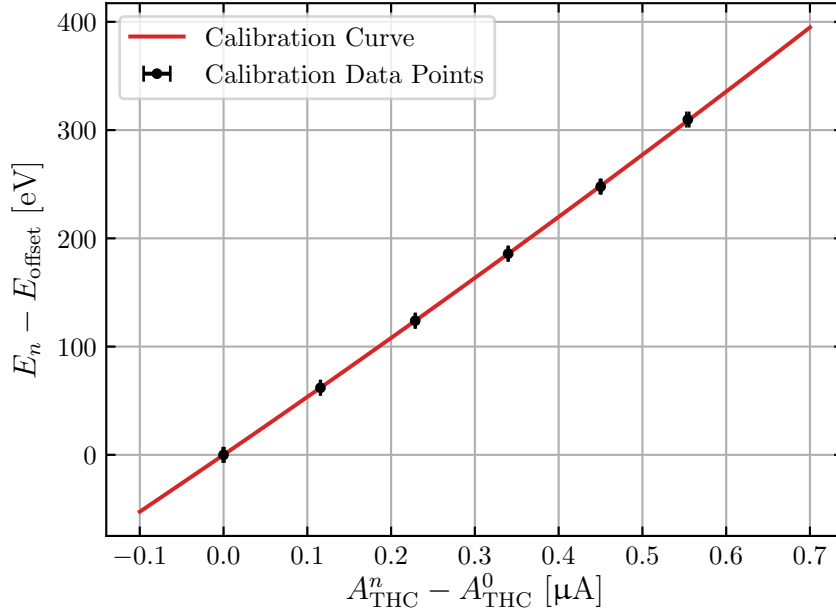


Figure 4.25: Calibration data points and curve from one day of laser-calibration data used to convert the measured OF amplitudes to true energies. The x-axis corresponds to the position of the n^{th} peak from the temperature- and HV-corrected OF amplitude spectrum, A_{THC}^n , less the offset due to QET photon absorption estimated by the zeroth peak position, A_{THC}^0 . The y-axis corresponds to the expected energy of the n^{th} e^-h^+ -pair peak, E_n , less the energy offset due to QET photon absorption, E_{offset} , as described in Eq. 4.14. The red curve is the fitted calibration curve described by the quadratic function in Eq. 4.15. Courtesy of Valentina Novati.

is denoted as ΔE_{cal} . The middle plots in Fig. 4.27 show that all e^-h^+ -pair peaks fall within $\pm 0.2\%$ of their expected locations. The bottom plots in Fig. 4.27 show that all the e^-h^+ -pair peaks differ from their expected locations by less than ± 0.5 eV, with most data points being consistent or nearly consistent with zero. The high precision of the calibration of the laser-calibration spectra shown by the results in Fig. 4.27 validates the energy correction and calibration procedure described throughout this section. The procedure was therefore also applied to the background and ^{57}Co datasets. Lastly, the small calibration errors shown in Fig. 4.27 are considered when evaluating the uncertainty in the final limit results.

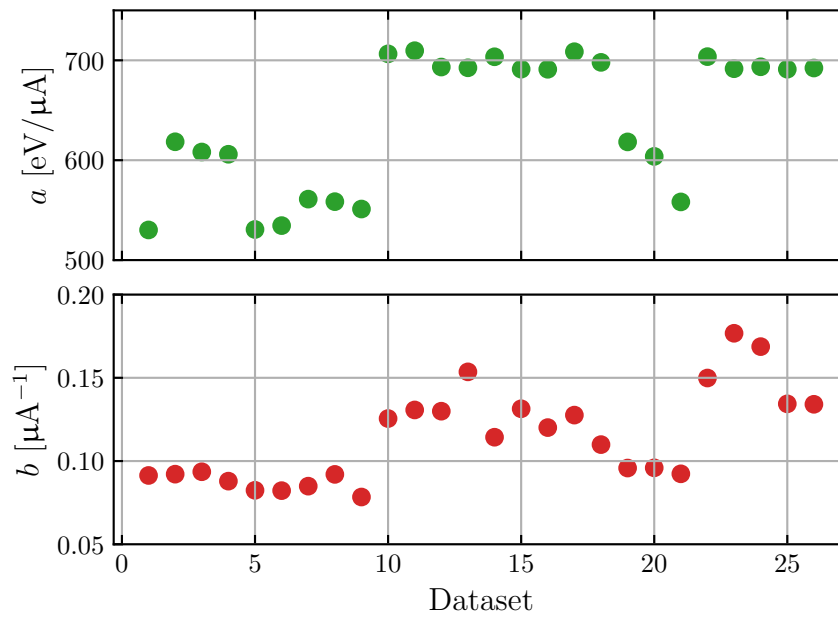


Figure 4.26: Results of fitting the Eq. 4.15 to the calibration data points from each laser-calibration dataset. The values of a and $a \cdot b$ correspond to the linear and quadratic terms, respectively, of the polynomial fit. Courtesy of Valentina Novati.

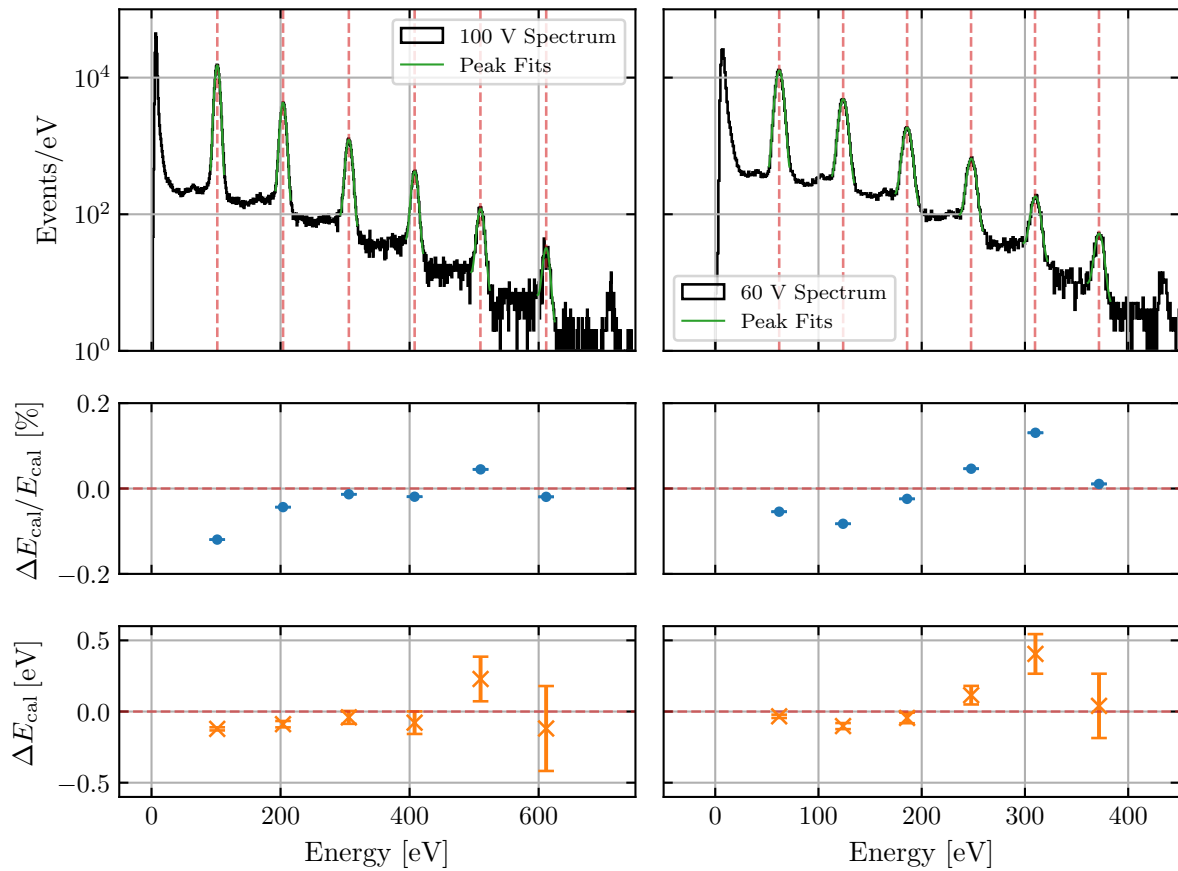


Figure 4.27: Top: full laser-calibration spectrum after applying the energy corrections and calibration described in this section for the 100 V (left) and 60 V (right) measurement. The vertical dashed lines correspond to the expected calibration energy of each peak, E_{cal} . The green curves are the fitted Gaussian function to each e^-h^+ -pair peak. Middle: percent difference between the fitted location and E_{cal} , ΔE_{cal} , of each e^-h^+ -pair peak. The error bars are included but are too small to be visible. Bottom: absolute difference between the fitted location and E_{cal} of each e^-h^+ -pair peak. Courtesy of Valentina Novati.

4.4 Analysis Selection Criteria

This section describes the data selection criteria (denoted as cuts) developed for this analysis. The cuts are divided into two categories: livetime cuts and data-quality (DQ) cuts. The livetime cuts, outlined in Sec. 4.4.1, are defined based on quantities not directly related to individual event pulses, such as the fridge temperature and trigger rates. These cuts evaluate the good periods of time during data acquisition in which events were measured by removing bad periods of time when data collection was not optimal. Furthermore, these cuts are used to evaluate the science exposure for this experiment. Unlike the livetime cuts, the DQ cuts, as outlined in Sec. 4.4.2, are defined based on quantities related to the event pulses themselves, such as the goodness of fit χ^2 quantities. These cuts are used to clean the data by selecting good-quality events and rejecting those that are not well reconstructed. As such, the detector efficiency for this analysis is determined based on these DQ cuts. Section 4.4.2 includes the channel partition cut that was intended to be used in this analysis but, for reasons explained therein, cannot ultimately be used.

The livetime cuts are developed separately for the laser-calibration and background datasets that have been corrected and calibrated in energy. The DQ cuts are developed only using daily laser-calibration datasets, and initial results of these cuts are examined using the stage-0 background data. The cuts are developed using the same procedure for the data acquired with a voltage bias of 60 and 100 V; however because this analysis produces separate limit results at 60 and 100 V, the cuts are calculated and applied separately for the two datasets.

4.4.1 Livetime Selection Criteria

The livetime cuts are used to remove the periods of time when the detector was not in an optimal condition for data collection. This analysis uses three different categories of livetime cuts: (i) two fridge temperature cuts to remove periods of time when the ADR fridge temperature regulation was lost; (ii) a mean base cut to remove periods of time when the detector was not in a stable operating condition; and (iii) a trigger burst and leakage burst cut to remove periods of time with excessive trigger rates.

Fridge Temperature Cut

The temperature of the detector, characterized by the fridge temperature parameter with a sampling frequency of 1 Hz, was stable within $\sim 20 \mu\text{K}$ during normal operation. However the fridge temperature did experience fluctuation, including periods when the temperature regulation was temporarily lost as well as end-of-day periods when the fridge warmed. In order to remove the periods when the fridge was not within its stable operating temperature, two temperature cuts are implemented: a coarsely binned cut followed by a finely binned cut. The cuts are implemented separately for the data measured at an operating temperature of 50 and 52 mK.

First, a rough temperature cut is performed by binning the data in 30 s-long intervals and calculating the average fridge temperature in each bin. After constructing the distribution of the averaged fridge temperature, a Gaussian function is fitted to the peak, and the 30 s intervals that fall outside $\pm 3\sigma$ of the peak position are removed. This 30 s cut is primarily intended to remove the large periods of time when the fridge temperature was unregulated as well as the end-of-day periods when the fridge warmed. Figure 4.28 shows the removed periods of time after this 30 s temperature cut for one day of stage-0 background data.

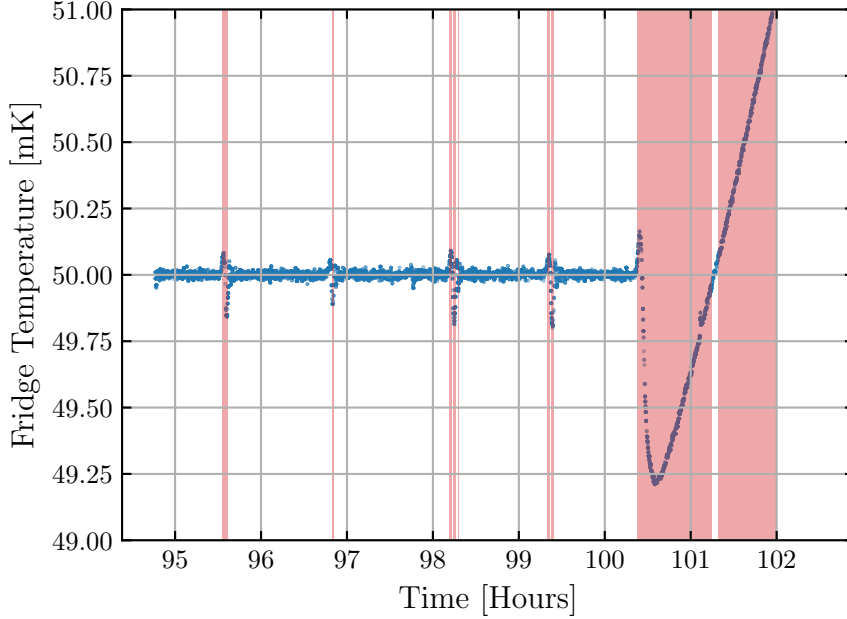


Figure 4.28: Fridge temperature versus time for events from one day of stage-0 background data. The red, shaded regions indicate periods of time that are removed due to the 30 s temperature cut. Courtesy of Yen-Yung Chang.

Next, a finer temperature cut is performed by binning the remaining data in 1 s-long intervals, which matches the sampling frequency of the temperature readout. After constructing again the distribution and fitting a Gaussian function to the peak, the 1 s intervals that fall outside $\pm 3\sigma$ of the peak position are removed. This cut is intended to remove smaller variations in temperature that may have been caused by small vibrations in the laboratory, as well as periods just before or after removed 30 s intervals that are also at unstable temperatures. The 1 s temperature cut isn't used by alone because of temperature oscillations that occurred as the temperature controller re-stabilized the temperature after a period of lost regulation. These periods of oscillations are not optimal for data acquisition, yet because of the precision of the 1 s temperature cut, it may accept some of this time. Conversely, the 30 s temperature cut is coarse enough to remove these oscillation periods entirely. Figure 4.29 shows the distribution of the fridge temperature before and after the 30 s and 1 s temperature cuts for the stage-0 background data measured at 50 and 52 mK.

Due to the temporal nature of the blinding scheme as outlined in Sec. 4.2.4, for every 1 s bin in the stage-0 background data removed by the 1 s temperature cut, the corresponding 10 s interval is also assumed to be removed. This provides a conservative estimate of the livetime calculation for the stage-0 background data. For the stage-2, fully unblinded data, this assumption is lifted and the cuts are recalculated.

Mean Base Cut

The mean base parameter, which is a measure of the mean of the pre-trigger trace of each event, is a complementary assessment of the detector stability along with the fridge temperature parameter. Although the mean base and fridge temperature parameters are highly correlated, there are two main

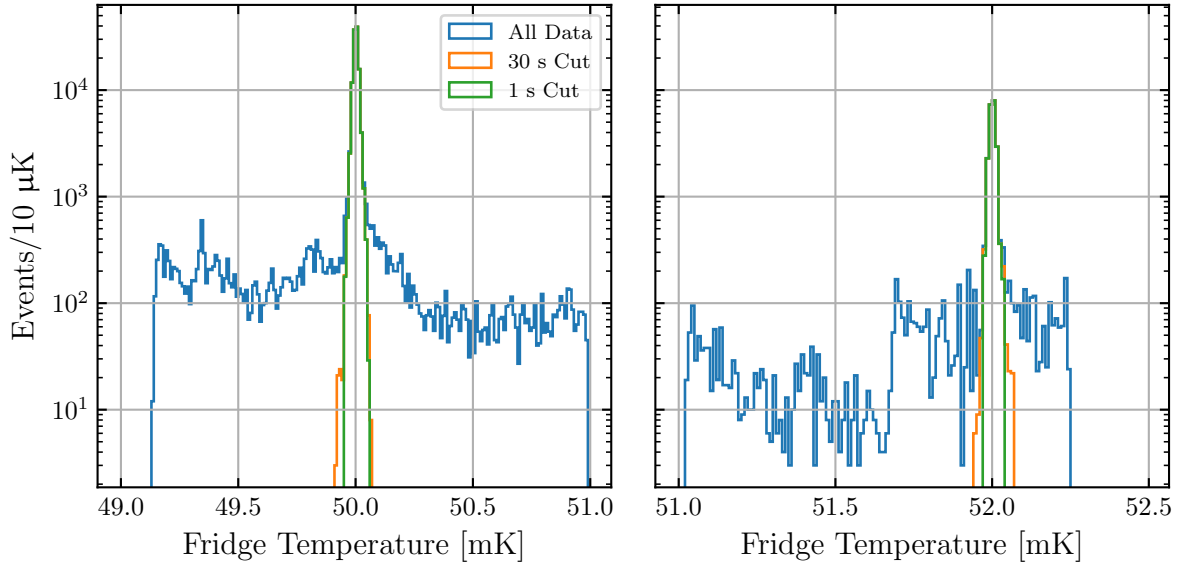


Figure 4.29: Distributions of the fridge temperature data from the stage-0 background data measured at 50 mK (left) and 52 mK (right). Distributions of the data are shown before the temperature cuts (blue), after the 30 s temperature cut (orange), and after the 1 s temperature cut (green). Courtesy of Yen-Yung Chang.

advantages with using the mean base to assess detector stability. First, the mean base is measured for each event compared to the 1 Hz readout of the fridge temperature parameter. Second, it is a better measure of the actual crystal temperature compared to the fridge temperature readout which can only estimate the crystal temperature based on the coldest stage of the ADR. These advantages mean that the mean base parameter is more sensitive to quick changes to the crystal temperature caused by, for example, a muon interaction with the detector. Even though the mean base is measured for each individual event, it can be used to develop a livetime cut by averaging the values over distinct periods of time. Therefore using the mean base parameter for a livetime cut removes periods of time when the detector is not in an ideal state for energy reconstruction, such as sitting on a long pulse tail of a prior high-energy event.

The absolute value of the mean base parameter is subject to a DC offset caused by the lock point of the SQUIDs, and therefore changed slightly each day when the SQUIDs were re-locked. Furthermore, there are a few instances where the SQUIDs spontaneously re-locked, or “jumped”, during data acquisition, and abruptly changed the nominal mean base value. To account for these effects, the mean base cut is performed separately on the dataset from each day, as well as separately for the laser-calibration and background datasets. In addition, only the difference between the mean base value for each event and the stable, nominal mean base value, denoted as Δ Mean Base, holds any physical information, and is therefore the parameter this cut is developed on.

The data that pass the temperature cut are binned in 1 s intervals, and the average Δ Mean Base value in each bin is calculated. A Gaussian function is then fitted to the distribution of averaged Δ Mean Base values, and the 1 s intervals that fall outside $\pm 2.5\sigma$ of the peak position from each day are removed. The value of $\pm 2.5\sigma$ is chosen because of the long, high-mean-base tails that exist in the Δ Mean Base

distributions. Figure 4.30 shows the Δ Mean Base values from a portion of the laser-calibration data, as well as the periods of time removed by the mean base cut.

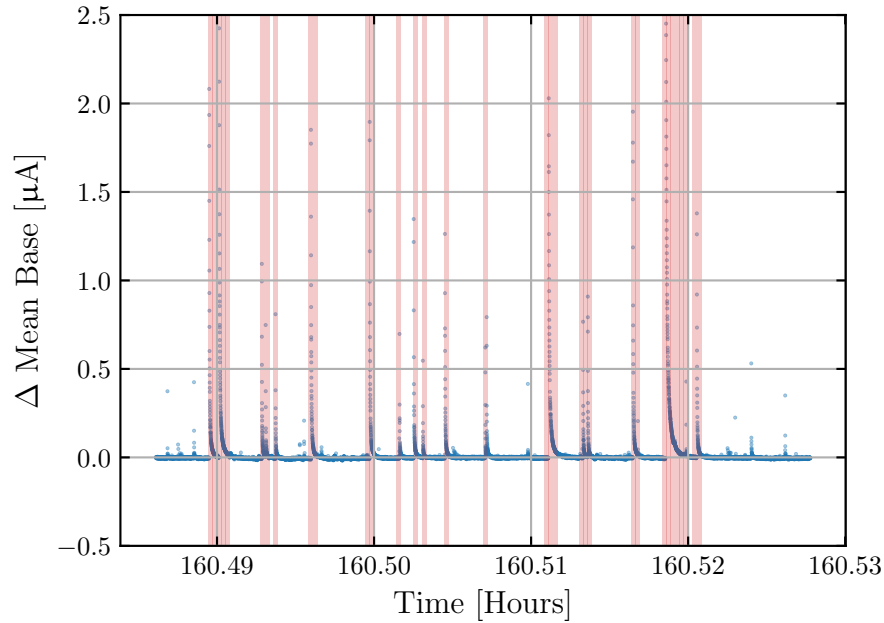


Figure 4.30: Difference between the mean base value and the nominal mean base value, Δ Mean Base, for a portion of laser-calibration data. The shaded regions correspond to periods removed by the mean base livetime cut. The elevated periods of mean base are due to high-energy cosmic ray interactions with the detector. Courtesy of Yen-Yung Chang.

Figure 4.30 illustrates how the mean base cut removes periods of time when the detector was not in an ideal state for energy reconstruction due to muon or similarly high-energy events. It also demonstrates that the 1 s time intervals used for this cut are sufficiently shorter than the mean base characteristic recovering time for these types of interactions. Finally, the frequency of high-energy events interacting with the detector is found to be ~ 0.2 Hz. The sources of these high-energy events likely include Compton scatters due to naturally occurring X-ray emitting radioisotopes such as ^{40}K , as well as cosmic muons. Figure 4.31 shows the distribution of Δ Mean Base before and after the mean base cut combined from each day of stage-0 background data measured at 50 and 52 mK.

As with the fridge temperature cut, for every 1 s bin in the stage-0 background data removed by the mean base cut, the corresponding 10 s interval is also assumed to be removed in order to calculate a conservative estimate of the livetime for the stage-0 background data. For the stage-2, fully unblinded data, this assumption is lifted and the cut is recalculated.

Trigger and Leakage Burst Cut

The DM signal models considered in this analysis are expected to have a uniform interaction rate with the detector over time. A series of many event triggers identified over a short period of time, called a burst, is not consistent with these models and therefore such periods of time should be removed. Two types of event burst cuts are applied to the data: (i) a *trigger* burst cut to remove noisy periods of time with a high trigger rate caused by environment instability, such as a cellphone ringing in the laboratory;

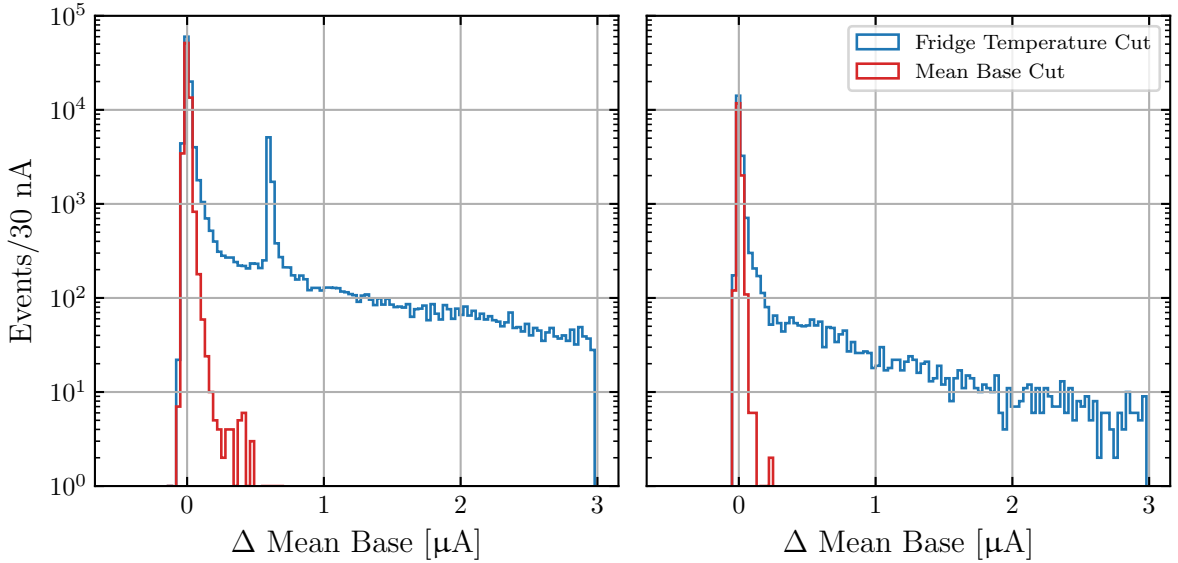


Figure 4.31: Distributions of Δ Mean Base from the data that pass the fridge temperature cut (blue) and the data that subsequently pass the mean base cut (red). The distributions are shown for the combined stage-0 background data measured at 50 mK (left) and 52 mK (right). Courtesy of Yen-Yung Chang.

and (ii) a *leakage* burst cut to remove periods of time with a high trigger rate caused by a high-energy particle hitting the detector or a nearby material leading to a series of excited states that decay within a short period of time. The procedure for the two cuts are very similar; the main difference is that the trigger burst cut calculates the trigger rate using all events, whereas the leakage burst cut calculates the trigger rate only using events $> 0.8 e^-h^+$ pairs. This energy constraint ensures that the trigger rate for the leakage burst cut is calculated from physical events rather than noise triggers. The cuts described in this sub-section are applied to the background datasets, but not the laser-calibration datasets due to the expectantly high trigger rates and the TTL coincident trigger that is used to identify laser events.

The trigger rates are calculated using a binning procedure that is dynamically adjusted based on the data in each series in order to accommodate variations in the nominal trigger rate over time. As mentioned in Sec. 4.2.2, each series in the background data corresponds to 1 hour of data acquisition. The bin size in each series is calculated so that twice the mean number of events within each time bin is equivalent to seven standard deviations assuming Poisson statistics. More formally, for a bin size of t and a nominal trigger rate of Γ , the mean number of events per bin is $\lambda = \Gamma t$ and the standard deviation is $\sigma = \sqrt{\lambda} = \sqrt{\Gamma t}$. Imposing the aforementioned condition therefore gives

$$n\Gamma t = m\sqrt{\Gamma t}, \quad (4.16)$$

where $n = 2$ and $m = 7$. Solving for t gives

$$t = \frac{m^2}{n^2\Gamma}. \quad (4.17)$$

Equation 4.17 ensures that an observed trigger rate of twice the nominal trigger rate is rejected at a 7σ level. Furthermore, it balances the need for finer binning to minimize the livetime loss with having course enough binning necessary to calculate trigger rates that are less subject to statistical fluctuations.

The trigger burst cut is determined by first determining the nominal trigger rate in each series and then using Eq. 4.17 to find the time bin size. After calculating the trigger rates with the new binning, time bins that are $> 3\sigma$ above the mean rate are removed. Assuming Poisson statistics, the cut threshold Γ_c for each series is given by

$$\begin{aligned}\Gamma_c &= \frac{\lambda}{t} + 3\frac{\sigma}{t} \\ &= \Gamma + 3\sqrt{\frac{\Gamma}{t}}.\end{aligned}\tag{4.18}$$

Additionally a flat cut is applied by removing any time bin from any series that exceeds 15 Hz. The leakage burst cut follows the same procedure as the trigger burst cut, except that the only events used to calculate the trigger rates are those that are $> 0.8 e^-h^+$ pairs in energy and that pass a cut on $\chi^2(f)$ from the inner, outer, and total channels using a constant cut-off value. The leakage burst cut also applies a flat cut, but does so by removing time bins that exceed 10 Hz. The flat-cut values of 15 and 10 Hz are chosen based on prior knowledge of typical event rates seen by this and similar detectors. Lastly, the combined result of the trigger and leakage burst cuts is the removal of the time bins that are rejected by either cut.

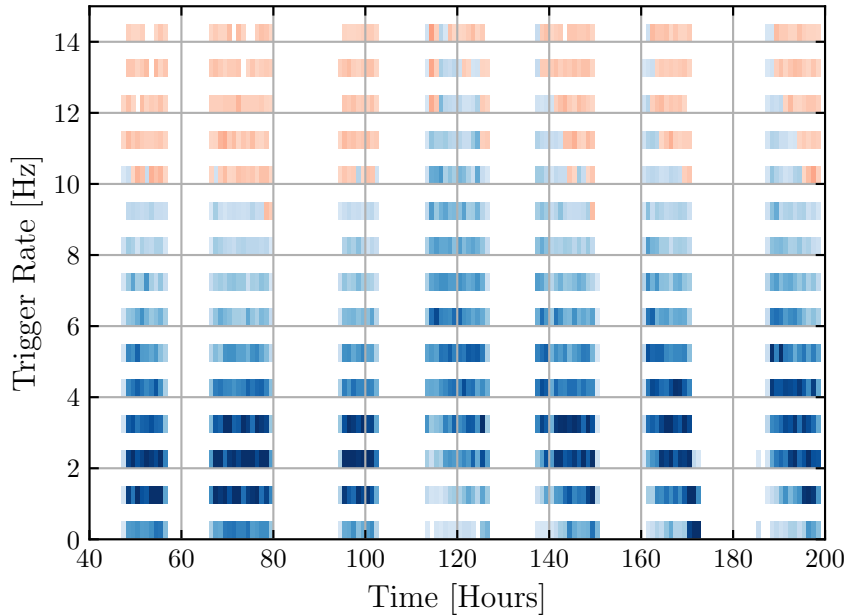


Figure 4.32: Density map of the time bins and their corresponding trigger rates over time calculated for the *trigger burst cut* from the stage-0 background data measured at 100 V. Each slice in the density map relates to one hour of data acquisition. The blue and red slices show the time bins that pass and fail the trigger burst cut, respectively. Slices with a darker shade indicate a greater number of time bins within that slice.

A modified approach to the trigger and leakage burst cuts is required due to the temporal blinding scheme used in this analysis. Because the stage-0 background data contains only the first of every ten seconds, the dynamic binning procedure would underestimate the trigger rates if the bin size is larger than one second. Furthermore, simply removing the dead time in each ten second interval could artificially introduce periods of higher or lower trigger rates. Therefore to accommodate the blinding scheme for the stage-0 background data, the calculated bin size is constrained to $t \leq 1$ s. For the stage-1 background data, the bin size is similarly constrained to $t \leq 3$ s. Finally for the stage-2, fully unblinded data, no constraints are imposed on the binning calculation. Typical bin sizes computed using this dynamic binning procedure for the unblinded background data are 3–4 s. Figure 4.32 shows the density map of the time bins and their corresponding trigger rates calculated for the trigger burst cut from the 100 V stage-0 background data.

Figure 4.33 shows the density map of the time bins and their corresponding trigger rates calculated for the leakage burst cut from the 100 V stage-0 background data. An interesting point of comparison between Fig. 4.32 and 4.33 is the observed decrease in the average trigger rates over time on certain days of data acquisition when calculated for the trigger burst cut. In the stage-0 background data, same decrease is not observed when the trigger rates are calculated for the leakage burst cut, which suggests that there was elevated environmental noise activity during the start of data acquisition on certain days.

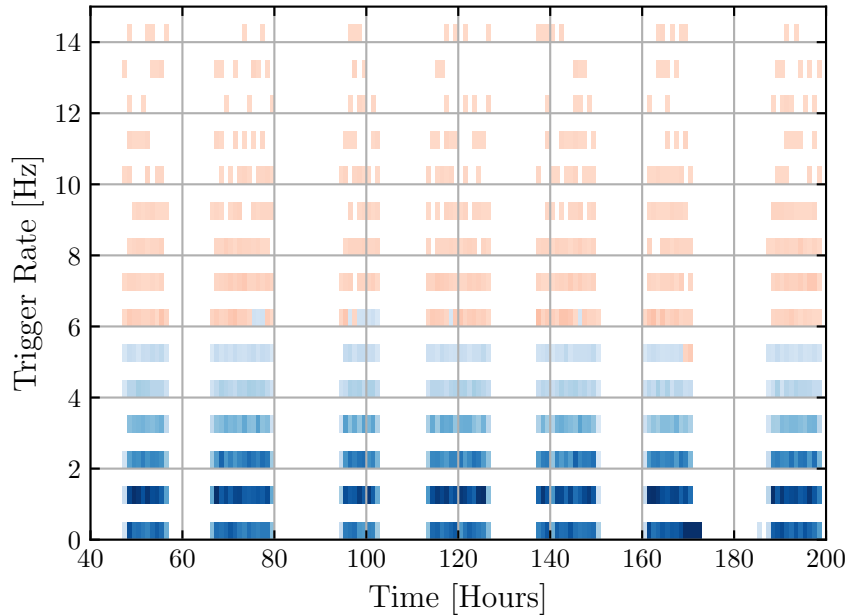


Figure 4.33: Density map of the time bins and their corresponding trigger rates over time calculated for the *leakage burst cut* from the stage-0 background data measured at 100 V. The only events used to calculate the trigger rates are those that are $> 0.8 e^-h^+$ pairs in energy and that pass a cut on $\chi^2(f)$ from the inner, outer, and total channels using a constant cut-off value. Each slice in the density map relates to one hour of data acquisition. The blue and red slices show the time bins that pass and fail the leakage burst cut, respectively. Slices with a darker shade indicate a greater number of time bins within that slice.

In order to verify that the trigger and leakage burst cuts perform equally on the stage-0 background data and the stage-2 background data, the cuts are also applied to the ^{57}Co -calibration data measured at

60 V twice. First, the cuts are applied after artificially blinding the data to mimic the blinding scheme of the stage-0 background data. Second, the cuts are applied again to the entire ^{57}Co -calibration dataset. Fig. 4.34 shows a comparison between the density maps of the time bins and their corresponding trigger rates calculated for the leakage burst cut with and without the artificial blinding scheme applied.

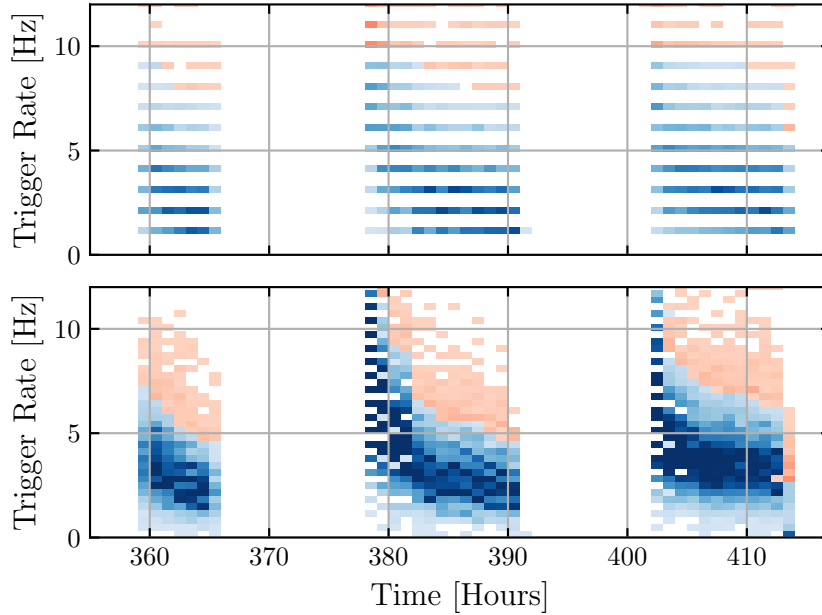


Figure 4.34: Density map of the time bins and their corresponding trigger rates over time calculated for the leakage burst cut from the ^{57}Co -calibration data measured at 60 V. The top plot shows the trigger rates calculated using only 10 % of the data with the artificial blinding scheme, whereas the bottom plot shows the trigger rates calculated using all of the data. Each slice in the density map relates to one hour of data acquisition. The blue and red slices show the time bins that pass and fail the leakage burst cut, respectively. Slices with a darker shade indicate a greater number of time bins within that slice.

Figure 4.34 shows that the leakage burst cut is at least qualitatively similar after the data is “unblinded”, and similar trends in the trigger rate over time are observed. For a more quantitative verification, the average trigger rate, passage fraction, and percent of livetime lost are measured for when the cut is applied to the data with and without the artificial blinding scheme. Table 4.3 lists these quantities for both the trigger and leakage burst cuts, and shows the percent difference in each quantity after the data is “unblinded”.

The actual values of the quantities calculated from the ^{57}Co -calibration data are not necessarily expected to be similar to those from the background data; however it is important to check whether there is a significant change in the performance of these cuts after unblinding the data. Overall as Tab. 4.3 shows, the changes to these quantities after the ^{57}Co -calibration data are “unblinded” is small, with most values changing by less than 10 %. The only exception is the percentage of livetime lost for the leakage burst case. However it should be noted that the absolute change in this quantity, 0.5 percentage points, is a small effect. Therefore despite the binning constraints to accommodate the blinding scheme, the trigger and leakage burst cuts can justifiably be used on the background data after unblinding.

Table 4.3: Comparison of quantities after applying the trigger and leakage burst cuts to the ^{57}Co -calibration data measured at 60 V. The same quantities are shown for when the cuts are applied using 10% of the data with the artificial blinding scheme, as well as when the cuts are applied using the full dataset.

Trigger Burst Cut			
Quantity	10% Dataset	Full Dataset	Percent Difference
Average Trigger Rate	11.3 Hz	11.1 Hz	-1.8 %
Passage Fraction	41.5 %	44.3 %	6.7 %
Livetime Lost	36.4 %	34.4 %	-5.5 %
Leakage Burst Cut			
Quantity	10% Dataset	Full Dataset	Percent Difference
Average Trigger Rate	4.1 Hz	3.9 Hz	-4.9 %
Passage Fraction	91.7 %	92.1 %	0.4 %
Livetime Lost	4.2 %	4.7 %	11.9 %

Summary of Livetime Cuts

Figure 4.35 summarizes the results of the livetime cuts by showing the energy spectrum after each cut is successively applied to both the laser-calibration and stage-0 background data measured at 60 and 100 V. The laser-calibration data do not have the trigger or leakage burst cuts applied to them, and instead are filtered for events that are coincident with the laser TTL trigger. The final spectra of the background and laser-calibration data that pass all of the livetime cuts define the “science exposure” and “livetime selection” datasets, respectively. The calculated livetime as well as the breakdown of the livetime lost due to each cut are summarized in Sec. 4.5.

Figure 4.35 shows that the livetime cuts are relatively independent of energy, with two prominent exceptions. First, the laser TTL trigger coincidence filter applied to the laser-calibration data has a higher rejection rate at energies below $1 e^-h^+$ pair as a result of discarding events from noise triggers. Second, the trigger and leakage burst cuts applied to the 60 V stage-0 background data also have a higher rejection rate at energies below $1 e^-h^+$ pair. This is likely due to a significant amount the noise bursts that occurred during the acquisition of this data. The following sub-section describes the data-quality cuts that are applied to the science exposure and livetime selection datasets.

4.4.2 Data-Quality Selection Criteria

The DQ cuts are used to select the events whose trace matches that of an idealized event. This sub-section describes five categories of DQ cuts: (i) a trigger offset cut to reject events caused by noise triggers and pulses affected by pile-up; (ii) a mean base cut to reject events that were measured on the tail of a pulse from a prior high-energy event; (iii) two χ^2 cuts to reject pile-up events and pulses with shapes unlikely to be caused by DM; (iv) a veto detector cut to reject events that are coincident with a trigger from the veto detector; and (v) a partition cut to reject events that occurred in the outer channel of the detector. Because the partition cut cannot be successfully implemented, this analysis uses only the four previously mentioned DQ cuts to select for good events.

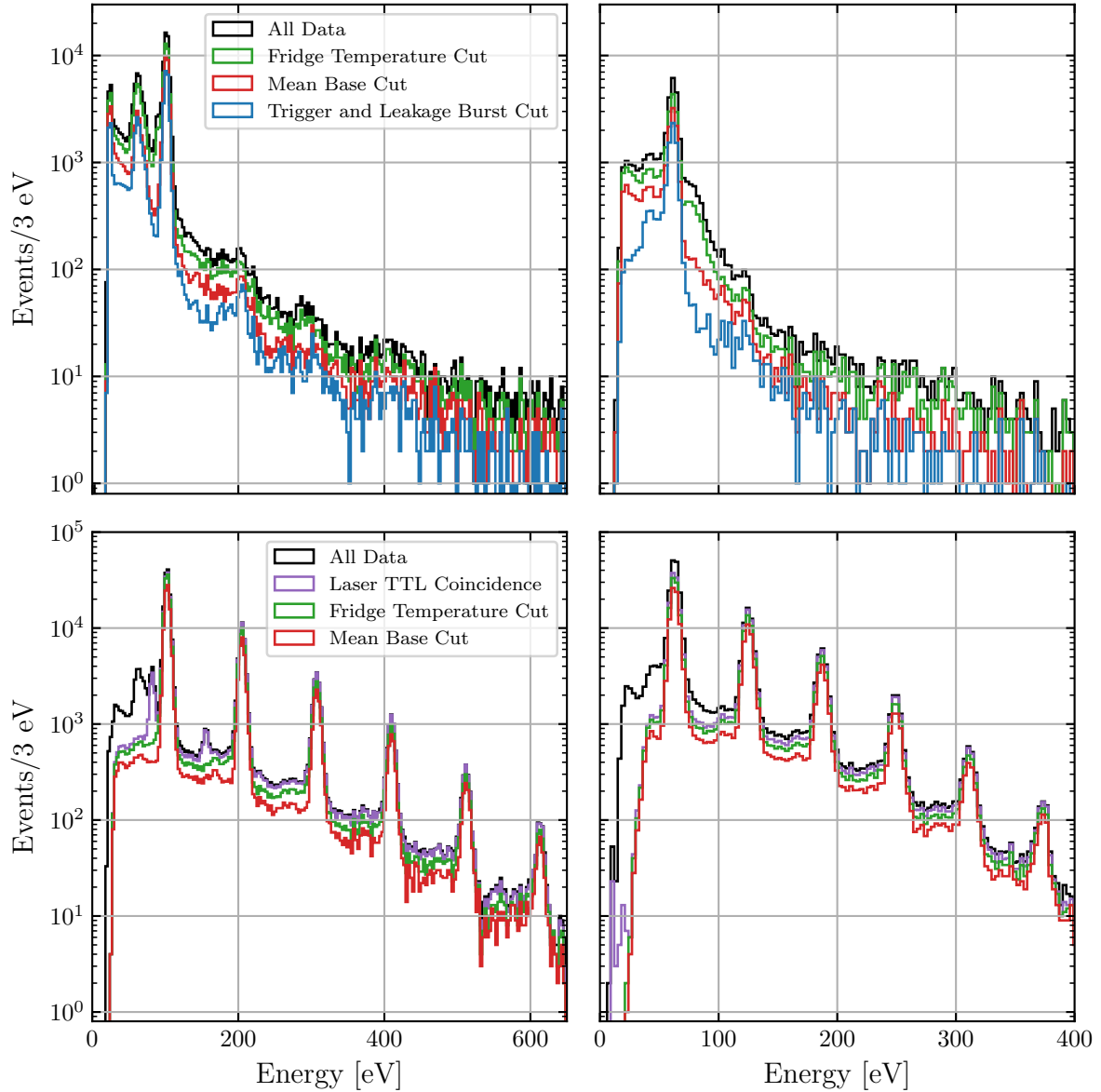


Figure 4.35: Summary of the energy spectra produced after successively applying the livetime cuts to the stage-0 background data (top) and laser-calibration data (bottom) measured at 100 V (left) and 60 V (right). The laser-calibration spectra do not have the trigger and leakage burst cuts applied, but the data is filtered for events coincident with the laser TTL trigger. The final spectra of the background and laser-calibration data that pass all of the livetime cuts define the “science exposure” and “livetime selection” datasets, respectively.

Trigger Offset Cut

The main energy estimator in this analysis is the OF amplitude A of the total channel, such that the OF algorithm allows for a time offset t_0 between the trigger time and the time which, along with A , minimizes $\chi^2(f)$. This method allows the OF algorithm to compensate for any trigger time offsets, and leads to better energy reconstruction. However in situations where the raw trace has peaks of comparable heights as the main event pulse, such as pile-up events and low-energy events with a low

signal-to-noise ratio, the OF algorithm can falsely assign the value of t_0 due to its bias toward higher peaks. Therefore the cases where the OF algorithm erroneously fits to a pile-up pulse or a noise peak are generally associated with larger t_0 values, whereas good pulses have small values of t_0 .

The trigger offset cut uses the laser-calibration data that pass the livetime cuts defined in the previous section and are coincident with the laser TTL trigger. A Gaussian function is fit to the distribution of t_0 separately for the 60 and 100 V datasets, and the best-fit mean value and standard deviation σ are extracted. Events with t_0 outside of $\pm 3\sigma$ of the mean are rejected. Figure 4.36 shows the distribution of t_0 from the 60 V and 100 V data, as well as the $\pm 3\sigma$ cut thresholds. The corresponding distributions from the stage-0 science exposure datasets are also seen in Fig. 4.36. Finally for comparison, the distributions of t_0 from the laser-calibration data that pass the livetime cuts but have not been filtered for events coincident with the laser TTL trigger are shown.

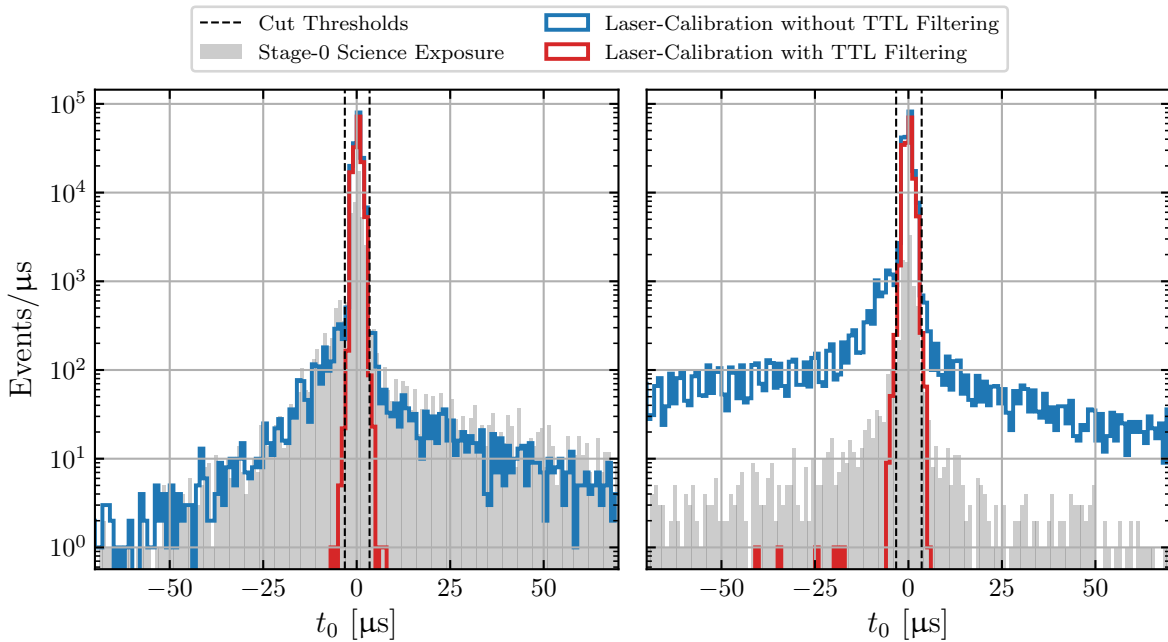


Figure 4.36: Distributions of the trigger offset t_0 for the data measured at 100 V (left) and 60 V (right). The distributions are shown for the laser-calibration data that pass the livetime cuts with (red) and without (blue) filtering for events that are coincident with the laser TTL trigger. The gray, shaded distributions are the stage-0 science exposure datasets. The dashed, vertical lines are the $\pm 3\sigma$ trigger offset cut thresholds. Courtesy of Yen-Yung Chang.

The trigger delay cuts for the 60 and 100 V data are subsequently applied to the corresponding stage-0 science exposure datasets. The widths $\sigma \sim 1 \mu\text{s}$ of fitted Gaussian functions are in good coincidence with the timing resolution set by the digitization rate of 1.51 MHz. It is also interesting to note that the width of the t_0 distributions are inversely proportional to A , and thus to the reconstructed energies. As a result, the cut threshold choices of $\pm 3\sigma$ implicitly impact the energy thresholds for this analysis. This is reflected in the cut efficiency calculation described in Sec. 4.5.

Mean Base Cut

The mean base parameter can identify events that were measured on the pulse of a prior high-energy event. Unlike the livetime mean base cut described in Sec. 4.4.1, which takes averages of the mean base parameter over time intervals, the DQ mean base cut is performed on an event-by-event basis. Due to slight differences in the SQUID lock point of each day, instances of spontaneous SQUID re-locking, temperature-related shifts, and general discrepancies between the laser-calibration and background data, the nominal mean base value for each dataset differs. Therefore the DQ mean base cut is developed and applied to the dataset acquired from each day, as well as the laser-calibration and background datasets, separately. A Gaussian function is fitted to the mean base distribution from each dataset, and the mean and standard deviation σ are extracted. Events that are outside of $\pm 3\sigma$ of the mean value are rejected. Figure. 4.37 shows the mean base distributions for the laser livetime selection and stage-0 science exposure datasets from one day of data acquisition, as well as the corresponding cut thresholds.

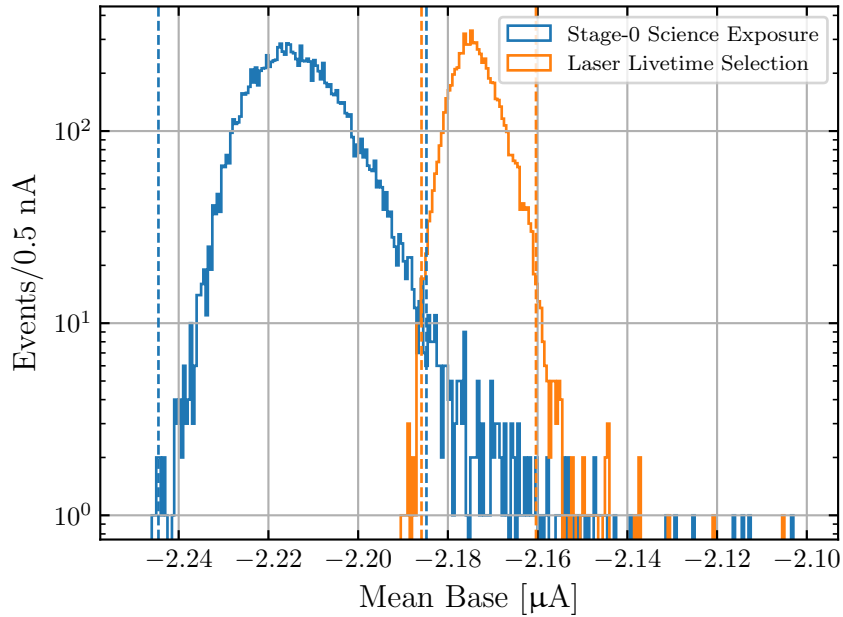


Figure 4.37: Distributions of the mean base parameter for the laser livetime selection (orange) and stage-0 science exposure (blue) datasets from one day of data acquisition. The dashed, vertical lines are to the $\pm 3\sigma$ cut thresholds of the dataset of matching colour. Courtesy of Yen-Yung Chang.

Although there is a lot of redundancy between the livetime and DQ versions of the mean base cut, the DQ cut is able to reject individual events with an outlying mean base value that are missed by the livetime cut. There are also noticeable difference between the mean base distributions from the laser-calibration and background datasets. The distributions from the background datasets tend to be wider, which is likely due to the greater temperature variation that occurred during the acquisition of background data. Furthermore, the laser-calibration datasets tend to be shifted to slightly higher mean base values. One possibility for these observed shifts is due to the laser pulses directly hitting the QET channels that caused the photon absorption offsets described in Sec. 4.3.4. The photons that were directly absorbed by the QETs may have produced a slight heating effect in the TESs, thereby increasing the nominal mean base value of the detector.

χ^2 Cut

The quality of the pulse from each event is assessed using two goodness-of-fit parameters: (i) $\chi^2(f)$, which measures the goodness-of-fit of the fitted pulse template in the frequency domain and is also the quantity minimized in the OF algorithm; and (ii) $\chi^2(t)$, which measures the goodness-of-fit of the same fitted pulse template but in the time domain. Both of these parameters are used to produce two separate goodness-of-fit cuts. Although the cuts appear to be similar, they serve distinct purposes. The $\chi^2(f)$ cut is better able to assess how well the shape of a given pulse matches with the expected pulse template and ensures the correct evaluation of pulse amplitudes and therefore of event energies. Conversely the $\chi^2(t)$ cut is more sensitive to phase shifts or temporal misalignment in the pulses that are hard to observe in the frequency domain, and can therefore be a better identifier of pile-up events. The cuts are developed using the events from the calibrated laser-calibration data coincident with the laser TTL trigger, and are subsequently applied to the background data.

The $\chi^2(f)$ and $\chi^2(t)$ cut thresholds allow for a slight energy dependence. The energy dependence in the χ^2 parameters comes from small variations in the pulse shape at higher energies due to small amounts of saturation. The procedure to implement the two cuts are identical. First, a distribution of the $\chi^2(f)$ or $\chi^2(t)$ is constructed at each e^-h^+ -pair peak observed in the data. A Gaussian function is then fitted to each peak, and the mean μ and standard deviation σ values are extracted. The $\chi^2(f)$ and $\chi^2(t)$ distributions at each e^-h^+ -pair peak are not exactly Gaussian due to the extended tails of high $\chi^2(f)$ or $\chi^2(t)$ values, and therefore the fits exclude the data that constitute these extended tails. The energy-dependent cut thresholds $C(E)$ are determined by considering the $\chi^2(f)$ and $\chi^2(t)$ points 3σ above μ at each e^-h^+ -pair peak. The points are fitted to the equation

$$C(E) = a \cdot E^b + c, \quad (4.19)$$

where a , b , and c are fit parameters. The parameter b is allowed to float in order to allow for an arbitrary energy dependency. Equation 4.19 is fit to the points $\mu + 3\sigma$ at each e^-h^+ -pair peak at energy E . Figure 4.38 shows a scatter plot of the $\chi^2(f)$ and $\chi^2(t)$ values over energy from the 100 V laser-calibration data, as well as the fitted $C(E)$ curves. Table 4.4 lists the results from fitting Eq. 4.19 to the $\chi^2(f)$ or $\chi^2(t)$ data from the 60 and 100 V laser-calibration data.

Table 4.4: Results from fitting Eq. 4.19 to the points $\mu + 3\sigma$ at each e^-h^+ -pair peak at energy E from the $\chi^2(f)$ and $\chi^2(t)$ laser-calibration data. The results are shown separately for the data measured at 60 and 100 V.

Parameter	60 V		100 V	
	$\chi^2(f)$	$\chi^2(t)$	$\chi^2(f)$	$\chi^2(t)$
a [eV $^{-b}$]	$(0.5 \pm 2.3) \times 10^{-12}$	$(0.5 \pm 1.5) \times 10^5$	$(2 \pm 7) \times 10^{-11}$	$(5 \pm 5) \times 10^{-6}$
b	3.8 ± 0.7	1.6 ± 0.6	3.0 ± 0.4	1.5 ± 0.2
c	0.1674 ± 0.0001	1.028 ± 0.006	0.1669 ± 0.0001	1.014 ± 0.001

Figure 4.38 and Tab. 4.4 show a slight energy dependence on the $\chi^2(f)$ and $\chi^2(t)$ parameters over the region of interest for this analysis (six e^-h^+ pairs). Moreover, there is a greater energy dependence in the $\chi^2(f)$ parameter compared to $\chi^2(t)$. This suggests that deviations from the expected pulse shape

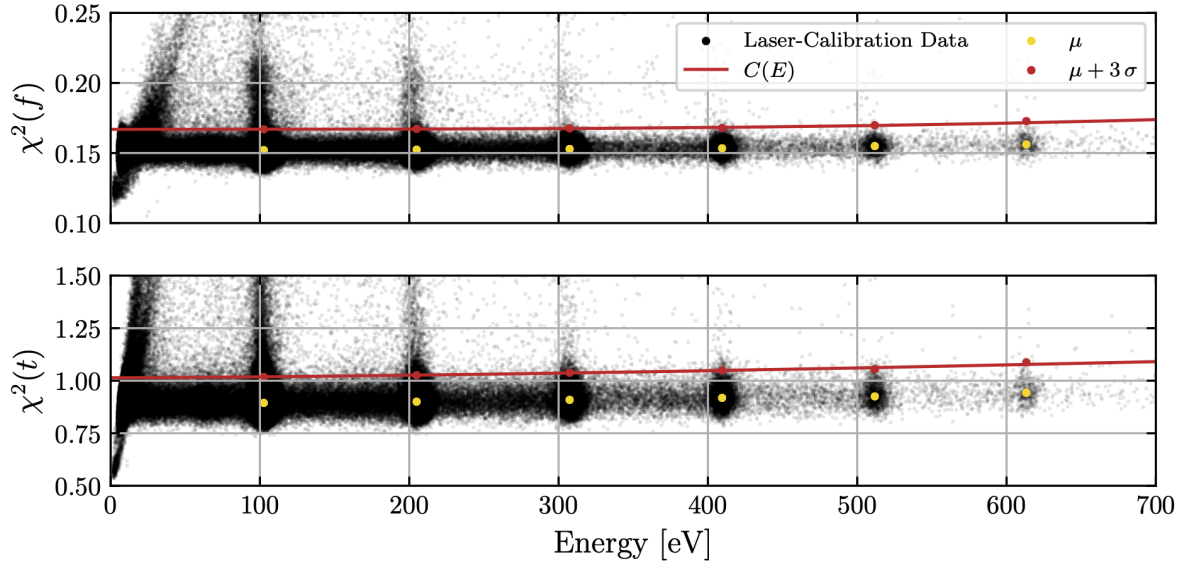


Figure 4.38: Scatter plot of the $\chi^2(f)$ (top) and $\chi^2(t)$ (bottom) data from the laser-calibration data measured at 100 V. The yellow points correspond to the fitted mean value μ from the $\chi^2(f)$ or $\chi^2(t)$ distribution at each e^-h^+ -pair peak. The red points correspond to the $\mu + 3\sigma$ value at each e^-h^+ -pair peak used to determine the cut thresholds. The red curves are the fitted cut threshold curves $C(E)$ described by Eq. 4.19. Courtesy of Valentina Novati.

that occur at high energies have greater impact in the frequency domain compared to the time domain. Additionally the fitted parameters from the 60 V data show a slightly larger energy dependence compared to those from the 100 V data. Although the cause of this is unknown, it may be related to differences in the events at comparable energies. At ~ 420 eV, the 60 V data are measuring events comprised of 7 absorbed photons, whereas the 100 V data are measuring events comprised of only 4 absorbed photons. If the pulse shape depends on the positional spread of photons, there would be a larger spread in the χ^2 parameter in the 60 V data.

Figure 4.39 compares the result of the $\chi^2(f)$ and $\chi^2(t)$ cuts on the 100 V data relative to one another. The top plot shows the scatter plot of $\chi^2(f)$ over energy from both the entire dataset and from the data that pass the $\chi^2(t)$ cut, and shows the $C(E)$ curve for the $\chi^2(f)$ data. Conversely, the bottom plot shows the scatter plot of $\chi^2(t)$ over energy from both the entire dataset and from the data that pass the $\chi^2(f)$ cut, as well as the $C(E)$ curve for the $\chi^2(t)$ data.

As observed in Fig. 4.39, although nearly all the events that pass the $\chi^2(t)$ also pass the $\chi^2(f)$ cut, there are a significant number of events that pass the $\chi^2(f)$ cut but do not pass the $\chi^2(t)$ cut, particularly at low energies. Figure 4.40 shows two examples of traces that pass the $\chi^2(f)$ cut yet are rejected by the $\chi^2(t)$ cut. This select group of events is primarily comprised of pile-up events and events measured on the tail of a prior high-energy event. For these events, a nearby pulse or a high-energy tail correspond to low-frequency components of the trace in frequency space which are highly suppressed by the OF algorithm. The $\chi^2(f)$ cut is therefore not sensitive enough to reject traces with these types of deviations. Conversely because the expected pulse shape has a flat baseline and only one pulse, traces with these types of deviations are rejected by the $\chi^2(t)$ cut.

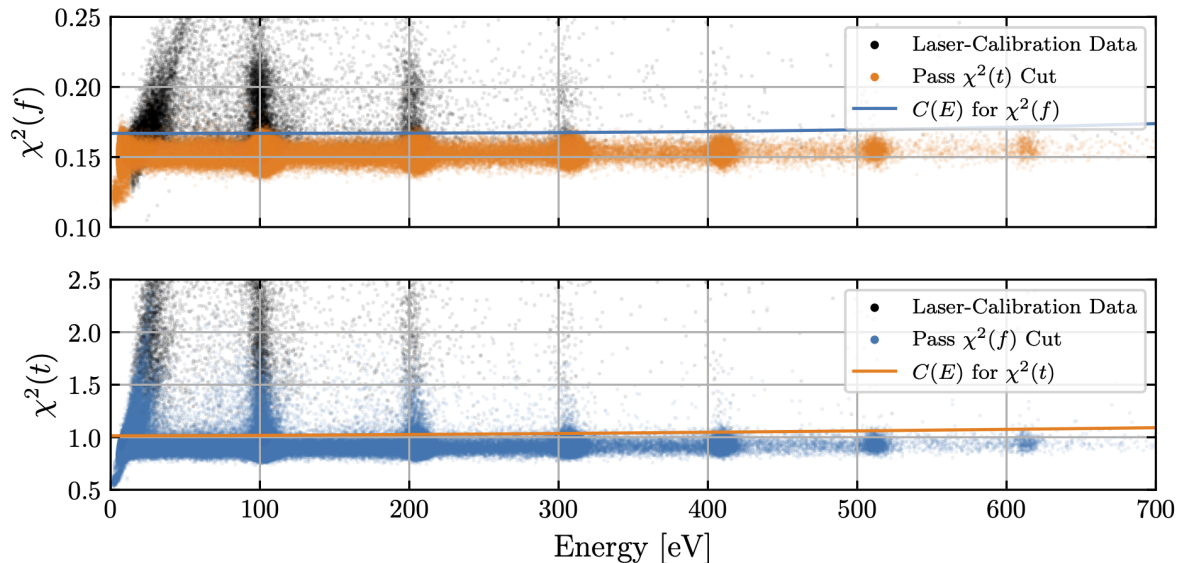


Figure 4.39: Top: scatter plot of the $\chi^2(f)$ data from the laser-calibration dataset measured at 100 V. Events that pass the $\chi^2(t)$ cut are shown in orange, and the blue curve is the fitted cut threshold curve $C(E)$ described by Eq. 4.19 for the $\chi^2(f)$ cut. Bottom: scatter plot of the $\chi^2(t)$ data from the laser-calibration dataset measured at 100 V. Events that pass the $\chi^2(f)$ cut are shown in blue, and the orange curve is the fitted cut threshold curve $C(E)$ described by Eq. 4.19 for the $\chi^2(t)$ cut. Courtesy of Valentina Novati.

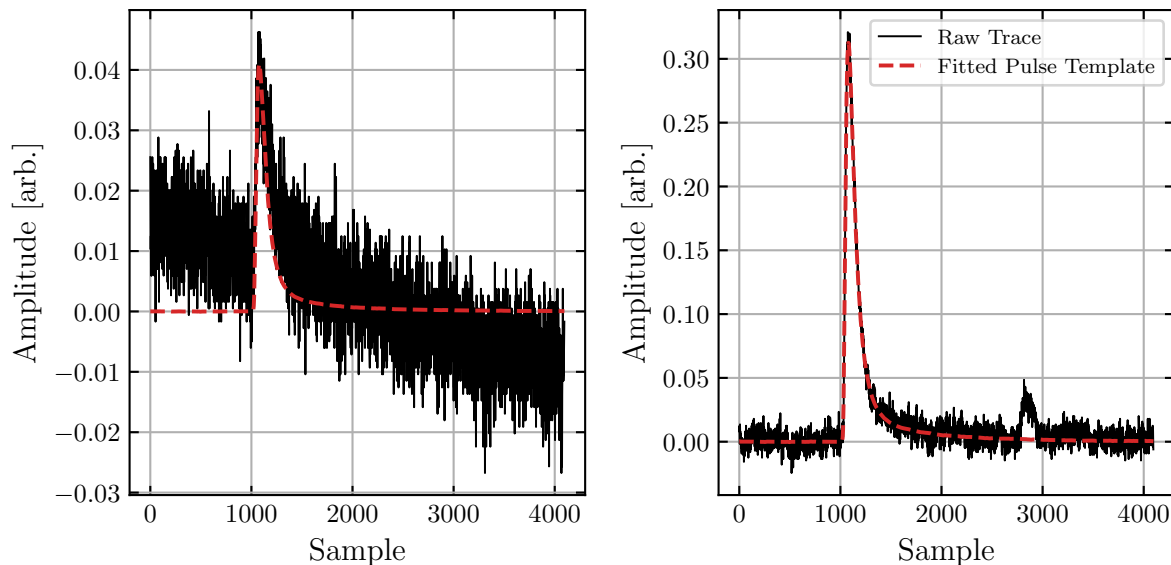


Figure 4.40: Examples of the traces from events that pass the $\chi^2(f)$ cut but are rejected by the $\chi^2(t)$ cut. These types of events are typically events measured on the tail of a prior high-energy event (left) or a pile-up event with multiple pulses in the trace (right). The dashed curves show the fitted pulse template for each event.

Veto Detector Cut

As mentioned in Sec 4.2, this experiment ran with a veto detector adjacent to the main HVEV detector that is composed of a single TES. Although this individual TES is unaffected by energy depositions in

the main detector, it is sensitive to electronic noise coupled with the readout system shared by both detectors. The purpose of the veto detector cut is to identify and reject events that are coincident in both the HVEV and veto detector that are caused by either noise triggers from the electronic readout system or external events such as telegraph noise bursts and cosmic-ray-induced particle bursts.

For every event that caused a trigger in the HVEV detector, the OF amplitude A_0 is measured from the trace from the veto detector. Recall that A_0 is the OF amplitude using a fixed time or, said differently, with no time offset from the triggered time. Therefore the A_0 values from the veto detector, A_0^V , are computed at the times coincident with the triggered events from the HVEV detector. A distribution of the A_0^V values are constructed in order to identify the events with coincident pulses in both detectors. A Gaussian function is fitted to the A_0^V distribution and the mean value and standard deviation σ are extracted. Events with a coincident pulse amplitude that is $> 3\sigma$ above the mean are rejected. The cut threshold is determined by the laser livetime selection data and is subsequently applied to the background data. Figure 4.41 shows the distribution of A_0^V values from the laser livetime selection and stage-0 science exposure datasets measured at 100 V.

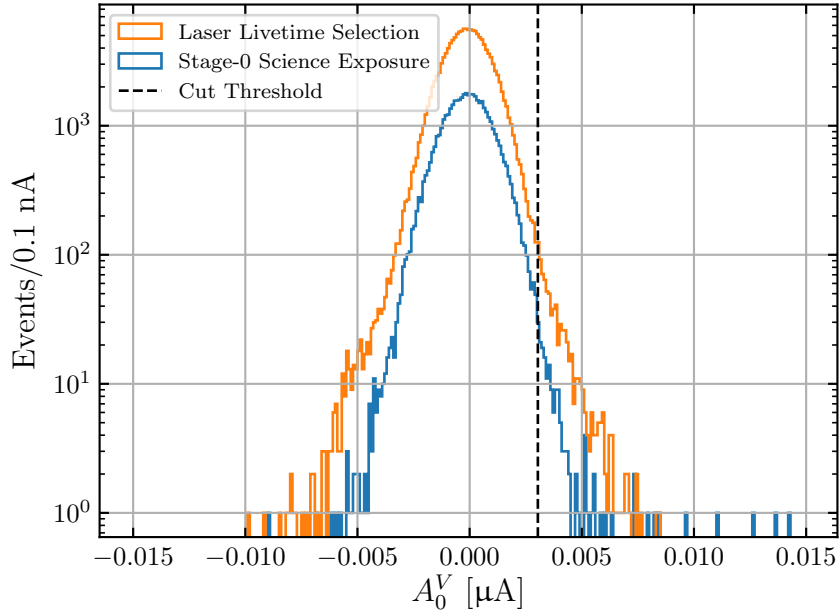


Figure 4.41: Distributions of the OF amplitudes measured from the veto detector traces when triggered by an event in the HVEV detector, A_0^V , from the laser livetime selection (orange) and stage-0 science exposure (blue) datasets measured at 100 V. The dashed, vertical line corresponds to the 3σ cut threshold. Courtesy of Yen-Yung Chang.

The absolute energy scale of the pulses from the veto detector are irrelevant for this analysis, and thus A_0^V is not calibrated to a true energy. The cut seen in Fig. 4.41 has no correlation with energy, and is consistent with randomly rejecting events at a sub-percent level. As described in Sec. 4.2, the veto detector has a critical temperature of $T_c = 52$ mK and therefore was inoperable on the days of data acquisition when the detectors were operated at 52 mK. This means that the veto detector cut is applied only to the data that were measured at 50 mK, which include all the data measured at 100 V and one day of data measured at 60 V.

Partition Cut

The HVEV detector was designed with two channels in order to extract the positional information of events. The goal within this analysis is to use this position information to reject events that are effected by the sidewalls of the detector and therefore to improve the final event spectra used for producing the limit results. As will become evident, the partition cut is not ultimately used in the analysis. But because the two-channel design of the HVEV Run 2 detector is a large point of emphasis, the details of this cut are still provided here.

The type of events that could be removed include those whose liberated e^-h^+ pairs reach a detector sidewall before reaching the top or bottom surface of the detector thus lowering the total energy measured, and leakage events that are caused by imperfections in the sidewalls themselves. The positional information of events is measured by the channel partition. For each event, the OF amplitudes of the inner and outer channels, A_I and A_O , respectively, are used to calculate the partition, defined as

$$\text{Partition} = \frac{A_I - A_O}{A_I + A_O}. \quad (4.20)$$

Therefore events whose energy is all measured in the inner channel will have a partition of +1, whereas events whose energy is all measured in the outer channel will have a partition of -1. A cut to remove events that originated in the outer channel region is done by rejecting events with a partition closer to -1.

As a partition cut is a DQ cut, the cut efficiency must be calculated. Unfortunately the laser-calibration data are insufficient for this purpose because the laser is pointed directly at the inner channel and thus the partition from laser-calibration events are heavily biased toward a partition of +1. The DM candidates are conversely expected to interact uniformly within the detector and not exhibit such a partition bias. The ^{57}Co -calibration data are instead used to develop the partition cut and calculate the cut efficiency.

The main decay mode of ^{57}Co of interest for this analysis is the electron capture to the 136.47 keV ^{57}Fe excited state and the subsequent emission of 122 keV gammas due to de-excitation [146]. Photons of this energy will predominantly interact with the Si detector through Compton scattering with a mean-free-path of ~ 3 cm, larger than the size of the detector. The energy depositions are therefore obtained over a broad energy range and events are uniformly distributed throughout the detector, thereby making a suitable source of data to study the position dependence and partition. ^{57}Co -calibration data were acquired with an applied bias voltage of 0 and 60 V. Because the Compton energy spectrum extends much further than the detector saturation level (~ 1 keV in the measured phonon energy), acquiring the ^{57}Co -calibration data at 60 V compared to 100 V allows for a greater number of unsaturated events to be measured. The 0 V ^{57}Co -calibration data is not applicable for this study because of the different mechanisms for measuring energy depositions. Therefore the cut is developed using the 57 hours of 60 V ^{57}Co -calibration data only.

The ^{57}Co -calibration data are first calibrated in energy to the number of e^-h^+ pairs n_{eh} . Good events are then selected by applying a series of cuts: (i) a fridge temperate cut developed separately from the ^{57}Co -calibration data; (ii) a trigger offset cut using the same threshold values obtained from the laser-calibration data; (iii) an event-by-event mean base cut developed for each day of ^{57}Co -calibration data; (iv) a $\chi^2(f)$ and $\chi^2(t)$ cut using the same thresholds obtained from the laser-calibration data; and

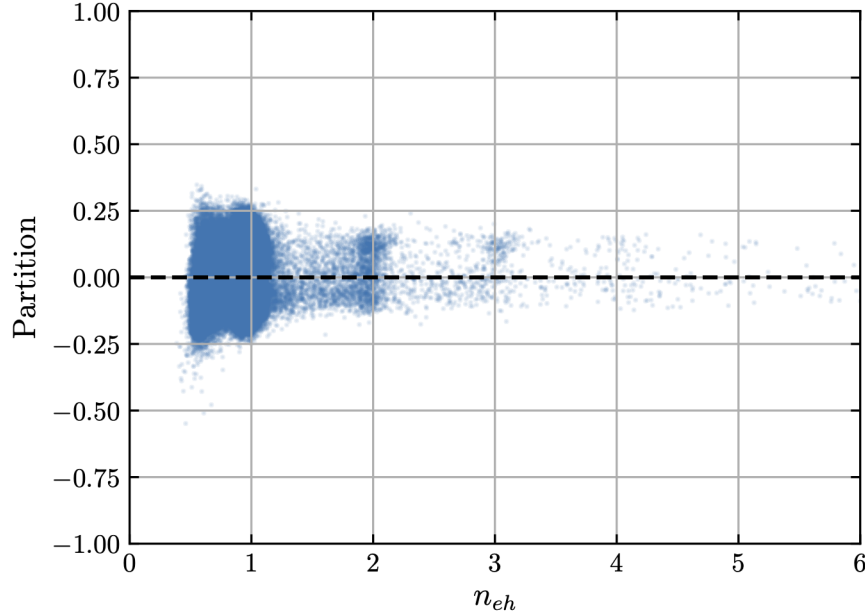


Figure 4.42: Channel partition versus number of e^-h^+ pairs n_{eh} for events from the ^{57}Co -calibration data that pass the series of quality cuts. The partition is defined by Eq. 4.20; events with a partition closer to +1 (-1) correspond to a greater proportion of the measured energy in the inner (outer) channel. The black, horizontal line indicates equal energy deposition in both channels.

(v) a veto detector cut developed separately from the ^{57}Co -calibration data. The partition values from the remaining events that pass all of the cuts are calculated and shown in Fig. 4.42.

The events in Fig. 4.42 are relatively uniform in partition, as expected for the ^{57}Co -calibration data. Using the easiest example, a flat partition cut is defined to reject events with a partition of < 0 , corresponding to events below the black, horizontal line in Fig. 4.42. Figure 4.43 shows the energy spectrum of ^{57}Co -calibration events after applying each of the previously mentioned cuts to the data, including the partition cut.

The reason why a partition cut cannot be developed and implemented in this analysis is evident in Fig. 4.43. As the energy calibration of this analysis is valid up to six e^-h^+ pairs, the efficiency of each DQ cut must also be valid up to six e^-h^+ pairs. However there is not a sufficient number of good events from the ^{57}Co -calibration data above three e^-h^+ pairs to confidently calculate a partition cut efficiency. Specifically, there are only 134 events *in total* between three and six e^-h^+ pairs before the partition cut, and only 59 events after the partition cut over the same range. The reason why there are such few events at high energy is due to the large number of saturated and pile-up events that are rejected by the quality cuts. Even with the detector having an applied voltage of 60 V, the quality of the vast majority of ^{57}Co -calibration events is too poor. It is also observed that the ^{57}Co -calibration and 60 V background energy spectra (seen in Fig. 4.44) after their respective quality cuts are applied to the data are comparable in both shape and in the ratios between the heights of the e^-h^+ -pair peaks. This suggests that the ^{57}Co -calibration spectrum is dominated by background events instead of ^{57}Co events that, due to Compton scattering, are expected to produce a flat energy spectrum. This is another indicator that the ^{57}Co -calibration data cannot be used to develop a partition cut for this analysis.

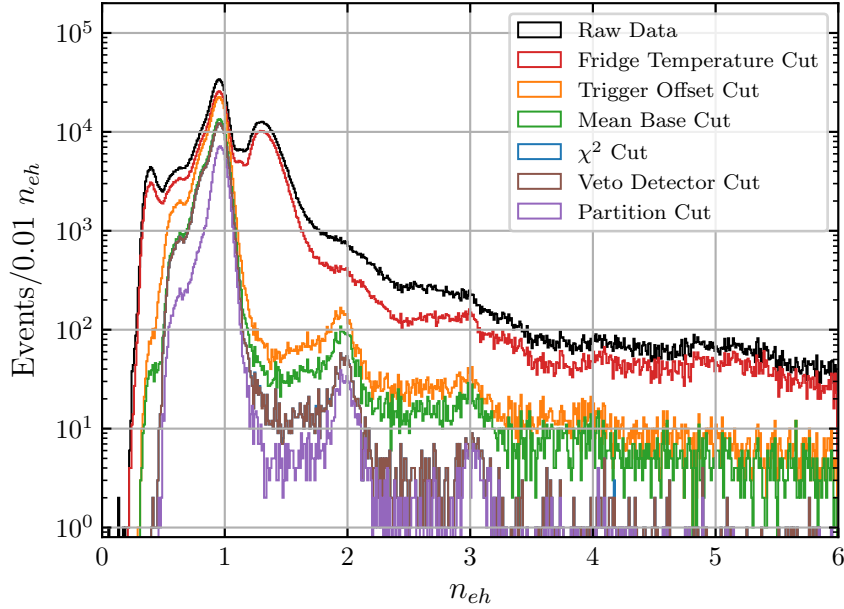


Figure 4.43: Energy spectrum of ^{57}Co -calibration events after applying each quality cut to the data and after applying the simple partition cut. The energy is measured as the number of e^-h^+ pairs n_{eh} . The partition cut rejects events with a partition of < 0 .

Although the development of a partition cut is unsuccessful for this analysis, the two-channel design of the detector and methodology outlined here are encouraging signs that a partition cut could be developed in the future with the right data. Future studies could investigate how this and other similar detectors respond to radioisotopes used as calibration sources, or use simulated data obtained by sophisticated detector and particle simulations. Furthermore, low-energy events could be generated by using optical photons with a different experimental setup. For instance, a mechanical system could be installed to direct the laser pulses to different regions of the detector (as is done in Chapter 6), or the beam spot of the laser could be made purposefully larger than the area of the detector.

Summary of Data-Quality Cuts

Figure 4.44 summarizes the results of the DQ cuts by showing the energy spectrum after each cut is successively applied to both the laser livetime selection and stage-0 science exposure datasets measured at 60 and 100 V. The final spectra of events from the background datasets measured at 60 and 100 V that pass the DQ cuts define the “DM-search” spectra that are used to produce the limit results. The cut efficiency is calculated using the laser-calibration data that pass the DQ cuts and is summarized in Sec. 4.5.

4.5 Livetime, Efficiency, and Experimental Parameters

This section describes the calculations of necessary experimental parameters required to produce the limit results. These parameters include: (i) the experimental livetime; (ii) the detector efficiency; (iii) the detector resolution; and (iv) the detector charge trapping (CT) and impact ionization (II) probabilities.

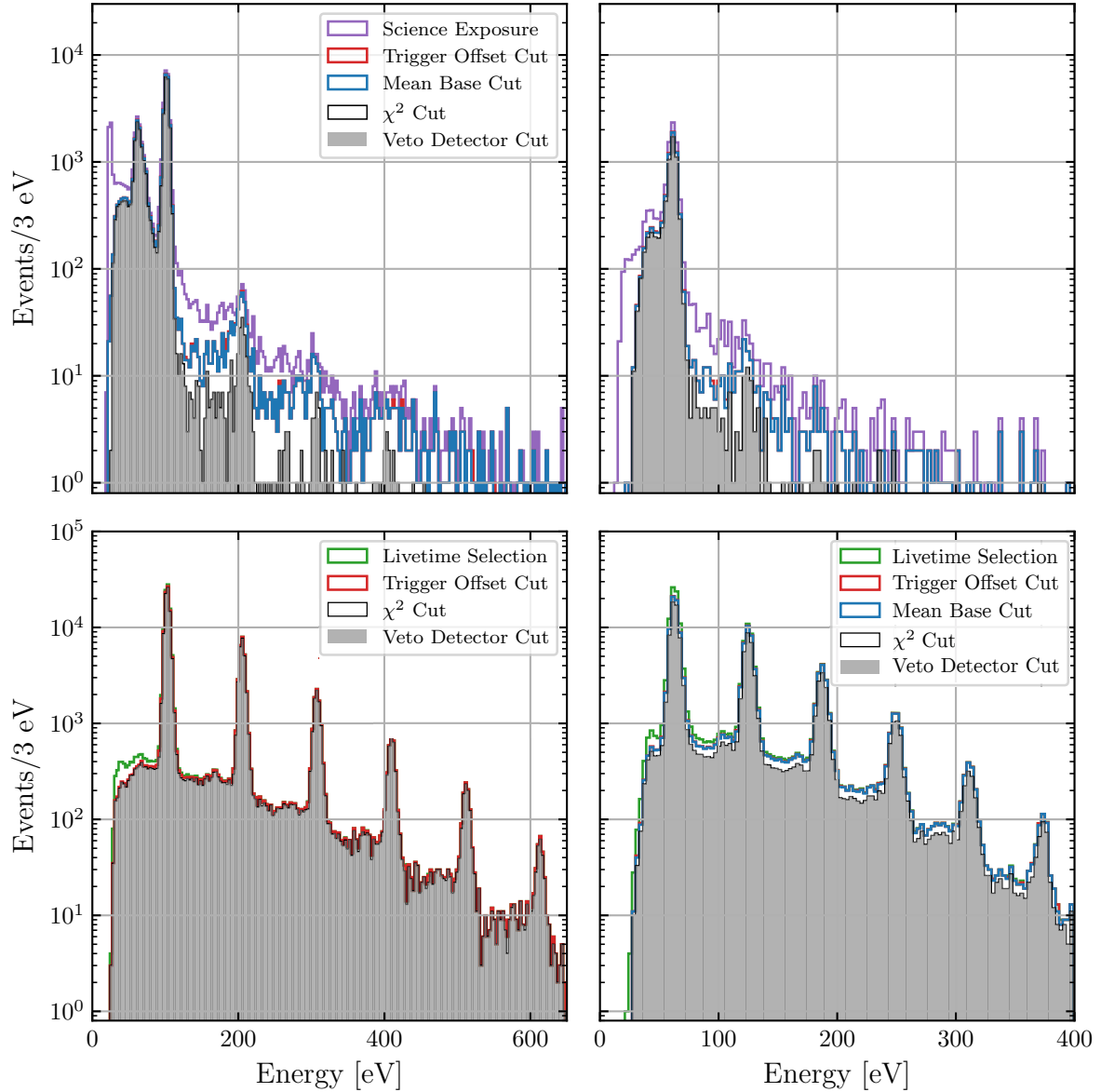


Figure 4.44: Summary of the energy spectra produced after successively applying the DQ cuts to the stage-0 science exposure data (top) and the laser livetime selection (bottom) measured at 100 V (left) and 60 V (right). Due to a miscommunication that occurred during the analysis, the mean base cut is not applied to the 100 V laser livetime selection data (see Sec. 4.5.2). The gray, shaded regions are the final spectra produced after applying all of the DQ cuts used in this analysis. For the background data, these final spectra define the “DM-search” spectra that are used to produce the limit results. For the laser-calibration data, these spectra are used to calculate the cut efficiency.

4.5.1 Livetime

The livetime measures the amount of good operating time the detector had during data acquisition, and therefore the amount of time required to record the science exposure data measured at 60 and 100 V. The raw livetime of detector operation is defined as the total time between the first and last recorded trigger in each series. The times before the first trigger and after the last trigger in each series are

ignored due to an inability to confirm that the DAQ was operating properly. However this neglected time is estimated to be $\ll 1\%$ of the total raw livetime from each day.

The livetime is calculated after successively applying the livetime cuts described in Sec. 4.4.1 to the background data, with final livetime simply as the livetime remaining after all of the cuts have been applied to the data. Recall that for the stage-0 background datasets, certain considerations and assumptions are made to account for the temporal blinding scheme. Specifically for the 1 s temperature cut and the mean base cut, which also bins the data in 1 s intervals, it is conservatively assumed that any time bin removed also removes the entire 10 s interval for the purposes of calculating the livetime. Let T_R be the raw livetime and $T_{T, MB}^r$ be the livetime *removed* after the fridge temperature and mean base cuts. The livetime *available* after the fridge temperature and mean base cuts, $T_{T, MB}^a$, for the stage-0 background data (which accounts for 10% of the entire dataset) is calculated as

$$T_{T, MB}^a = (T_R - T_{T, MB}^r) \times 0.1. \quad (4.21)$$

For the trigger and leakage burst cuts applied to the stage-0 background data, the time bins are constrained to be no larger than the 1 s interval implemented for the blinding scheme. Because the time bins for these cuts are necessarily aligned with the time bins from the blinding scheme, no further assumptions are required to calculate the livetime. Let $T_{TB, LB}^r$ be the livetime removed due to the trigger and leakage burst cuts. The final livetime T_F for the stage-0 background data is calculated as

$$T_F = T_{T, MB}^a - (T_{TB, LB}^r \setminus T_{T, MB}^r), \quad (4.22)$$

where $T_{TB, LB}^r \setminus T_{T, MB}^r$ is the livetime removed by the trigger and leakage burst cuts that isn't also removed by the fridge temperature and mean base cuts. The same logic for calculating the livetime is also applied to the stage-1 background data that includes an additional 20% of the data. When the data is fully unblinded, the livetime assumptions and constraints are lifted, and the livetime is trivially calculated as the time remaining after the livetime cuts are applied to the data. For the stage-2 background data, the final livetime is the total livetime of the entire dataset less the livetime from second 1 or seconds 1–3 of every 10-s interval, depending on the outcome of the unblinding verification tests described in Sec. 5.3. Table 4.5 summarizes the livetime calculations after each livetime cut is applied to the stage-0 background data measured at 60 and 100 V. The final livetime is converted to an exposure by multiplying the value by 0.93 g, the mass of the detector.

The comparison between the calculated livetimes in Tab. 4.5 after the mean base and the 1 s fridge temperature cuts are applied to the data further illustrates the strong correlation between the fridge temperature and the mean base value; nearly all of the livetime removed by the 1 s fridge temperature cut is also removed by the mean base. Unsurprisingly the 30 s fridge temperature cut removes the largest amount of livetime. As Fig. 4.28 shows, this cut removes long periods of time when the fridge temperature was unstable or was rising at the ADR warming at the end of each day.

4.5.2 Efficiency Calculation

The detector efficiency for this analysis combines the trigger efficiency from the trigger data and the cut efficiency induced by the DQ cuts. Together these efficiencies are used to compute efficiency curves for the data measured at 60 and 100 V that are required to produce the limit results.

Table 4.5: Summary of the livetime calculations after each livetime cut is applied to the stage-0 background data measured at 60 and 100 V. The final livetime and exposure for each dataset given a detector mass of 0.93 g are also reported.

	60 V		100 V	
	Livetime [Hours]	%	Livetime [Hours]	%
Raw Livetime	2.49	100.00	7.8	100.00
30 s Fridge Temperature Cut	1.71	68.44	5.2	66.80
Mean Base Cut	1.33	53.44	3.9	50.80
1 s Fridge Temperature Cut	1.33	53.44	3.9	50.78
Trigger and Leakage Burst Cut	1.25	49.91	3.6	46.62
Stage-0 Background Dataset	Final Livetime [Days]		Exposure [g-days]	
60 V	0.052		0.048	
100 V	0.15		0.14	

Trigger Efficiency

The trigger efficiency measures how efficient the triggering procedure is at identifying events. For low-energy events the trigger efficiency is poor due to a low signal-to-noise ratio, whereas the reverse is true for high-energy events. The trigger efficiency curve therefore acts as a “turn-on” curve which shows the transition between noise-induced triggered events and events triggered by real energy depositions. The point in energy at which all the triggered events are due to real energy depositions refers to the trigger threshold, and also provides the low-energy threshold of the analysis range. Because this analysis relies on e^-h^+ -pair quantization, the DM signal models for the purposes of limit setting are not relevant below the first e^-h^+ -pair peak, which corresponds to ~ 60 eV and ~ 100 eV for the data measured at 60 and 100 V, respectively. Fortunately this means that the exact value of the trigger threshold is not critical to this analysis as long as it is below the first e^-h^+ -pair peak.

The trigger efficiency is calculated using the laser-calibration data with the OF amplitude A_0 , calibrated to phonon energy, as the energy estimator. A_0 is used in order to have better energy estimation of events in the zeroth-energy peak. Two triggering procedures are applied to the data streams to identify events: one using the normal triggering procedure used for data acquisition, and another that uses the laser TTL trigger to identify events coincident with the laser pulses. The energy spectra from these two datasets are constructed by binning the data in 3 eV bins; the trigger efficiency is calculated as the ratio of the number of events from the two spectra in each energy bin. The efficiency data is then fit to with the trigger efficiency curve $f(E)$, given by:

$$f(E) = \frac{1}{1 + e^{-\frac{E-a}{b}}}, \quad (4.23)$$

where E is the phonon energy, and a and b are fit parameters. The fit is performed separately on the data measured at 50 and 52 mK in order to account for differences in the QET channel gain and energy estimation at the two temperatures. Figure 4.45 compares the energy spectra of events triggered by the normal triggering procedure and events triggered by the laser TTL, as well as the trigger efficiency data

and the fitted trigger efficiency curve described by Eq. 4.23. The unevenly spaced peaks are due to the energy spectra consisting of data measured at both 60 and 100 V, but do not affect the trigger efficiency estimation. Table 4.6 lists the results of fitting $f(E)$ to the laser-calibration data measured at 50 and 52 mK.

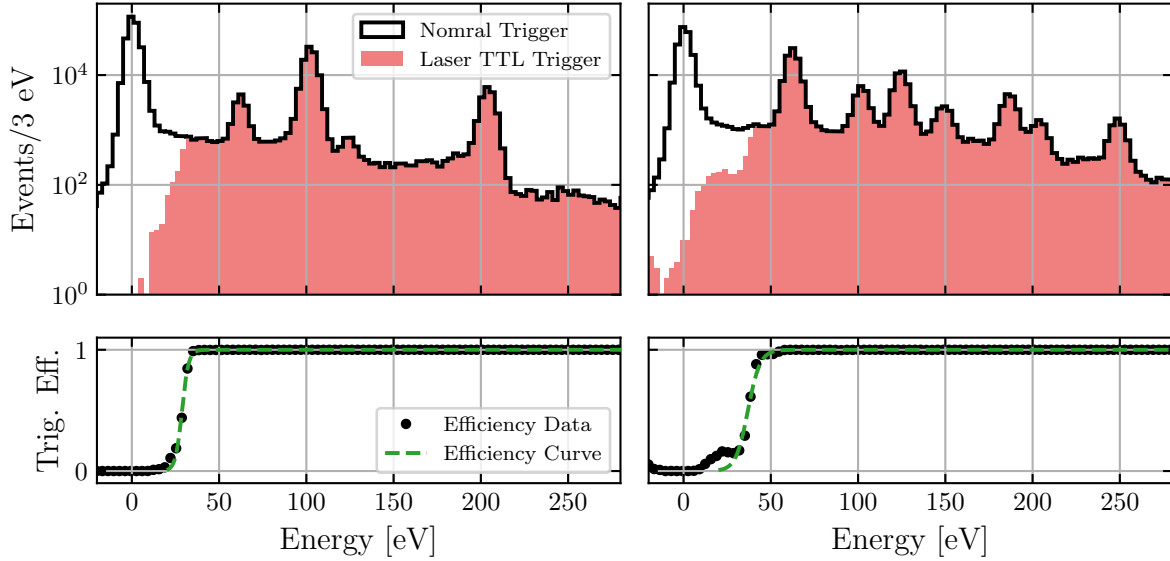


Figure 4.45: Top: energy spectra of laser-calibration events measured at 50 mK (left) and 52 mK (right). The black spectra correspond to events identified by the normal triggering procedure used for data acquisition, whereas the red, shaded spectra correspond to events identified by the laser TTL trigger. The uneven peaks in the spectra are due to the combination of data measured at 60 and 100 V. Bottom: trigger efficiency for the data measured at 50 mK (left) and 52 mK (right). The data points are the efficiency calculated as the ratio of the number of events in each 3 eV bin from the two corresponding energy spectra in the top panel. The green curves are the fitted trigger efficiency curves $f(E)$ described by Eq. 4.23. Courtesy of Valentina Novati.

Table 4.6: Results from fitting the trigger efficiency curve $f(E)$ described by Eq. 4.23 to the trigger efficiency data from laser-calibration data measured at 50 and 52 mK.

Parameter	50 mK	52 mK
a [eV]	28 ± 1	36.9 ± 0.6
b [eV]	1.9 ± 0.4	3.7 ± 0.2

The trigger threshold is defined as the point where the trigger efficiency becomes 100%. As shown in Fig. 4.45, the trigger threshold for the data measured at 50 mK and 52 mK is ~ 40 eV and ~ 50 eV, respectively. For the purposes of calculating the limit results, a uniform trigger threshold of 50 eV is chosen in order to avoid combining different energy thresholds in the limit calculations. Although this threshold is close to the energy of the first e^-h^+ -pair peak at 60 V, it is still sufficiently far away at $> 3\sigma_{(E)}$, where $\sigma_{(E)}$ is the energy resolution, to not affect the limit calculations.

Cut Efficiency

Laser-calibration events are used to approximate DM interactions with the detector in terms of the detector response to energy depositions and the expected pulse shape of good events. In lieu of a trusted model to simulate DM interactions in an HVEV detector, the efficiency must ultimately be estimated from the laser-calibration data. It is, however, important to mention key differences between laser events and potential DM events. First, due to the high cross section of photon absorption, the energy deposition from laser events occurs near the surface of the detector, whereas DM events are expected to uniformly interact with the detector. Because the energy deposition of both event types is dominated by the phonon amplification of liberated e^-h^+ pairs, there is assumed to be no difference in the pulse shape nor energy estimation. Second, laser events with an energy above one e^-h^+ pair correspond to multiple photons being absorbed at different times and different locations. Conversely events from DM interactions are expected to correspond to a single energy deposition regardless of how many e^-h^+ pairs are produced. Because the time scale of multi-photon absorption in the detector is much smaller than the timing resolution of the detector, there are assumed to be no differences in the pulse shape of multi-photon laser events due to differing absorption times. Although with no direct dataset to verify, but with no data indicating otherwise, there are also assumed to be no differences in the pulse shape of multi-photon laser events due to differing absorption positions. Lastly, the energy deposition is slightly different for laser events than what is expected for DM events. Both types of events produce the same phonon energy from the phonon amplification of liberated e^-h^+ pairs. However laser events additionally produce the absorption energy E_γ from n absorbed photon, $n \cdot E_\gamma$, whereas DM events are expected to additionally produce the varying recoil or absorption energy E_r from the scattered or absorbed DM particle. This means that mono-energetic sources, whether laser events or otherwise, will result in e^-h^+ -pair peaks at different energies in the energy spectrum. This manifests itself in terms of the observed energy-dependent efficiency dips, discussed in detail below, that would differ between different event sources.

The cut efficiency is calculated for the 60 and 100 V data using the laser livetime selection datasets. After the data is sorted into energy bins 3 eV in length, the efficiency after each successive DQ cut in each bin is calculated as the ratio of the number of events that pass the cut and the initial number of events. There is one notable exception regarding the mean base cut described in Sec. 4.4.2. The observed inherent differences between the mean base distributions of background and laser-calibration data introduce some uncertainty into the efficiency calculated from this cut. Implementing the mean base cut as described, whereby the cut thresholds are determined separately for background and laser-calibration datasets, assumes that the differences in the respective mean base distributions are solely due to inherent differences between the sources of events and not due to different proportions of good versus bad events. The other extreme is to not apply the mean base cut to the laser-calibration data while still applying it to the background data, which assumes that the efficiency loss from the mean base cut is negligible. The true efficiency from this cut likely exists somewhere between these extremes. Ultimately, this uncertainty in the efficiency due to the mean base cut is negligible compared to uncertainty due to the efficiency dips, as discussed below.

Due to a miscommunication that occurred during the analysis development, separate procedures are developed for the 60 and 100 V data. The mean base cut is applied to the 60 V laser-calibration data, but it is not applied to the 100 V laser-calibration data; the cut is still applied to both the 60 and 100 V the background data. Despite the different procedures and the uncertainty in the mean base cut efficiency,

it is confirmed that due to redundancies between the cut and other analysis cuts the effect on the overall efficiency is negligible. The final cut efficiency is the efficiency calculated after all DQ cuts are applied to the data. The efficiency after each successive cut is applied to the data, as well as the final detector efficiency, are shown in Figs. 4.46 and 4.47.

The detector efficiency is modelled by the energy-dependent detector efficiency curve $\epsilon(E)$ given by:

$$\epsilon(E) = f(E) \times (c_0 \cdot E + c_1) \times \left(1 - e^{-\frac{E-c_2}{c_3}}\right), \quad (4.24)$$

where E is again the phonon energy, and $c_{i=0\dots3}$ are the fit parameters. Equation 4.24 is comprised of three terms: (i) the aforementioned fitted trigger efficiency curve $f(E)$; (ii) a linear term that describes the maximal cut efficiency and that is close to horizontal ($c_1 \gg c_0$); and (iii) an exponential term that describes the cut efficiency “turn-on” point that is highly correlated with the previously described trigger offset cut. The detector efficiency is estimated by fitting $\epsilon(E)$ separately to the cut efficiency data measured at 60 and 100 V. Recall that the $f(E)$ curve is fitted separately to the data measured at 50 and 52 mK. For the data measured at 60 V, which was acquired at both temperatures, $\epsilon(E)$ is fit separately to the laser-calibration data measured at each temperature to confirm that the fitted $\epsilon(E)$ curves for the data measured at each temperature are consistent. For the final 60 V detector efficiency, the data is combined to produce a single $\epsilon(E)$ curve using the $f(E)$ curve fitted to the 50 mK data. Although a more ideal choice may be to use the $f(E)$ curve fitted to the 52 mK data, it is inconsequential since the lower energy threshold of the analysis range for all data is set to 50 eV.

The energy calibration described in Sec. 4.3 is valid up to six e^-h^+ pairs, and therefore only the laser-calibration events with an energy of $\leq 6.5 e^-h^+$ pairs are considered for calculating the detector efficiency. This condition sets the high-energy thresholds for this analysis: [50 eV, 390 eV] and [50 eV, 650 eV] for the data measured at 60 and 100 V, respectively. For the purposes of calculating the limit results, $\epsilon(E) = 0$ for energies outside of the respective energy range for the data measured at each voltage bias. Table 4.7 lists the results of fitting $\epsilon(E)$ to the cut efficiency data from the 60 and 100 V laser-calibration data, and the corresponding fitted $\epsilon(E)$ curves are shown in Figs. 4.46 and 4.47.

Table 4.7: Results from fitting the detector efficiency curve $\epsilon(E)$ described by Eq. 4.24 to the cut efficiency data from the laser-calibration data measured at 60 and 100 V.

Parameter	60 V	100 V
c_0 [eV ⁻¹]	$(2 \pm 25) \times 10^{-5}$	$(3 \pm 1) \times 10^{-5}$
c_1	0.78 ± 0.06	0.948 ± 0.003
c_2 [eV]	0.000009 ± 10	17 ± 2
c_3 [eV]	31 ± 7	27 ± 1

To estimate the uncertainty in the detector efficiency, $\epsilon(E)$ is calculated 5000 times using random variates of the fit parameters $c_{i=0\dots3}$. The random variates are chosen from Gaussian distributions constructed using the best-fit value and corresponding uncertainty of each individual parameter listed in Tab. 4.7. The uncertainties in the $\epsilon(E)$ curves are estimated as the energy-dependent standard deviation of the 5000 $\epsilon(E)$ curves and correspond to the shaded regions in Figs. 4.46 and 4.47.

As shown by the cut efficiency data in Figs. 4.46 and 4.47, the largest drop in efficiency is due to the $\chi^2(f)$ and $\chi^2(t)$ cuts. Together these cuts, whose purpose is to reject events that have a bad pulse

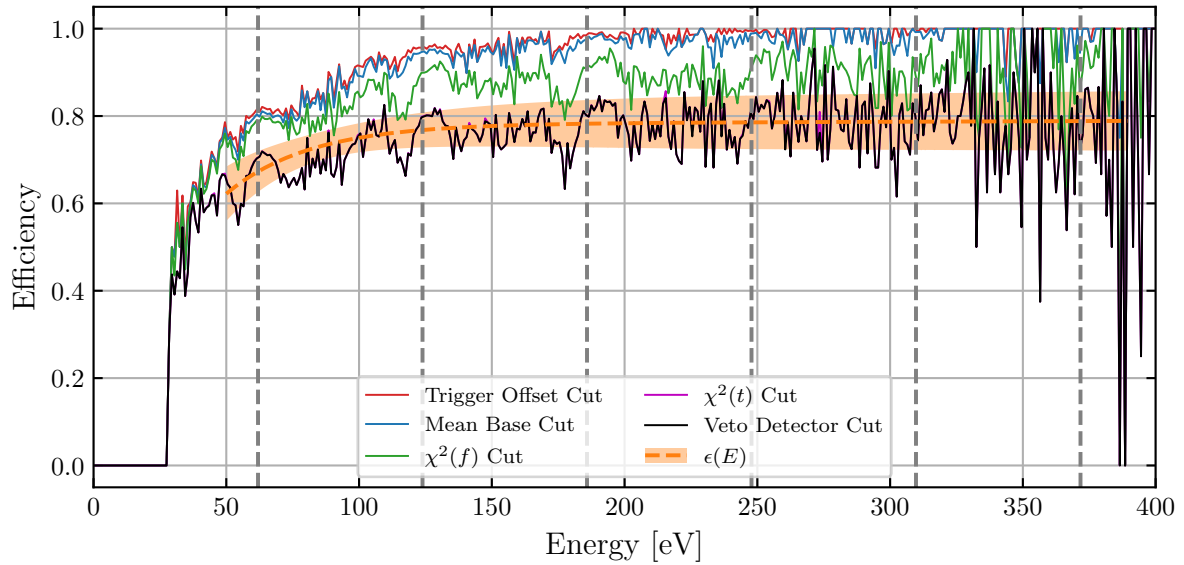


Figure 4.46: Efficiency data from the laser livetime selection data measured at 60 V. The cut efficiency in each 3 eV bin after each data-quality cut is successively applied to the data is shown. The dashed, orange curve is the fitted detector efficiency curve $\epsilon(E)$ described by Eq. 4.24, with the shaded region describing the uncertainty in the detector efficiency. The dashed, vertical lines correspond to the positions of the first six e^-h^+ -pair peaks for the data measured at 60V. Courtesy of Yen-Yung Chang.

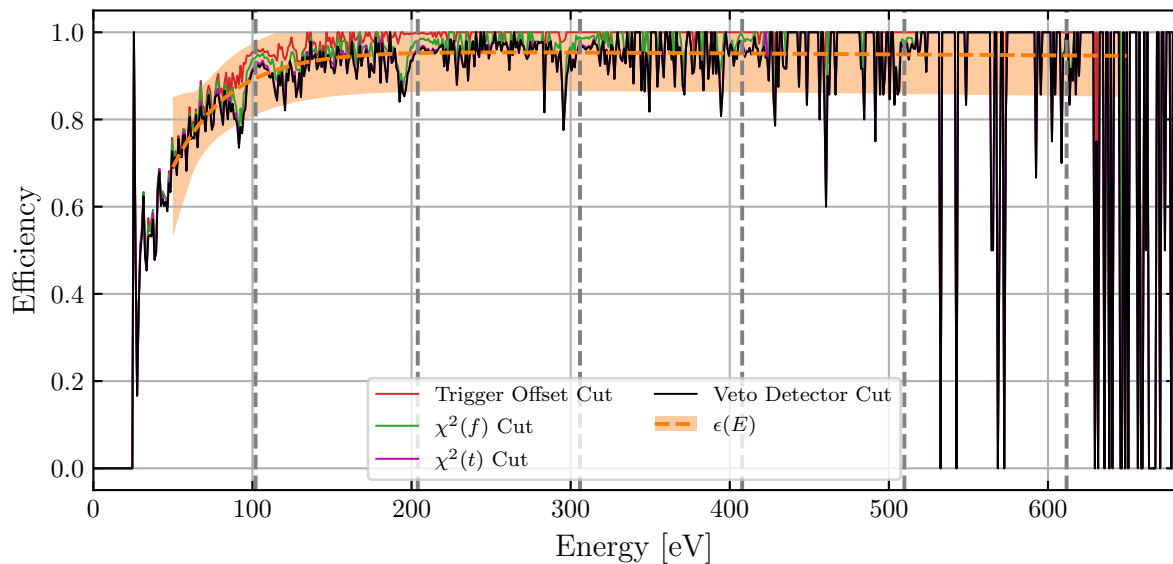


Figure 4.47: Efficiency data from the laser livetime selection data measured at 100 V. The cut efficiency in each 3 eV bin after each data-quality cut except for the mean base cut is successively applied to the data is shown. The dashed, orange curve is the fitted detector efficiency curve $\epsilon(E)$ described by Eq. 4.24, with the shaded region describing the uncertainty in the detector efficiency. The dashed, vertical lines correspond to the positions of the first six e^-h^+ -pair peaks for the data measured at 100V. Courtesy of Yen-Yung Chang.

shape or to reject pile-up events, account for the largest drop in efficiency over the entire energy range for the data measured at 60 and 100 V. Table 4.8 summarizes the event rejection rates of each of the DQ cuts when *individually* applied to the various datasets. The total rejection rates after all the DQ cuts are applied to the data are also shown. For the laser-calibration data, the cut efficiency of each DQ cut is 100 % less the corresponding rejection rate. The two χ^2 cuts together also account for the largest rejection of events in the stage-0 background data, but at a significantly higher rate compared to the laser-calibration data. Unsurprisingly, the total rejection rates after all of the DQ cuts are applied to the stage-0 background data is much larger compared to those of the laser-calibration data.

Table 4.8: Summary of the event rejection rates of each of the data-quality (DQ) cuts when individually applied to the various datasets, as well as the total rejection rate after all of the DQ cuts are applied to the data. For the laser-calibration data, the cut efficiency of each DQ cut is 100 % less the corresponding rejection rate. The mean base cut is not applied to the 100 V laser-calibration data, but is still applied to the 100 V background data.

DQ Cut Rejection Rate [%]	Laser Livetime Selection Data		Stage-0 Science Exposure Data	
	60 V	100 V	60 V	100 V
Trigger Offset	12.3	4.24	30.3	23.6
Mean Base	1.33	N/A	2.81	1.62
$\chi^2(f)$	5.55	6.07	22.3	16.4
$\chi^2(t)$	16.7	3.87	30.4	26.5
Veto Detector	0.076	0.52	0.11	0.43
All DQ Cuts	26.8	8.59	40.3	31.4

Efficiency Dips

The cut efficiency data in Figs. 4.46 and 4.47 also show apparent dips in the efficiency that occur right before the e^-h^+ -pair peak locations. These dips are observed in the data measured at both 60 and 100 V. They start to appear after the trigger offset cut but are greatly emphasized after the χ^2 cuts are applied to the data. To understand the cause of these efficiency dips, Fig. 4.48 shows the density map of events over the $\chi^2(f)$ -energy parameter space for the laser livetime selection data measured at 100 V.

As shown in Fig. 4.48, the density of bad- $\chi^2(f)$ events right before each e^-h^+ -pair peak is higher than the density right after each peak. Comparatively, the density of good- $\chi^2(t)$ events is relatively constant right before and right after each e^-h^+ -pair peak. This is caused by a flaw in the OF algorithm which correlates the OF amplitude, i.e. the energy estimation, with the pulse quality, i.e. the χ^2 values. Take, for example, a good laser event that liberates one e^-h^+ pair in the detector. If the detector had a bias voltage of 100 V, that event would have a measured energy of 101.95 eV within resolution, and would also have low χ^2 values. Now consider the same laser event, but the trace contains a small pile-up pulse. Because the OF algorithm has no way to remove or subtract pile-up pulses, it will necessarily underestimate the amplitude of the main pulse to compensate for the pile-up pulse. Therefore this event will have a measured energy of slightly less than 101.95 eV, and will also have elevated χ^2 values. Figure 4.49 shows two examples of traces from events that are rejected by the χ^2 cuts and have an energy just below one e^-h^+ -pair peak.

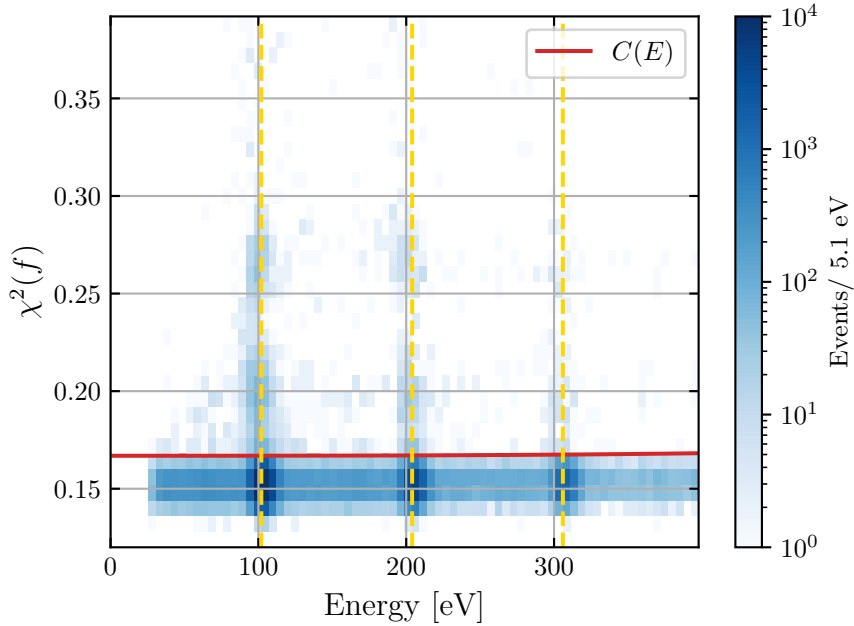


Figure 4.48: Density map of events over the $\chi^2(f)$ -energy parameter space for the laser livetime selection data measured at 100 V. The yellow, vertical lines correspond to the energies of the first three e^-h^+ -pair peaks. The red curve is the energy-dependent cut threshold $C(E)$ for the $\chi^2(f)$ cut. Above $C(E)$ the density of events is slightly higher just below each e^-h^+ -pair peak compared to just after each peak. Courtesy of Valentina Novati.

For most events sampled from the laser-calibration data, and in all events sampled in the stage-0 background data, the OF algorithm underestimates the pulse amplitude due to the presence of a pile-up pulse. For a small number of events sampled from the laser-calibration data where the events are measured on the tail of a prior high-energy event, the OF algorithm has the opposite effect and overestimates the pulse amplitude.

In summary, the efficiency dips seen in Figs. 4.46 and 4.47 are real artifacts due to flaws in the OF algorithm which affect both the laser-calibration and background datasets. However the locations of these dips are dependent on the e^-h^+ -pair peak locations, and can therefore differ between laser events, background events, and expected DM events. The detector efficiencies are instead assumed to be smooth curves, and the magnitude and potential locations of the efficiency dips are accounted for by the large estimated uncertainties. Because the limit setting method used in this analysis predominately relies on the data within e^-h^+ -pair peaks, it is verified that limit results are negligibly affected by using the smooth efficiency curve versus the efficiency data that contain the dips.

4.5.3 Detector Resolution

The detector energy resolution is determined from the width of the e^-h^+ -pair peaks of the laser-calibration energy spectra produced after energy calibration, as seen in Fig. 4.27. Although there is expected to be no voltage dependence in the energy resolution, it is calculated separately for the data measured at 60 and 100 V. A Gaussian function is fitted to each of the first six e^-h^+ -pair peaks in the

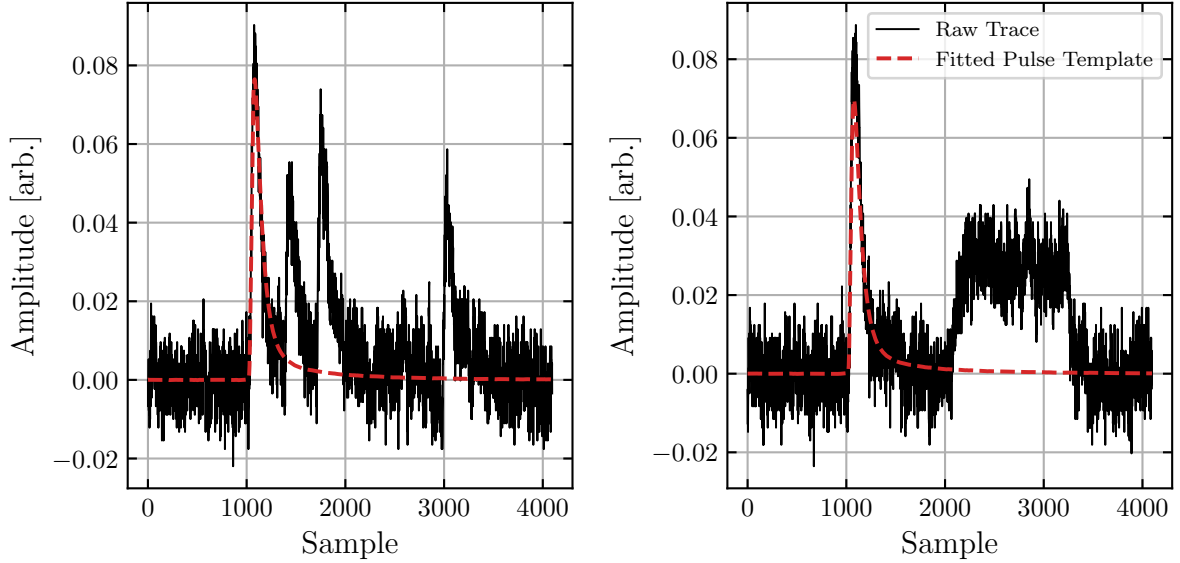


Figure 4.49: Examples of traces from laser events with a measured energy just below one e^-h^+ pair and that fail the $\chi^2(f)$ cut. The presence of pile-up events (left) or radio-frequency noise (right) in trace makes the OF algorithm underestimate the amplitude of the main pulse; this can be seen by comparing the fitted pulse template with the raw traces in the examples shown. These types of events have an underestimated measured energy and elevated χ^2 values, and result in the dips observed in the efficiency data. Courtesy of Valentina Novati.

energy spectra, and the standard deviation is extracted to measure the energy resolution σ_E of each peak. Table 4.9 summarizes the σ_E values measured from the laser-calibration data.

Table 4.9: Summary of the energy resolution σ_E measured for each e^-h^+ -pair peak from the laser-calibration data after energy calibration. The weighted average energy resolution $\sigma_{\langle E \rangle}$ is also shown for each dataset.

	σ_E [eV]	
	60 V	100 V
$1 e^-h^+$	3.35 ± 0.01	3.48 ± 0.01
$2 e^-h^+$	3.74 ± 0.02	3.98 ± 0.02
$3 e^-h^+$	4.10 ± 0.04	4.57 ± 0.04
$4 e^-h^+$	4.20 ± 0.07	4.67 ± 0.83
$5 e^-h^+$	4.6 ± 0.2	4.9 ± 0.2
$6 e^-h^+$	4.0 ± 0.2	4.8 ± 0.3
$\sigma_{\langle E \rangle}$ [eV]	3.5 ± 0.3	3.6 ± 0.3

The energy resolutions listed in Tab. 4.9 are consistent with the resolutions measured individually from the laser-calibration data of each day at the first and second e^-h^+ -pair peaks, which varied between ~ 2.5 – 4 eV. Although the energy resolution appears to increase with higher e^-h^+ -pair peaks, it is presently unclear how describe this apparent energy dependence physically or mathematically. In lieu of

a model to describe the energy resolution over increased energy, the weighted averaged energy resolution $\sigma_{\langle E \rangle}$ of the laser-calibration data measured at 60 and 100 V is instead calculated. $\sigma_{\langle E \rangle}$ is determined by weighting the resolution over the first six e^-h^+ -pair peaks by their corresponding uncertainty, and the uncertainty in $\sigma_{\langle E \rangle}$ is determined by the weighted sample variance. The computed values of $\sigma_{\langle E \rangle}$, also listed in Tab. 4.9, are used for the calculating the final limit results.

4.5.4 Charge Trapping and Impact Ionization Probabilities

Charge trapping and impact ionization, described in detail in Sec. 2.2.2, refer to processes in which a traversing electron or hole either falls into a charge vacancy in the detector or liberates an additional loosely bound charge. The process of CT lowers the energy measured for an event, whereas II increases the measured energy. In the resulting energy spectra, CT and II contribute to the events sitting between the quantized e^-h^+ -pair peaks.

These processes are accounted for in the detector response model described in Sec. 2.2, and therefore influence the DM signal models that are used for limit setting. The laser-calibration data that pass the livetime and DQ cuts are used to measure the CT and II probabilities of the detector during this experiment. Because there may be many factors that influence CT and II, it is possible that the daily ADR cycling and detector characterization and calibration led to day-to-day variations in the CT and II probabilities in the detector. Therefore the probabilities are measured separately for each day of laser-calibration data, and a weighted average is calculated for the data measured at 60 and 100 V. The CT and II model described in Appendix D.1 is fitted to the laser-calibration data from each day, and the CT and II probabilities are extracted. Many parameters in the CT and II model, including e^-h^+ -pair peak positions, energy resolution values, and λ values, are allowed to float when the fit is performed, although only the CT and II probabilities are used. Figure. 4.50 shows the CT and II model fitted to the laser-calibration data from one day of data acquisition.

The fit of the CT and II model performs well to the data in Fig. 4.50 as well as to the data from most other days. In some instances, however, the fitted CT and II model substantially deviates from the data at energies above $\sim 4e^-h^+$ pairs. Figure 4.51 summarizes the CT and II probabilities calculated from each day of laser-calibration data measured at 60 and 100 V.

Figure 4.51 also shows the averaged CT and II probabilities for the 60 and 100 V datasets, which are determined by taking the average of the probabilities measured from each day weighted by their respective uncertainties. For the data measured at 60 V, the weighted averaged CT and II probabilities are $16.0 \pm 0.7\%$ and $(3 \pm 4) \times 10^{-11}\%$, respectively. For the data measured at 100 V, the weighted average CT and II probabilities are $11 \pm 3\%$ and $2 \pm 3\%$, respectively. As seen in Fig. 4.51, the values measured using the 60 V data are consistent between datasets; however the II probabilities from three datasets measured using the 100 V data greatly deviate from the other values. These inconsistencies correspond to fits that performed poorly to the data at high energies. Both the weighted averaged II probabilities measured using the 60 and 100 V data are consistent with zero. However, the CT probability measured using the 60 V data is notably higher than the probability measured at 100 V. It is unclear whether this difference is due to some relationship between the CT probability and the bias voltage applied to the detector, or rather some difference in the data acquisition procedure that inadvertently led to a higher CT probability when the 60 V data was acquired.

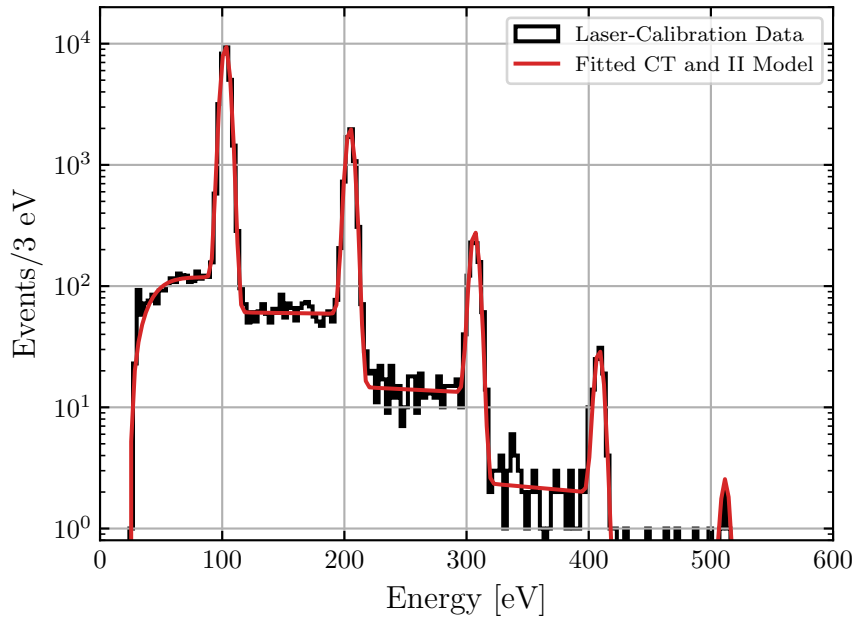


Figure 4.50: Charge trapping (CT) and impact ionization (II) model fitted to the laser-calibration data from one day of data acquisition measured at 100 V that pass the livetime and DQ cuts. The CT and II model, described in Appendix D.1, is fitted to the data in order to extract the CT and II probabilities in the detector for each day. Courtesy of Francisco Ponce.

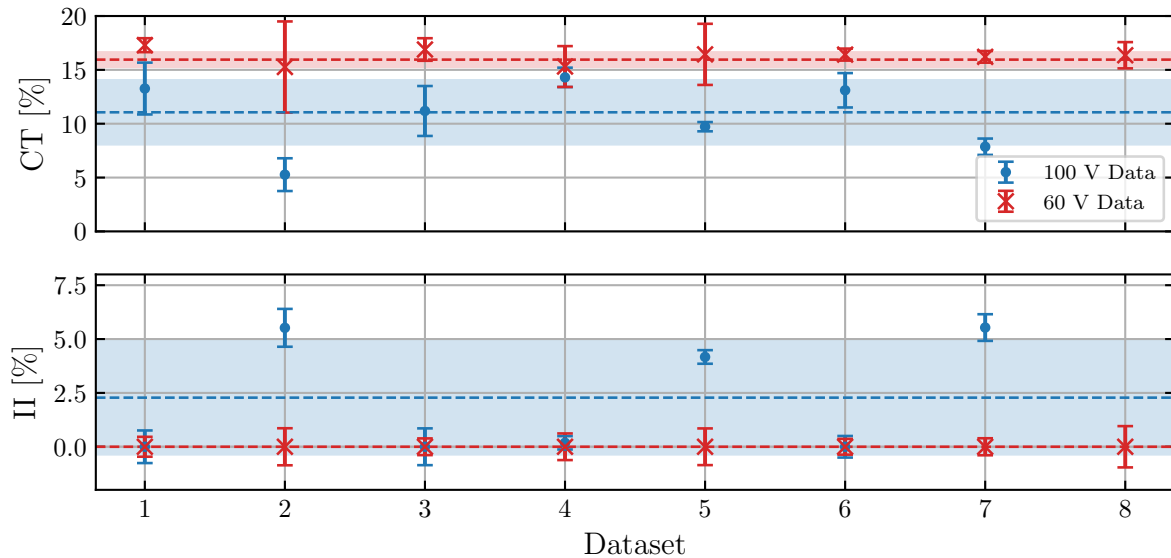


Figure 4.51: Summary of the charge trapping (CT) and impact ionization (II) probabilities measured using the laser-calibration data from each day that pass the livetime and DQ cuts at 60 V (red) and 100 V (blue). The horizontal, dashed lines correspond to the weighted average CT and II values for the data of matching colour. The shaded regions of matching colour correspond to the uncertainty in the weighted averages. Courtesy of Francisco Ponce.

Chapter 5

HVeV Run 2 Dark Matter Search: Limit Setting, Unblinding, and Final Results

This chapter is the final chapter presenting the dark matter (DM) search experiment and blinded analysis denoted as high-voltage eV-scale (HVeV) Run 2. The previous chapter described the experimental setup, energy calibration, and data selection. So far, the detector efficiency has been determined using the laser-calibration datasets, and the livetime and energy spectra for the stage-0, DM-search data have been reported. Recall that “stage-0” refers to the initial 10% of the entire background dataset that is used to develop the analysis pipeline before unblinding (see Sec. 4.2.4), and “DM-search” refers to the background data selected after all the analysis cuts are applied. Furthermore, recall that the analysis is performed separately for data measured while the detector was biased at 60 and 100 V. In this chapter, the limit setting procedure is described in Sec. 5.1, and the initial (pre-unblinded) results are shown in Sec. 5.2. Section 5.3 outlines the unblinding procedure and presents the unblinding verification checks. The final results are reported in Sec. 5.4, including the DM exclusion limits on light dark matter (LDM)-electron inelastic scattering, as well as dark photon and axion-like particle (ALP) absorption. Lastly, a short discussion is provided in Sec. 5.5.

5.1 Limit Setting Methods

Under ideal circumstances, the DM exclusion limits for this analysis would be computed using a likelihood-based approach. However, such an approach cannot be implemented because the observed event spectra from this analysis are comprised of one or more unknown background sources. In lieu of a likelihood-based approach, a reasonable alternative is to use the optimum interval (OI) method outlined in Sec. 5.1.1 that can produce exclusion limits in the presence of an unknown background source, and that was implemented in the HVeV Run 1 analysis [106]. Another option is to use a Poisson counting based approach, like the one outlined in Sec. 5.1.2. For reasons that will be explained in Sec. 5.1.3, the Poisson method is deemed to be the better limit setting approach for this analysis.

5.1.1 OI Limit Setting Method

The OI limit setting method is a powerful technique to produce exclusion limits in situations where a given data spectrum is partially or fully comprised of an unknown background source that cannot be subtracted from the data. For this reason, it was the chosen limit setting method for the HVEV Run 1 analysis, and the initial method chosen for this analysis. A brief explanation of the OI method is provided below, and the full details can be found in Refs. [142] and [143].

A precursor to the OI method is the maximum gap method [147]. A DM signal model will have a differential event distribution dN/dE of the number of events N across the relevant parameter, normally some energy E , that is proportional to the parameter of interest, normally some cross section σ . A larger value of σ will increase the expected number of events measured during an experiment, and will thus increase dN/dE . The goal of this method is to vary the value of σ until it is just high enough to be rejected based on some criteria. The maximum gap method evaluates the integral of the signal distribution x_i between any two adjacent events in the data spectrum, E_i and E_{i+1} , defined as:

$$x_i = \int_{E_i}^{E_{i+1}} \frac{dN}{dE} dE. \quad (5.1)$$

The largest gap x_{\max} is the largest of all the x_i , which also identifies the interval that will determine the smallest value of σ to be rejected at a given confidence level (C.L.) and therefore the strongest limit. The criterion for rejection is such that if the maximum x_i for a random experiment is less than the observed x_{\max} with probability C_0 , the assumed σ is rejected as too high with a C.L. of C_0 . A random experiment is defined as n events randomly distributed according to the expected DM event distribution dN/dE at the assumed σ . By transforming the E parameter such that dN/dE transforms into a uniform distribution with a total length μ equal to the total number of events expected from dN/dE given σ , the probability C_0 of the maximum x_i value of a random experiment being smaller than a particular value of x is given as:

$$C_0(x, \mu) = \sum_{k=0}^m \frac{(kx - \mu)^k e^{-kx}}{k!} \left(1 + \frac{k}{\mu - kx} \right), \quad (5.2)$$

where m is the largest integer $\leq \mu/x$. To find the 90% C.L. upper limit, σ is iteratively increased until μ and the observed x_{\max} are such that $C_0 = 0.9$.

The OI method is a logical extension of the maximum gap method. Instead of only considering intervals between adjacent events, the OI method considers intervals over which 1 event, 2 events, or n events are observed. $C_n(x, \mu)$ is defined as the probability that, for all intervals with $\leq n$ events, the expected number of events is $\leq x$. $C_n(x, \mu)$ is tabulated using a Monte Carlo program, wherein the maximum gap method becomes a special case of the OI method with $n = 0$ that can be analytically evaluated using Eq. 5.2. The optimum interval, of which this method is named, is determined by computing $C_n(x, \mu)$ for each interval with n observed events. Comparing the $C_n(x, \mu)$ values from different intervals but calculated using the same σ (and therefore the same μ), the larger $C_n(x, \mu)$ value indicates a stronger rejection of the proposed σ . Thus optimum interval is the interval such that $C_n(x, \mu) = C_{\text{Max}}$, where C_{Max} is the maximum over all possible intervals of $C_n(x, \mu)$. The 90% C.L. upper limit is found by determining the value of σ such that for a random experiment, there is a 90% probability that its C_{Max} value will be smaller than C_{Max} observed from the data.

The OI method described above is ideal for when the number of background events observed is $\lesssim 50$. When there is a large number of background events observed, as is the case in this analysis, this exact method becomes computationally impractical to set an upper limit. Details of how the OI method is expanded to the case of high statistics can be found in Ref. [143].

5.1.2 Poisson Limit Setting Method

As with the OI method, the Poisson counting method assumes a signal-only hypothesis, meaning all of the observed events are assumed to be DM signal events. In contrast to a background-only hypothesis, which assumes that all of the measured events are explicitly not DM signal events, the signal-only hypothesis results in a more conservative upper limit in the presence of an unknown background. The Poisson method starts by counting the number of observed events N between some limit setting interval, and subsequently determining N_u , the Poisson upper limit on the number of events observed in the interval at a particular C.L. For example if N events are observed in a limit setting interval that spans from a to b , N_u is determined at a 90% C.L. as the mean of a Poisson distribution such that a repeated experiment has a 90% chance of observing $> N$ events in the same interval. This method is reliant on the relationship between the expected rate R , and therefore the expected number of events N , of the proposed DM signal model and its relevant coupling parameter σ of which the limit is set. For each DM model constrained in this analysis, $R \cdot X = N \propto \sigma$, where X is the exposure. Due to this relationship, an expected number of events N_0 evaluated from a reference σ_0 is related to N_u and the corresponding upper limit on σ , σ_u :

$$\frac{\sigma_u}{\sigma_0} = \frac{N_u}{N_0}. \quad (5.3)$$

N_0 is calculated as the integral between a and b of the product of the differential event rate dR/dE , the detector efficiency $\epsilon(E)$, and the exposure X , where dR/dE itself is calculated using σ_0 . Substituting this into Eq. 5.3 and isolating for σ_u provides the formula for calculating the upper limit on the cross section:

$$\sigma_u = \frac{N_u \sigma_0}{X \int_a^b dE \frac{dR}{dE} \epsilon(E)}. \quad (5.4)$$

Equation 5.4 is used for setting the upper limit on each of the coupling parameters studied in this analysis by replacing dR/dE and σ with the appropriate signal model and coupling parameter, respectively, for each DM candidate. The relevant coupling parameters are: the LDM-electron scattering cross section $\bar{\sigma}_e$, the dark photon kinetic mixing parameter ϵ , and the axioelectric coupling constant g_{ae} . See Sec. 1.5 for more details about each DM model. For the dark photon and ALP models, the signal rates have a quadratic dependence on their respective coupling parameters, and thus Eq. 5.4 is used by replacing $\sigma \rightarrow \epsilon^2$ or $\sigma \rightarrow g_{ae}^2$. As such, a square root on the R.H.S. of Eq. 5.4 is required for calculating the upper limit of these coupling parameters. The reference σ_0 values used in all limit calculations are $\bar{\sigma}_{e,0} = 10^{-37} \text{ cm}^2$, $\epsilon_0 = 5 \times 10^{-13}$, and $g_{ae,0} = 5 \times 10^{-11}$, which are the reference values that have been used for prior analyses [106, 148].

For the HVEV Run 2 analysis, the differential rate dR/dE in Eq. 5.4 is the differential rate of the *quantized* signal spectrum over the measured phonon energies (dR/dE_{ph} from Sec. 2.2.3), which takes into account the detector response model. Due to the quantized nature of the observed energy spectra, and of the expected DM signal models, a natural choice of intervals for limit setting are the e^-h^+ -pair peaks. For each DM signal model at each DM sampled mass, an interval is positioned around each e^-h^+ -pair

peak in the signal model having a width of $\pm 3\sigma_E$, where σ_E is the energy resolution. Therefore at each sampled mass, an upper limit is calculated for as many e^-h^+ -pair peaks that exist in the expected signal within the analysis range; at most this means an upper limit for the 1st–6th e^-h^+ -pair peaks. Because there is greater confidence in the signals models in the e^-h^+ -pair peak regions and, in contrast, less confidence in the between-peak regions that are modeled by charge trapping (CT) and impact ionization (II) (see Sec. 4.5.4), upper limits are not calculated in cases where the between-peak contribution to the signal model is more dominant than the e^-h^+ -pair peak contribution. At each sampled DM mass, the lowest upper limit amongst those calculated at each e^-h^+ -pair peak is selected as the final result. However calculating more upper limits for a single sampled DM mass comes at the cost of lowering the overall C.L. of the final result. Section 5.2 describes the selection process used to restrict the number of upper limits are considered for selecting the final result.

5.1.3 Comparison of Methods

Given the same limit setting interval and C.L., the OI and Poisson methods will produce very similar results. Furthermore for most sampled DM masses, the OI method is able to find a limit setting interval that can set a stronger limit than the Poisson upper limit. Due to the cost that the OI method pays in order to have the freedom to choose the limit setting interval, there are some cases, as observed in Ref. [142], in which the Poisson method can produce a stronger limit than the OI method. However in this analysis the choice of limit setting method is not decided based on which produces the strongest limits. Rather, the choice is made based on how each method responds to experimental uncertainties.

One of the most significant differences observed between the two methods is how sensitive the computed upper limit σ_u is to the energy resolution σ_E . σ_E determines the width of the e^-h^+ -pair peaks in the DM signal models and, for the Poisson method, also determines the limit setting interval. As listed in Tab. 4.9, the energy resolution for the data measured at 100 V is $\sigma_{\langle E \rangle} = 3.6 \pm 0.3$ eV. The impact of the uncertainty in $\sigma_{\langle E \rangle}$ can be studied by comparing the upper limits produced when using three choices of energy resolution: $\sigma_E = \sigma_{\langle E \rangle}$, $\sigma_E = \sigma_{\langle E \rangle} + 2\Delta_{\sigma_{\langle E \rangle}}$, and $\sigma_E = \sigma_{\langle E \rangle} - 2\Delta_{\sigma_{\langle E \rangle}}$, where $\Delta_{\sigma_{\langle E \rangle}}$ is the uncertainty in $\sigma_{\langle E \rangle}$. Figure 5.1 shows the LDM-electron scattering signal models produced for each choice of σ_E , along with the 100 V, stage-0, DM-search data. The signal models are scaled by the upper limit cross sections computed from each respective model using either the OI method (left) or Poisson method (right).

Figure 5.1 illustrates one of the main problems with using the OI method for limit setting in this analysis. Due to the extremely small energy resolution of the detector, the OI method is hyper-sensitive to the shape of the DM signal model around the e^-h^+ -pair peaks. In the left plot of Fig. 5.1, the signal model with largest σ_E (corresponding to the orange curve) produces a very aggressive upper limit. This occurs because the OI method can take advantage of the fact that the peak width in the signal model is slightly larger than the peak width in the data. In contrast, the same variations in the signal model leads to very small differences in the upper limit when the Poisson method is used, as is evidenced by the nearly matching heights of the three curves in the right plot of Fig. 5.1. In short, a small uncertainty in the detector resolution results in a large uncertainty in the upper limit when using the OI method, while only a negligible uncertainty when using the Poisson method. Figure 5.2 shows the impact on the LDM-electron scattering cross section $\bar{\sigma}_e$ upper limit computed using either the OI or Poisson method when σ_E is varied from $\sigma_{\langle E \rangle} - 2\Delta_{\sigma_{\langle E \rangle}}$ to $\sigma_{\langle E \rangle} + 2\Delta_{\sigma_{\langle E \rangle}}$.

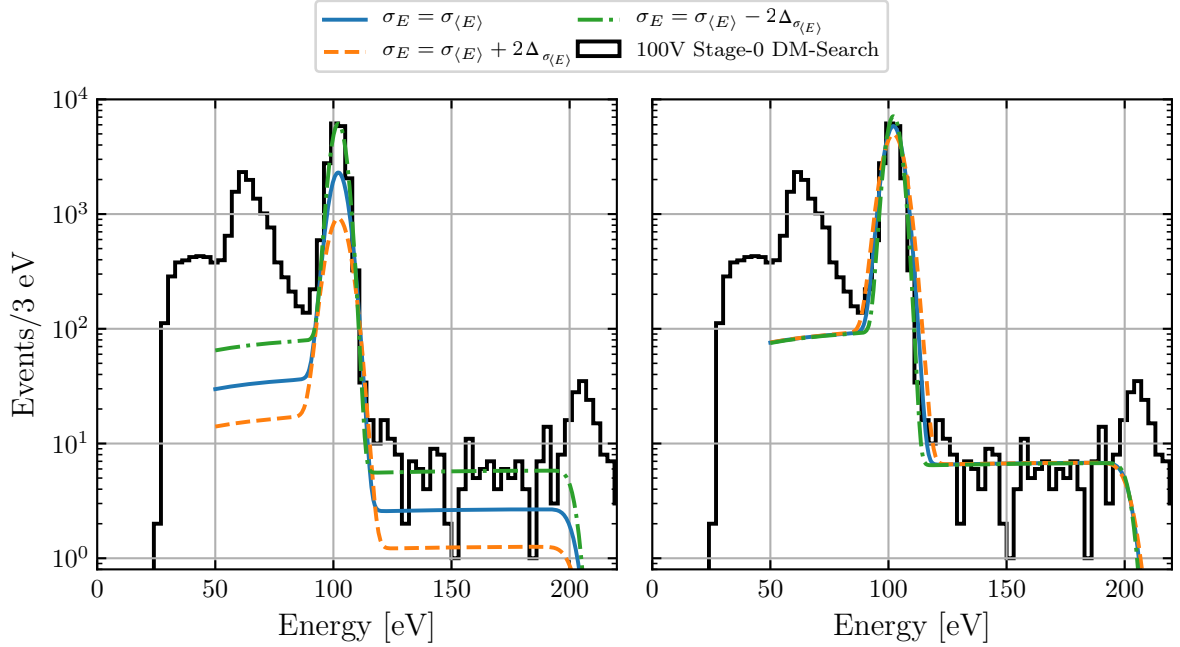


Figure 5.1: Comparison of the LDM-electron scattering signal model produced at a mass of $1 \text{ MeV}/c^2$ with varying choices of the detector energy resolution σ_E . The signal models are scaled by the upper limit cross sections computed from each respective model using the optimum interval (left) or Poisson counting (right) limit setting method. The upper limits are calculated on the 100 V, stage-0, DM-search data.

Another problem with the OI method is that it can choose a limit setting interval that spans multiple e^-h^+ -pair peaks in a signal model. Therefore it is possible that an upper limit may be set by partially or fully using the regions of a signal model which have the lowest confidence or highest uncertainty. Figure 5.3 illustrates this point by showing the dark photon absorption signal models that are produced using varying choices of the Fano factor F in the detector response model (see Sec. 2.2.1). The signal models are scaled by the upper limit kinetic mixing parameters computed from each respective signal model using the OI method, and are shown along with the 100 V, stage-0, DM-search data. The red shaded region identifies the limit setting interval chosen by the OI method; the interval is identical for each signal model.

The most dominant regions of the signal models shown in Fig. 5.3 are outside of the analysis range, and thus the OI method must set the upper limits using the sub-dominant regions, or the signal “tails”, that span across multiple e^-h^+ -pair peaks. However as the green curve Fig. 5.3 shows, when a small Fano factor is used, the signal in these “tail” regions becomes completely dominated by the between-peak contribution to the signal model. The result is that the upper limit is extremely sensitive not only to the choice of Fano factor, but also to the measured charge trapping probability and its uncertainty. The sensitivity from these parameters is dampened when the Poisson limit setting method is used. Perhaps more importantly, the Poisson method would elect not to calculate an upper limit on the $F = 10^{-4}$ signal model in Fig. 5.3 due to the lack of prominent e^-h^+ -pair peaks in the signal.

Overall, these examples summarize why the Poisson counting method is chosen over the OI method for limit setting in this analysis. Although the OI method can produce stronger upper limits, the Poisson

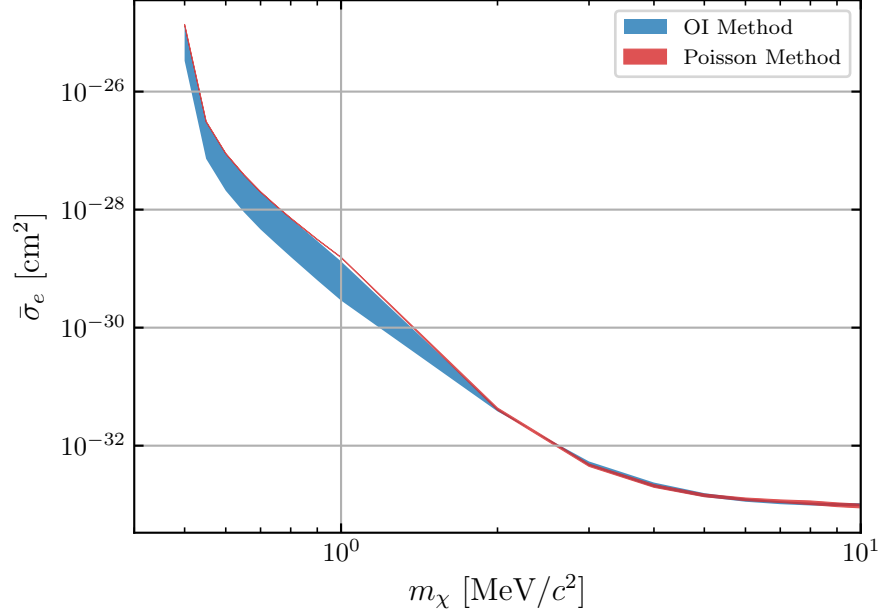


Figure 5.2: Variation in the LDM-electron scattering cross section $\bar{\sigma}_e$ upper limit as a result of varying the detector energy resolution σ_E in the signal model from $\sigma_{\langle E \rangle} - 2\Delta_{\sigma_{\langle E \rangle}}$ to $\sigma_{\langle E \rangle} + 2\Delta_{\sigma_{\langle E \rangle}}$. The variations in $\bar{\sigma}_e$ are shown for when the optimum interval (OI) (blue) or Poisson counting (red) limit setting method is used.

method is generally less sensitive to experimental and model uncertainties, and therefore provides greater confidence in the limit results. It is also important to acknowledge that neither the OI nor the Poisson method include a proper way of incorporating uncertainties into the limit. For some other limit setting techniques, uncertainties in the limit are directly reflected in the position of the computed limit. A maximum likelihood method would be able to properly incorporate uncertainties into the limit, although this method requires the sources of background events to be known and well-understood.

5.2 Initial Limit Results

The initial exclusion limit results are calculated using the stage-0, DM-search spectra measured at 60 and 100 V described in Sec. 4.4.2 in order to establish the limit setting procedure and to check whether any unexpected results arise in the limits produced. Along with the data spectra, the limits are calculated using the efficiency curves described in Sec. 4.5.2 and the 60 and 100 V, stage-0, exposures calculated in Sec. 4.5.1. The DM signal models are produced using a detector energy resolution of 3.4 eV and 3.5 eV for the 60 and 100 V measurements, respectively; these values are from early calculations of the energy resolution and thus differ slightly from the final values tabulated in Tab. 4.9. As mentioned in Sec. 2.2, the parameters inputted into the detector response model for both the 60 and 100 V measurement include $F = 0.155$ for the Fano factor and $\epsilon_{eh} = 3.8$ eV for the average energy per e^-h^+ pair. Furthermore, the band gap energy of Si is taken to be $E_g = 1.2$ eV, and the CT and II probabilities are taken to be 15% and 1%, respectively. The CT and II probability values are obtained from early estimates and differ from the final values calculated in Sec. 4.5.4. They are therefore only used for computing the initial

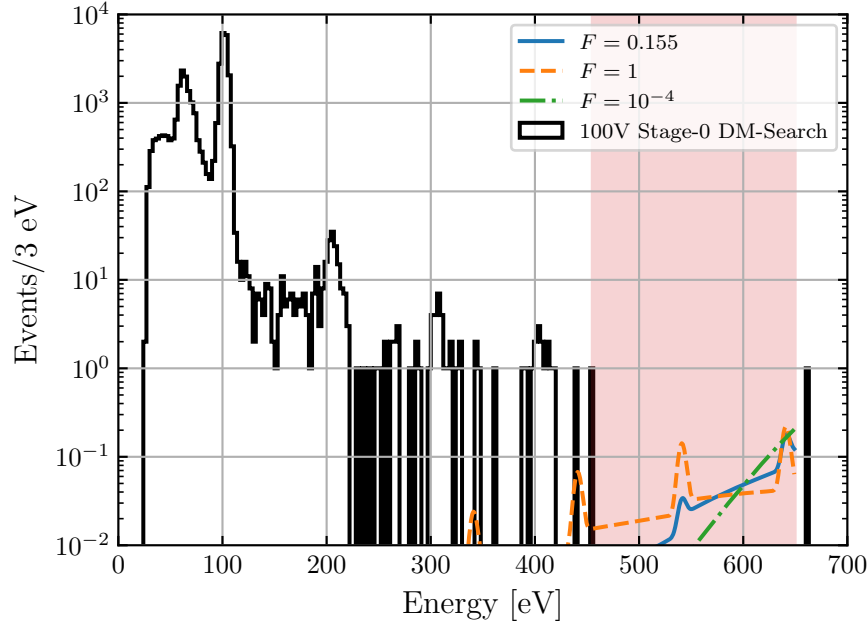


Figure 5.3: Comparison of the dark photon absorption signal model produced at a mass of $41 \text{ eV}/c^2$ with varying choices of the Fano factor F in the detector response model. The signal models are scaled by the upper limit kinetic mixing parameters computed from each respective signal model using the optimum interval limit setting method. The upper limits are calculated on the 100 V, stage-0, DM-search data, and the red, shaded region corresponds to the limit setting interval chosen for all three signal models.

limit results. Lastly, the DM absorption models use the nominal photoelectric absorption cross section curve described in Sec. 2.3.3.

As mentioned in the previous sub-section, the Poisson limit setting method involves producing an upper limit at each possible e^-h^+ -pair peak in the DM-signal model for each sampled DM mass. The lowest upper limit amongst those computed is then selected as the final result. However due to an effect similar to the look-elsewhere effect, computing and comparing multiple upper limits lowers the overall confidence in the selected result. Broadly speaking, computing an upper limit at multiple e^-h^+ -pair peaks can be thought of as performing multiple tests (or “looking elsewhere”) on the same dataset. The upper limit that is ultimately selected may be chosen just by chance due to the number of tests performed. To account for the look-elsewhere-like effect, the C.L. of each individual e^-h^+ -pair upper limit is adjusted such that the C.L. of the selected upper limit is 90%. Specifically if an upper limit is calculated for n e^-h^+ -pair peaks, the C.L. that each individual upper limit must have, C_n , so that the selected upper limit has a C.L. of $c = 0.9$ is given by [149]:

$$C_n = c^{\frac{1}{n}}. \quad (5.5)$$

For example, if an upper limit is calculated for all six e^-h^+ -pair peaks within the analysis range, each upper limit must be calculated with a C.L. of $\sim 98\%$ in order for the selected upper limit to have a C.L. of 90%. Equation 5.5 is an ansatz that is used to approximate the effect of counting multiple peaks. This approach has not yet been shown to produce limits that have the proper statistical coverage given the nature of DM signal models to contribute to multiple e^-h^+ -pair peaks. However, it is believed

to result in conservative upper limits. Naturally this approach invokes a trade-off between calculating more individual upper limits to have a better chance of selecting the lowest (i.e. strongest) upper limit possible, and raising (i.e. weakening) the value of each individual upper limit. It is not always necessary or practical to calculate an upper limit for each possible e^-h^+ -pair peak. For instance, for small DM masses the signal models only have one e^-h^+ -pair peak, and therefore only one upper limit is calculated and selected. At large DM masses, the shape of the signal models often makes it statistically improbable that the upper limit calculated for the first e^-h^+ -pair peak will be selected; it is therefore prudent to neglect this upper limit in order to lower the C.L. required for the other upper limits. These scenarios are illustrated in Fig. 5.4, which shows the upper limits on the LDM-electron scattering cross section $\bar{\sigma}_e$ with form factor $F_{\text{DM}} = 1$ and the dark photon kinetic mixing parameter ϵ calculated from the 100 V, stage-0, DM-search spectrum for each e^-h^+ -pair peak using a 90% C.L. Also shown are the lower envelopes determined by selecting the lowest upper limit at each sampled DM mass.

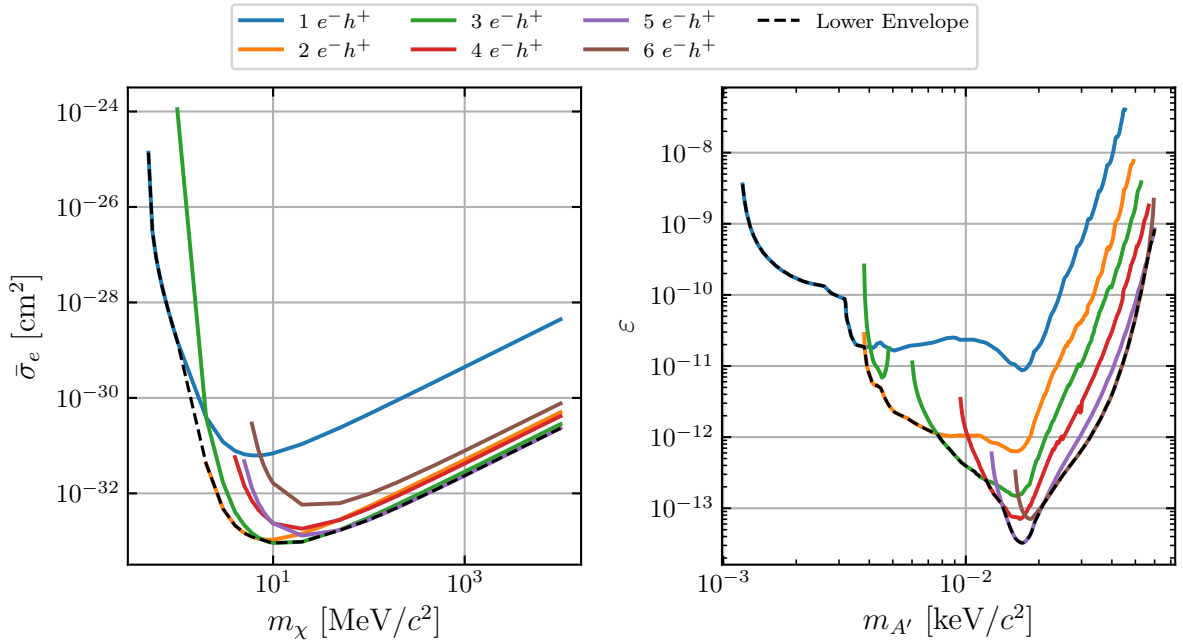


Figure 5.4: Upper limits calculated at each e^-h^+ -pair peak on the LDM-electron scattering cross section with form factor $F_{\text{DM}} = 1$ (left) and dark photon kinetic mixing parameter (right). The limits are calculating using the stage-0, DM-search data measured at 100 V. The lower envelopes are determined by selecting the lowest upper limits are each DM mass.

There is a need to develop a procedure to decide how many upper limits at which e^-h^+ -pair peaks should be calculated at each sampled DM mass for each DM signal model. Furthermore this procedure must be developed using the stage-0, DM-search spectra in order to avoid introducing bias. This last point is critical; any procedure that requires an initial calculation of the limit results on a particular dataset inherently introduces bias in the final result for that dataset. Conversely a procedure that only uses the stage-0 datasets to decide which upper limits to calculate for the stage-2, unblinded datasets is not biased because the upper limit results from the stage-2 datasets are unknown.

The procedure starts by calculating the upper limits at a 90% C.L. from the stage-0, DM-search spectra for all e^-h^+ -pair peaks possible at each DM mass sampled. Instead of simply selecting the

lowest upper limit, the procedure is supplemented by asking two questions: (i) what if the upper limit results are due to random statistical fluctuations? and (ii) what if the upper limit results are dependent on the experiment exposure? To address the first question, the upper limits are recalculated assuming that the observed number of events within any e^-h^+ -pair peak interval, N_{obs} , is a statistical under- or over-fluctuation. For the case of assuming a statistical *under*-fluctuation, the number of observed events is adjusted to N_{adj} such that $N_{\text{adj}} - \sigma = N_{\text{obs}}$, where σ the standard deviation of a Poisson distribution that has a mean of N_{adj} . Conversely for the case of assuming a statistical *over*-fluctuation, the number of observed events is adjusted to N_{adj} such that $N_{\text{adj}} + \sigma = N_{\text{obs}}$. For each DM mass sampled, any e^-h^+ -pair peak whose upper limit is selected as the lowest limit under any combination of statistical fluctuation assumptions is added to a list of e^-h^+ -pair peaks whose upper limit will be considered for selection. This step has two main functions. First, it will neglect those e^-h^+ -pair peaks whose upper limits are very unlikely to be selected as the lowest limit, such as the first e^-h^+ -pair peak at high DM masses. Second, it will include those e^-h^+ -pair peaks that may be selected given various scenarios of measuring statistical fluctuation.

The second question is addressed by recalculating the upper limits for each e^-h^+ -pair peak after multiplying the number of observed events in each limit setting interval, as well as the experiment exposure, by a factor of 9. This scaling is meant to approximate how the upper limits calculated for each e^-h^+ -pair peak will change if the stage-2, unblinded, DM-search spectra with 90% of the data is used. The number of events observed in the fifth and sixth e^-h^+ -pair peak intervals from stage-0, DM-search spectra is often zero, and thus the upper limits calculated for these e^-h^+ -pair peaks are entirely exposure limited. Conversely there are often $\mathcal{O}(10^3 - 10^4)$ events observed in the first e^-h^+ -pair peak interval, and therefore the corresponding upper limits are minimally affected by exposure. After recalculating the upper limits with the scaled exposure, they are again recalculated with the scaled exposure but with also assuming statistical under- or over-fluctuations in the same manner as before. Any e^-h^+ -pair peak whose upper limit is selected as the lowest limit at the scaled exposure under any combination of statistical fluctuation assumptions is added to the list of e^-h^+ -pair peaks whose upper limit will be considered for selection. The entire selection procedure is done separately for the 60 and 100 V measurements, and for the various assumptions of the Fano factor in the detector response model. Figure 5.5 shows the results of this procedure for the LDM-electron scattering limit with form factor $F_{\text{DM}} = 1$ and dark photon absorption limit for the 100 V measurement using the assumed value of $F = 0.155$ for the Fano factor.

The procedure described above has most importantly determined which e^-h^+ -pair peak upper limits at each DM mass sampled will be considered for selecting the final limit results after the data is unblinded. This information, although somewhat redundantly, is also used to calculate the initial limit results. Figure 5.6 shows the initial exclusion results for each DM interaction channel from the stage-0, DM-search data spectra measured at 60 and 100 V, along with the HVEV Run 1 limit results for comparison where applicable.

The initial limit results shown in Fig. 5.6 appear reasonable, and some qualitative assessments can be made. The differences between the 60 and 100 V limit results can be understood by knowing where the exclusion limits are background or exposure limited. The event rates in the first and second e^-h^+ -pair peaks are similar in the two measurements, however the 100 V measurement has about three times the exposure. Therefore in the regions where the limits are selected from the first or second e^-h^+ -pair peak, which include the low DM mass regions in all interaction channels, the limit results are similar.

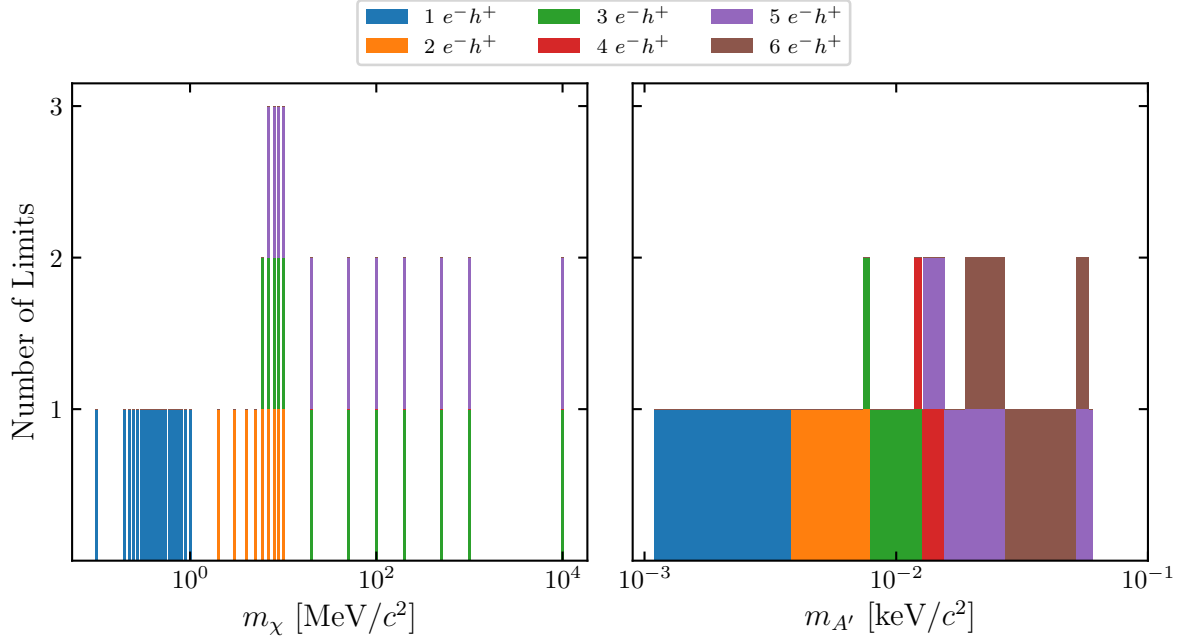


Figure 5.5: Results of the selection procedure to determine how many upper limits at which e^-h^+ -pair peaks will be considered for selection when calculating the final exclusion limits. The results shown correspond to LDM-electron scattering with form factor $F_{\text{DM}} = 1$ (left) and dark photon absorption (right) for the data measured at 100 V using the assumed value of $F = 0.155$ for the Fano factor.

Conversely in the regions the limits are selected from higher e^-h^+ -pair peaks, including the high mass regions of the absorption interaction channels as well as the high mass regions of the $F_{\text{DM}} = 1$ LDM-electron scattering limit, the 100 V measurement produces a stronger limit due to greater exposure. The same assessment can generally be applied to compare these results with the HVeV Run 1 results. Because the event rates in the first and second e^-h^+ -pair peaks are comparable, the exclusion limits are also comparable in background limited regions. In the exposure limit regions, the HVeV Run 1 results are stronger due to the 3.5 times greater exposure.

These results also provide some expectations for the final limit results after the data is unblinded. The final results are unlikely to exceed the HVeV Run 1 results in the background-limited regions unless the event rates in the lower e^-h^+ -pair peaks are significantly reduced. The final results may exceed the HVeV Run 1 results in some high mass regions if those regions remain exposure limited after unblinding. Lastly these initial results do not incorporate experimental and model uncertainties. An initial study shows that the Fano factor and the photoelectric absorption cross section appear to be the most dominant sources of uncertainties in the limit results. All of the uncertainties are incorporated into the final limit results, as is described in Sec. 5.4.

5.3 Unblinding

Before the final limit results can be produced, the remaining 90% of the measured background data must be unblinded and processed using the same corrections, calibrations, and cuts described in the previous sections.

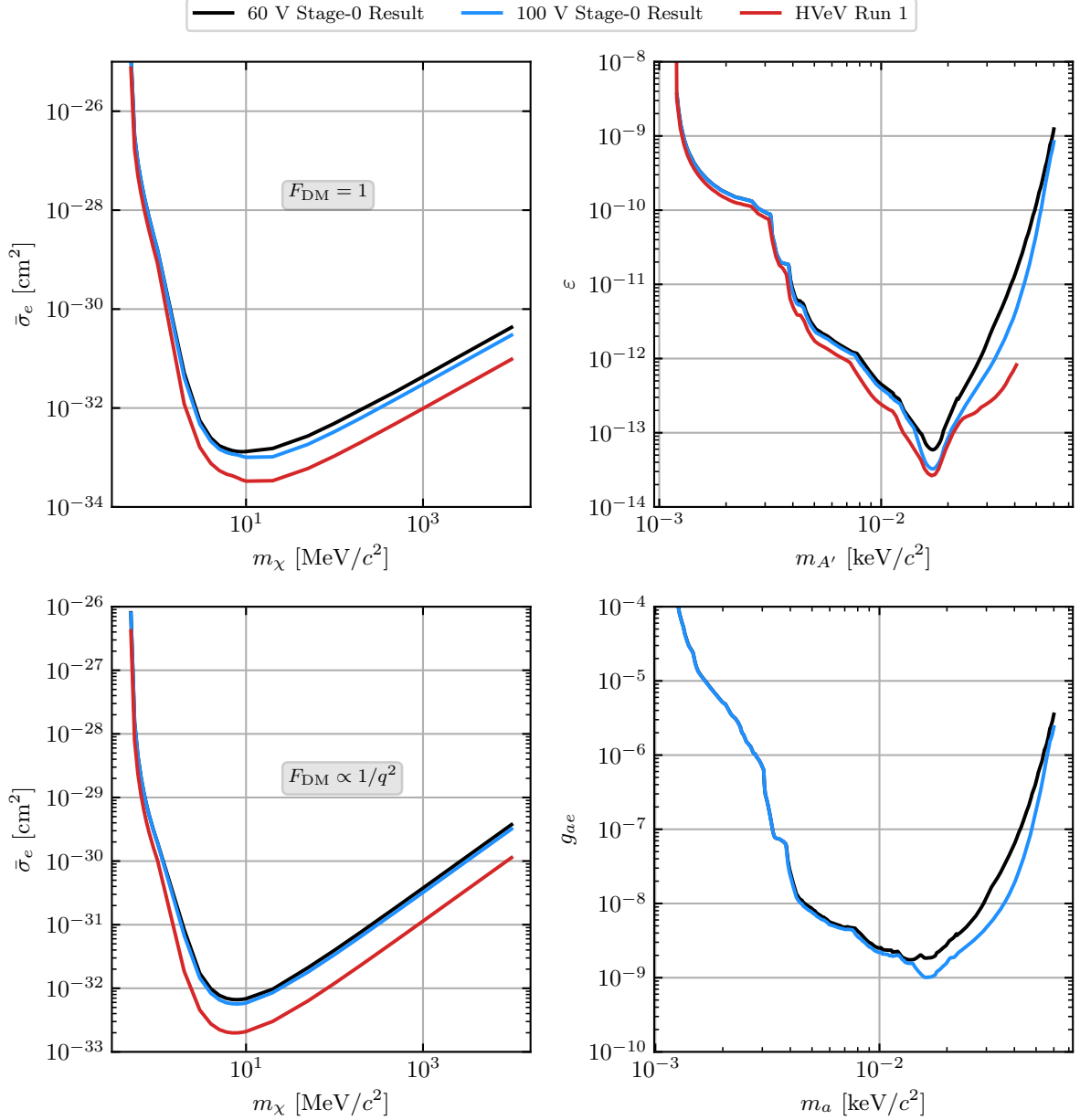


Figure 5.6: Initial 90% C.L. upper limits calculated using the stage-0, DM-search data measured at 60 V (black) and 100 V (blue). Clockwise starting from the top-left plot, the limit results are shown for the LDM-electron scattering cross section $\bar{\sigma}_e$ with form factor $F_{\text{DM}} = 1$, the dark photon kinetic mixing parameter ϵ , the axioelectric coupling constant g_{ae} , and $\bar{\sigma}_e$ with form factor $F_{\text{DM}} \propto 1/q^2$. The results from the HVeV Run 1 analysis [106] (red), which did not produce a result for g_{ae} , are shown for comparison.

The temporal blinding scheme and data partitioning is outlined in Sec. 4.2.4. So far only the stage-0 background data, which amounts to 10% of the entire dataset, has been processed and analyzed. The unblinding strategy for this analysis consists of two stages. First, the stage-1 data, which amounts to an additional 20% of the entire dataset, is unblinded and processed. If the stage-1 datasets pass a series of verification tests, they will be included in the final results. Second, the stage-2 data, which consists of

the remaining 70% of the background data, is unblinded and processed. If the stage-2 datasets pass the same series of verification test, it will also be used to produce the final results. If the verification tests on the stage-2 datasets fail and any part of the analysis pipeline is altered, the unblinding is considered unsuccessful and the final results are produced for a non-blinded analysis. Thus final results for a 90% blinded analysis are possible if and only if both the stage-1 and stage-2 datasets pass the verification tests and no alterations are made to the analysis pipeline.

The unblinding verification tests are separated into three categories: (i) livetime cuts; (ii) data-quality (DQ) cut parameters; and (iii) energy spectra. The livetime cut verification tests are performed by successively applying the livetime cuts described in Sec. 4.4.1 to either the stage-1 or stage-2 datasets. For the stage-1 unblinding, the livetime cuts are considered successful if the passage fraction after each successive cut on the combined stage-0 and stage-1 data is within 5 percentage points of that of the stage-0 data alone. Likewise for the stage-2 unblinding, the livetime cuts are considered successful if the passage fraction after each successive cut on the entire dataset is within 5 percentage points of that of the combined stage-0 and stage-1 data.

The DQ cut parameter verification tests are performed by successively applying the each of the DQ cuts described in Sec. 4.4.2 (except for the unused partition cut) to either the stage-1 or stage-2 datasets. Before each DQ cut is applied, the distributions in the relevant cut parameter are compared in order to assess the consistency of the distributed parameter; if two distributions are consistent, then the cut performance will also be consistent. Although the mean base cut is applied separately to each daily background dataset, the verification test is performed on the Δ Mean Base parameter distributions that combine the data from all days. Finally the energy spectra verification tests are performed by comparing the energy spectra of the stage-1 or stage-2 datasets after all livetime and DQ cuts are applied. For the stage-1 unblinding, the distributions from the stage-1 datasets are compared to those from the stage-0 data; for the stage-2 unblinding, the distributions from the stage-2 datasets are compared to those from the combined stage-0 and stage-1 data. For the purposes of plotting or visual inspection, only the normalized distributions are constructed in order to keep the total number of events in a distribution unknown.

The cut parameter and energy distributions are compared using two-sample Kolmogorov-Smirnov (KS) tests [150]. The null-hypothesis for a two-sample KS test is that the samples are drawn from the same underlying distribution. Therefore the KS test will evaluate the probability that the underlying distribution in a particular parameter is the same between two different stages of unblinding. For comparing two samples with empirical distribution functions (EDFs) $F_{1,n}(x)$ and $F_{2,m}(x)$ with sizes n and m , respectively, distributed over some parameter x , the KS statistic is given by:

$$D_{n,m} = \sup_x |F_{1,n}(x) - F_{2,m}(x)|, \quad (5.6)$$

where \sup is the supremum function that finds the maximum absolute difference between the EDFs of the two samples. The null hypothesis is rejected at a level α if

$$D_{n,m} > c(\alpha) \sqrt{\frac{n+m}{n \cdot m}}, \quad (5.7)$$

where $c(\alpha) = \sqrt{-\ln(\alpha/2) \cdot 1/2}$. The dependence on m and n means a smaller $D_{n,m}$ is required for larger samples to reject the null hypothesis at a given α . By rearranging Eq. 5.7, the null hypothesis is

rejected at a level α if

$$\text{KS}_t = 2e^{-\frac{2D_{n,m}^2}{n+m}} < \alpha, \quad (5.8)$$

where KS_t is simply a rearranged form of the KS statistic. For the DQ cut parameter and energy spectra verification tests, a level $\alpha = 0.01$ is chosen, and thus a test is considered successful for a distribution comparison if $\text{KS}_t > 0.01$ or, in terms of percentages, $\text{KS}_t > 1\%$.

The KS test strictly evaluates the similarity between two samples, rather than evaluating the similarity to some known distribution. This makes the test ideal for this analysis, as some samples, particularly the energy spectra, do not have a known or expected underlying distribution. Furthermore the KS tests performed on the energy spectra also provide a verification of the energy calibration after unblinding; an error in calibration would lead to a larger $D_{n,m}$ and thus a larger chance of rejecting the null hypothesis.

5.3.1 Stage-1 Unblinding

Table 5.1 summarizes the passage fraction of events for each livetime cut after the stage-1 unblinding. Also listed is the absolute difference $|\Delta|$ in the passage fraction for each cut before and after unblinding, which is the quantity of interest for the verification study. Table 5.2 summarizes the KS statistic KS_t defined by Eq. 5.8 computed for each DQ cut parameter distribution and the final energy spectra after the stage-1 unblinding. In order to negate any temperature effects in the various distributions, the KS_t values are evaluated separately for the data measured at 50 and 52 mK in the 60 V measurement.

Table 5.1: Summary of the passage fractions computed after each livetime cut is successively applied either to the combined stage-0 and stage-1 data or the stage-0 data alone for the 60 and 100 V measurements. The absolute difference $|\Delta|$ in the passage fractions are also reported in percentage points. The unblinding verification test for a livetime cut is considered successful if $|\Delta| < 5$.

Passage Fraction [%]	60 V			100 V		
	Stage-0+1	Stage-0	$ \Delta $	Stage-0+1	Stage-0	$ \Delta $
Raw Livetime	100.00	100.00	0.00	100.00	100.00	0.00
30 s Fridge Temperature Cut	66.54	68.44	1.90	67.90	66.80	1.10
Mean Base Cut	51.16	53.44	2.28	49.63	50.80	1.17
1 s Fridge Temperature Cut	51.05	53.44	2.39	49.60	50.78	1.18
Trigger and Leakage Burst Cut	45.42	49.91	4.49	44.97	46.62	1.65

As seen in Tab. 5.1, all of the livetime cuts for both the 60 and 100 V measurements pass the verification criterion. Table 5.2 shows that all of the DQ cut parameters and the final energy spectrum for both the 60 and 100 V measurement pass the verification criterion. Based on these results, the stage-1 unblinding is considered to be successful, and the stage-1 datasets can be included in the final results.

5.3.2 Stage-2 Unblinding

Table 5.3 summarizes the passage fraction of events for each livetime cut after the stage-2 unblinding. Also listed is the absolute difference $|\Delta|$ in the passage fraction for each cut before and after unblinding, which is the quantity of interest for the verification study. Table 5.4 summarizes the KS statistic KS_t

Table 5.2: Summary of the KS statistic KS_t defined by Eq. 5.8 computed for each data-quality (DQ) cut parameter distributed for the stage-0 and stage-1 datasets. KS_t is evaluated using the distributions constructed in each cut parameter before the corresponding cut is applied, as well as the final energy spectra after all cuts are applied to the datasets. For the 60 V measurement, KS_t is evaluated separately for the data measured at 50 and 52 mK. The unblinding verification test for a DQ cut parameter or an energy spectrum is considered successful if $KS_t > 1\%$.

KS_t [%]	60 V		100 V
	50 mK	52 mK	50 mK
Trigger Offset Cut	95.7	47.9	12.2
Mean Base Cut	65.2	1.1	73.5
$\chi^2(f)$ Cut	38.0	69.2	8.2
$\chi^2(t)$ Cut	45.1	25.0	63.4
Veto Detector Cut	60.0	56.4	4.9
Energy Spectrum	28.8	39.9	16.7

defined by Eq. 5.8 computed for each DQ cut parameter distribution and the final energy spectra after the stage-2 unblinding. Like with the stage-1 unblinding, the KS_t values are evaluated separately for the data measured at 50 and 52 mK in the 60 V measurement.

Table 5.3: Summary of the passage fractions computed after each livetime cut is successively applied either to the entire dataset (stage-0, stage-1, and stage-2 combined) or the stage-0 and stage-1 combined data for the 60 and 100 V measurements. The absolute difference $|\Delta|$ in the passage fractions are also reported in percentage points. The unblinding verification test for a livetime cut is considered successful if $|\Delta| < 5$.

Passage Fraction [%]	60 V			100 V		
	Stage-0+1+2	Stage-0+1	$ \Delta $	Stage-0+1+2	Stage-0+1	$ \Delta $
Raw Livetime	100.00	100.00	0.00	100.00	100.00	0.00
30 s Fridge Temperature Cut	65.90	66.54	0.64	67.93	67.90	0.03
Mean Base Cut	51.69	51.16	0.53	51.33	49.63	1.70
1 s Fridge Temperature Cut	51.60	51.05	0.55	51.27	49.60	1.67
Trigger and Leakage Burst Cut	43.76	45.42	1.66	44.60	44.97	0.37

As seen in Tab. 5.3, all of the livetime cuts for both the 60 and 100 V measurements again pass the verification criterion. Table 5.4 shows that the final energy spectrum for the 60 and 100 V measurement and all of the DQ cuts for the 60 V measurement pass the verification criterion. However for the 100 V measurement, all the DQ cuts pass the verification criterion except for the mean base cut; because the mean base cut has $KS_t = 0.2\%$, the null hypothesis is rejected a level $\alpha = 1\%$. This failed verification test warrants a closer inspection of the mean base distributions, but does not necessarily mean that alterations to the analysis pipeline are required. Figure 5.7 compares the normalized distributions of the Δ Mean Base parameter from the stage-2 and combined stage-0 and stage-1 datasets measured at 100 V. Recall that Δ Mean Base is used to combine the mean base distributions from each day of data acquisition.

Table 5.4: Summary of the KS statistic KS_t defined by Eq. 5.8 computed for each data-quality (DQ) cut parameter distributed for the stage-2 and the combined stage-0 and stage-1 datasets. KS_t is evaluated using the distributions constructed in each cut parameter before the corresponding cut is applied, as well as the final energy spectra after all cuts are applied to the datasets. For the 60 V measurement, KS_t is evaluated separately for the data measured at 50 and 52 mK. The unblinding verification test for a DQ cut parameter or an energy spectrum is considered successful if $KS_t > 1\%$.

KS_t [%]	60 V		100 V
	50 mK	52 mK	50 mK
Trigger Offset Cut	14.4	19.7	94.3
Mean Base Cut	65.9	41.0	0.2
$\chi^2(f)$ Cut	77.3	47.7	71.5
$\chi^2(t)$ Cut	65.4	76.9	83.6
Veto Detector Cut	74.4	1.6	29.3
Energy Spectrum	14.6	99.3	70.7

Overlaid is the absolute difference between the EDFs from each data set. The maximum value of this curve is the KS statistic $D_{n,m}$ defined by Eq. 5.6; for the distributions in Fig. 5.7, $D_{n,m} = 0.66\%$.

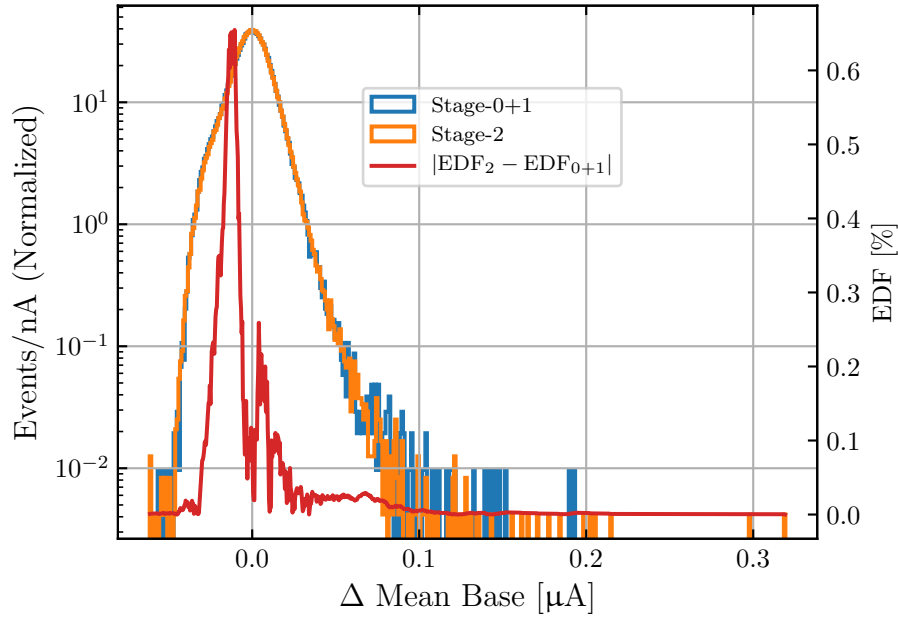


Figure 5.7: Left y-axis: comparison of the normalized Δ Mean Base distributions produced using the stage-2 (orange) and combined stage-0 and stage-1 (blue) datasets measured at 100 V. The distributions contain the background data measured during all days of data acquisition. Right y-axis: the red curve shows the absolute difference between the empirical distribution functions (EDFs) of the two distributions shown in the plot in units of percent. Courtesy of Yen-Yung Chang.

Although the Δ Mean Base distributions in Fig. 5.7 result in a failed KS test, better insight can be gained by comparing the mean base distributions and corresponding EDFs from each day separately.

Figure 5.8 compares the normalized distributions of the mean base parameter from the stage-2 and combined stage-0 and stage-1 datasets measured at 100 V. The individual peaks that are visible in Fig. 5.8 correspond to each day of data acquisition. Also shown is the absolute difference between the EDFs computed separately from the data acquired each day.

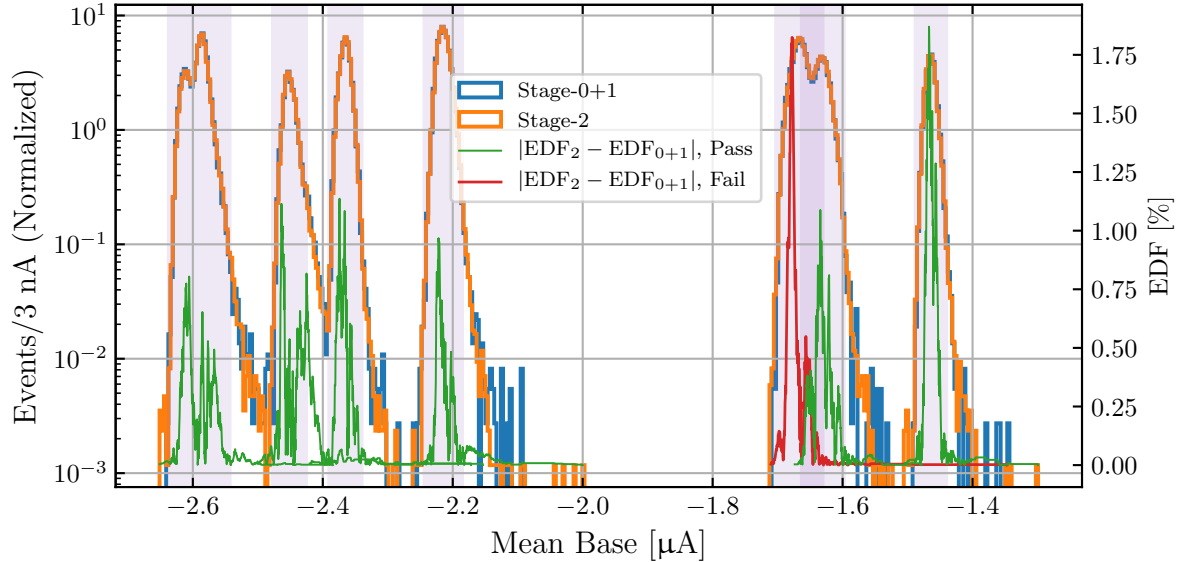


Figure 5.8: Left y-axis: comparison of the normalized mean base distributions produced using the stage-2 (orange) and combined stage-0 and stage-1 (blue) datasets measured at 100 V. The different peaks correspond to the background data measured on separate days of data acquisition. Right y-axis: the absolute difference between the empirical distribution functions (EDFs) computed separately from the data measured on each day in units of percent. The green (red) curves correspond to the distributions that result in a KS_t value $> 1\%$ ($< 1\%$) and thus pass (fail) the validation test. The shaded purple bands indicate the mean base cut thresholds used for the data measured on each day, with some bands overlapping. Courtesy of Yen-Yung Chang.

As Fig. 5.8 shows, the mean base distributions and corresponding EDFs from only one day of data acquisition result in a KS_t value $< 1\%$ and thus a failed validation test. However it is clear in Fig. 5.8 that the region with the largest absolute differences in the EDFs is contained within the mean base cut thresholds for that day (i.e. within the region that passes the mean base cut). This means that when the mean base cut is applied to the stage-2 and combined stage-0 and stage-1 datasets, the difference between the resulting event passage fractions are negligible ($\ll 1\%$). Furthermore if the cut threshold values were determined using the stage-2 data rather than the stage-0 data, the effect on the passage fraction would also be negligible.

Although the KS validation test failed for the mean base parameter for the stage-2 unblinding of the 100 V data, there is no reason to believe that the slight difference in the distributions will have any meaningful impact on the performance of the mean base cut. Therefore the stage-2 unblinding is considered successful, and the stage-2 data for both the 60 and 100 V measurements can be included in the final results. Because the stage-1 unblinding is also considered to be successful, the final results are produced using the combined stage-1 and stage-2 datasets, totalling 90% of the entire dataset. The initial stage-0 data that is used to develop the analysis pipeline are now discarded.

5.4 Final Results

The final results are computed using the final-stage data, which are comprised of the combined stage-1 and stage-2 data. Before the exclusion limit results are produced, properties of the 60 and 100 V final-stage data are examined.

5.4.1 Exposure and Energy Spectra

Table 5.5 summarizes the livetimes measured for the stage-0 and entire datasets, as well as the final livetimes and exposures measured for the final-stage data. The final-stage, DM-search energy spectrum for the 60 and 100 V measurements are shown in Fig. 5.9. These spectra are used to compute the exclusion limits for this analysis. The stage-0 energy spectra are also shown for comparison.

Table 5.5: Summary of the livetime measured for the entire 60 and 100 V datasets compared to the livetime measured for the stage-0 and final-stage data. Because the livetime cuts are recalculated when the data is unblinded, the separate livetime measurements from the stage-0 and final-stage data do not necessarily sum to the livetime of the entire dataset. The exposure of the final-stage data is also reported for a 0.93 g detector.

		Livetime [Hours]			Exposure [g-days]
		Stage-0 (10 %)	All Data (100 %)	Final-Stage (90 %)	Final-Stage (90 %)
60 V	1.25	10.9	9.9	0.39	
100 V	3.6	35.6	31.5	1.22	

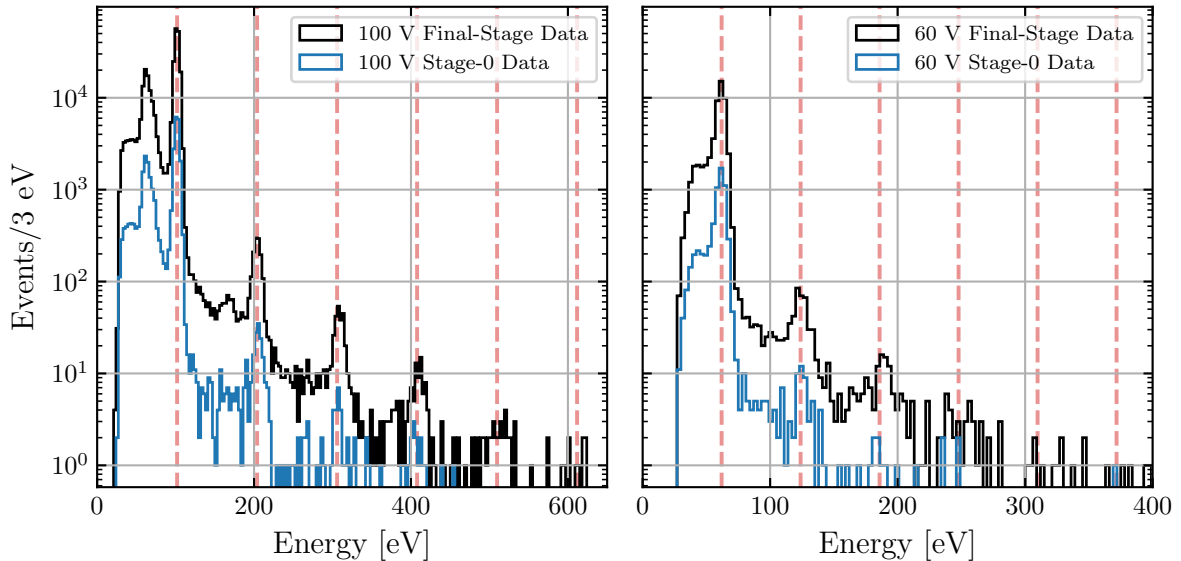


Figure 5.9: Energy spectra of the DM-search data measured at 100 V (left) and 60 V (right). The final-stage, DM-search spectra (black) contain 90% of the entire dataset and are used to produce the final exclusion limits. For comparison, the stage-0, DM-search spectra (blue) used to develop the analysis pipeline are also shown. The red, vertical lines correspond to the calibration energies for the *laser-calibration* data.

Some initial observations can be made regarding the final-stage, DM-search spectra in Fig. 5.9. First, the final-stage datasets reveal events in the fifth and sixth e^-h^+ -pair peak regions that are not observed in the stage-0 datasets. For the purposes of limit setting, this means that these regions are not exposure limited. Second, the prominent peak in the 100 V, DM-search spectra at $\sim 0.5 e^-h^+$ pairs (~ 50 eV) is due to non-quantized events restricted to the outer QET channel. This peak is not present in the 60 V spectra because it is below the 50 eV analysis threshold. Although this peak could be removed with a successful partition cut, it does not impact the final limit results because the limit setting intervals do not fall below $1 e^-h^+$ pair.

Lastly, Tab. 5.6 lists the position E and resolution σ_E of each e^-h^+ -pair peak that can be measured in the final-stage, DM-search energy spectra. For comparison, the same values for the laser-calibration data are also listed. While the positions of the e^-h^+ -pair peaks between the final-stage, DM-search datasets and the laser-calibration datasets are generally in good agreement, the resolutions of some of the peaks appear to significantly differ. Most notably, the resolutions of the second to fourth peak from the 100 V DM-search data are much larger than the corresponding peaks from the laser-calibration data. The source of this discrepancy is unknown, but it may be indicative of a different underlying energy distribution of background events.

Table 5.6: Summary of the positions E and resolutions σ_E of each e^-h^+ -pair peak measured from the final-stage, DM-search data and laser-calibration data. These quantities are only measured up to the third and fourth e^-h^+ -pair peak of the 60 V and 100 V, final-stage, DM-search spectrum, respectively.

60 V				
	Final-Stage DM-Search		Laser-Calibration	
	E [eV]	σ_E [eV]	E [eV]	σ_E [eV]
$1 e^-h^+$	61.45 ± 0.05	3.38 ± 0.05	61.92 ± 0.02	3.35 ± 0.01
$2 e^-h^+$	123.4 ± 0.2	4.0 ± 0.1	123.80 ± 0.02	3.74 ± 0.02
$3 e^-h^+$	186.5 ± 0.3	3.74 ± 0.07	185.80 ± 0.04	4.10 ± 0.04
$4 e^-h^+$	-	-	247.91 ± 0.07	4.20 ± 0.07
$5 e^-h^+$	-	-	310.2 ± 0.1	4.6 ± 0.2
$6 e^-h^+$	-	-	371.7 ± 0.2	4.0 ± 0.2
100 V				
	Final-Stage DM-Search		Laser-Calibration	
	E [eV]	σ_E [eV]	E [eV]	σ_E [eV]
$1 e^-h^+$	101.73 ± 0.06	3.13 ± 0.01	101.83 ± 0.01	3.48 ± 0.01
$2 e^-h^+$	203.83 ± 0.08	5.01 ± 0.04	203.81 ± 0.02	3.98 ± 0.02
$3 e^-h^+$	308.03 ± 0.04	5.43 ± 0.09	305.81 ± 0.05	4.57 ± 0.04
$4 e^-h^+$	408.9 ± 0.2	7.3 ± 0.2	407.72 ± 0.08	4.67 ± 0.83
$5 e^-h^+$	-	-	510.0 ± 0.2	4.9 ± 0.2
$6 e^-h^+$	-	-	611.6 ± 0.3	4.8 ± 0.3

5.4.2 Exclusion Limits

The final DM exclusion limits for this analysis are produced using the 60 and 100 V, final-stage, DM-search spectra shown in Fig. 5.9 and the detector efficiency curves shown in Figs. 4.46 and 4.47. The results are obtained using the Poisson limit setting method outlined in Sec. 5.1.2, and the choices of which e^-h^+ -pair-peak upper limits to select from at each sampled DM mass along with the corresponding C.L. of each individual e^-h^+ -pair-peak upper limit are determined from the initial limit results in Sec. 5.2.

As with the initial results, final exclusion limits are produced on the LDM-electron scattering cross section $\bar{\sigma}_e$ for LDM-electron inelastic scattering the DM form factors $F_{\text{DM}} = 1$ and $F_{\text{DM}} \propto 1/q^2$ for DM masses between 0.5 to $10^4 \text{ MeV}/c^2$; the dark photon kinetic mixing parameter ε for dark photon absorption for dark photon masses between 1.2 to $50 \text{ eV}/c^2$; and the axioelectric coupling constant g_{ae} for ALP absorption for ALP masses between 1.2 to $50 \text{ eV}/c^2$. The expected signal model for a given DM candidate at a given mass requires both experimental and model parameter inputs. The models use the weighted average energy resolutions $\sigma_{\langle E \rangle}$ listed in Tab. 4.9 and the CT and II probabilities stated in Sec. 4.5.4. Furthermore the dark photon and ALP absorption models use the photoelectric absorption cross section $\sigma_{\text{p.e.}}$ curves for Si outlined in Sec. 2.3.3. The detector response model assumes the commonly used values of $E_g = 1.2 \text{ eV}$ and $\epsilon_{eh} = 3.8 \text{ eV}$ for the Si band gap energy and energy per e^-h^+ pair, respectively. The Fano factor F input in the detector response model is treated as a variable parameter.

A method is developed in order to quantify and incorporate the various experimental and model parameter uncertainties into the final limit results. This is done by first constructing a probability distribution for every parameter with an uncertainty. For the energy resolutions and CT/II probabilities, Gaussian distributions are made using the stated values and uncertainties as the Gaussian means and standard deviations, respectively. The uncertainty in the energy calibration as described in Sec. 4.3.5 and parameterized by ΔE_{cal} is considered by constructing a Gaussian distribution with a mean of 0 eV and standard deviation of 0.5 eV. The uncertainties in the efficiency curves are translated to a new parameter n_σ describing the number of standard deviations a new efficiency curve $\epsilon'(E)$ is away from the fitted efficiency curve $\epsilon(E)$. $\epsilon'(E)$ is therefore given by

$$\epsilon'(E) = \epsilon(E) + n_\sigma \cdot \sigma_\epsilon(E), \quad (5.9)$$

where $\sigma_\epsilon(E)$ is the 1σ uncertainty curve of $\epsilon(E)$. The uncertainty bounds seen in Figs. 4.46 and 4.47 correspond to the $\epsilon'(E)$ curves with $n_\sigma = \pm 1$. A Gaussian distribution is constructed for the n_σ parameter with a mean of 0 and standard deviation of 1. The uncertainty in $\sigma_{\text{p.e.}}$ cannot be described by a Gaussian distribution. Instead a uniform distribution is used to randomly select between the nominal, lower bound, and upper bound $\sigma_{\text{p.e.}}$ curves described in Sec. 2.3.3. A summary of the each parameter and corresponding probability distribution is provided in Tab. 5.7.

For each DM model and each DM mass sampled, the limit setting procedure is repeated 5000 times using random variates selected according to the probability distributions described above. This results in limit distributions containing 5000 trails for each possible e^-h^+ -pair peak. At each DM mass sampled, the *average* upper limit at each e^-h^+ -pair peak is calculated, and the *lowest* averaged upper limit is selected as the 90% C.L. result at that DM mass. Recall that not all e^-h^+ -pair peaks are considered when selecting the lowest upper limit; this selection process is predetermined from the initial limit results described in Sec. 5.2. For the selected averaged upper limit at each sampled DM mass, the

Table 5.7: Summary of the experimental and model parameter inputs and probability distributions used to compute the final limit results. In order to incorporate parameter uncertainties into the final results, random variates are selected according to the distributions listed below. The means and widths of the Gaussian and truncated (T.) Gaussian distributions are also listed.

Parameter	Distribution	Mean		Width		Comments
		60 V	100 V	60 V	100 V	
$\sigma_{\langle E \rangle}$ [eV]	Gaussian	3.5	3.6	0.3	0.3	See Sec. 4.5.3.
f_{CT} [%]	T. Gaussian	16.0	11	0.7	3	Truncated at 0%; see Sec. 4.5.4.
f_{II} [%]	T. Gaussian	3×10^{-11}	2	4×10^{-11}	3	Truncated at 0%; see Sec. 4.5.4.
ΔE_{cal} [eV]	Gaussian	0	0	0.5	0.5	See Sec. 4.3.5.
n_{σ}	Gaussian	0	0	1	1	See Eq. 5.9.
$\sigma_{\text{p.e.}}$	Uniform			N/A		Random choice; see Sec. 2.3.3.
Parameter	Value	Comments				
E_g [eV]	1.2	Constant parameter.				
ϵ_{eh} [eV]	3.8	Constant parameter.				
F	10^{-4} -0.3	Separate results for $F = 0.155$, $F = 10^{-4}$, and $F = 0.3$; see Sec. 2.2.1.				

uncertainty in the limit result is determined by evaluating the *equivalent* $\pm 1\sigma$ values from its limit distribution. The equivalent $\pm 1\sigma$ values correspond to the 15.9% and 84.1% points on the distribution's empirical distribution function, regardless of the shape of the distribution. Not all of the resulting limit distributions are Gaussian in shape. This can be due to multiple reasons, including: discrete parameter choices such as the $\sigma_{\text{p.e.}}$ curve, parameters such as the CT or II probability with nonlinear effects on the limit, and edge cases when a single event in a low-event region may or may not be included in the limit setting interval depending on the energy resolution and energy calibration random variates.

Additional consideration is required for certain parameter variates that can produce non-physical results. The first is for the uncertainty in the detector efficiency. Due to the large uncertainty band around the fitted efficiency curve, particularly for the 100 V measurement, many random variates of the n_{σ} parameter will result in a $\epsilon'(E)$ curve that exceeds 1 (i.e. 100% efficiency). Although these cases clearly lead to non-physical limit results, the relationship between the detector efficiency and the upper limits is well understood, and there are no otherwise adverse effects on the limits that would occur if $\epsilon'(E) > 1$. Therefore the limit distributions are computed using all random variates of n_{σ} even if $\epsilon'(E) > 1$. The average upper limits at each $e^{-}h^{+}$ -pair peak are calculated using all limit trials, whereas the equivalent $\pm 1\sigma$ values are calculated only using the limit trails with $\epsilon'(E) \leq 1$ at all energies.

The second parameter that needs consideration is the II probability. For both the 60 and 100 V measurement, the II probability is consistent with zero. Therefore many random variates of the II probability fall below zero, leading to non-physical limit results. Unlike the efficiency curve, non-physical values of the II probability lead to extreme adverse effects on the limits. Specifically, negative II probabilities ultimately result in nonsensical, negative upper limit values. To avoid this issue, the Gaussian probability distributions constructed for the II probability measured at 60 and 100 V are truncated at 0%. The effect of using a truncated distribution for the II probability random variates is dependant on

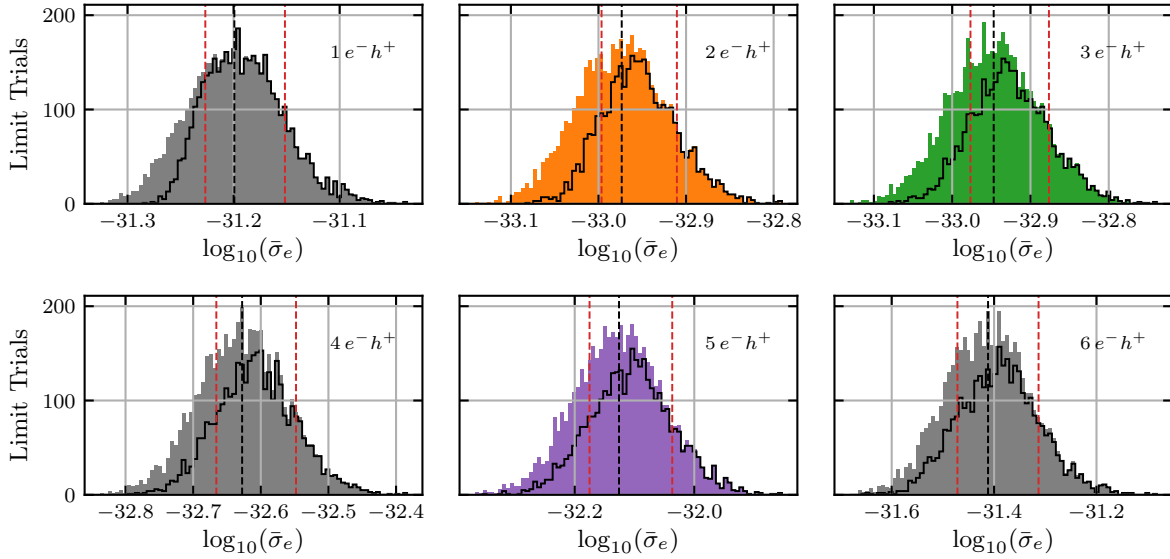


Figure 5.10: Limit distributions at each e^-h^+ -pair peak produced for the LDM-electron scattering cross section $\bar{\sigma}_e$ with Fano factor $F = 0.155$, DM form factor $F_{\text{DM}} = 1$, and a DM mass of $7 \text{ MeV}/c^2$ for the 100 V measurement. The distributions are the results of 5000 trials of calculating the upper limit using random variates of experiment and model parameters with uncertainty. The black, vertical lines indicated the average of each limit distribution. The black, overlaid distributions are the limit trials that were computed using only a physical efficiency curve. The red, vertical lines indicate the $\pm 1 \sigma$ uncertainty values. The distributions that are coloured indicate which of the e^-h^+ -pair peaks are considered for selecting the lowest averaged limit and thus the 90% C.L. result at each sampled DM mass. In this example, the lowest averaged limit occurs at the second e^-h^+ -pair peak.

many factors, including the DM model and mass that are being considered and which e^-h^+ -pair peak is being used to calculate the limit. Generally the magnitude of this effect is expected to be small and skew the upper limits to be, at most, 6% weaker. Overall this effect is subdominant compared to the other sources of uncertainty.

Finally to consider the uncertainty in the Fano factor F , the limits and their propagated uncertainty are calculated separately using three different values for F : the one measured at high energy, $F = 0.155$ [108], and the values of $F = 10^{-4}$ and $F = 0.3$ assumed to cover the systematic uncertainty of the Fano factor at these energies. Figure 5.10 shows the limit distributions at each e^-h^+ -pair peak produced for the LDM-electron scattering cross section $\bar{\sigma}_e$ with $F = 0.155$, $F_{\text{DM}} = 1$, and a DM mass of $7 \text{ MeV}/c^2$ for the 100 V measurement. The average limit at each e^-h^+ -pair peak is calculated using the entire limit distribution. The black, overlaid distributions are the distributions with the non-physical efficiency curves removed, and are used to calculate the equivalent 1σ uncertainty values. The coloured distributions indicate which of the e^-h^+ -pair peaks are considered for selecting the lowest averaged limit; for the example in Fig. 5.10, the lowest averaged limit occurs at the second e^-h^+ -pair peak.

For each DM model for each of the 60 and 100 V measurements, the final limit result is the limit obtained using $F = 0.155$, and the final estimate of the systematic uncertainty is the envelope of the equivalent $\pm 1 \sigma$ values of all three limits obtained using the different Fano factor assumptions. The final 90% C.L. exclusion limit results for this analysis for LDM-electron scattering and dark photon/ALP absorption are shown in Figs. 5.11 and 5.12, respectively. The limits on $\bar{\sigma}_e$ assume a DM form factor of

either $F_{\text{DM}} = 1$ or $F_{\text{DM}} \propto 1/q^2$ [71]. The light blue and light grey bands represent the estimates of the systematic uncertainty for the 100 V and 60 V measurements, respectively.

5.4.3 Characterizing the Limit Uncertainty Estimates

Although uncertainty estimates shown in Figs. 5.11 and 5.12 help to understand the overall magnitude of the effects that uncertainties of experimental and model parameters have on the limit results, they do not hold much statistical weight or meaning. However it is still worth analyzing the results further to understand how each parameter individually contributes to the overall limit uncertainty. Take for example the limit distribution results in Fig. 5.10, which ultimately selected the averaged limit at the second e^-h^+ -pair peak. The random parameter variates used to produce this limit distribution are split into two categories: those that resulted in an upper limit that is either lower or higher than the average of the limit distribution. These random parameter variate distributions are shown in Fig. 5.13.

By observing the plots in Fig. 5.13, it is clear that n_σ , and therefore the efficiency curve uncertainty, is the largest contributor to the spread in the limit distribution at the second e^-h^+ -pair peak in Fig. 5.10. The CT and II probabilities are the next largest contributors, while the energy resolution and calibration appear to negligibly affect the spread in the limit distribution. This result, however, is qualitative and is only applicable to the specific DM model and mass used to compute the limits in the Fig. 5.10 example. To obtain a broader and more quantitative result, the effects of experimental and parameter uncertainties are studied using a linear regression analysis. Given a data set of observed values y_j and independent or predictor variables x_{ji} for $j = 1, \dots, N$ and $i = 0, \dots, p$, the predictive linear regression model is expressed as

$$\begin{pmatrix} y_1 \\ \vdots \\ y_j \\ \vdots \\ y_N \end{pmatrix} = \begin{pmatrix} 1 & x_{11} & \cdots & x_{1i} & \cdots & x_{1p} \\ \vdots & \vdots & \ddots & \vdots & \ddots & \vdots \\ 1 & x_{j1} & \cdots & x_{ji} & \cdots & x_{jp} \\ \vdots & \vdots & \ddots & \vdots & \ddots & \vdots \\ 1 & x_{N1} & \cdots & x_{Ni} & \cdots & x_{Np} \end{pmatrix} \begin{pmatrix} \beta_0 \\ \vdots \\ \beta_i \\ \vdots \\ \beta_p \end{pmatrix} + \begin{pmatrix} \epsilon_1 \\ \vdots \\ \epsilon_j \\ \vdots \\ \epsilon_N \end{pmatrix}, \quad (5.10)$$

where β_i are the regression coefficients for each predictor variable and ϵ_j are the error elements. The model includes a constant intercept term β_0 by setting $x_{j0} = 1$. Completing the inner product in Eq. 5.10, the dependant variable y_j can be predicted from the set of x_{ji} predictor variables:

$$y_j = \beta_0 + \beta_1 x_{j1} + \dots + \beta_p x_{jp} + \epsilon_j. \quad (5.11)$$

Given $(p - 1)$ predictor variables, the linear regression model finds the set of β_i coefficients that best predict the y_j observed values from the input x_{ji} variables. This model can be applied to this analysis in order to assess how the experimental and model parameters impact the limit distribution data. Each limit distribution has $N = 5000$ observations, and there are $(p - 1) = 7$ predictor variables related to the energy resolution, energy calibration, CT and II probabilities, detector efficiency, Fano factor, and the photoelectric absorption cross section. For this analysis, x_{ji} represents the number of standard deviations away from the mean of the underlying distribution of parameter i for the j^{th} observation, and y_j represents the number of standard deviations the observed j^{th} limit is away from the average of the

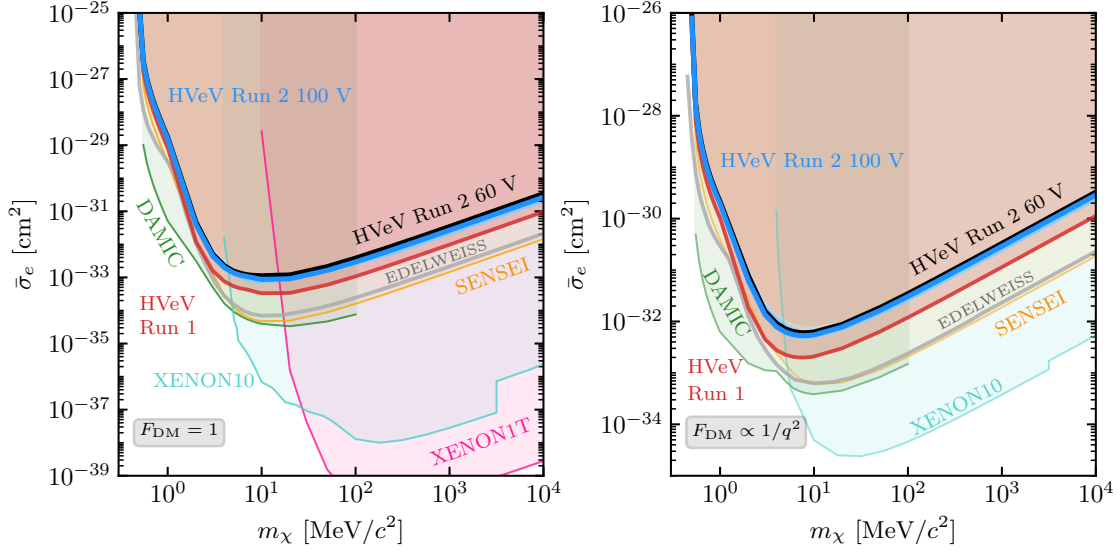


Figure 5.11: 90% C.L. limits on the effective dark matter-electron scattering cross section with form factor $F_{\text{DM}} = 1$ (left) and $F_{\text{DM}} \propto 1/q^2$ (right) and with Fano factor of 0.155 for the 100 V (solid-blue curve) and 60 V (black curve) measurement. The light blue and light grey bands represent the estimates of the systematic uncertainty for the 100 V and 60 V measurement, respectively. Other direct detection constraints shown include SuperCDMS HVeV Run 1 [106] (red), DAMIC [151] (green), SENSEI [152] (orange), EDELWEISS [153] (grey), XENON10 [154, 155] (teal), and XENON1T [52] (pink).

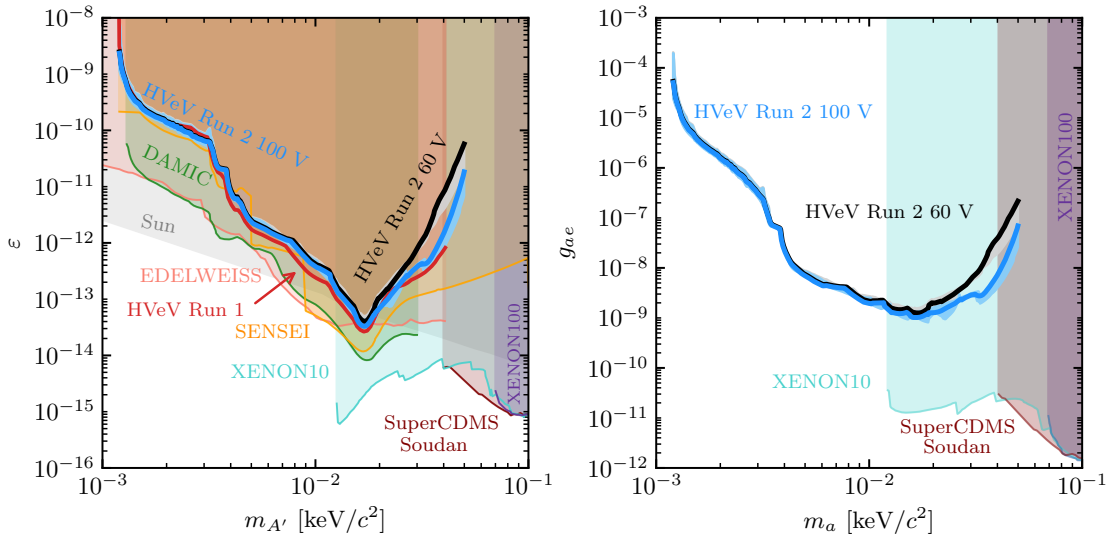


Figure 5.12: 90% C.L. limits on the dark photon (A') kinetic mixing parameter ϵ (left) and axioelectric coupling constant g_{ae} (right) with Fano factor of 0.155 for the 100 V (solid-blue curve) and 60 V (black curve) measurement. The light blue and light grey bands represent the estimates of the systematic uncertainty for the 100 V and 60 V measurement, respectively. Other direct detection constraints shown for A' and ALPs include SuperCDMS Soudan [148] (maroon), XENON10 (teal), and XENON100 (purple) [78]; additional constraints on A' include SuperCDMS HVeV Run 1 [106] (red), DAMIC [151] (green), SENSEI [152] (orange), EDELWEISS [153] (salmon), and anomalous energy loss mechanisms in the Sun [156]. For the axioelectric coupling, the entire region shown is disfavored by the observed cooling of red giant [157, 82] and white dwarf stars [158, 82].

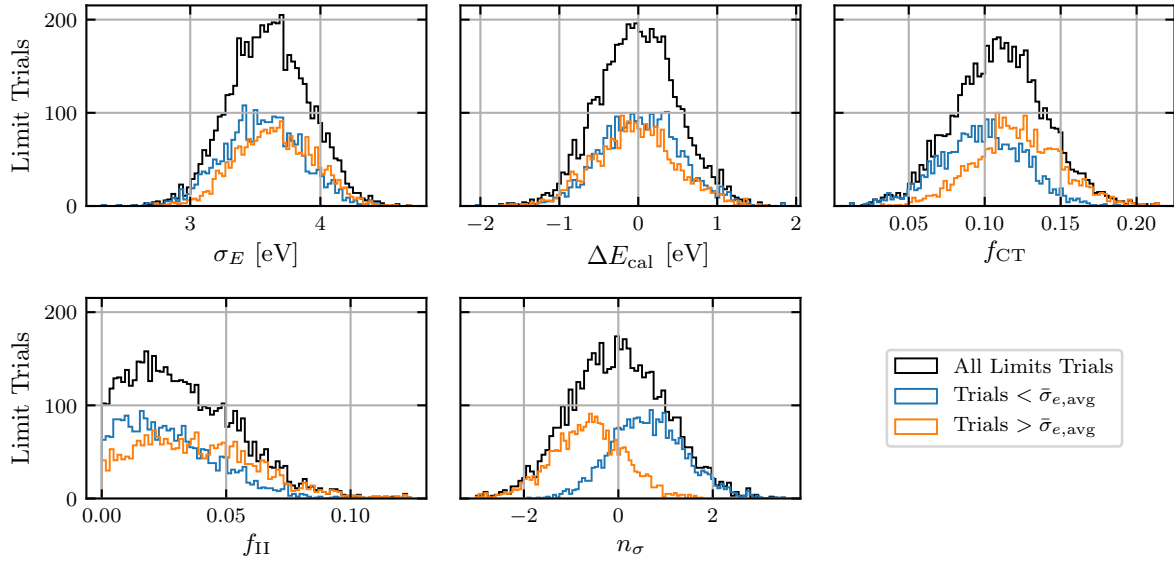


Figure 5.13: Distributions of the random parameter variates used to produce the limit distribution at the second e^-h^+ -pair peak seen in Fig. 5.10. The random variates include the energy resolution σ_E , the energy calibration ΔE_{cal} , the fractional charge trapping (CT) probability f_{CT} , the fractional impact ionization (II) probability f_{II} , and the efficiency parameter n_σ described by Eq. 5.9. Each distribution is split into the random variates that resulted in an upper limit that is lower (blue) or higher (orange) than the average of limit distribution, $\bar{\sigma}_{e, \text{avg}}$.

limit distribution. Therefore this linear regression analysis assesses how the *uncertainty* of the various parameters impact the *uncertainty* in the limit. A larger β_i coefficient means that the uncertainty of parameter i has a larger impact on the uncertainty observed in the limit.

It is also important to point out the limitations of applying this model to the limit distribution data. First, the observed limit distributions and parameter distributions are not always Gaussian in shape, which introduces uncertainty into the y_j and x_{ji} data points. Second, parameters such as the CT and II probabilities and Fano factor have a non-linear effect on the limits, which introduces additional uncertainty into the regression model. Lastly, the Fano factor and photoelectric absorption cross section curve are chosen randomly from three discrete choices rather than from some distribution. In order to fold these uncertainties into the regression model, the discrete choices are assigned x_{ji} values of -1 , 0 , or 1 . For example for the Fano factor (with $i = 7$), the choices of $F = 10^{-4}$, $F = 0.155$, and $F = 0.3$ correspond to $x_{j7} = -1$, $x_{j7} = 0$, and $x_{j7} = 1$, respectively. The Fano factor coefficient β_7 being larger than another coefficient β_n can be interpreted as the *choice* of Fano factor having a larger impact on the limit uncertainty than a 1σ deviation in parameter n . Figure 5.14 shows the absolute values of the β_i coefficients as a function of DM mass for the limits produced for LDM-electron scattering with $F_{\text{DM}} = 1$ and for dark photon absorption. The plots are shown for the limits produced for the 100 V measurement, but the results are similar for the 60 V measurement. The results are also similar when the linear regression model is applied to the LDM-electron scattering with $F_{\text{DM}} \propto 1/q^2$ and ALP absorption limit distributions.

Figure 5.14 provides insight into which parameters have the most impact on the limit uncertainty. At DM masses where expected signal model depends on the Fano factor ($> 1 \text{ MeV}/c^2$ for χ and $> 3.8 \text{ eV}/c^2$

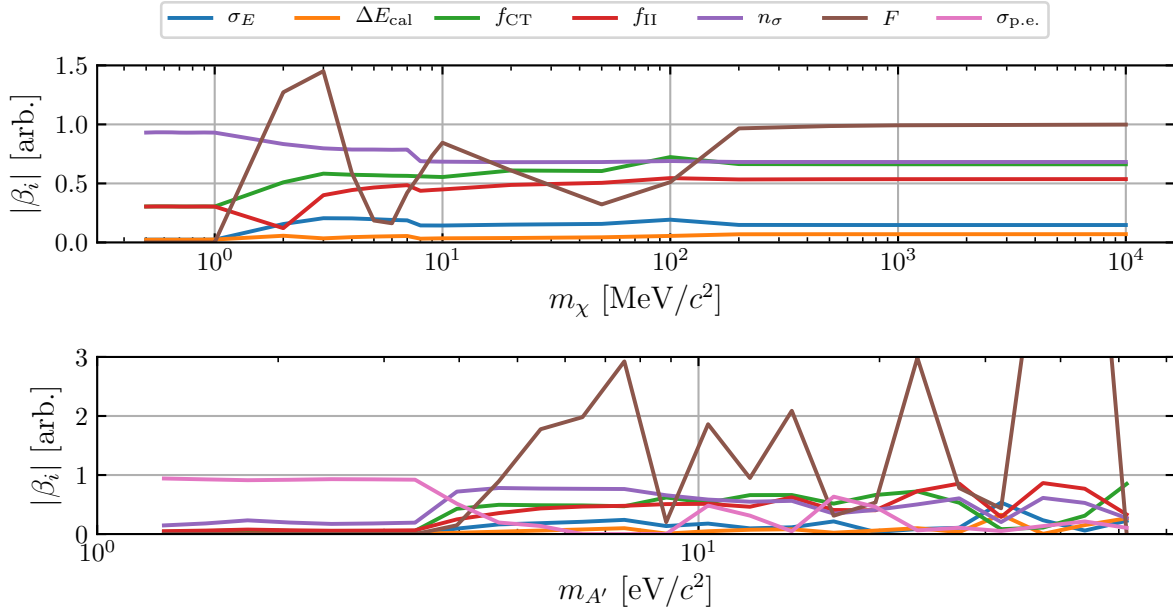


Figure 5.14: Absolute values of the regression coefficients β_i as a function of DM mass resulting from the linear regression model applied to the limit distributions for LDM-electron scattering with $F_{\text{DM}} = 1$ (top) and for dark photon absorption (bottom) for the 100 V measurement. The β_i coefficients are related to the energy resolution σ_E , energy calibration ΔE_{cal} , fractional charge trapping (CT) probability f_{CT} , fractional impact ionization (II) probability f_{II} , the efficiency parameter n_σ described by Eq. 5.9, the Fano factor F , and the photoelectric absorption cross section $\sigma_{\text{p.e.}}$. A larger $|\beta_i|$ indicates that the uncertainty from parameter i has a larger impact on the uncertainty in the limit.

for dark photons and ALPs), the Fano factor is generally the most dominant source of uncertainty. For LDM-electron scattering, the detector efficiency and CT probability are the next leading sources of uncertainty. For the absorption channels at masses $\lesssim 4 \text{ eV}/c^2$, $\sigma_{\text{p.e.}}$ is the most dominant source of uncertainty. For all DM channels, the energy resolution and calibration are generally the least dominant source of uncertainty in the limit.

5.5 Discussion

This chapter presents an analysis and resulting exclusion limits on LDM scattering off of electrons, dark photon absorption, and ALP absorption using a 0.93 g, second-generation HVeV detector. Energy spectra are produced from a blind analysis with 1.2 g-days of exposure measured at 100 V and 0.39 g-days of exposure measured at 60 V acquired in an above-ground laboratory. The results from the 100 V measurement are reported in Ref. [1].

This second generation HVeV detector used in this analysis has shown an improved performance compared to the first-generation detector used in the HVeV Run 1 analysis. The HVeV Run 2 detector operated at 100 V is able to achieve an unparalleled energy resolution in the first e^-h^+ -pair peak as low as 3 eV, corresponding to a charge resolution of $0.03 e^-h^+$ pairs. This resolution is ~ 3.3 times better than the $0.1 e^-h^+$ pair charge resolution obtained by the HVeV Run 1 detector [106]. Furthermore, the HVeV Run 2 detector design successfully implemented a second QET channel that allows for events to

be distinguished between those originating in the inner or outer area of the detector. Although Sec. 4.3.1 shows that both channels have equal energy gain, a partition cut to remove outer-channel events could not be successfully utilized, as outlined in Sec. 4.4.2.

Despite the clear improvements in the detector design, the limit results from this analysis do not reach the projected limits shown in Figs. 4.2 and 4.3, nor are they able to exceed the DM exclusion limits achieved by the HVeV Run 1 analysis despite ~ 2.5 times more exposure. The most notable differences between this analysis compared to the HVeV Run 1 results are seen in the LDM-electron scattering limits for DM masses $\gtrsim 2 \text{ MeV}/c^2$. In this mass region, the 100 V HVeV Run 2 limits are weaker by a factor of $\lesssim 3.2$ and $\lesssim 3.4$ compared to HVeV Run 1 assuming a DM form factor $F_{\text{DM}} = 1$ and $F_{\text{DM}} \propto 1/q^2$, respectively. While different limit-setting techniques do play some role, the discovery reach of these HVeV-style detectors is limited primarily by the background events of unknown origin.

A large amount of the differences in the LDM-electron scattering limits between HVeV Run 1 and HVeV Run 2 can be attributed to the different limit setting approaches taken by each analysis. This analysis utilizes the conservative Poisson counting method described in Sec. 5.1.2 that tends to result in weaker limits. Conversely, the HVeV Run 1 analysis utilizes the OI limit setting method, that due to the ability of the OI method to freely choose the limit setting interval, tends to produce stronger limits. A more apt comparison of HVeV Run 1 and HVeV Run 2 limit results is made by employing the same limit setting procedure to both datasets. Specifically, a Poisson counting method is used for both analyses, whereby the 90% upper limit is computed at each e^-h^+ -pair peak, and the lowest limit at each DM mass is selected as the final limit. This is the same limit setting procedure that is used for HVeV Run 2, except without involving the e^-h^+ -pair peak selection procedure. When the same limit setting procedure is used, the 100 V HVeV Run 2 limits on LDM-electron scattering above $\gtrsim 2 \text{ MeV}/c^2$ are weaker by only a factor of $\lesssim 1.6$ and $\lesssim 1.4$ compared to HVeV Run 1 for $F_{\text{DM}} = 1$ and $F_{\text{DM}} \propto 1/q^2$, respectively. Figure 5.15 shows the LDM-electron scattering limits with $F_{\text{DM}} \propto 1/q^2$ produced at each e^-h^+ -pair peak for HVeV Run 1 and HVeV Run 2 using the same Poisson counting method.

The remaining differences in the LDM-electron scattering limits between HVeV Run 1 and HVeV Run 2 are due to the detector-specific CT and II values, that differ for the detectors used in each run. The Poisson method sets the limit values by calculating the ratio between the event rate determined from the 90% upper limit of the observed number of events and the expected event rate determined from the DM signal model. Table 5.8 compares the efficiency-corrected event rates for each e^-h^+ -pair peak within a $\pm 3\sigma_E$ window between the 60 and 100 V measurements in this analysis and the HVeV Run 1 analysis. The event rate observed at each e^-h^+ -pair peak is similar in this analysis compared to HVeV Run 1. Yet due to the larger exposure for HVeV Run 2, the event rate determined from 90% upper limit of the observed number of events is lower at all except the third e^-h^+ -pair peak. Therefore with all else being equal, this analysis would produce stronger limits compared to HVeV Run 1, except if the limit is set at the third e^-h^+ -pair peak. However this analysis measured CT and II probabilities of 11 and 2%, respectively, for the data measured at 100 V, and incorporated these values into the detector response model. Conversely, CT and II probabilities were not incorporated into the HVeV Run 1 analysis, but recent measurements observed CT and II probabilities in the HVeV Run 1 detector of 0.713 and 1.1576%, respectively [109].

The effect of CT and II moves events from the peak regions and into the between-peak regions. Therefore in general, higher values of CT and II reduce the expected event rate at each e^-h^+ -pair peak, and thus contribute to a weaker limit. Indeed for the LDM-electron scattering signal model, the

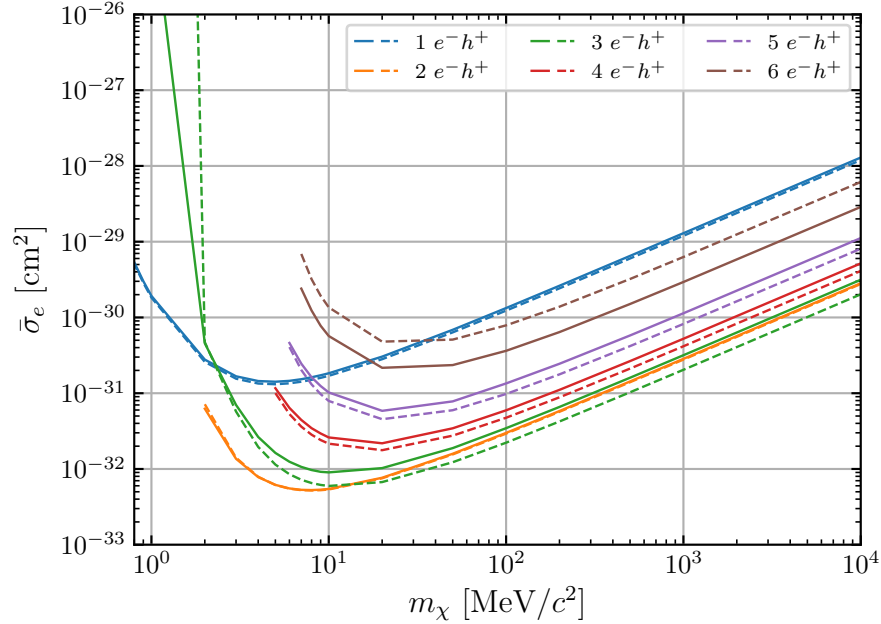


Figure 5.15: Limit on the LDM-electron scattering cross section $\bar{\sigma}_e$ with $F_{\text{DM}} \propto 1/q^2$ produced at each e^-h^+ -pair peak for the 100 V measurement of this analysis (solid curves) and for the HVeV Run 1 analysis (dashed curves). All of the limits are produced using the Poisson limit setting method.

Table 5.8: Comparison of the efficiency-corrected event rate at each e^-h^+ -pair peak between this analysis and HVeV Run 1 [106]. The event rates displayed from this analysis are calculated from the DM-search datasets measured with a bias voltage of 100 V and 60 V. For each number of e^-h^+ pairs, the event rate is determined by counting the number of observed events within a $\pm 3\sigma_E$ window centered on the peak. The uncertainty shown is the 1σ uncertainty in the number of observed events assuming Poisson statistics.

Voltage [V]	HVeV Run 2		HVeV Run 1 [106]
	100	60	-140
σ_E [e^-h^+]	0.03	0.05	0.1
Events/(g-day)			
1 e^-h^+	$(149 \pm 0.3) \times 10^3$	$(165 \pm 0.7) \times 10^3$	$(157 \pm 0.7) \times 10^3$
2 e^-h^+	$(1.1 \pm 0.03) \times 10^3$	$(1.2 \pm 0.07) \times 10^3$	$(1.3 \pm 0.07) \times 10^3$
3 e^-h^+	207 ± 13	245 ± 29	171 ± 20
4 e^-h^+	53 ± 7	77 ± 16	58 ± 11
5 e^-h^+	16 ± 4	20 ± 8	16 ± 6
6 e^-h^+	5 ± 2	10 ± 6	24 ± 7

expected event rate at each of the first six e^-h^+ -pair peaks is reduced by a factor of roughly 0.9, 0.8, 0.71, 0.64, 0.58, and 0.52, respectively, when computed with the CT and II values measured at 100 V compared to assuming no CT or II. These reductions in the expected event rate are often enough to overcome the advantageous exposure of HVeV Run 2. In order to demonstrate the effect that the CT

and II probabilities have on the limit results, the limits on LDM-electron scattering determined from this analysis are computed again but without incorporating the CT and II probabilities into the detector response model, as was done in HVeV Run 1. When the CT and II probabilities are not incorporated into the detector response model, the 100 V HVeV Run 2 limits on LDM-electron scattering are *stronger* by a factor of $\lesssim 1.35$ for both $F_{\text{DM}} = 1$ and $F_{\text{DM}} \propto 1/q^2$ compared to the Poisson HVeV Run 1 limits for regions where the limits are not set at the third e^-h^+ -pair peak. In regions where the limits are set at the third e^-h^+ -pair peak, the 100 V HVeV Run 2 limits are still weaker by a factor of $\lesssim 1.1$ for both $F_{\text{DM}} = 1$ and $F_{\text{DM}} \propto 1/q^2$ compared to the Poisson HVeV Run 1 limits. Putting aside the different limit setting methods for HVeV Run 1 and HVeV Run 2, the differences in the LDM-electron scattering limits can be attributed to the fact that the observed event rates at the e^-h^+ -pair peaks and the larger exposure of HVeV Run 2 do not overcome the higher CT and II probabilities measured for the HVeV Run 2 detector. This may be indicative of a slightly higher overall event rate in HVeV Run 2 compared to HVeV Run 1. The total event rate observed at and above the second e^-h^+ -pair peak is ~ 10 Hz/kg for HVeV Run 1 and ~ 15 Hz/kg for HVeV Run 2 operated at 100 V.

The limit results in this analysis between the 60 and 100 V measurements are very comparable. Furthermore, Tab. 5.8 also shows that the observed event rate in each e^-h^+ -pair peak between the 60 and 100 V measurements are similar. This, along with the similar CT and II probabilities, suggest a result that is not strongly dependent on the applied voltage. Indeed the limit results as seen in Figs. 5.11 and 5.12 are comparable between the 60 and 100 V measurements. For dark photon and ALP masses $\gtrsim 20$ eV/ c^2 , the 100 V measurement produces stronger limits due to the e^-h^+ -pair peaks from the DM signal models “walking away” from the observed e^-h^+ -pair peaks, combined with a greater exposure for the 100 V measurement.

Furthermore, this analysis provides a more thorough study of the uncertainty in the limit results compared to the HVeV Run 1 analysis, and indicates which parameters are key to reducing the uncertainty in the limits of future analyses. As Sec. 5.4 outlined, the uncertainty in the Fano factor in Si is the most dominant source of uncertainty in the limit results, followed by the uncertainties in the efficiency curves (caused by the efficiency dips described in Sec. 4.5.2) and CT/II probabilities. For dark photon and ALP masses below $\lesssim 4$ eV/ c^2 , the most dominant source of uncertainty in the limits are due to the uncertainty in the photoelectric absorption cross section in Si. Chapter 6 presents a new measurement of the photoelectric absorption cross section at cryogenic temperatures that greatly reduces this source of uncertainty. The uncertainties in the energy resolution and energy calibration are the least dominant sources of uncertainty in the limit results.

Overall, it is clear that apart from marginal gains that can be made by utilizing different limit setting techniques, the discovery reach that is possible using these HVeV-style detectors is limited by the observed background events of unknown origin. Sufficient understanding of these background events would allow for a likelihood-based approach to be used to set the limits. Not only are likelihood-based approaches well established, but they can also incorporate experimental uncertainties into the limit result, and could be used to combine the results from HVeV Run 1 and HVeV Run 2. Yet given how much is still unknown about these backgrounds, experiments in the near future using HVeV-style detectors will likely implement the limit setting approach used for this analysis introduced in Secs. 5.1.2 and 5.2. It will therefore be beneficial, if not prudent, to further investigate this limit setting approach, and use Monte Carlo (MC) simulations to understand the statistical coverage and thus the C.L. of the limit

results computed using this method. Chapter 7 discusses further the topic of unknown backgrounds, and outlines some key areas of focus for future experiments operating HVeV-style detectors.

Chapter 6

Photoelectric Absorption Cross Section Measurement in Silicon

This chapter describes a novel technique for measuring the photoelectric absorption cross section $\sigma_{\text{p.e.}}$ near the Si band gap at cryogenic temperatures. Apart from obtaining an accurate and precise measurement of $\sigma_{\text{p.e.}}$, this analysis also investigates how this new result affects certain dark matter exclusion limits. The analysis and results presented in this chapter are also reported in Ref. [2] and [3]. Furthermore, the work presented here was made by a collaborative effort, with the other leading contributor being Chris Stanford.

6.1 Motivation

The expected event rate and signal distribution of several dark matter (DM) candidates depend on $\sigma_{\text{p.e.}}$ of the target material. As the sensitivity of direct DM search experiments reach lower and lower DM masses, there becomes a greater need of precisely knowing $\sigma_{\text{p.e.}}$ at lower photon energies. For these experiments and DM models, there is a natural low-energy limit that exists at the band gap energy of the target material; for Si, the lowest band gap energy is ~ 1.1 eV. Recently there have been many experiments that have reached this low energy limit, including DAMIC [151], SENSEI [152], and, as shown in the previous chapter, SuperCDMS HVeV [1].

The need for precise measurements of $\sigma_{\text{p.e.}}$ near the band gap for DM search experiments is abundantly clear. As seen in Sec. 2.3, there is a lot of discrepancy in the data available from literature for photon energies below the direct band gap energy of Si (~ 3.2 eV). Moreover only a sparse amount of the literature data were measured at the cryogenic temperatures that are required for solid-state DM search experiments; the data that were measured at cryogenic temperature do not span the entire energy range of interest. Recall that a temperature dependence in $\sigma_{\text{p.e.}}$ is expected in Si at energies below the direct band gap due to indirect photon absorption (see Sec. 2.3.1). Even after correcting the literature data for temperature, the uncertainty in $\sigma_{\text{p.e.}}$ near the Si band gap is the most dominant source of uncertainty in the dark photon and axion-like particle (ALP) absorption exclusion limits at masses $\lesssim 4$ eV/ c^2 , as seen by the HVeV Run 2 results in Sec. 5.4. A more accurate and precise measurement of $\sigma_{\text{p.e.}}$ near the Si band gap at sub-Kelvin temperatures will reduce the uncertainty in the exclusion limits for DM models that depend on this parameter.

6.2 Experimental Setup

6.2.1 Experiment Design

To measure $\sigma_{p.e.}$, a new experiment was designed whereby monochromatic light is passed through thin Si filters of varying thickness. Values of $\sigma_{p.e.}$ are obtained by comparing the relative transmission of light through each filter. Using the relative transmissions removes much of the difficulties and systematic uncertainties that would occur if absolute transmission values are used to measure $\sigma_{p.e.}$.

The entire experiment is contained within a ^3He fridge that has been previously used to measure charge propagation in Si and Ge at low temperatures [159, 160, 161, 162]. The filters and detection apparatus are coupled to the coldest stage of the ^3He fridge. A multi-mode fiber optic cable fed into the fridge via a vacuum feedthrough is used to illuminate the filters with light from external LED/laser diode sources of various wavelengths. Table 6.1 lists the different wavelengths used in this experiment. The light exiting the fiber optic cable is focused to a diameter of $\sim 200\ \mu\text{m}$ onto the filters $\sim 150\ \text{mm}$ away after reflecting off of a 2-axis micro-electro-mechanical system (MEMS) mirror. The tilt of the MEMS mirror is controlled and automated to direct the light toward the various Si filters.

Behind the Si filters is a high-purity Si crystal detector with dimensions of $1 \times 1 \times 0.4\ \text{cm}^3$. The side of the detector facing the incoming light is patterned with an aluminum-tungsten mesh electrode, with 20% coverage, that provides a voltage bias of 50 V across the detector. The electrode is a tri-layer of 40 nm of W on 20 nm of Al on 40 nm of amorphous Si. The opposite side of the detector is covered almost fully with aluminum thin film that is used as a ground electrode. Light that is absorbed by the Si detector releases e^-h^+ pairs within the crystal that are then propagated due to the applied voltage. The drifting charges are collected and measured as a charge signal. Figure 6.1 shows an illustration of the experiment setup.

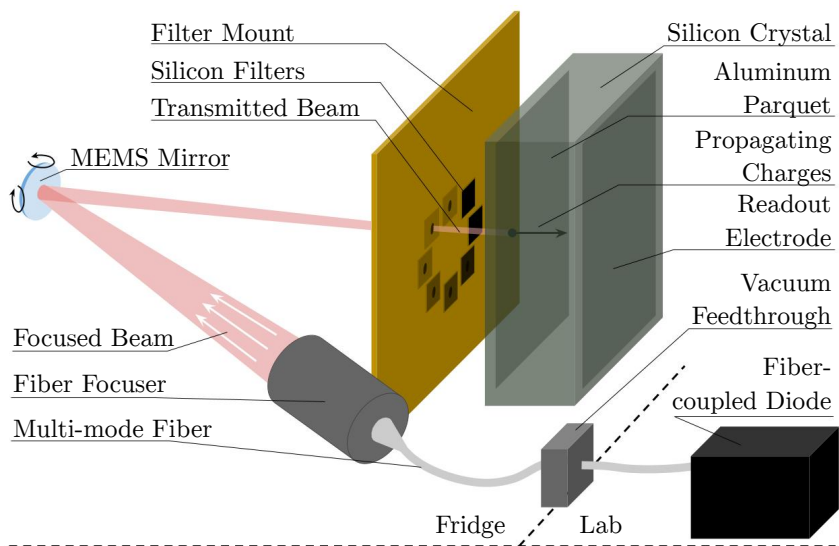


Figure 6.1: Illustration of the experiment setup used to measure $\sigma_{p.e.}$. A multi-mode fiber is fed into the fridge in order to transmit light through the Si filters. The transmitted light is measured as a charge signal from the Si crystal detector. The MEMS mirror is used to direct the light through the various filters. Courtesy of Chris Stanford.

Table 6.1: Summary of the various monochromatic light sources used in this experiment. The transmission curves for each light source provided by the manufacturer is summarized by the peak, lower half-maximum (LHM), and upper half-maximum (UHM) values. The peak values in units of eV are also shown.

Peak [nm]	LHM [nm]	UHM [nm]	Peak [eV]	Type
448	447	449	2.77	Laser
530	521	547	2.34	LED
639.5	639	640	1.94	Laser
660	651	667	1.88	LED
787	786	788	1.58	Laser
950	905	970	1.31	LED
972	970	973	1.28	Laser
1028	1027	1029	1.21	Laser

The filter mount shown in Fig. 6.1 is made from a 6 cm² brass plate. The front side of the mount contains eight through-holes 0.5 mm in diameter that are radially symmetric around the mount center and are spaced 2 mm apart. The back side of the mount contains square indents centered on each through-hole that are used to mount the 1.5 × 1.5 mm² Si filters. GE varnish is used to hold the filters in place. Seven filters are cut from high-purity, Czochralski (Cz)-grown Si wafers with independently-measured thicknesses of 5.1 ± 0.1, 10.0 ± 0.1, 24.0 ± 0.2, 49.4 ± 0.1, 100.2 ± 0.1, 149.7 ± 0.2, and 198.8 ± 0.1 μm. The filter mount design is illustrated in Fig. 6.2, where the top-through hole is left empty for calibration purposes.

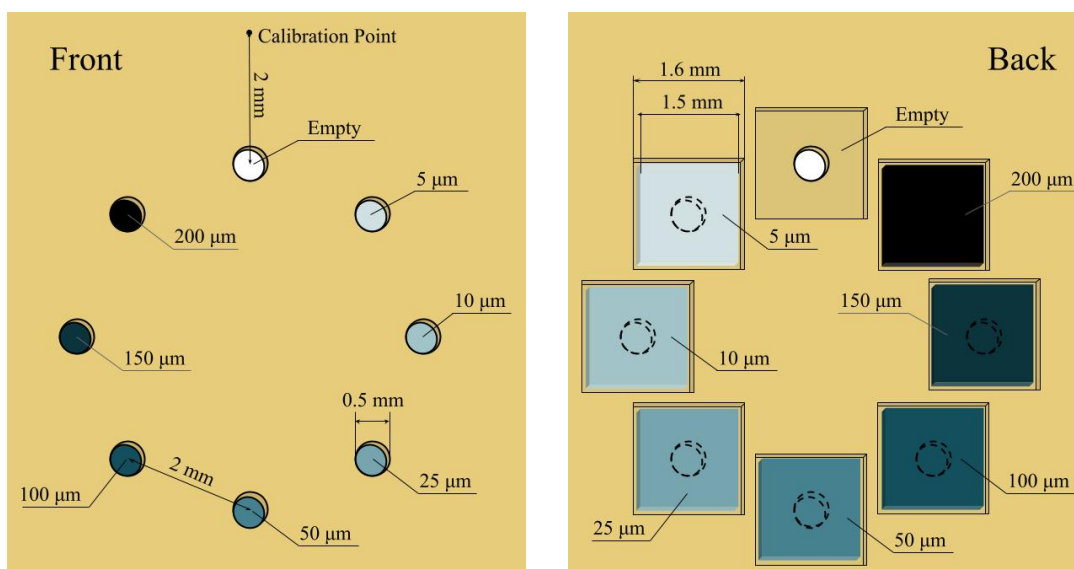


Figure 6.2: Illustration of the front (left) and back (right) filter mount design. The front side contains eight 0.5 mm-diameter through-holes spaced radially symmetric around the center of the mount. The back of the mount is used to hold the seven Si filters of varying thickness, with the top through-hole left empty for calibration purposes. Courtesy of Chris Stanford.

6.2.2 Data Acquisition

Data was acquired by first cooling the fridge to the desired temperature and connecting one of the monochromatic light sources in Tab. 6.1 to the optical fiber. Next, a series of measurements were executed that define the run performed at that temperature and wavelength. The main $\sigma_{\text{p.e.}}$ results from this work are obtained for the various light sources listed in Tab. 6.1 measured separately at temperatures of 0.5, 5, 77, and 295 K. A run involved making a scan of the beam spot over each hole in the filter mount, with each scan consisting of a 14×14 grid of individual measurements. As the light was sent through the optical fiber, the MEMS mirror was positioned to direct the light to one of the (x, y) grid points over one of the holes. The grid over each hole covers an area of $0.6 \times 0.6 \text{ mm}^2$, and is used to ensure that best alignment of the beam spot with the hole can be used for the analysis.

An individual measurement was made by pulsing the light source in a train of 32 pulses. A Thorlabs DC2200 LED driver [163] was used to control the light sources and produce square pulses with widths of $20 \mu\text{s}$ that are spread 8 ms apart. The 450 and 530 nm light sources required longer pulse widths due to the large amount of attenuation that occurs as the light travels through the optical fiber. However the pulse widths for all of the individual measurements using a single light source remained constant. When the light pulses reached the Si detector, the liberated charges were collected by the electrode and the signals were amplified using a cryogenic amplifying circuit described in Ref. [164]. The charge signal for each measurement was therefore a voltage trace recorded by the DAQ consisting of 32 pulses. The analogue traces were digitized at a sampling frequency of 48 kHz before being stored. Each voltage trace is processed by splitting it into 32 sections that are summed together to form an averaged pulse. The amplitude of the averaged pulse is used as the measure of the amount of light that passed through the Si filter at a particular (x, y) grid point and subsequently absorbed by the detector. An example of the voltage trace acquired for an individual measurement is shown in Fig. 6.3, along with the averaged pulse. Although the light pulses themselves are square-shaped, the pulses measured by the Si detector are exponential-shaped due to the recovery time of the capacitors in the amplifying circuit.

Between each measurement, the MEMS mirror was positioned to direct the beam toward the empty hole in order to reduce the effect of charge buildup in the Si detector. While grounded, a 1 ms pulse of light was sent into the detector to help neutralize any charge buildup. The bias voltage was then reapplied to take the next measurement. Lastly, the run procedure was modified in order to reduce any temporal effects that may occur during data acquisition, such as a slight increase in the fridge temperature over time. Instead of measuring the (x, y) grid points of each hole sequentially, the ordering of (x, y) grid points from all holes was shuffled as to not favour any hole in particular.

Secondary Filter Mount

A secondary filter mount was used in order to accommodate two specific measurements that were difficult to make using the original filter mount. The first is the $\sigma_{\text{p.e.}}$ measurement using the 448 nm light source. Due to the high absorption cross section that occurs at this wavelength, the intensity of the light pulses had to be increased so that enough light could transmit through even the thinnest Si filters. However the increased intensity also led to an overwhelming amount of reflected light that reached the detector either through the empty hole or by wrapping around the filter mount itself. The measurements obtained in this situation were found to be unusable. To address this issue, the secondary mount does not contain an empty hole and was spray-painted black in order to reduce the amount of reflected light. The

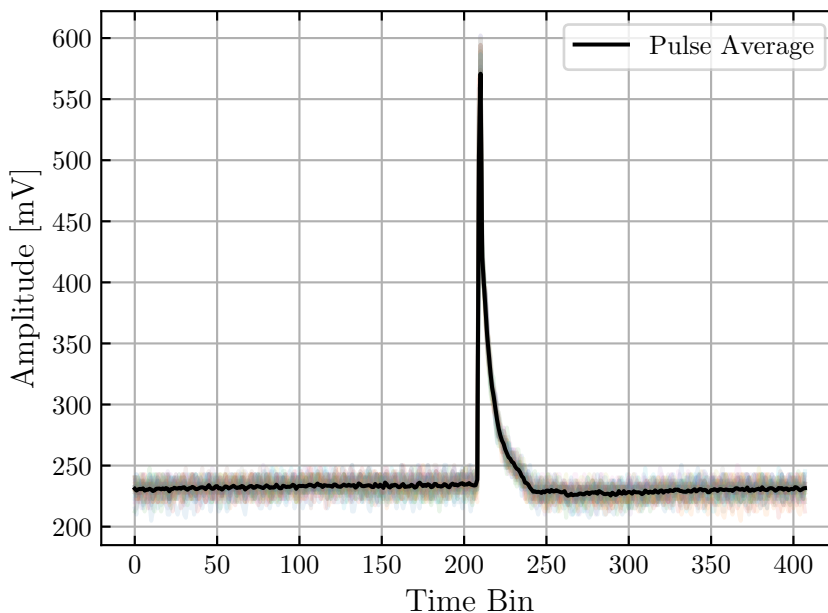


Figure 6.3: Example of the voltage trace acquired for an individual measurement. The raw trace was digitized at a sampling frequency of 48 kHz and split into 32 segments that each contain a pulse. The 32 separate pulse traces are overlaid, along with the averaged pulse trace.

$\sigma_{\text{p.e.}}$ measurement using the 448 nm light source was successfully acquired using the secondary mount, although, due to time constraints, it was measured at only one fridge temperature (5 K).

The second issue that the secondary filter mount addresses is the $\sigma_{\text{p.e.}}$ measurement using the 1028 nm light source. Due to the extremely low absorption cross section that occurs at this wavelength, the transmission through each of the Si filters is almost identical, making it difficult to extract the $\sigma_{\text{p.e.}}$ value. To solve this problem, the secondary filter mount included two new Si filters with thicknesses of 299.4 μm and 397.6 μm . The secondary mount with these thicker filters was used for the $\sigma_{\text{p.e.}}$ measurement with the 1028 nm light source at a temperature of 295 K. For all of the measurements acquired using this secondary filter mount, the neutralization step was done by directing a sufficient amount of light through the 5.1 μm filter.

6.3 Calibration

This experiment was designed to reduce the number of systematic uncertainties and minimize the amount of calibration required. Multiple Si filters of varying thickness are used so that $\sigma_{\text{p.e.}}$ can be measured with relative rather than absolute transmission measurements. Furthermore, the filters are arranged radially symmetric around the MEMS mirror. This ensures that the angle of incidence of the incoming beam at each filter surface, and therefore the proportion of light reflected at each filter-vacuum interface, is constant. Due to this design decision, the $\sigma_{\text{p.e.}}$ measurements do not require calibration for the amount of light that is reflected rather than transmitted through the filters. Nonetheless, there are still effects that may require calibration or corrections to the $\sigma_{\text{p.e.}}$ measurements. These include: (i) pulse amplitude linearity; (ii) hole transmission dependence; and (iii) light reflection.

Pulse Amplitude Linearity

In order to compare pulses of different amplitudes, the absolute pulse heights measured from the Si crystal detector need to be calibrated. To do this calibration, the 950 nm light source was attached to the system, and the MEMS mirror was positioned to direct the beam through the empty hole. Next, a sweep over the applied current to the light source in steps of ~ 5.3 mA was performed and the average pulse measured at each current step was recorded. The light source was then placed inside a dark box along with a photomultiplier tube (PMT) capable of measuring single photoelectrons. The same current sweep was performed using the PMT, but in steps of 20 mA, and the average pulse measured from the PMT at each current step was recorded. Note that this measurement is used to examine the detector response to a given amount of light intensity, and is thus independent of the specific light source used. The results of the current sweeps are shown in Fig. 6.4.

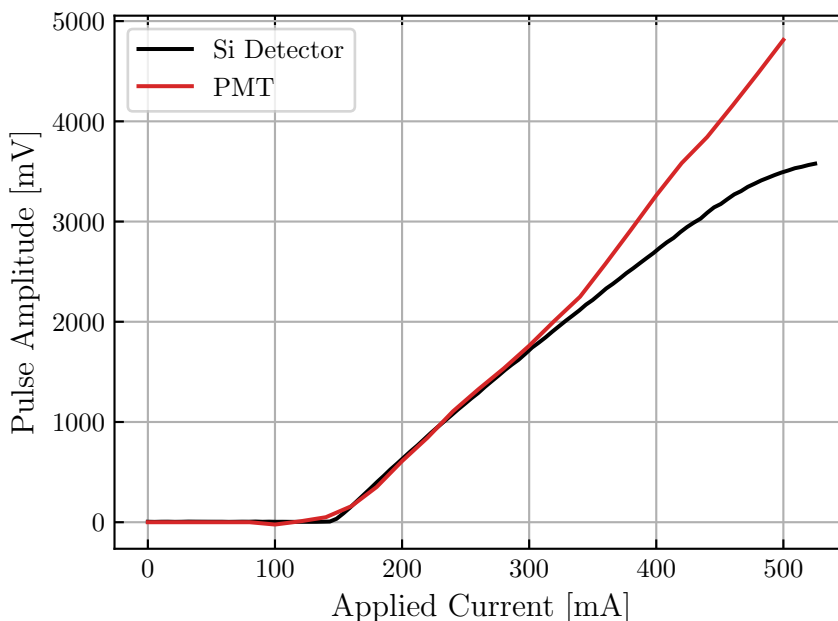


Figure 6.4: Results of performing a sweep of the applied current to the 950 nm light source. At each current, the resulting pulse amplitude was measured separately using the Si detector (black) and a photomultiplier tube (PMT) (red). Courtesy of Chris Stanford.

As Fig. 6.4 shows, the Si detector responds linearly with the amount of incident light up until pulse amplitudes of ~ 2 V. For larger amounts of incident light, the detector begins to saturate. The majority of measurements were tuned so that the averaged pulse heights fall within this linear region. However some measurements, particularly those using the short-wavelength light sources, required a larger amount of incident light. An amplitude correction is performed on any measurement whose averaged pulse amplitude is > 1 V. This is done by first using the Si detector curve in Fig. 6.4 to determine the applied current corresponding to the measured pulse amplitude, and then adjusting the amplitude to the height of the PMT curve at the matching current.

Hole Transmission Dependence

Despite the careful design of the filter mount, small differences in the size of each hole or slight asymmetries in the hole positions lead to variances in the amount of light transmitted through each hole, regardless of any Si filters placed in the mount. To investigate this hole transmission dependence, measurements were taken through each hole *without* the Si filters placed in the mount. The data were collected using the 530, 660, and 950 nm light sources with the fridge set at 5 K. The other light sources were not available at the time these measurements were made. Figure. 6.5 shows the averaged pulse amplitude for each (x, y) grid point for each hole from the 950 nm measurements. For these measurements, a 15×15 grid around each hole was used. Holes 0–7 in Fig. 6.5 correspond to the eight holes as seen in the left diagram of Fig 6.2 counting counter-clockwise, starting with hole 0 as the hole that normally contains the $50 \mu\text{m}$ filter.

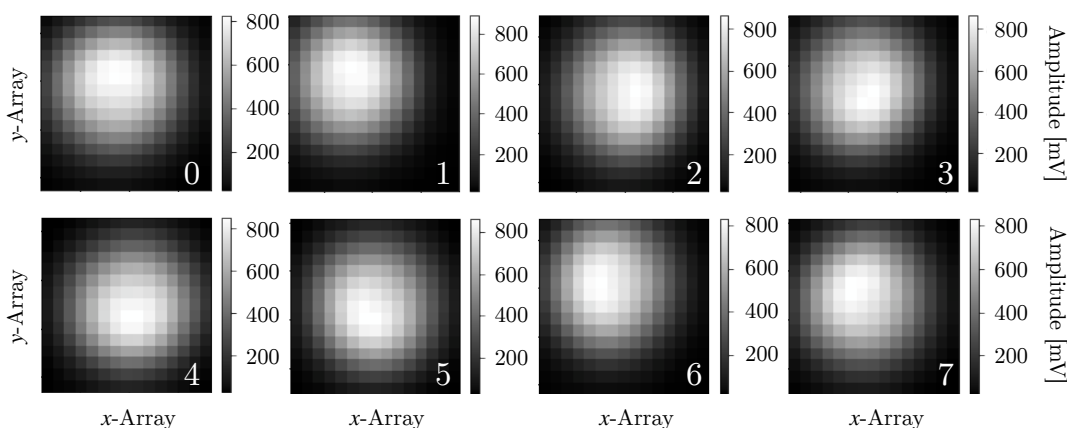


Figure 6.5: Averaged pulse amplitude resulting from the measurements obtained for each (x, y) grid point for each hole in the filter mount *without* the Si filters placed inside. Holes 0–7 correspond to the eight holes as seen in the left diagram of Fig 6.2 counting counter-clockwise, starting with hole 0 as the hole that normally contains the $50 \mu\text{m}$ filter. These measurements were obtained using the 950 nm light source at 5 K. Courtesy of Chris Stanford.

For each hole measured at each wavelength, the five (x, y) grid points with the largest averaged pulse amplitude are selected, and the median amplitude of the selected five is taken as the transmission value for the whole scan. The left plot of Fig. 6.6 shows the transmission values for each hole relative to the transmission value of hole 0.

As seen in the left plot of Fig. 6.6, the transmission through each hole can vary up to $\sim 15\%$. Although this indicates a need to develop a correction to account for the transmission variation through each hole, such a correction is impractical for this experiment. It is found that re-installing the filter mount, even to insert the Si filters, produces the same overall transmission variation but changes the variation from hole to hole. The same results are found when using the secondary filter mount. Therefore instead of developing a transmission correction, the results from the left plot of Fig. 6.6 are used to determine an uncertainty in the transmission measurements. Specifically, the standard deviation of the relative transmission measurements at each wavelength is taken as the uncertainty in the transmission measured due to hole variation. The light sources that were not measured adopt the uncertainty from the closest matching wavelength. The resulting uncertainties are: 5% for the 448 and 530 nm light sources; 4% for the 639.5, 660, and 787 nm light sources; and 2% for the 950, 972, and 1028 nm light sources. Lastly,

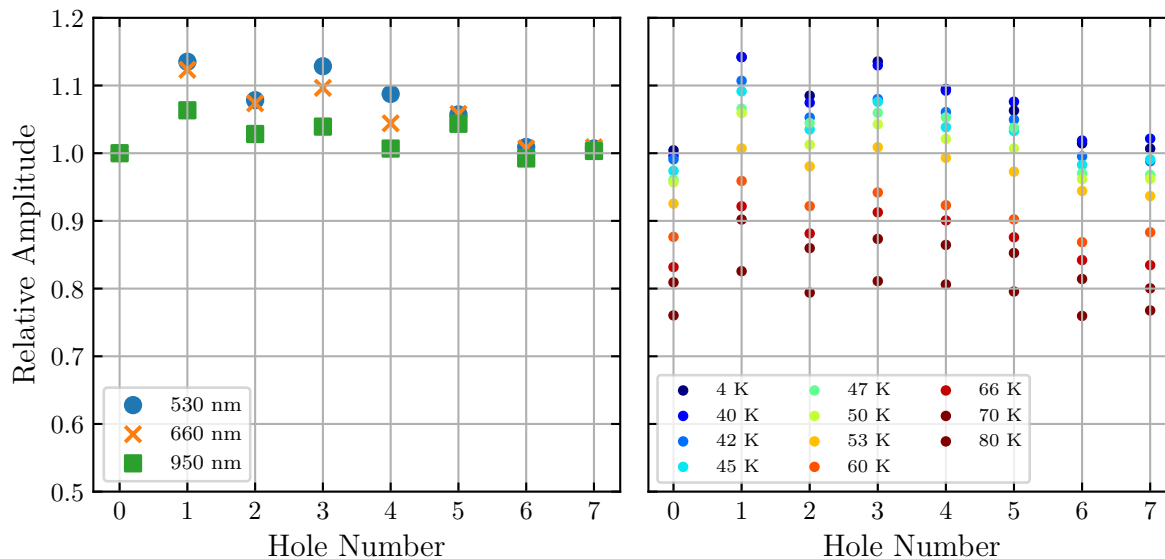


Figure 6.6: Relative transmission measured through each hole in the filter mount *without* the Si filters placed inside. Left: the measurements were made using the 530, 660, and 950 nm light sources at a temperature of 5 K, and are relative to the transmission through hole 0 for each wavelength. Right: the measurements were made using the 530 nm light source at temperatures ranging from 4 to 80 K. All measurements are relative to the transmission of the 530 nm light source through hole 0 at 5 K. Courtesy of Chris Stanford.

it is found that the magnitude of the overall transmission variation is consistent at each temperature. The right plot of Fig. 6.6 shows the relative transmission through each hole at various temperatures using the 530 nm light source. Although there is an overall trend in transmission over temperature, the hole transmission variation at each temperature is relatively consistent. The standard deviations of the hole variation calculated at the various temperatures also fall between 2 and 5%. Therefore the same uncertainty values previously stated are used for the measurements taken at all temperatures.

In most cases, the magnitude of this uncertainty is small compared to the transmission variation that occurs when the Si filters are used. However this is not true for the measurements using the 1028 nm light source. At this wavelength, the extremely low value of $\sigma_{p.e.}$ results in little variation in the transmission of light through the different filters, thereby making the observed hole transmission variation a significant factor. To improve the results, the measured amplitudes obtained from the 1028 nm data are corrected for the hole transmission variation. Yet, as previously stated, these corrections cannot be developed using the empty filter mount. Rather the corrections are developed from measurements using the filter mount with the Si filters in place. These measurements were acquired at each desired temperature by performing a scan of each hole using the 972 nm light source. This wavelength was chosen because it has good transmission through all of the filters at all temperatures.

At each temperature, the transmission through each filter is determined and used to fit a function describing transmission as a function of filter thickness. This process is described in detail in Sec. 6.4. Then for each transmission data point, the ratio between the measured and best-fit transmission values is used to approximate the hole variation. A correction factor for each hole is applied to the 1028 nm measurements as the inverse of the approximated hole variation. For example, if the ratio between the measured and best-fit transmission values in hole h is 1.05, then the 1028 nm transmission measurement

at hole h will have a correction factor of ~ 0.95 applied. The left plot of Fig. 6.7 shows the transmission data points and fitted curve for the data acquired at 0.5 K. The hole correction factors derived from this data are shown in the right plot of Fig. 6.7, along with the correction factors determined at the other temperatures.

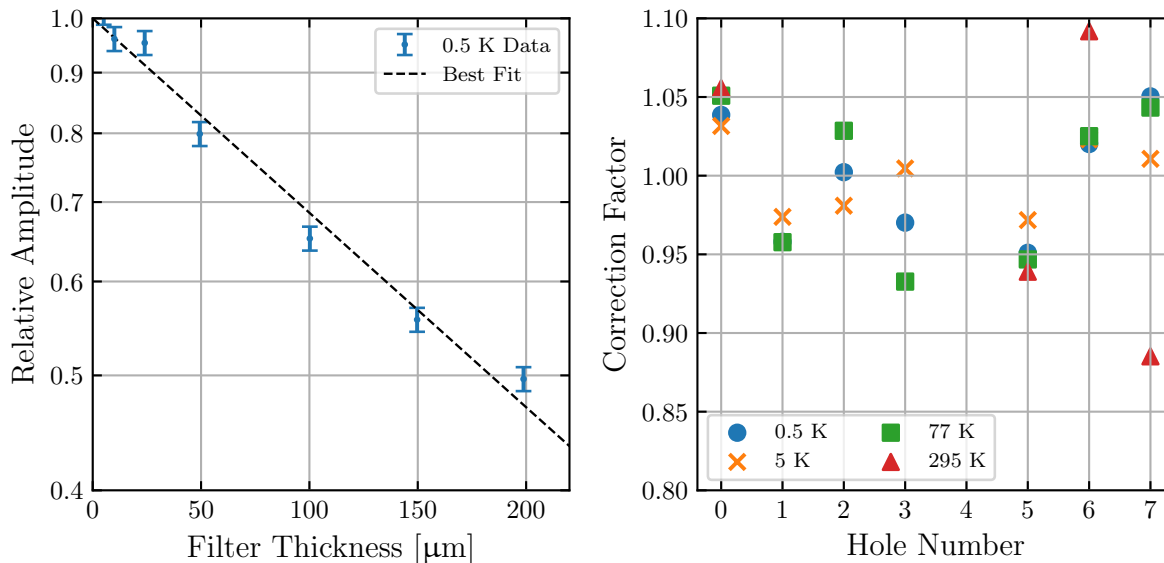


Figure 6.7: Left: light transmission as a function of Si filter thickness. The transmission data points are from the measurements using the 950 nm light source at a temperature of 0.5 K, and the dashed-curve is an exponential function fitted to the data points. The ratio between the measured and best-fit transmission values is used to approximate the hole transmission variation. Right: summary of the hole transmission correction factors used to adjust the transmission measurements from the 1028 nm light source at each temperature. Hole 4 corresponds to the empty hole in the filter mount, and therefore requires no correction factor.

Light Reflection

The issue of light reflecting off of the filter mount and affecting the signal measurements is discussed in Sec. 6.2.2 in regards to the secondary filter mount. For the measurements using the 448 nm light source, the amount of reflected light was so overwhelming that transmission measurements could not be made with the original filter mount. Although this was not the case for the other light sources, the amount of reflected light is still significant enough to motivate the development of a correction procedure.

In order measure the amount of light reflection at a given wavelength and temperature, an additional measurement was made by positioning the MEMS mirror to direct the beam to a blank part of the filter mount away from any of the holes. As with the normal transmission measurements, a scan of the beam spot consisting of a 14×14 grid of individual measurements was made. The mean amplitude of all (x, y) grid points is taken as the amplitude of light reflection. Furthermore, the amount of background in the voltage trace at a given wavelength and temperature was measured by following the same scan procedure without actually pulsing the light source. This blank scan is then used to extract the mean and standard deviation σ of the background amplitude. If the amplitude of light reflection is $> 3\sigma$ above the mean background amplitude, it is subtracted from the amplitudes of the normal transmission

measurements at the same wavelength and temperature. This criterion ensures that the transmission amplitudes measured are adjusted only if the amount of reflected light is significantly larger than the background.

The amount of reflected light is found only to be significant for the 530, 660, and 950 nm light sources at 0.5 K, and the 530, 639.5, 660, 950, and 1028 nm light sources at 5 K. The amplitude of reflected light in these cases range from 10–35 mV. These values are small compared to the majority of transmission measurements, the amplitudes of which are generally > 100 mV.

6.4 Analysis

The analysis procedure starts with the averaged pulse amplitude from each (x, y) grid point from the scan performed over each Si filter at each wavelength and temperature. Each scan is used to produce a 2D image to visually confirm that the beam is aligned with the hole. An example of a set of these scan images is shown in Fig. 6.8, where the decrease in amplitude is seen as the thickness of Si filter increases.

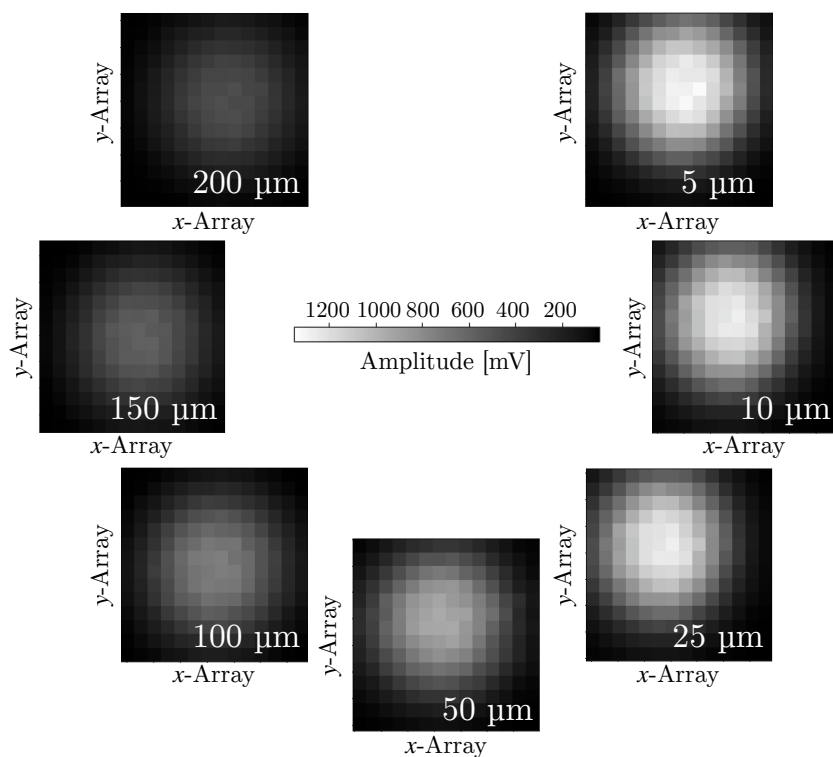


Figure 6.8: Set of 2D scan images from the transmission measurements performed over each Si filter, where the thickness of each filter is indicated on each scan image. The data in this plot were acquired using the 950 nm light source at a temperature of 5 K. The amplitude refers to the averaged pulse amplitude from each (x, y) grid point. Courtesy of Chris Stanford.

To turn a set of scans into a value for $\sigma_{p.e.}$, a series of post-processing steps is performed. First, the set of 14×14 grid points for each scan is divided into thirds based on time of acquisition. Recall that the ordering of individual measurements of the grid points from all the scans was chosen at random. Each scan is then separated into three “sub-scans” of lower resolution representing the first, second, and final third of grid points measured. Next, in order to reduce the impact of outliers, the median

amplitude amongst the five grid points of largest amplitude is taken as the transmission value for that sub-scan. Lastly, the median value amongst the transmission values of the three sub-scans is taken as the transmission value of the entire scan. The temporal division of the grid points is done to reduce the impact of any transient effects at the start of a run that are present in only the first sub-scan.

Once the transmission value for a scan is determined, the calibrations and corrections outlined in Sec. 6.3 are applied as appropriate. This includes calibrating for the pulse amplitude linearity, correcting for the hole transmission variation for the 1028 nm light source, and subtracting the reflected light amplitude if necessary. The calibrated and corrected transmission values are then plotted against the corresponding Si filter thickness. The error bars on these data points result from investigating biases induced from various sources, including the applied bias voltage, light intensity, linearity correction, neutralization procedure, and day-to-day variability. However, the most dominant source of error is found to be the hole transmission variation discussed in Sec. 6.3. The uncertainty due to the hole transmission variation is therefore taken as the uncertainty in the transmission values for each light source. The normalized transmission results from the several runs at the different wavelengths and temperatures are shown in Fig. 6.9. Note that some wavelengths do not have as many transmission data points. This is because the transmission of the shorter wavelengths could not be measured through the thicker Si filters.

To extract the value of $\sigma_{\text{p.e.}}$, an exponential function is fit to the transmission data points with their corresponding transmission uncertainties. The function is described according to the Beers-Lambert law:

$$Ae^{-\rho\sigma_{\text{p.e.}}t}, \quad (6.1)$$

where A (an arbitrary constant) and $\sigma_{\text{p.e.}}$ are the fit parameters, $\rho = 2.33 \text{ g/cm}^3$ is the density of Si, and t is the Si thickness. The fitted functions for each wavelength and temperature are also shown in Fig. 6.9. The fitted values of $\sigma_{\text{p.e.}}$ are shown in the right plot of Fig. 6.10 plotted at their corresponding photon energies. The uncertainty in the $\sigma_{\text{p.e.}}$ values is determined from the statistical uncertainty in the fits, whereas the uncertainty in the photon energies is derived from the uncertainty in the light sources. For the photon energy uncertainty values, the lower and upper bounds are determined from the upper half-maximum and lower half-maximum wavelengths, respectively, that are listed in Tab. 6.1.

Although the $\sigma_{\text{p.e.}}$ measurements in this work are measured at temperatures only as low as 0.5 K, there is not expected to be much of a difference between the values of $\sigma_{\text{p.e.}}$ between 0.5 and 0 K. As the results in the right plot of Fig. 6.10 show, the $\sigma_{\text{p.e.}}$ measurements are similar when measured at 0.5, 5, or 77 K, but significantly increase when measured at 295 K. This observation is also confirmed by a separate $\sigma_{\text{p.e.}}$ measurement performed at a fixed wavelength as the fridge was warming up.

In order to use these new results for dark matter limit setting, a continuous $\sigma_{\text{p.e.}}$ curve over energy is preferred. To obtain this curve, the same indirect photon absorption model described by Eq. F.5 in Appendix F is fit to the discrete $\sigma_{\text{p.e.}}$ measurements:

$$\alpha(T) = \sum_{i,j=1,2} C_i A_j \left(\frac{(E_\gamma - E_{g,j}(T) + E_{p,i})^2}{e^{E_{p,i}/k_b T} - 1} + \frac{(E_\gamma - E_{g,j}(T) - E_{p,i})^2}{1 - e^{-E_{p,i}/k_b T}} \right) + A_d (E_\gamma - E_{gd}(T))^{1/2}, \quad (6.2)$$

where $\alpha(T) = \sigma_{\text{p.e.}}(T)\rho$ is the linear absorption coefficient, E_γ is the photon energy, and T is the temperature. The summation term in Eq. 6.2 accounts for indirect photon absorption via phonon

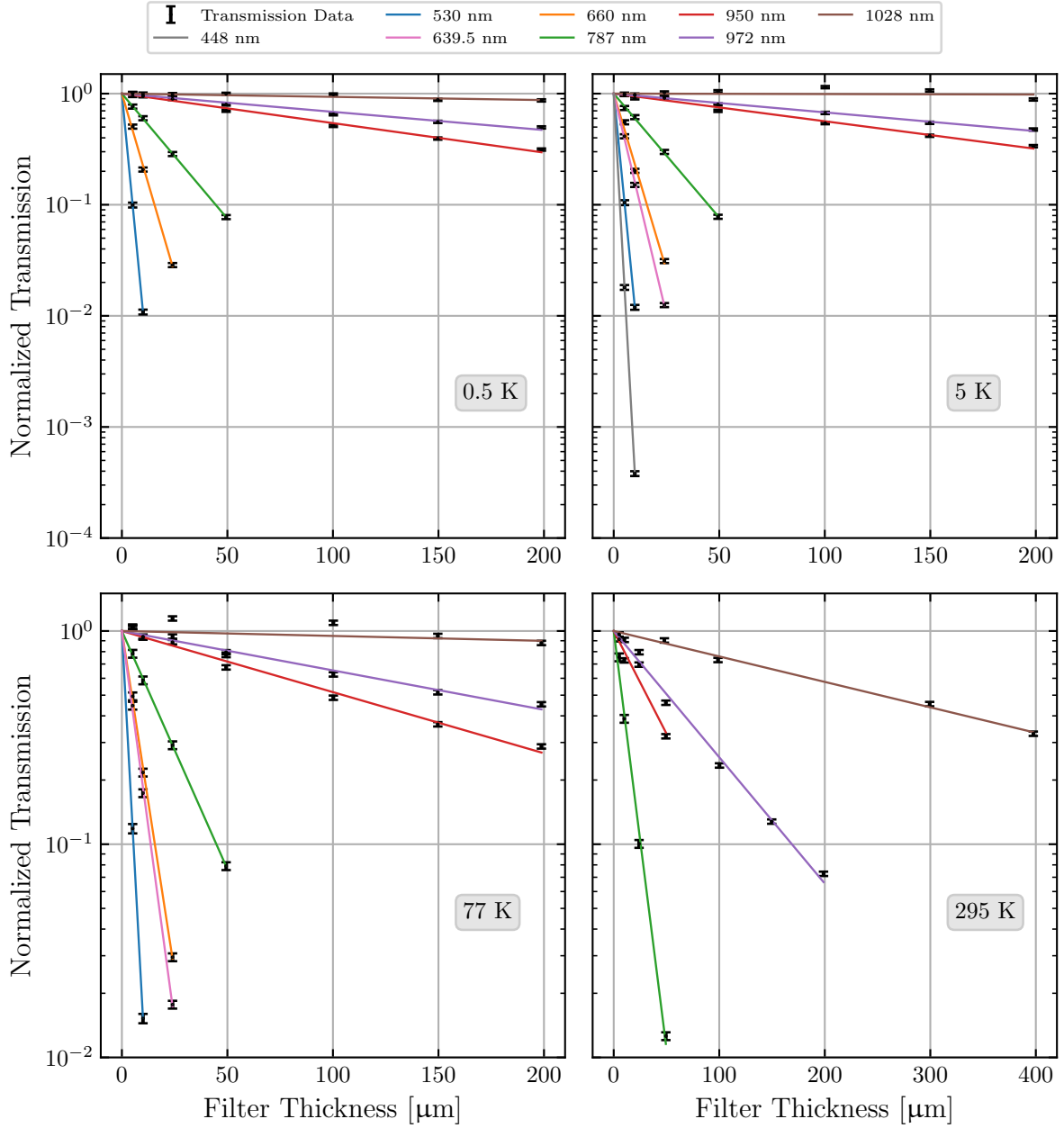


Figure 6.9: Summary of the transmission results versus Si filter thickness for the various wavelengths and temperatures. The temperature of each set of results is indicated on each plot, and the coloured curves are the exponential functions described by Eq. 6.1 fitted to the transmission data at the various wavelengths. The results are normalized to the arbitrary amplitude parameter A computed for each fit. Courtesy of Chris Stanford.

absorption and phonon emission, where the suffix i refers to the two phonon energies considered, $E_{p,i}$, and the suffix j refers to the two indirect band gaps with energies $E_{g,j}(T)$ that are active in photon absorption. The coefficients C_i describe the electron-phonon coupling constants, and the A_j coefficients are proportionality constants. Lastly, the final term in Eq. 6.2 describes direct photon absorption, with a direct band gap energy of $E_{gd}(T)$ and a proportionality constant A_d . The band gap energies $E_{g,j}(T)$

and $E_{gd}(T)$ in Eq. 6.2 have a temperature dependence according to:

$$E_{g,\ell}(T) = E_{g,\ell}(0) - \frac{\beta T^2}{T + \gamma}, \quad (6.3)$$

where $\ell = j, d$, $E_{g,j}(0)$ is the band gap energy at 0 K, and $\beta = 7.021 \times 10^{-4}$ eV/K and $\gamma = 1108$ K for Si. This photon absorption model is valid for photon energies up to 4 eV, and does not include any direct contributions from possible boron-oxygen complexes in the Cz-grown Si filters [165, 166]. More details about regarding this model are found in Appendix F, along with the values for the various parameters. Although it was previously used to apply a temperature correction to the existing $\sigma_{p.e.}$ data found in literature, this model can now be used to describe the new photoelectric cross section values over the various temperatures and energies.

First, the model is simultaneously fit to the four sets of $\sigma_{p.e.}$ measurements taken at 0.5, 5, 77, and 295 K by allowing to float the proportionality constants A_1 and A_2 of the first and second indirect band gap, respectively. To improve the fit of the model to the lower energy measurements, the lowest indirect band gap energy $E_{g1}(0)$ is also allowed to float while using the fixed value of $E_{g2}(0) = 2.5$ eV for the second indirect band gap energy, where there is not enough data to constrain. $E_{g1}(0)$ is held constant across all temperatures, but in order to investigate a possible temperature dependence in A_1 , A_1 is allowed to vary. Because the form of such temperature dependence is unknown, A_1 is initially fit separately to the $\sigma_{p.e.}$ measurements at each of the four temperatures. Only one measurement was taken at an energy above the second indirect band gap, so the temperature dependence in A_2 is not investigated.

The results of the fit for A_2 and $E_{g1}(0)$ are $(6 \pm 3) \times 10^3$ eV $^{-2}$ cm $^{-1}$ and (1.134 ± 0.004) eV, respectively. The fit results of A_1 at each of the four temperatures are shown in the left plot of Fig. 6.10 and demonstrate a significant temperature dependence. This observation may be a result of temperature-dependant effects that the phenomenological absorption model does not account for, such as the effect that temperature has on the density of states or on the electron-phonon coupling. To improve the fit of the model to the measurements, a second fit is performed by constraining A_1 to have an exponential temperature dependence according to:

$$A_1(T) = c_0 e^{-c_1 T}, \quad (6.4)$$

where c_0 and c_1 are additional fit parameters. An exponential function is chosen to describe the temperature dependence of A_1 for empirical reasons as it is physically plausible and requires only two parameters to sufficiently fit to the A_1 values. This second fit is still applied simultaneously to all of the $\sigma_{p.e.}$ measurements, but uses the previously determined A_2 and $E_{g1}(0)$ as fixed constants. The fitted values of c_0 and c_1 are (325 ± 6) eV $^{-2}$ cm $^{-1}$ and $(1.7 \pm 0.1) \times 10^{-3}$ K $^{-1}$, respectively. The result of the secondary fit are shown in Fig. 6.10; the left plot shows the exponential $A_1(T)$ function with the fitted c_0 and c_1 parameters, and the right plot shows the fitted absorption model evaluated at the same four temperatures as the $\sigma_{p.e.}$ measurements.

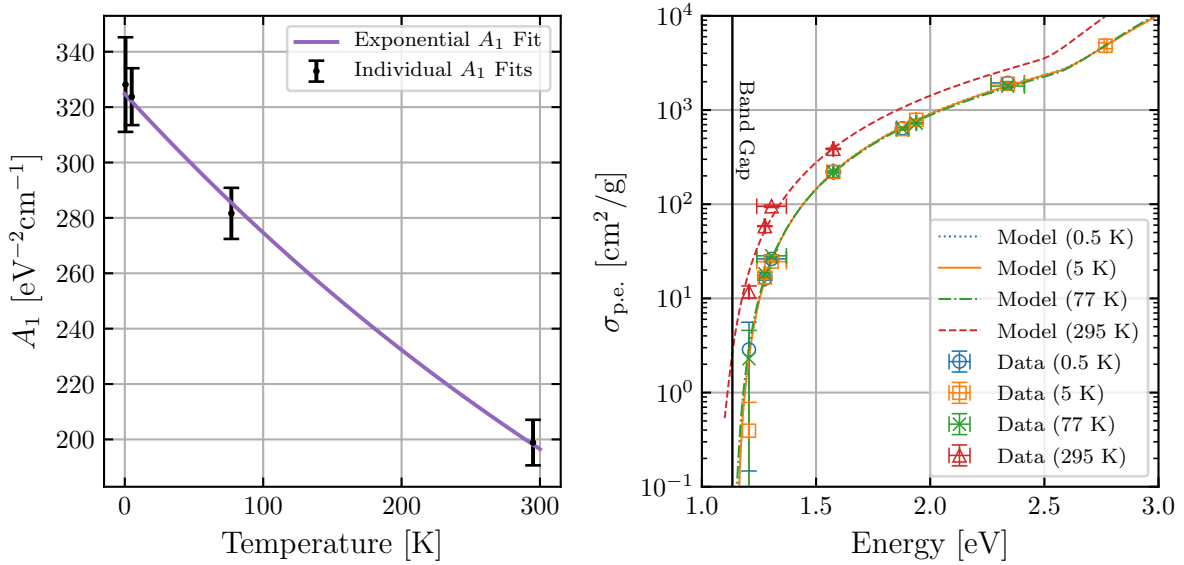


Figure 6.10: Left: results of the fitted proportionality constant of the first indirect band gap A_1 . The black data points are the separately fitted A_1 values at each of the measured temperatures, and the purple curve is the fitted $A_1(T)$ obtained when A_1 is constrained to an exponential function described by Eq. 6.4. Right: summary of the new $\sigma_{\text{p.e.}}$ measurements acquired in this work at the four discrete temperatures, and the results of the simultaneous fit of the absorption model to all of the measurements evaluated at the same four temperatures. The black, vertical line is the fitted first indirect band gap energy $E_{g1}(0)$.

6.5 Effect on Dark Matter Exclusion Limits

This section will probe the effects that the new $\sigma_{\text{p.e.}}$ measurements have on dark matter exclusion limits. Several DM direct detection channels are similar in that they are related to $\sigma_{\text{p.e.}}$. In this work, the relevant processes include the absorption of dark photons and ALP by a target material, and inelastic DM-nuclear scattering of Weakly Interacting Massive Particles (WIMPs) or light dark matter (LDM). The absorption channels cause the emission of one or more electrons, whereas the inelastic scattering channels lead to the Bremsstrahlung emission of a photon or the emission of an electron via the Migdal effect; the details of the absorption and inelastic scattering processes, as well as their dependence on $\sigma_{\text{p.e.}}$, are outlined in Sec. 1.5.3 and Appendix A, respectively.

To measure the impact of the new $\sigma_{\text{p.e.}}$ measurement, the signal models of the various DM interaction channels are calculated using two different $\sigma_{\text{p.e.}}$ curves: the *nominal* and the *fitted* curve. The nominal $\sigma_{\text{p.e.}}$ curve is defined in Sec. 2.3.3 for energies ≤ 50 keV and consists of commonly used data. The fitted $\sigma_{\text{p.e.}}$ curve is the result of evaluating the fitted absorption model from Sec. 6.4 at a temperature of 50 mK. This temperature is purposefully chosen to match the operating temperature during the HVeV Run 2 experiment. The absorption model used to describe the $\sigma_{\text{p.e.}}$ measurements is valid up to 4 eV, yet the DM signal models require $\sigma_{\text{p.e.}}$ values over a much wider range of energies. Thus for energies above 4 eV, the fitted $\sigma_{\text{p.e.}}$ curve uses the same data as the nominal $\sigma_{\text{p.e.}}$ curve starting at 4.02 eV, interpolating in the region between. Above 4 eV both the nominal and fitted curves are identical, and therefore any differences in the computed DM signal models and resulting exclusion limits are directly attributed to

the temperature dependence of $\sigma_{\text{p.e.}}$. Figure 6.11 compares the nominal and fitted curves used in this study between 1 and 10 eV.

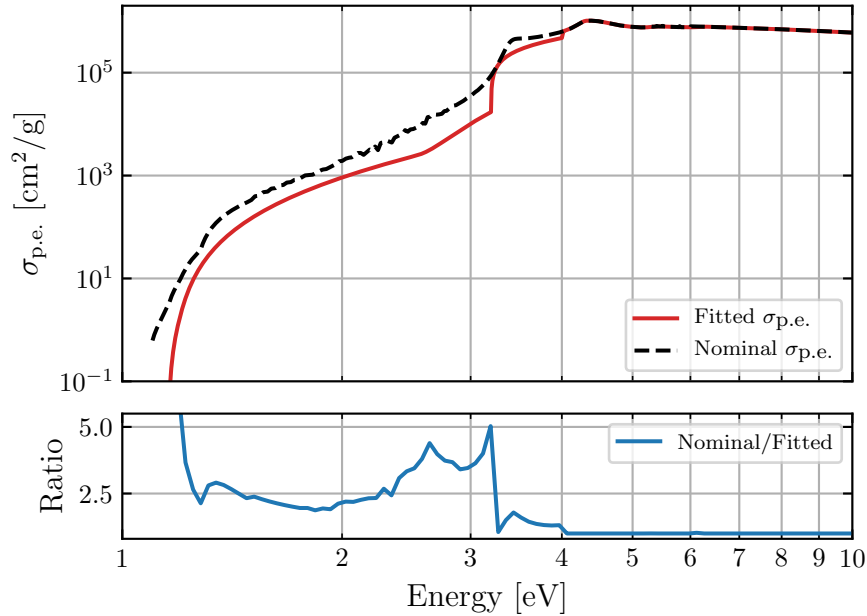


Figure 6.11: Top: comparison of the nominal (black) and fitted (red) $\sigma_{\text{p.e.}}$ curves used in this study. The nominal curve is comprised of commonly used $\sigma_{\text{p.e.}}$ data, whereas the fitted curve is the result of evaluating the fitted absorption model from Sec. 6.4 at 50 mK. The model is valid up to 4 eV. Above that energy, the two curves are identical. Bottom: ratio between the nominal and fitted $\sigma_{\text{p.e.}}$ curves.

Exclusion limits are calculated on the dark photon kinetic mixing parameter ε and the axioelectric coupling constant g_{ae} from the dark photon and ALP absorption models, respectively, for DM masses between 1.1 and 10 eV/ c^2 , as well as on the spin-independent, DM-nucleon scattering cross section σ_n^{SI} from the inelastic DM-nuclear scattering models under the emission of a Migdal electron or Bremsstrahlung photon for DM masses between 10^{-2} and 10 GeV/ c^2 . To demonstrate the effect of the new $\sigma_{\text{p.e.}}$ measurements on these limits, a low background dataset at electron recoil energies as low as the Si band gap is required. Such a dataset can be found from the HVEV Run 2 analysis in Chapters 4 and 5. Specifically, the exclusion limits calculated in this work use the quantized, 100 V energy spectrum from the HVEV Run 2 experiment obtained from a Si detector operated at 50 mK with 1.22 g-days of exposure. The 90% confidence level (C.L.) limits are calculated using the same Poisson limit setting method as described in Sec. 5.1.2. Because the limits on ε and g_{ae} were also calculated in Chapter 5, this analysis uses the same procedure to determine which e^-h^+ -pair peaks are considered to select the final limit result at each DM mass. For the limits on σ_n^{SI} , which were not calculated in Chapter 5, all six e^-h^+ -pair peaks are considered at all DM masses to select the final limit results.

For the case of the Bremsstrahlung and Migdal models, the limits are also examined using an additional toy experiment. In this idealized experiment, there are no events in the data spectrum, the detector efficiency is unity at all energies, and there is no charge trapping (CT) or impact ionization (II). Furthermore, the limits produced using this toy experiment are calculated only from the first e^-h^+ -pair peak. As will soon become evident, this toy experiment maximizes the effect on the σ_n^{SI} limits due to the discussed differences in $\sigma_{\text{p.e.}}$.

The DM signal models are calculated separately using either the nominal or fitted $\sigma_{\text{p.e.}}$ curve. The dependence on $\sigma_{\text{p.e.}}$, however, is quite different for the absorption and inelastic scattering models. The absorption models assume that the total interaction energy is the mass energy of the proposed DM particle, and so the dynamic range of the experiment is equal to the mass range accessible in the absorption processes. Furthermore as described in Sec. 1.5.3, the signal from each of these processes is a delta function at the DM mass with a rate proportional to $\sigma_{\text{p.e.}}$ at the DM mass energy. A different value of $\sigma_{\text{p.e.}}$ therefore results in a different overall scaling of the expected signal rate. For the inelastic scattering channels, the dependence on $\sigma_{\text{p.e.}}$ is more indirect and less obvious, as evident in Appendix A. For both the Bremsstrahlung and Migdal models, the expected signal at a given DM mass is a continuous spectrum of the differential interaction rate over the energy of the emitted photon or electron. Figure 6.12 shows an example of the spectra for these models given a DM mass of $m_\chi = 0.1 \text{ GeV}/c^2$, and shows how the spectra differ when calculated using either the nominal or fitted $\sigma_{\text{p.e.}}$ curve.

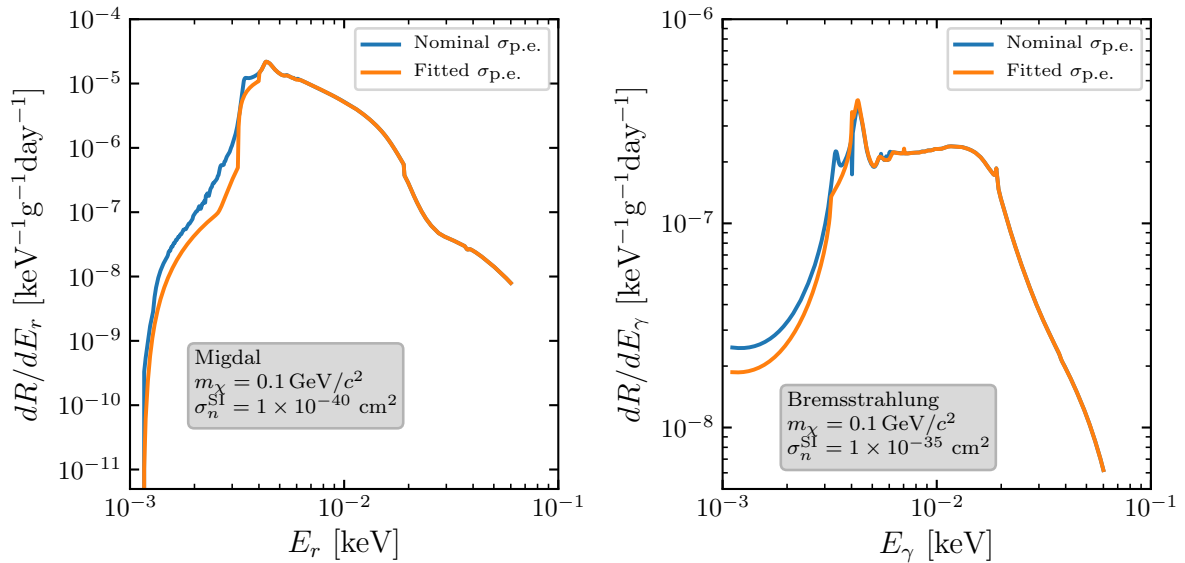


Figure 6.12: Differential interaction rate of inelastic DM-nucleus scattering under the emission of a Migdal electron with energy E_r (left) or a Bremsstrahlung photon with energy E_γ (right). The energy is the energy of the emitted particle. The assumed DM-nucleon cross section σ_n^{SI} and DM mass m_χ for each spectrum is given in the text box. The differential rate is calculated once with the nominal $\sigma_{\text{p.e.}}$ curve (blue) and once with the fitted $\sigma_{\text{p.e.}}$ curve (orange).

The signal models are transposed into the quantized e^-h^+ -pair energy space using the same detector response model used in Chapter 5 and described in Sec. 2.2, using the assumed value of $F = 0.155$ for the Fano factor. Instead of assuming a Si band gap energy of $E_g = 1.2 \text{ eV}$ like in Chapter 5, the detector response model in this work uses the fitted band gap energy of $E_g = 1.134 \text{ eV}$ that was determined in Sec. 6.4. The difference in E_g is negligible to nearly all of the DM signal models, however it does allow the limits for the absorption channels to extend to slightly lower masses. To quantize the continuous signals of the Migdal and Bremsstrahlung models, the spectrum at each DM mass is split into energy bins 1 eV in length. For each bin, a quantized signal is produced using the detector response model with an energy equal to the midpoint energy of the bin and an amplitude equal to the integral of the continuous signal within the bin. The final quantized signal at each DM mass is therefore the sum of

the individual quantized signals produced for each energy bin. Figure 6.13 shows the quantized signal model of dark photon absorption computed for a dark photon of mass $m_{A'} = 2 \text{ eV}/c^2$ and of the Migdal process computed for a DM particle of mass $m_\chi = 0.1 \text{ GeV}/c^2$, calculated using either the nominal or fitted $\sigma_{\text{p.e.}}$ curve. All of the signal models displayed are scaled by the HVeV Run 2 100 V exposure and efficiency, and are shown along with the 100 V HVeV Run 2 energy spectrum. The two Migdal signals in Fig. 6.13 are nearly identical. However, the inset plot shows the signals zoomed-in around the first e^-h^+ -pair peak where the difference between them is the most prominent.

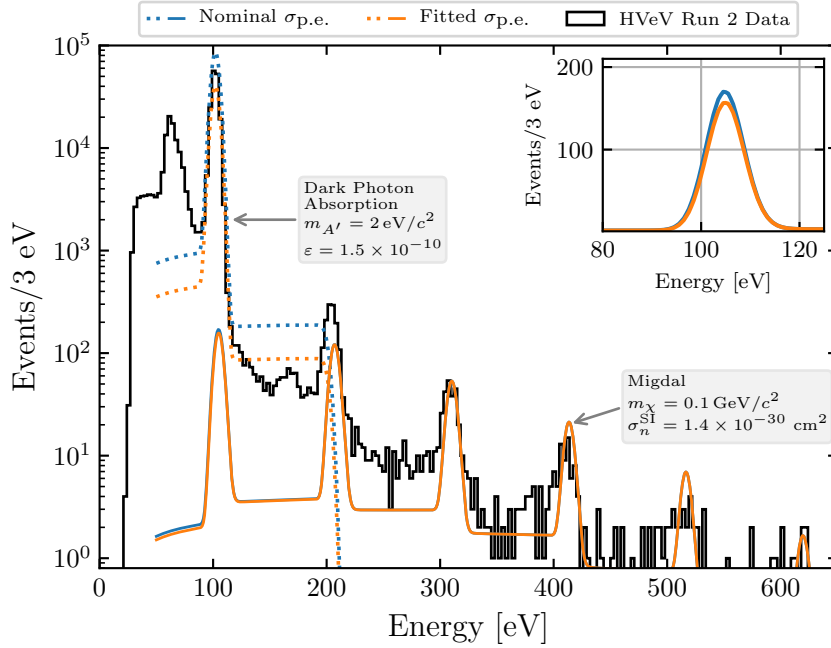


Figure 6.13: Quantized DM signal models for inelastic DM-nucleus scattering under the emission of a Migdal electron (solid curves) and for dark photon absorption (dotted curves). The assumed DM mass m_χ or $m_{A'}$ and relevant coupling parameter σ_n^{SI} or ϵ for the signal models of the corresponding interaction channel are given in the text box. The signal models are calculated once with the nominal $\sigma_{\text{p.e.}}$ curve (blue) and once with the fitted $\sigma_{\text{p.e.}}$ curve (orange). Also shown is the HVeV Run 2 data spectrum measured at 100 V. The inset plot shows the Migdal signal models zoomed-in around the first e^-h^+ -pair peak.

The final 90% C.L. limits on the absorption coupling parameters ϵ and g_{ae} calculated using either the nominal or fitted $\sigma_{\text{p.e.}}$ curve are compared in Fig. 6.14. The limit results from the 100 V HVeV Run 2 analysis are also shown for additional comparison. The inset in these plots show the ratio between the two newly calculated limits up to a mass of $4 \text{ eV}/c^2$; above that mass there is no difference between the limits as the same $\sigma_{\text{p.e.}}$ information is used.

It is no coincidence that the ratio between the limits calculated with the fitted and nominal $\sigma_{\text{p.e.}}$ curve is similar to the ratio of two $\sigma_{\text{p.e.}}$ curves themselves shown in Fig. 6.11. Because a different $\sigma_{\text{p.e.}}$ value at a given mass affects the overall scaling of the signal model for a given ϵ and g_{ae} , the limit at that mass is also affected by an overall scaling. Note that the signal rates for these processes are proportional to ϵ^2 or g_{ae}^2 , and so the corresponding limits are proportional to $\sigma_{\text{p.e.}}^{1/2}$. For both absorption processes, a lower $\sigma_{\text{p.e.}}$ value results in a higher, and thus weaker, limit on ϵ or g_{ae} . The largest effect of the newly

fitted $\sigma_{\text{p.e.}}$ curve has on the resulting limits is closest to the Si band gap, where the ratio between the $\sigma_{\text{p.e.}}$ curves exhibits asymptotic behaviour. At masses $> 1.3 \text{ eV}/c^2$ where the fitted and nominal $\sigma_{\text{p.e.}}$ curves differ, the difference between the limit results is also non-negligible. The limits are up to a factor of 2 weaker when calculated using the fitted $\sigma_{\text{p.e.}}$ curve compared to the nominal $\sigma_{\text{p.e.}}$ curve. The only exception is the limit on ε at dark photon masses above $\sim 3.5 \text{ eV}/c^2$. In this region, the limit calculated using the fitted $\sigma_{\text{p.e.}}$ curve is slightly stronger due to the in-medium correction applied to ε that is also dependent on $\sigma_{\text{p.e.}}$, as outlined in Sec. 1.5.3.

The final 90% C.L. limits on σ_n^{SI} for the Migdal and Bremsstrahlung inelastic scattering processes calculated using either the nominal or fitted $\sigma_{\text{p.e.}}$ curve are compared in Fig. 6.15. The limits that are set using the 100 V HVeV Run 2 data spectrum are virtually identical. These results can be explained by observing the Migdal signals shown in Figs. 6.12 and 6.13. The largest difference in the continuous signal spectra due to the choice of $\sigma_{\text{p.e.}}$ curve occurs for recoil or photon energies below $\sim 4 \text{ eV}$. However recoil and photon energies in this range predominately produce only one e^-h^+ pair. Therefore as Fig. 6.13 shows, the expected phonon signal to be observed using an HVeV detector differs predominately at the first e^-h^+ -pair peak due to the choice of $\sigma_{\text{p.e.}}$ curve. The difference between the signals is largest at low e^-h^+ pairs and negligible at higher e^-h^+ pairs. Yet the 100 V HVeV Run 2 data spectrum is highest at the first e^-h^+ -pair peak, as is typical with single-electron sensitive devices due to detector leakage. The resulting limits for these processes are therefore set on either the third, fourth, or fifth e^-h^+ -pair peak, where the choice of $\sigma_{\text{p.e.}}$ curve makes negligible difference.

To decouple these results from the specific data spectrum and to understand the maximum impact the fitted $\sigma_{\text{p.e.}}$ curve can have on the limits, the limit calculations are repeated using the previously defined zero-background toy experiment. Under the assumptions of the toy experiment, the strongest limits are set at the first e^-h^+ -pair peak. This also happens to be the region with the largest difference between the expected signals when calculated with the different $\sigma_{\text{p.e.}}$ curves. A weaker limit by about 10% and 5% for the Migdal and Bremsstrahlung process, respectively, is observed over the entire DM mass range when the fitted $\sigma_{\text{p.e.}}$ curve is used instead the nominal curve.

It should be noted that neither the absorption nor inelastic scattering limit results are corrected for Earth and atmosphere shielding effects that may be expected for a surface-operated experiment such as HVeV Run 2. The dark photon and ALP results are consistent with the community practice of not correcting for these effects, and these limit positions are several orders of magnitude below the upper bound for detection that is found as a result of absorption in the Earth's atmosphere or crust [167]. However given that these potential effects may be significantly suppressing the DM-scattering rates for a cross section at which the inelastic scattering limits are set (in contrast to the absorption rates at the set limits), these limit results should not be considered as actual constraints on σ_n^{SI} derived from the 100 V HVeV Run 2 data. Nevertheless, the conclusions from these results are unaffected by potential shielding effects, and are only intended to demonstrate the effect of $\sigma_{\text{p.e.}}$ on the limits.

6.6 Discussion

This chapter presents a novel experimental technique and analysis for precise measuring of the photoelectric absorption cross section $\sigma_{\text{p.e.}}$ of Si near the band gap at cryogenic temperatures. Furthermore, this chapter demonstrates the effect that this new $\sigma_{\text{p.e.}}$ measurement has on the limits for certain absorption and inelastic scattering DM models. The results of this work are reported in Ref. [2] and [3].

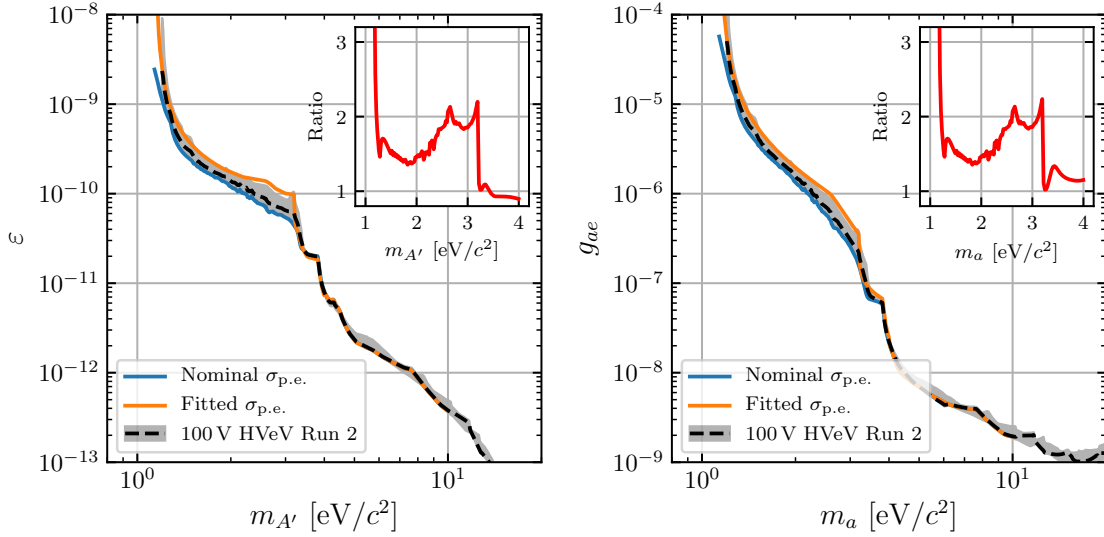


Figure 6.14: 90% C.L. exclusion limits on the dark photon kinetic mixing parameter ϵ over the dark photon mass $m_{A'}$ (left) and on the axioelectric coupling constant g_{ae} over the ALP mass m_a (right). All limits are based on the 100 V HVeV Run 2 data. The blue limit assumes the *nominal* dependence of $\sigma_{p.e.}$ on energy, whereas the orange limit uses the *fitted* absorption model to the new $\sigma_{p.e.}$ measurements discussed in Sec.6.4 evaluated at 50 mK. Both limits consider the Si band gap energy of 1.134 eV that was also fitted in Sec. 6.4. Their ratio is shown in the inset plot on a linear scale. The black limit is the 100 V HVeV Run 2 limit result from Chapter 5, including its uncertainty band in gray.

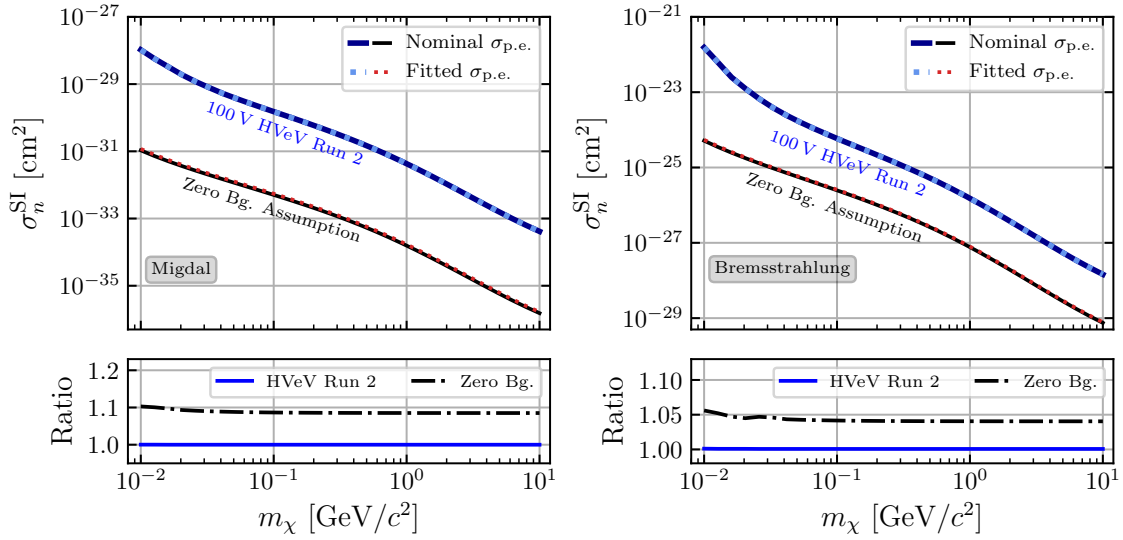


Figure 6.15: 90% C.L. exclusion limits on the spin-independent DM-nucleon scattering cross section σ_n^{SI} over the dark matter mass m_χ . The underlying interaction is inelastic DM-nucleus scattering under the emission of a Migdal electron (left) or Bremsstrahlung photon (right). The solid limits assume the *nominal* dependence of $\sigma_{p.e.}$ on energy, whereas the dotted limits use the *fitted* absorption model to the new $\sigma_{p.e.}$ measurements discussed in Sec.6.4 evaluated at 50 mK. Two sets of limits are shown: one based on the 100 V HVeV Run 2 data and another based on a zero-background toy experiment. Also shown for both scenarios is the ratio of the limit using the fitted $\sigma_{p.e.}$ curve over the limit using the nominal $\sigma_{p.e.}$ curve. All limits consider the Si band gap energy of 1.134 eV that was fitted in Sec. 6.4.

Future work can improve upon the $\sigma_{\text{p.e.}}$ result by measuring $\sigma_{\text{p.e.}}$ over a finer sampling of wavelengths, and by extending the range of measurements to lower wavelengths (higher photon energies). Extending the range of measurements to $\sim 4\text{ eV}$ would allow for a better fit of the absorption model to regions relevant to the second indirect band gap as well as the direct band gap of Si. However such measurements would require the manufacturing and implementation of Si filters with thicknesses $< 1\ \mu\text{m}$. A finer wavelength sampling may be accomplished by modifying the signal readout to accommodate a filtered xenon flash lamp or a longer time-constant tunable light source with a conventional shutter, with switching times on the scale of milliseconds. The experimental setup from this work is restricted to pulses from single-wavelength LEDs or lasers due to the nature of the AC-coupled charge amplifier detector design that is optimized for fast charge transport measurements. Future work may benefit from using a detector designed to optimize the total integrated power of charge transport measurements.

Furthermore, the experimental technique outline in this chapter can be easily adapted to measure $\sigma_{\text{p.e.}}$ of other target materials by replacing them with the Si filters in the filter mount. Of particular interest to dark matter searches are other semiconductors that can be used as target materials [168, 169, 170, 171], including germanium, the other detector material used in SuperCDMS experiments [148]. However to measure $\sigma_{\text{p.e.}}$ at photon energies below the band gap energy of silicon, such as germanium that has a band gap energy of $\sim 0.7\text{ eV}$, a detector with a smaller band gap would be required.

For both dark photon absorption and ALP absorption, the use of the fitted $\sigma_{\text{p.e.}}$ curve derived from the new $\sigma_{\text{p.e.}}$ measurements in this work to account for the temperature dependence over the nominal $\sigma_{\text{p.e.}}$ curve results in an exclusion limit up to two times greater (weaker) at masses below $4\text{ eV}/c^2$. Starting from $\sim 1.3\text{ eV}/c^2$, the difference becomes asymptotically greater as the mass approaches the band gap. Although these results are found by setting the limits on the 100 V HVeV Run 2 data, they are expected to be qualitatively applicable to comparable experiments such as SENSEI and DAMIC [152, 151]. Overall the effect the new $\sigma_{\text{p.e.}}$ measurements have on dark photon and ALP absorption searches using state-of-the-art cryogenic Si detectors cannot be ignored.

For the Migdal and Bremsstrahlung interaction channels, the fitted $\sigma_{\text{p.e.}}$ curve over the nominal curve bares no significant effect on the exclusion limits set using the 100 V HVeV Run 2 data. This result, however, depends on which e^-h^+ -pair peaks in the energy spectrum contribute to setting the limits. Calculating the limits for an idealized experiment with no events and perfect efficiency, where the limits are entirely determined using the first e^-h^+ -pair peak, maximizes the difference in the limits that could be observed when using the different $\sigma_{\text{p.e.}}$ curves. For the Migdal and Bremsstrahlung models, the difference in the limits in this scenario are about a factor of 1.1 and 1.05, respectively. Whether or not this effect is relevant depends on the size of the various systematic uncertainties that may exist in a given experiment. For instance, this effect is sub-dominant compared to the systematic uncertainties due to the Fano factor assumption and detector efficiency that exist in the HVeV Run 2 experiment. Additionally for the Migdal interaction channel, it is also important to note that the variation in the predicted signal due to the choice of model used to compute the signal is much larger than variation due to the $\sigma_{\text{p.e.}}$ curves. For example, Fig. 3 from Ref. [172] compares the predicted differential recoil spectrum computed using the Migdal model used in this work with the predicted differential recoil spectrum computed using a different Migdal model from Ref. [173] assuming a DM mass of $1\text{ GeV}/c^2$. The total predicted signal for recoil energies $\lesssim 50\text{ eV}$ differs by $\sim 30\%$ when computed using the two different approaches of modelling the Migdal effect, whereas over the same energy region and DM mass, the total predicted signal differs by only $\sim 3\%$ when computed using the two different $\sigma_{\text{p.e.}}$ curves.

In general, this work highlights the importance of considering the near-band-gap temperature effects of $\sigma_{\text{p.e.}}$ when conducting analyses on low-mass DM candidates that depend on this parameter. Although the focus of this work is with the use of silicon, similar considerations should be made for other solid-state DM search experiments that use a different semiconductor as the target material.

Chapter 7

Conclusions and Outlook

This final chapter will provide some concluding remarks on the analyses presented in this dissertation. However before making such remarks, it is worthwhile summarizing the key elements of each of the previous chapters. The purpose of the first three chapters in this dissertation was to lay a foundation of background knowledge and information in service of the dark matter (DM) search experiment and analysis presented in Chapters 4 and 5. Chapter 1 provided the motivations for DM searches and introduced various DM candidates, Chapter 2 described how DM can be detected using cryogenically-cooled semiconductor detectors, and Chapter 3 detailed the design of the second-generation high-voltage eV-scale (HVeV) detector. The analysis presented in Chapters 4 and 5 showed that exposure and energy resolution are not the key factors in improving the overall DM exclusion limits. This indicates that future experiments need to shift their focus to the identification and mitigation of low-energy backgrounds, which previous generations of detectors had not been sufficiently sensitive to encounter. Lastly, Chapter 6 presented a new measurement of the photoelectric absorption cross section at cryogenic temperatures, and showed the effect that the new measurement has on the exclusion limits for various DM models. The result from Chapter 6 is significant and impactful; not only does this photoelectric absorption cross section measurement bring clarity to the previously discrepant measurements found in the literature, but, importantly, it also greatly reduces what had been the most dominant source of uncertainty in the exclusion limits of the DM absorption channels for masses $\lesssim 4 \text{ eV}/c^2$. In this chapter, Sec. 7.1 discusses identifying sources of unknown background events, and Sec. 7.2 discusses other sources of experimental and model uncertainties. Finally, Sec. 7.3 provides a brief outlook on future DM search experiments that utilize low-threshold detectors.

7.1 Unknown Backgrounds

Table 5.8 compares the efficiency-corrected event rates at each e^-h^+ -pair peak observed in HVeV Run 1 and HVeV Run 2. The rates are similar between the two analyses despite a different detector design, cryostat, location, overburden, and shielding. Figure 7.1 compares the event rate spectra from HVeV Run 1 and HVeV Run 2 operated at 100 V. Note that the HVeV Run 1 detector has a charge resolution of $0.1 e^-h^+$ pairs, and the equivalent charge resolution for the HVeV Run 2 detector operated at 100 V is $0.036 e^-h^+$ pairs. These comparisons not only help to explain the similarities in the exclusion limits (as discussed in Sec. 5.5), but also add to the growing narrative of unexplained, $\mathcal{O}(\text{Hz}/\text{kg})$ low-energy excesses

measured in many sub-GeV DM searches (Refs. [174, 175, 176] and references therein). Specifically, the event rate observed above the second e^-h^+ -pair peak is ~ 10 Hz/Kg in the HVeV Run 1 detector, and ~ 15 Hz/Kg in the HVeV Run 2 detector operated at both 60 and 100 V. These rates are comparable to those found in recent EDELWEISS and SENSEI experiments [174]. Furthermore, the event rates observed in the HVeV Run 2 detector above the first e^-h^+ -pair peak is similar to those seen in other charge-readout experiments [106, 152, 151, 153]. The similarities in these observed event rates are notable, as the experiments differ greatly between their location, exposure, and depth.

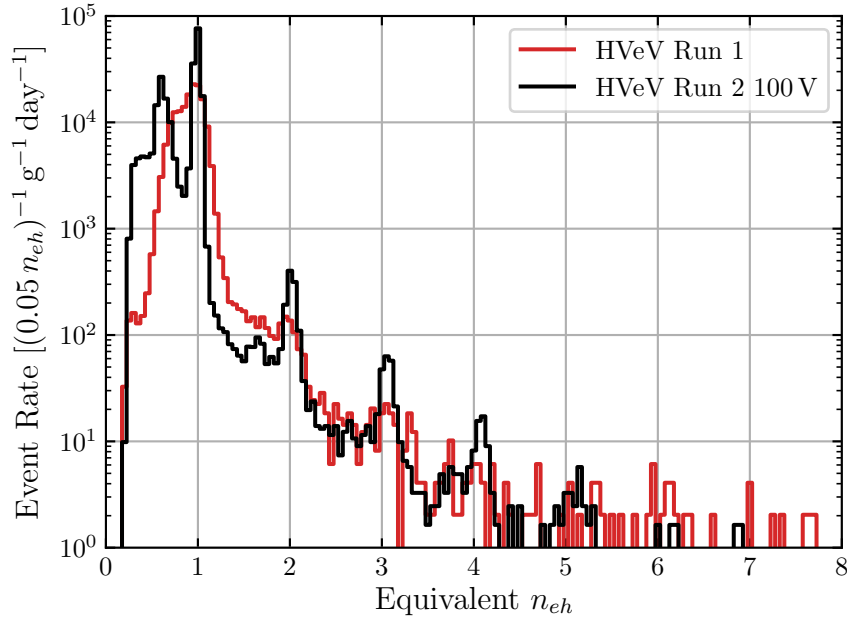


Figure 7.1: Comparison of the event rate spectra from HVeV Run 1 [106] and HVeV Run 2 operated at 100 V. The HVeV Run 2 spectrum is converted to equivalent number of e^-h^+ pairs n_{eh} in order to provide a better visual comparison.

Much of the focus of future experiments is therefore being put toward understanding the origin of these unknown background events. It is possible that detector leakage (see Sec. 2.4) is contributing to the high event rate observed in the first e^-h^+ -pair peak. Yet the events at higher e^-h^+ -pair peaks are likely due to particle interactions with the detector. The final-stage, energy-calibrated, DM-search spectra from the HVeV Run 2 analysis as outlined in Fig. 5.9 and Tab. 5.6 show that the e^-h^+ -pair peaks above $1 e^-h^+$ are positioned at energies greater than integer $n_{eh} \cdot e \cdot V_{\text{bias}}$ values. This indicates that the unidentified sources of background events are producing an excess amount of energy when they interact with the detector, and may suggest that the sources are external to the detector. It remains unclear what proportion of the background rate is due to detector leakage or external particle interactions, or what the origins of such external particle interactions are.

One theorized background source is the interaction of muons with SiO_2 that exists in the printed circuit boards (PCBs) that surround the detector, whereby the excitation of electrons produces a spectrum of photoluminescent photons between 2 and 6 eV [177]. Specifically, electron excitations due to a muon interaction can result in fluorescence and phosphorescence which may cause a signal in the detector. The left plot in Fig. 7.2 shows the photoluminescence for SiO_2 from Ref. [177]. It is unclear

how many photoluminescent photons would be produced per muon interaction, nor whether events from individual photons could be resolved. Yet the energy spectrum that may result from this photoluminescence can be investigated by using Monte Carlo (MC) simulations. The right plot in Fig. 7.2 compares the 100 V HVeV Run 2 spectrum with the energy spectra resulting from MC simulations of detector leakage and the photoluminescence spectrum, assuming various value of the Fano factor F . The rate of photoluminescence events is arbitrarily set at 0.072 Hz. In the case of $F = 0.3$, photoluminescent photons can produce events with up to four e^-h^+ pairs. Other potential sources of background events include light leakage from black-body radiation that may be absorbed at impurity sites in the detectors, and transition radiation caused by charged particles crossing between two regions of different dielectric permittivities [178].

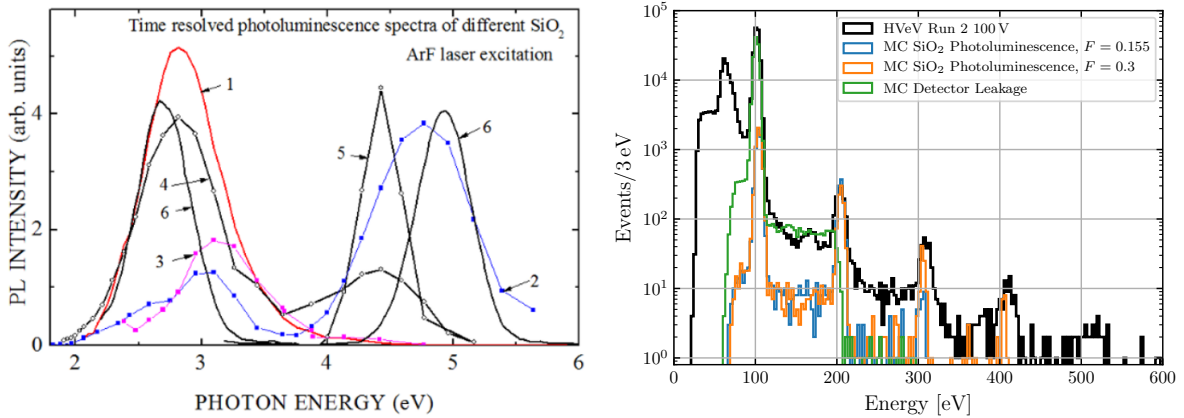


Figure 7.2: Left: photoluminescence spectrum for various SiO₂ materials, provided by Ref. [177]. Right: comparison of the 100 V HVeV Run 2 spectrum to various Monte Carlo (MC) simulations. The green histogram is a MC simulation of detector leakage with a surface leakage rate of 1.2 Hz and a bulk leakage rate of 1.6 Hz. The blue and orange histograms are MC simulations of the SiO₂ photoluminescence spectrum assuming a Fano factor F of 0.155 and 0.3, respectively. The rate of photoluminescence events is arbitrarily set at 0.072 Hz.

A third run using a detector with an identical design to the HVeV Run 2 detector is currently ongoing at Fermilab’s NEXUS Facility [72] (IL, USA). The overburden at the NEXUS site provides 255 m of water equivalent shielding, and the detectors are cooled using a dilution refrigerator that does not require temperature cycling like the ADR that was used for the HVeV Run 2 experiment (eliminating potential effects related to long cooling times of the detector materials). Furthermore, this third run is employing multiple detectors to improve upon the coincident veto method and help identify external background sources. Early results from NEXUS are already providing some insight into the origin of these unknown backgrounds [179]. Figure 7.3 compares the 100 V HVeV Run 2 event rate spectrum with the event rate spectrum measured at NEXUS. For this comparison, the HVeV Run 2 data are re-analyzed to use only a subset of the analysis cuts that could be applied to both datasets. Moreover as the NEXUS data in Fig. 7.3 do not (yet) have an independent source to calibrate the energy, the first three e^-h^+ -pair peaks are calibrated to the corresponding peaks from the 100 V HVeV Run 2 spectrum.

For the given amount of overburden at the underground NEXUS Facility, the flux of cosmic muons is roughly 60 events per m² per minute [180], which is a factor of ~ 100 – 1000 times smaller than the muon flux for surface-level experiments. Therefore the event rate of any muon-induced background would

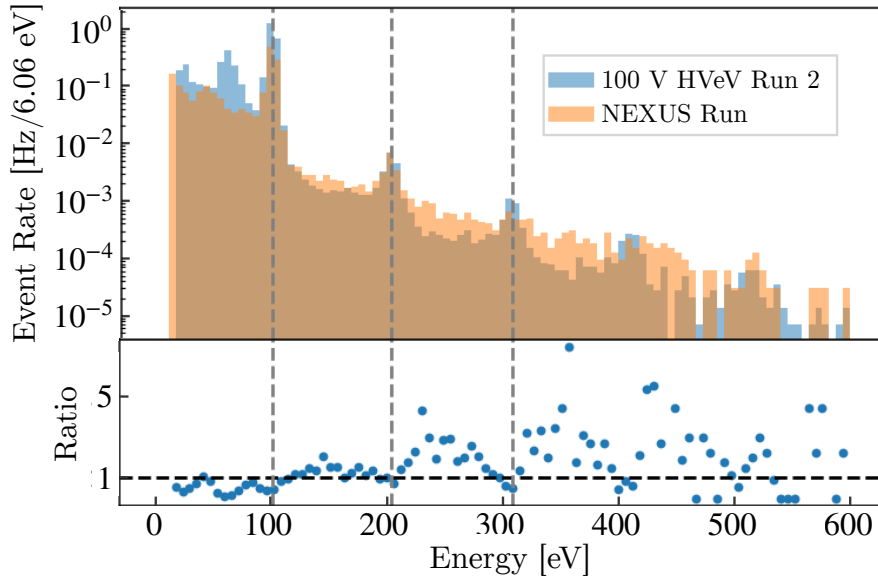


Figure 7.3: Top panel: Comparison of the event rates observed in the 100 V HVeV Run 2 data and from early data obtained using an identical detector at the NEXUS facility. The 100 V HVeV Run 2 data are re-analyzed to use only a subset of the analysis cuts that could be applied to both datasets, and the NEXUS data are calibrated in energy to the first three e^-h^+ -pair peaks of the HVeV Run 2 spectrum, as indicated by the dashed, vertical lines. Bottom panel: ratio between the NEXUS run and HVeV Run 2 spectra. Figure reproduced from Ref. [179].

also be reduced by a similar factor if measured at surface-level and at the NEXUS facility. However no such reduction is observed from the comparison of the HVeV Run 2 and NEXUS data in Fig. 7.3. This suggests that cosmic muons are not the predominant source of *single-pulse* background events measured by these detectors, and demonstrates that the rate of these low-energy events may not be influenced by the amount of overburden at a given facility. It is possible that cosmic muons create background events in the form of a primary particle interaction followed by multiple secondary interactions, or “burst” events containing multiple pulses in the trace. However these burst events would be removed by the analysis cuts, and thus would not appear in Fig. 7.3. There are also notable differences in two spectra shown in Fig. 7.3, as the NEXUS data show a higher event rate in the between-peak regions, and a slightly lower event rate at the e^-h^+ -pair peak regions. The cause of these differences are currently under investigation. Overall, the NEXUS run, as well as other future experiments with multiple detectors, will help to identify external background sources and further the understanding of these unknown lower-energy events. Doing so will enable the removal of background events (either experimentally or through data analysis), and will allow the use of more powerful and robust techniques like a likelihood-based method to set DM exclusion limits or find potential DM signals.

7.2 Experimental and Model Uncertainties

Another area of focus for future experiments is to identify and eliminate sources of experimental or model uncertainty. Figure 5.14 shows the impact that various sources of uncertainty have on the uncertainty in

the DM exclusion limits for the HVeV Run 2 experiment. Indeed the purpose of Chapter 6 is to present new and precise measurements of the photoelectric cross section, thereby reducing the uncertainty in this parameter at low energies. Yet there are still significant sources of uncertainty that impact DM search results. One such source of uncertainty, as is evident in Fig. 5.14, is the Fano factor F . The value of F determines the e^-h^+ -pair peak probabilities for a given amount of energy deposition, and is thus important to background and DM signals alike. Recently, a phenomenological model has been used to explore the ionization yield in Si for energies below 50 eV [102]. Figure 7.4 shows the best-fit results from Ref. [102] of the ionization yield as a function of energy deposition. For comparison, the same curves are shown for the ionization production model described in Sec. 2.2.1 that is used throughout this dissertation; the dashed curves in Fig. 7.4 are computed with nominal value of $F = 0.155$, and the shaded regions show the variation between $F = 10^{-4}$ and $F = 0.3$.

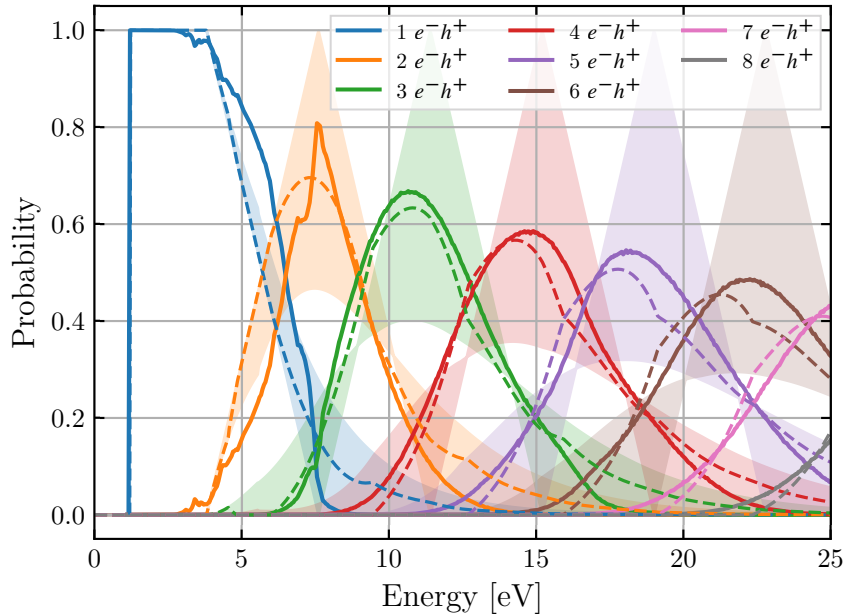


Figure 7.4: Probability distributions of e^-h^+ pair creation in Si. Each distribution corresponds to the probability of ionizing the labelled number of e^-h^+ pair for a given energy deposition. The solid curves are the best-fit results at 0 K obtained by Ref. [102], whereas the dashed curves are produced using the ionization production model described in Sec. 2.2.1 with the nominal Fano factor value of 0.155. The shaded regions show the variation between $F = 10^{-4}$ and $F = 0.3$, but are not shown for the seventh and eighth e^-h^+ -pair peak to reduce clutter. The values of either the solid or dashed curves at each point in energy sum to unity.

At most energies, the curves from Ref. [102] fall within the region spanned by the corresponding curves generated with the ionization production model used in this dissertation. However there are notable deviations, the most prominent being the difference in the probability of producing one e^-h^+ pair. This difference at the first e^-h^+ -pair peak would likely lead to stronger exclusion limits at low DM masses if computed using ionization probabilities from Ref. [102] compared to the current ionization model.

Another source of uncertainty comes from charge trapping (CT) and impact ionization (II). The two-parameter model described in Sec. 2.2.2 and Appendix D, whose inputs f_{CT} and f_{II} are the fraction

probabilities of CT and II, fits well to laser-calibration data that contain many e^-h^+ -pair peaks. However this model contains several assumptions, and may not be able to sufficiently describe data with fewer e^-h^+ -pair peaks. As alluded to in Appendix D.2, a more robust model might describe CT and II processes like an absorption process with a characteristic length. At the expense of more parameters and added complexity, such a model could disregard several of the assumptions made by the simplistic model, and could consider differences in f_{CT} and f_{II} between electrons and holes, second-order CT and II processes, and differences between surface- and bulk-generated events. Figure 7.5 shows an example of an expanded CT and II model compared to the current model. Here, the analytical models are meant to reproduce the results from a MC simulation of surface detector leakage with $f_{CT} = 0.1$ and $f_{II} = 0.3$. Although the value of f_{II} is much larger than what is typically measured, this example illustrates the limitations of the current model when the energy spectrum has only one e^-h^+ -pair peak. With the current limit setting methods that only use the e^-h^+ -pair peak regions to set limit values, an expanded CT and II model would not have much impact. However for the purposes of limit setting, an expanded model would be most useful, if not necessary, if the between-peak regions can also be used to set limit values.

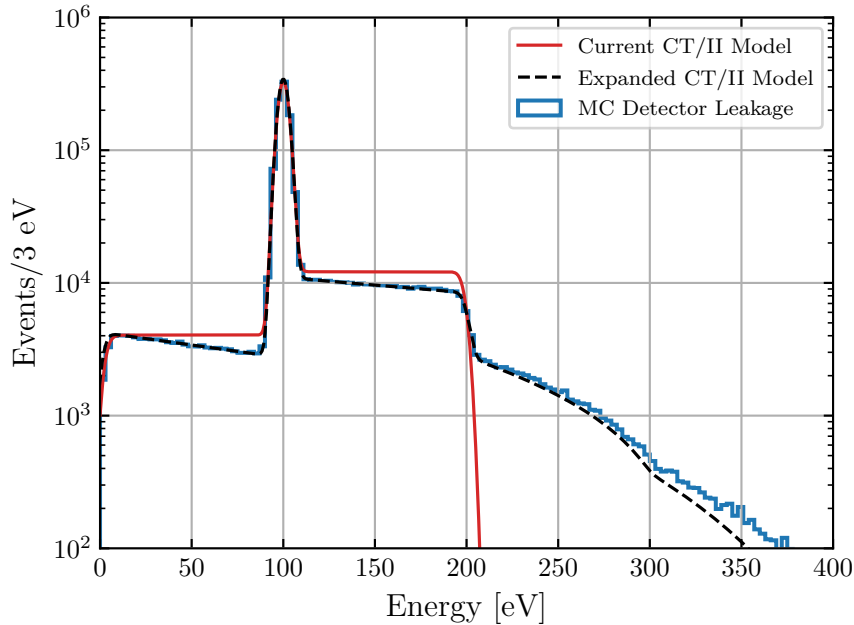


Figure 7.5: Comparison between the current model and an expanded model of charge trapping (CT) and impact ionization (II). Each model is meant to reproduce the results from a Monte Carlo (MC) simulation of surface detector leakage with fraction CT and II probabilities of $f_{CT} = 0.1$ and $f_{II} = 0.3$, respectively.

If a more robust CT and II model is to be used, it will be equally important to obtain precise measurements of the necessary parameters. As previously mentioned, the HVEV Run 2 experiment used a laser source pointed at only one surface of the detector. Having a laser source pointed at both detector surfaces would allow for separate measurements of f_{CT} and f_{II} for electrons and holes when the same polarity of voltage bias is applied across the detector. Another potentially important process that has not yet been mentioned is surface impact ionization, whereby there is some probability of an electron

or hole to release additional charges once it reaches the detector surface. A high probability of surface impact ionization could affect the expected energy spectra for both background sources and DM models, but this process could also be described by using an expanded CT and II model. Lastly, there is an ongoing effort toward understanding charge propagation processes [160, 159]. Future experiments can benefit by knowing which, if any, experimental factors affect the values of f_{CT} and f_{II} . Lower CT and II probabilities combined with a limit setting method that can exploit the between-peak regions can help improve the sensitivity of future experiments. A better understanding of CT and II processes, as well as the ionization yield, will also help to identify the sources of low-energy background events.

7.3 Outlook

The discussion so far has been focused on the challenges and interesting problems to be solved in upcoming R&D experiments using HVeV-type devices. While these smaller-scale studies and experiments have and will continue to report DM search results of their own, it is important to remember that they also serve to assist the upcoming SuperCDMS SNOLAB experiment. The SuperCDMS high voltage (HV) detectors are expected to have a phonon energy threshold of 100 eV and a phonon energy resolution of 5–10 eV [94], and are therefore likely to observe e^-h^+ pair quantization like with the HVeV detectors. So future experiments that can tackle the issues discussed in Secs. 7.1 and 7.2 using HVeV devices will also greatly benefit the SuperCDMS SNOLAB experiment.

Over the past several years, many collaborations have turned their attention to low-threshold DM search experiments in order to probe the parameter space of low-mass DM candidates. The SENSEI [36] and DAMIC-M [37] collaborations are utilizing charge-coupled devices with single- e^-h^+ -pair sensitivity and analysis thresholds comparable to the HVeV devices. The EDELWEISS collaboration (which also utilizes cryogenically-cooled semiconductor detectors) has recently been able to achieve sub- e^-h^+ -pair resolution and report constraints on sub-MeV/ c^2 DM candidates with a Ge target [153]. In short, the landscape for low-threshold DM search experiments remains quite competitive. Not only do R&D programs like the HVeV-based experiments help maintain a competitive advantage for SuperCDMS, but they also produce data and information that is useful to the field at large. And yet, the horizon of low-mass DM searches goes far past the limits of today’s detector technology. A likely path forward toward searches of even lighter DM candidates is to use new target materials. For example, doped semiconductor targets can have a lower band gap than their undoped counterparts, thereby lowering the energy range for absorption processes. Another material that has been proposed is superfluid helium, which can utilize similar detection technology as SuperCDMS detectors to achieve energy thresholds down to the meV scale [181]. Through the ongoing development of particle detection technologies, the expansion of our knowledge about low-energy background sources, and the continued mystery that is dark matter, the future of low-threshold DM search experiments promises to be very exciting.

Appendices

Appendix A

Inelastic Nuclear Scattering Models

As mentioned in Sec. 1.5.4, Weakly Interacting Massive Particles (WIMPs) and light dark matter (LDM) may undergo both elastic and inelastic nuclear scattering with a target material. Section 1.5.1 has outlined the model and expected event rate for the standard, elastic scattering process. This appendix will summarize two different models of inelastic nuclear scattering. The first model deals with the scenario where the inelastic scattering process is accompanied by an emitted photon, known as Bremsstrahlung. The second model describes a scenario in which the scattering process results in a dislodged electron through the so-called Migdal effect. Many formulations of the Migdal process exist, but the model described here is specifically summarized in detail because of its dependence on the photoelectric cross section $\sigma_{\text{p.e.}}$. As the Bremsstrahlung model also depends on $\sigma_{\text{p.e.}}$, they are both used in the analysis presented in Chapter 6.

A.1 Bremsstrahlung

For DM-nucleus elastic scattering, all of the energy deposited by the scattering DM particle is transferred to the recoil energy E_R of the target nucleus. For an inelastic scattering process, some of that energy may instead emit an accompanying photon with energy E_γ in the form of Bremsstrahlung. This scattering method provides a method of probing low-mass DM. Referring to Eq. 1.21, the maximum recoil energy that can be deposited by a WIMP with mass m_χ and velocity v for elastic scattering is:

$$E_{R, \max} = \frac{2\mu_N^2 v^2}{m_N}, \quad (\text{A.1})$$

where m_N is the mass of the target nucleus and μ_N is the DM-nucleus reduced mass. Conversely, the energy of the emitted photon is bounded by the energy of the relative motion of the DM and target nucleus [182]:

$$E_{\gamma, \max} = \frac{\mu_N v^2}{2}. \quad (\text{A.2})$$

Comparing Eqs. A.1 and A.2, it is clear that $E_{R, \max}$ and $E_{\gamma, \max}$ are related by:

$$E_{R, \max} = \frac{4\mu_N}{m_N} E_{\gamma, \max}. \quad (\text{A.3})$$

In the limit of $m_\chi \ll m_N$, $\mu_N \sim m_\chi$, and therefore $E_{R, \max} \sim 4(m_\chi/m_N)E_{\gamma, \max} \ll E_{\gamma, \max}$. In other words, for low DM masses, the upper bound of possible photon energies is much larger than that of nuclear recoil energies. By observing the electron signal resulting from the emitted Bremsstrahlung photons, experiments are able to probe DM masses below $90 \text{ MeV}/c^2$, the lowest mass probed to date in elastic DM-nucleus scattering searches [130]. The model and expected event rate for the Bremsstrahlung inelastic scattering process described here follows the work in Ref. [182]. For a scattering process that both deposits recoil energy and emits a photon, a double differential cross section is required:

$$\frac{d^2\sigma}{dE_R dE_\gamma} = \frac{\alpha}{3\pi E_\gamma} \frac{E_R}{m_N} |f(E_\gamma)|^2 \frac{d\sigma}{dE_R} \Theta(E_{\gamma, \max} - E_\gamma), \quad (\text{A.4})$$

where α is the fine-structure constant, $\Theta(E_{\gamma, \max} - E_\gamma)$ is the Heavyside step function, and $|f(E_\gamma)|$ is the atomic scattering form factor of the target material. Following Ref. [183], f can be written as a function of the photoelectric absorption cross section $\sigma_{\text{p.e.}}$:

$$|f|^2 = |f_1 + if_2|^2 = f_1^2 + f_2^2, \quad (\text{A.5})$$

where the imaginary component f_2 is given by:

$$f_2(E_\gamma) = \frac{\sigma_{\text{p.e.}}(E_\gamma)}{2r_e\lambda}, \quad (\text{A.6})$$

where r_e is the electron radius and λ is the photon wavelength. The real component f_1 is related to f_2 , and thus also related to $\sigma_{\text{p.e.}}$:

$$\begin{aligned} f_1(E_\gamma) &= Z^* + \frac{2}{\pi} \mathcal{P} \int_0^\infty \frac{E'_\gamma f_2(E'_\gamma)}{E_\gamma^2 - E'^2_\gamma} dE'_\gamma \\ &= Z^* + \frac{1}{\pi r_e h c} \mathcal{P} \int_0^\infty \frac{E'^2_\gamma \sigma_{\text{p.e.}}(E'_\gamma)}{E_\gamma^2 - E'^2_\gamma} dE'_\gamma. \end{aligned} \quad (\text{A.7})$$

Here, $Z^* \simeq Z - (Z/82.5)^{2.37}$ is the atomic number of the target material after a small relativistic correction [183], \mathcal{P} is the Cauchy principal value, c is the speed of light, h is Planck's constant, and $\lambda = hc/E_\gamma$ converts the photon energy to its wavelength. The differential event rate for the Bremsstrahlung scattering interaction is simplified by neglecting the energy deposition E_R as long as $E_{R, \max} \ll E_{\gamma, \max}$, taking the emitted photons as the only detectable signal. Given the large size of DM detectors compared to the absorption or scattering lengths of the emitted photons, the Bremsstrahlung model also makes the reasonable assumption that the emitted photons are always absorbed or scattered by the target material. For lighter materials such as silicon (Si) and germanium (Ge), the energy range of the emitted photons assures that all of the photons will be absorbed. With this in mind, the differential cross section over photon energies can be found simply as:

$$\frac{d\sigma}{dE_\gamma} = \int_{E_{R, \min}}^{E_{R, \max}} dE_R \frac{d^2\sigma}{dE_R dE_\gamma}, \quad (\text{A.8})$$

where the upper and lower bounds of the recoil energy integration are determined by kinematic constraints:

$$E_{R, \max/\min} = \frac{\mu_N^2 v^2}{m_N} \left[\left(1 - \frac{E_\gamma}{\mu_N v^2} \right) \pm \sqrt{1 - \frac{2E_\gamma}{\mu_N v^2}} \right]. \quad (\text{A.9})$$

The differential cross section term $d\sigma/dE_R$ found in Eq. A.4 can be substituted with the differential cross section for elastic scattering found in Eq. 1.24: $d\sigma/dE_R = (m_N/2\mu_N^2 v^2)\sigma_{N,0}^{\text{SI}}F^2(E_R)$. Recall that $F^2(E_R)$ is the nuclear form factor term and $\sigma_{N,0}^{\text{SI}}$ is the DM-*nucleus* cross section at zero momentum transfer that is related to the DM-*nucleon* cross section $\sigma_{n,0}^{\text{SI}}$ in Eq. 1.30. For the recoil energies considered, $F^2(E_R) \sim 1$, and therefore $\sigma_{N,0}^{\text{SI}} \approx \sigma_n^{\text{SI}}$. Putting this together, Eq. A.8 becomes:

$$\frac{d\sigma}{dE_\gamma} = \frac{4\alpha}{3\pi E_\gamma} |f(E_\gamma)|^2 \frac{\mu_N^2 v^2}{m_N^2} \sigma_n^{\text{SI}} \sqrt{1 - \frac{2E_\gamma}{\mu_N v^2}} \left(1 - \frac{E_\gamma}{\mu_N v^2} \right). \quad (\text{A.10})$$

Lastly, the differential event rate dR/dE_γ has the same construction as in Eq. 1.17, whereby the velocity-averaged differential cross section is found by integrating over the velocity distribution $f_v(\vec{v})$ of the DM particles:

$$\frac{dR}{dE_\gamma} = \frac{\rho_{\text{DM}}}{m_N m_\chi} \int_{v_{\min}}^{\infty} v f_v(\vec{v}) \frac{d\sigma}{dE_\gamma} d\vec{v}, \quad (\text{A.11})$$

where $v_{\min} = \sqrt{2E_\gamma/\mu_N}$ and there is an implicit maximum velocity set by the escape velocity of the galaxy. The validity of this model at energies as low as the band gap of the target material is subject to ongoing research [184]. Figure A.1 shows the total event rate (found by integrating Eq. A.11 over E_γ) as a function of DM mass for Si, assuming a spin-independent (SI) DM-nucleon cross section of $\sigma_n^{\text{SI}} = 10^{-35} \text{ cm}^2$. Also shown are the differential event rates at various DM masses for photon energies below 60 eV.

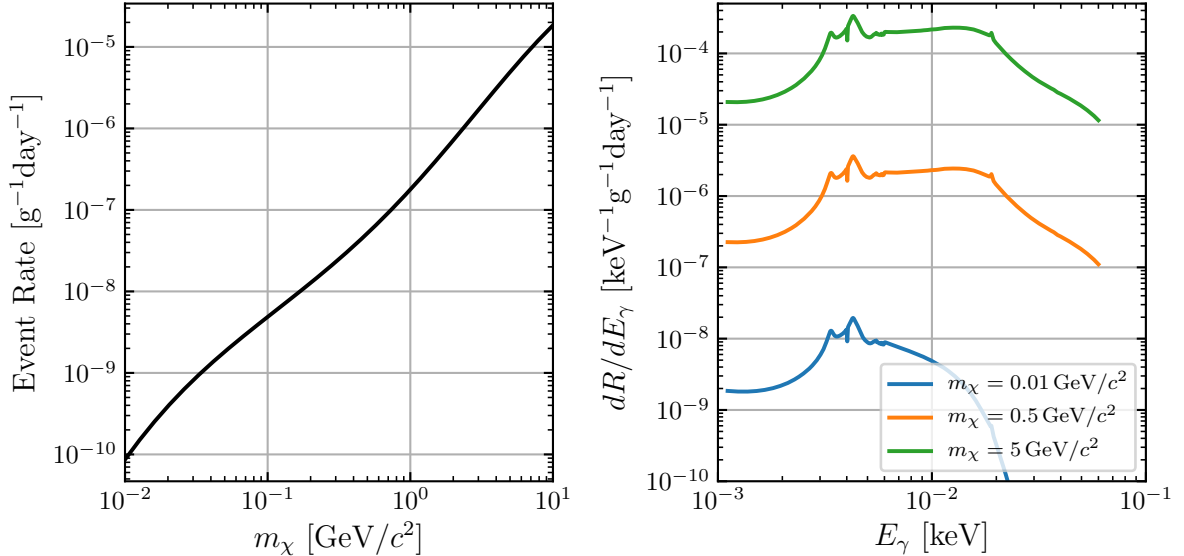


Figure A.1: Left: expected event rate for inelastic DM-nucleus scattering under the emission of a Bremsstrahlung photon as a function of DM mass m_χ for a Si target, assuming a spin-independent (SI) DM-nucleon cross section of $\sigma_n^{\text{SI}} = 10^{-35} \text{ cm}^2$. Right: differential event rate as a function of the emitted photon energy E_γ at various DM masses.

As stated in Ref. [182], the potential parameter space where the method of Bremsstrahlung photon emission yields an improvement in sensitivity is best identified where there is no sensitivity to elastic scattering interactions. This imposes the condition that there are no events induced above a detector-specific threshold $E_{R, \text{th}}$. In other words, for an elastic scattering rate of dR/dE_R ,

$$N(E_R > E_{R, \text{th}}) = \text{exposure} \times \int_{E_{R, \text{th}}}^{\infty} dE_R \frac{dR}{dE_R} < 1. \quad (\text{A.12})$$

For a low-threshold experiment such as the HVeV Run 2 experiment presented in Chapters 4 and 5, a similar argument can be made. Figure 5 in Ref. [94] shows the ionization yield for Si, including the minimum nuclear recoil energy of 40 eV required for ionization production. Given that the average energy to produce a single e^-h^+ pair in Si is 3.8 eV and the analysis range of the HVeV Run 2 experiment is 1–6 e^-h^+ pairs, only nuclear recoils between ~ 40 –400 eV would induce a measurable signal (see Eq. 2.3). For DM masses $\lesssim 0.4 \text{ GeV}/c^2$, the nuclear recoil energy spectrum falls below the 40 eV threshold for ionization production in Si. For large DM masses $\gtrsim 5 \text{ GeV}/c^2$, most of the nuclear recoil energy spectrum is outside the analysis range for the HVeV Run 2 experiment. In contrast, as photons can be measured at energies as low as the band gap of the target material, the HVeV Run 2 experiment has sensitivity to lower DM masses via Bremsstrahlung photon emission compared to elastic nuclear scattering.

Furthermore, as stated above and in Ref. [182], the model assumes that the energy deposition due to the recoil energy can be neglected as long as $E_{R, \text{max}} \ll E_{\gamma, \text{max}}$. For a heavy target material such as xenon (Xe), this assumption is fairly robust. However for larger DM masses and lighter targets, this assumption can start to break down. Referring to Eqs. A.9–A.11, there is no lower bound placed on E_{γ} . It is therefore kinematically possible for the recoil energy to exceed the emitted photon energy. This assumption can be examined further by considering the kinematically constrained parameter space of recoil and photon energies described by Eq. A.9. The area enclosed by $E_{R, \text{min}}$ and $E_{R, \text{max}}$ defines all the possible combinations of E_R and E_{γ} that may arise from an inelastic scattering event with a particular target mass, DM mass, and DM velocity. Figure A.2 shows this parameter space for a DM particle with a mass of $10 \text{ GeV}/c^2$ scattering off of a Si (left) and Xe (right) target with a velocity of 400 km/s.

The black, solid lines in Fig. A.2 are the difference between $E_{R, \text{max}}$ and E_{γ} , and are meant to identify regions where $E_R > E_{\gamma}$. For a given E_{γ} where $E_{R, \text{max}} - E_{\gamma} > 0$, there are at least some recoil energies that exceed the emitted photon energy. However the basis of the initial assumption is that the recoil energies are small enough to be neglected, and having only $E_{\gamma} > E_R$ is a low bar to set. A stronger condition may be to insist that, in order to reasonably neglect the recoil energy (i.e. $E_R \ll E_{\gamma}$), $E_R < 0.1 \cdot E_{\gamma}$. This condition is illustrated by the black, dashed lines in Fig. A.2. Like before, a given E_{γ} where $E_{R, \text{max}} - 0.1 \cdot E_{\gamma} > 0$ indicates that there are at least some recoil energies where $E_R < 0.1 \cdot E_{\gamma}$ is not fulfilled. For a lighter target like Si, these failed conditions take up a larger portion of the parameter space compared to a heavier target like Xe. Yet even for a target like Xe, the simplifying assumption that the recoil energies can be neglected in the rate equation may not hold for (relatively) larger DM masses.

Although the plots shown in Fig. A.2 seem to indicate that E_R should not be neglected, they were specifically calculated at a high DM mass to illustrate an extreme example of where this assumption may no longer be valid. Indeed for Si and a DM mass of $10 \text{ GeV}/c^2$, even the underlying condition of $E_{R, \text{max}} \ll E_{\gamma, \text{max}}$ fails. However this assumption can be tested more broadly for all of the sampled DM masses by introducing the parameter $\mathcal{F}(E_R \ll E_{\gamma})$. For each DM mass, $\mathcal{F}(E_R \ll E_{\gamma})$ is defined as

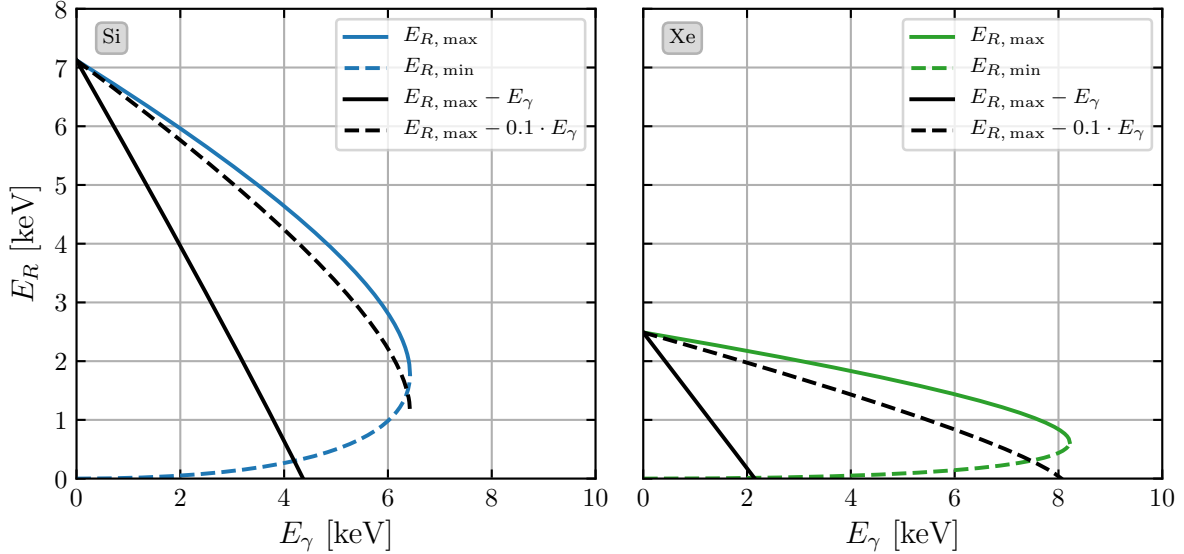


Figure A.2: Kinematically allowed parameter space of the recoil energy E_R and photon energy E_γ produced from a DM particle with mass $10 \text{ GeV}/c^2$ inelastically scattering off of a Si (left, blue curve) and Xe (right, green curve) target with an initial velocity of 400 km/s . The black, solid lines are the difference between $E_{R,\text{max}}$ and E_γ , and indicate where there are recoil energies that exceed the photon energy. The black, dashed lines are the difference between $E_{R,\text{max}}$ and $0.1 \cdot E_\gamma$, and indicate where there are recoil energies exceed a tenth of the photon energy.

the fraction of the kinematically allowed (E_R, E_γ) parameter space that satisfies $E_R \ll E_\gamma$. As before, $E_R \ll E_\gamma$ can be defined as the combinations of E_R and E_γ such that $E_R < 0.1 \cdot E_\gamma$. Using these definitions alone, the black curve in Fig. A.3 shows $\mathcal{F}(E_R \ll E_\gamma)$ as a function of DM mass for Si.

The definition of $E_R \ll E_\gamma$ can be supplemented by recalling that the minimum nuclear recoil energy for ionization production in Si is 40 eV . Therefore $E_R \ll E_\gamma$ can be defined as the combinations of E_R and E_γ that satisfy either $E_R < 0.1 \cdot E_\gamma$ or $E_R < 40 \text{ eV}$. Using this new definition, $\mathcal{F}(E_R \ll E_\gamma)$ as a function of DM mass is shown again by the blue curve in Fig. A.3. Without the ionization threshold condition, $\mathcal{F}(E_R \ll E_\gamma)$ is largely independent of the DM velocity. However a large velocity dependence emerges when the ionization threshold condition is used. The blue curve in Fig. A.3 is calculated assuming a DM velocity of 400 km/s , and the shaded region shows $\mathcal{F}(E_R \ll E_\gamma)$ when the velocity is varied from $100\text{--}650 \text{ km/s}$.

Figure A.3 shows that the simplifying assumption to neglect the recoil energies is reasonably valid in Si for DM masses $\lesssim 0.4 \text{ GeV}/c^2$. It should be noted that the analysis presented in Chapter 6 uses this inelastic scattering model as described in Ref. [182]. The point of examining the validity of the model assumptions is to highlight areas where the model may insufficiently describe the presumed interaction, specifically when using a Si target. Furthermore, the magnitude of $\mathcal{F}(E_R \ll E_\gamma)$ does not translate to any expected differences in the differential cross section nor the differential rate equations. Lifting the assumption that the recoil energies are neglected introduces complexities in these equations that are not discussed here.

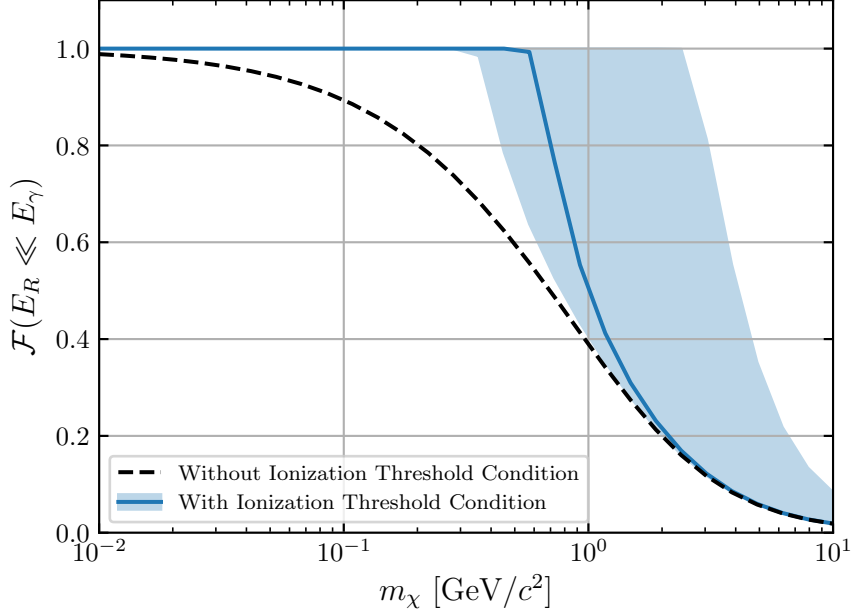


Figure A.3: $\mathcal{F}(E_R \ll E_\gamma)$ as a function of DM mass m_χ for a Si target, where $\mathcal{F}(E_R \ll E_\gamma)$ is defined as the fraction of the kinematically allowed parameter space of the recoil energy E_R and the photon energy E_γ that satisfies $E_R \ll E_\gamma$. The black, dashed curve shows $\mathcal{F}(E_R \ll E_\gamma)$ where the only condition for $E_R \ll E_\gamma$ is $E_R < 0.1 \cdot E_\gamma$, and is largely independent of the DM velocity. The blue curve defines $E_R \ll E_\gamma$ as the combinations of E_R and E_γ that satisfy $E_R < 0.1 \cdot E_\gamma$ or if E_R is below the ionization threshold for nuclear recoils: $E_R < 40$ eV. This added condition introduces a strong velocity dependence. The blue, shaded region shows $\mathcal{F}(E_R \ll E_\gamma)$ when the DM velocity is varied from 100–650 km/s.

A.2 Migdal Effect

Another proposed inelastic scattering process that is able to probe DM masses that are otherwise too small for the standard elastic DM-nucleus scattering interaction is the so-called Migdal effect [86]. Under elastic nuclear scattering, it is assumed that the surrounding electron cloud instantaneously follows the motion of the nucleus. In reality, the electron cloud does not immediately follow the nucleus, and the relative displacement within the atom represents an excited state. An electron emitted during the de-excitation of the atom produces an observable electron recoil spectrum, distinct from the nuclear recoil energy. This overall process is called the Migdal effect, which has recently been described in the context of dark matter search experiments [185]. There are various models that exist for calculating the differential event rate [185, 172, 173, 186, 187]. However only the approach taken in Ref. [172] is described here, as it is the only calculation based on the photoelectric absorption cross section $\sigma_{\text{p.e.}}$, thus making it uniquely relevant to the analysis presented in Chapter 6.

The differential cross section for this inelastic scattering process is a function of both the nuclear recoil energy E_R and the energy of the accompanying ionized electron E_r due to the Migdal effect. As described in Ref. [172], the dependence on $\sigma_{\text{p.e.}}$ is found by relating the dipole matrix element for electron transitions with the electron dipole approximation for photoelectric absorption:

$$\frac{d^2\sigma^{\text{MPA}}}{dE_R dE_r} = \frac{m_e^2}{\mu_N^2 v^2} \sigma_N^{\text{SI}} \frac{E_R}{E_r} \frac{\sigma_{\text{p.e.}}(E_r)}{4\pi^2 \alpha}. \quad (\text{A.13})$$

The expression above is referred to as the Migdal-photo-absorption (MPA) relation. Here, m_e is the electron mass, v is the DM velocity, α is the fine structure constant, μ_N is the DM-nucleus reduced mass, and σ_N^{SI} is the previously defined DM-nucleus cross section that is similarly related to the DM-nucleon cross section σ_n^{SI} . As usual, the differential event rate is found by calculating the velocity-averaged differential cross section and integrating over the velocity distribution $f(\vec{v})$ of the DM particles with mass m_χ :

$$\frac{d^2 R}{dE_R dE_r} = \frac{\rho_{\text{DM}}}{m_N m_\chi} \int_{v_{\text{min}}}^{\infty} v f(\vec{v}) \frac{d^2 \sigma^{\text{MPA}}}{dE_R dE_r} d\vec{v}, \quad (\text{A.14})$$

where $v_{\text{min}} = (m_N E_R + \mu_N E_r) / (\mu_N \sqrt{2m_N E_R})$ and m_N is the mass of the target nucleus. As before, there is an implicit maximum velocity set by the escape velocity of the galaxy. By only considering the case where the observed energy neglects the nuclear recoil energy, Eq. A.14 can be simplified to:

$$\frac{dR}{dE_r} = \frac{\rho_{\text{DM}}}{m_N m_\chi} \int dE_R \int_{v_{\text{min}}}^{\infty} v f(\vec{v}) \frac{d^2 \sigma^{\text{MPA}}}{dE_R dE_r} d\vec{v}. \quad (\text{A.15})$$

Reference [172] also provides the differential rate equation found when the observed energy is a combination of both the nuclear and electron signals, E_R and E_r . Like with the Bremsstrahlung model, the validity of the Migdal model at energies as low as the band gap is subject to ongoing research [184]. Another important caveat to mention is that although the Migdal effect is used as a proposed mechanism for DM interactions, the effect has not yet been observed in semiconductor crystal materials like Si or Ge. The total event rate (found by integrating Eq. A.15 over E_r) as a function of DM mass for Si is shown in Fig. A.4, assuming a SI DM-nucleon cross section of $\sigma_n^{\text{SI}} = 10^{-40} \text{ cm}^2$. Also shown are the differential event rates at various DM masses for electron recoil energies below 60 eV.

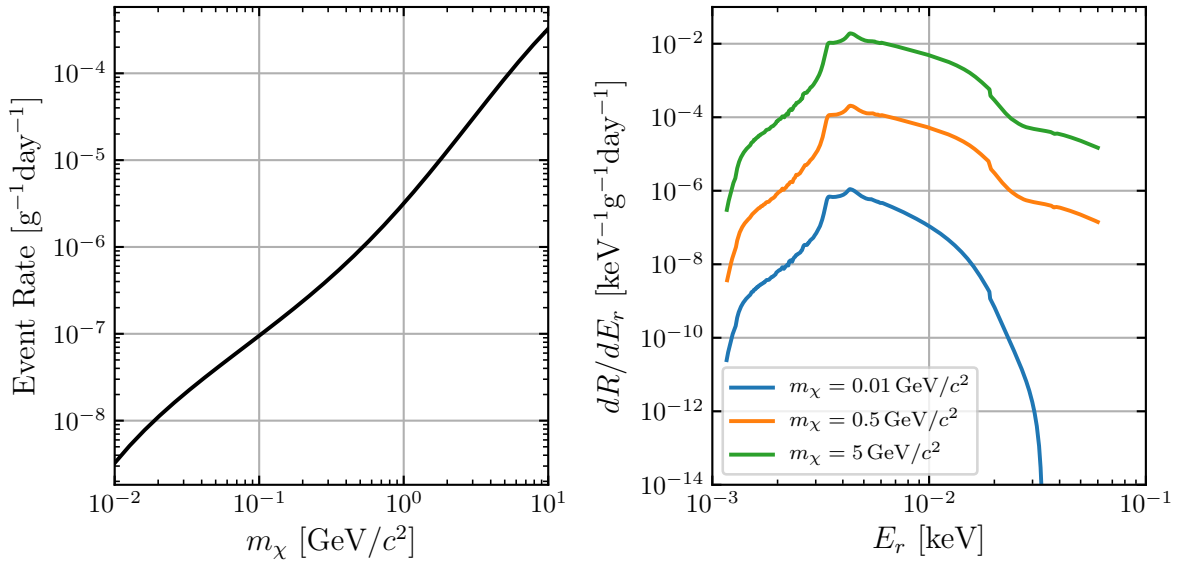


Figure A.4: Left: expected event rate for inelastic DM-nucleus scattering under the emission of a Migdal electron as a function of DM mass m_χ for a Si target, assuming a spin-independent (SI) DM-nucleon cross section of $\sigma_n^{\text{SI}} = 10^{-40} \text{ cm}^2$. Right: differential event rate as a function of the electron recoil energy E_r at various DM masses.

Appendix B

Relationship between Complex Conductivity and Photoelectric Absorption

The dark photon absorption model described in Sec. 1.5.3 shows that the expected interaction rate depends on the real part of the complex conductivity, σ_1 . The following derivation will outline the relationship between σ_1 and the photoelectric absorption cross section $\sigma_{\text{p.e.}}$. The optical properties of a target material can be parameterized by its complex conductivity $\hat{\sigma}$ and complex index of refraction \hat{n} , defined as:

$$\hat{\sigma} \equiv \sigma_1 + i\sigma_2 \tag{B.1}$$

$$\hat{n} \equiv n_1 + in_2. \tag{B.2}$$

As noted in Ref. [79], $\hat{\sigma}$ and \hat{n} are related by:

$$\hat{n}^2 = 1 + \frac{i\hat{\sigma}}{\omega}, \tag{B.3}$$

where ω is the energy of the photon. Furthermore, $\hat{\sigma}$ is related to the in-medium polarization tensor of the electromagnetic field $\Pi(\omega)$ [79]:

$$\Pi(\omega) \approx -i\hat{\sigma}\omega. \tag{B.4}$$

Substituting $\hat{\sigma}$ into Eq. B.4 gives:

$$\begin{aligned} \Pi(\omega) &= -i\sigma_1\omega + \sigma_2\omega \\ \rightarrow \text{Im} [\Pi(\omega)] &= -\sigma_1\omega \\ \frac{-\text{Im} [\Pi(\omega)]}{\omega} &= \sigma_1. \end{aligned} \tag{B.5}$$

The term $-\text{Im}[\Pi(\omega)]/\omega$ can also be evaluated by substituting in Eqs. B.3 and B.4:

$$\begin{aligned}
\frac{-\text{Im}[\Pi(\omega)]}{\omega} &= \frac{-\text{Im}[-i\hat{\sigma}\omega]}{\omega} \\
&= \frac{-\text{Im}[-i\omega \cdot -i\omega(\hat{n}^2 - 1)]}{\omega} \\
&= \frac{-\text{Im}[-\omega^2(n_1^2 - n_2^2 + 2in_1n_2 - 1)]}{\omega} \\
&= \frac{-(-\omega^2 \cdot 2n_1n_2)}{\omega} \\
&= 2\omega n_1 n_2.
\end{aligned} \tag{B.6}$$

Next, Eqs. B.5 and B.6 are compared to find:

$$\sigma_1 = 2\omega n_1 n_2. \tag{B.7}$$

The imaginary part of the complex index of refraction, n_2 , is also defined as the extinction coefficient κ , and is related to photon absorption by:

$$n_2 = \kappa = \frac{\alpha c}{4\pi f}, \tag{B.8}$$

where α is the *linear* absorption coefficient, c is the speed of light, and f is the frequency of the photon. Equation B.8 can be reduced into more relevant parameters by noting that the energy and frequency of the photon are related by $\omega = hf$, where h is the Planck constant. Furthermore, α (typically with units of cm^{-1}) and $\sigma_{\text{p.e.}}$ (typically with units of cm^2/g) are related by $\alpha = \sigma_{\text{p.e.}}\rho$, where ρ is the density of the material. Using these substitutions, Eq. B.8 becomes:

$$\begin{aligned}
n_2 &= \frac{\sigma_{\text{p.e.}}\rho ch}{4\pi\omega} \\
&= \frac{\sigma_{\text{p.e.}}\rho c\hbar}{2\omega},
\end{aligned} \tag{B.9}$$

where $\hbar = h/2\pi$ is simply the reduced Planck constant. Equation B.9 can be further reduced by doing a unit conversion on $\sigma_{\text{p.e.}}$:

$$\sigma_{\text{p.e.}}[\text{cm}^2/\text{g}] \cdot \rho[\text{g}/\text{cm}^3] \cdot c[\text{cm}/\text{s}] \cdot \hbar[\text{eV s}] \rightarrow \sigma_{\text{p.e.}}[\text{eV}]. \tag{B.10}$$

Lastly, substituting Eq. B.9 into Eq. B.7 gives:

$$\begin{aligned}
\sigma_1 &= 2\omega n_1 \frac{\sigma_{\text{p.e.}}[\text{eV}]}{2\omega} \\
&= n_1 \sigma_{\text{p.e.}}[\text{eV}] \\
\sigma_1(\omega) &= n_1(\omega) \cdot \sigma_{\text{p.e.}}(\omega).
\end{aligned} \tag{B.11}$$

The real part of the complex conductivity is therefore the product of the energy-dependent index of refraction and the energy-dependent photoelectric absorption cross section (in units of eV) of the absorbing material. As the index of refraction is a unitless quantity, σ_1 also has units of eV.

Appendix C

Derivation of Discrete Distributions of Electron-Hole Pair Probability

The detector response model described in Sec. 2.2 determines the discrete probability distribution for the number of e^-h^+ pairs n_{eh} produced given a recoil/absorption energy of E_r . If E_r is larger than the average energy to produce an e^-h^+ -pair, ϵ_{eh} , the distribution is determined with an arbitrary Fano factor F defined as $F = \sigma^2/\mu$, where $\mu = \langle n_{eh} \rangle$ is the mean of the distribution, and σ^2 is the variance. A completely uncorrelated (Poisson) process has a Fano factor of 1, but in most radiation detectors Fano factors on the order of 0.1–0.2 are found due to the fact that large deviations from the mean are kinematically suppressed.

Probability distributions for a given mean number of e^-h^+ pairs and Fano factor are generated using a binomial distribution with n trials of probability p . In other words, the selected values of F and μ are used to determine the n and p values of the binomial distribution and hence the probability distribution of e^-h^+ -pair production. The binomial distribution has variance σ^2 and mean μ that obey the relations:

$$\mu = np \tag{C.1}$$

$$\sigma^2 = np(1-p) = \mu(1-p). \tag{C.2}$$

The n and p values can then be calculated from the Fano factor and mean number of e^-h^+ pairs as:

$$F = \frac{\sigma^2}{\mu} = (1-p) \rightarrow p = 1 - F \tag{C.3}$$

$$n = \frac{\mu}{p} = \frac{\mu}{1-F} \tag{C.4}$$

The caveat to these equations is that the binomial distribution is quantized, and thus n and μ are expected to be integers. However in practice, μ can be any fractional value. To account for this, discrete binomial distributions are constructed using the integers directly above and below n . This sets an upper and lower bound on the number of e^-h^+ -pair trials (n_l and n_h), which can then be used to set an upper

and lower bound on the Fano factor (F_l and F_h), using the equations below:

$$n_l(\mu, F) = \text{floor} \left(\frac{\mu}{1-F} \right) \quad (\text{C.5})$$

$$n_h(\mu, F) = \text{ceil} \left(\frac{\mu}{1-F} \right) \quad (\text{C.6})$$

$$F_l(\mu, F) = 1 - \mu/n_l(\mu, F) \quad (\text{C.7})$$

$$F_h(\mu, F) = 1 - \mu/n_h(\mu, F) \quad (\text{C.8})$$

Using F_l and F_h , upper and lower binomial distributions (P_l and P_h) can be constructed. The final probability distribution $P(x|\mu, F)$ is found by interpolating between P_l and P_h , as outlined below:

$$\Delta F(\mu, F) = \frac{F - F_l(\mu, F)}{F_h(\mu, F) - F_l(\mu, F)} \quad (\text{C.9})$$

$$P_l(x|\mu, F) = \text{Binomial}(x|n_l(\mu, F), 1 - F_l(\mu, F)) \quad (\text{C.10})$$

$$P_h(x|\mu, F) = \text{Binomial}(x|n_h(\mu, F), 1 - F_h(\mu, F)) \quad (\text{C.11})$$

$$P(x|\mu, F) = P_l(x|\mu, F)(1 - \Delta F(\mu, F)) + P_h(x|\mu, F)\Delta F(\mu, F) \quad (\text{C.12})$$

$P(x|\mu, F)$ is the weighted mean of two binomial distributions given a non-integer mean, with weights defined by how close the Fano factor of the binomial distribution is to the intended Fano factor.

Appendix D

Charge Trapping and Impact Ionization Model

D.1 Description of the Model

The detector response model described in Sec. 2.2 includes a model to account for the effects of charge trapping (CT) and impact ionization (II) that occur for propagating charges in the detector. Following Ref. [110], CT and II in the detector is described by a two-parameter model, whose inputs are the fractional probabilities of charge trapping f_{CT} and impact ionization f_{II} . The model assumes that the probability of a CT or II process occurring for a single charge is a flat distribution across the thickness of the detector, and that the probabilities are consistent between electrons and holes. Finally, this model only accounts for first-order processes (i.e. CT or II after a prior II occurred is not considered), which is valid because the probabilities of these higher-order processes are sub-percent for detectors the size of HVeV detectors. The probability distribution function P as a function of energy E (in units of number of e^-h^+ pairs n_{eh}) and the fractional probabilities of CT and II up to N e^-h^+ pairs is given by:

$$P(E, f_{\text{CT}}, f_{\text{II}}) = \sum_{n_{eh}=1}^N \left[P_i(n_{eh}|\mu, F) \sum_{n_{\text{CT}}=0}^{n_{eh}} \left(\sum_{n_{\text{II}}=0}^{n_{eh}-n_{\text{CT}}} P_f(f_{\text{CT}}, f_{\text{II}}) p(E, n_{eh}, n_{\text{CT}}, n_{\text{II}}) \right) \right], \quad (\text{D.1})$$

where $P_i(n_{eh}|\mu, F)$ is the probability of n_{eh} e^-h^+ pairs for a given Fano factor and mean number of e^-h^+ pairs determined by the ionization production model (see Sec. 2.2.1). n_{CT} and n_{II} are the number of e^-h^+ pairs with an occurrence of CT and II, respectively, where $n_{\text{CT}} + n_{\text{II}} \leq n_{eh}$. The term $p(E, n_{\text{CT}}, n_{\text{II}}, n_{eh})$ describes the probability distribution function (PDF) shape as a function of E for a given n_{CT} and n_{II} , and is given by:

$$p(E, n_{eh}, n_{\text{CT}}, n_{\text{II}}) = \begin{cases} \frac{1}{\sigma_E \sqrt{2\pi}} \exp \left[-\frac{1}{2} \left(\frac{E - n_{eh}}{\sigma_E} \right)^2 \right] & n_k = 0 \\ \left[\frac{1}{2^{(n_k-1)!}} \sum_{l=0}^{n_k} (-1)^l \binom{n_k}{l} (u(E) - l)^{n_k-1} \text{sgn}(u(E) - l) \right] * G(\sigma_E) & n_k \geq 1, \end{cases} \quad (\text{D.2})$$

where $n_k = n_{\text{CT}} + n_{\text{II}}$, $u(E) = E - n_{eh} + n_{\text{CT}}$, and σ_E is the detector energy resolution. In the case where no e^-h^+ pairs have charge trapping or impact ionization ($n_k = 0$), $p(E, n_{eh}, n_{\text{CT}}, n_{\text{II}})$ describes a Gaussian distribution centered around n_{eh} . In the case where at least one e^-h^+ pair has charge trapping

or impact ionization ($n_k \geq 1$), $p(E, n_{eh}, n_{CT}, n_{II})$ describes the uniform sum distribution convolved with a Gaussian distribution $G(\sigma_E)$ representing the detector energy resolution. The term $u(E)$ places each PDF in the correct location in energy for a given number of e^-h^+ pairs.

Lastly, the term $P_f(f_{CT}, f_{II})$ in Eq. D.1 describes the probability of n_{CT} and n_{II} occurring given the fractional probabilities f_{CT} and f_{II} :

$$P_f(f_{CT}, f_{II}) = \frac{n_{eh}!}{n_{CT}!n_{II}!(n_{eh} - n_{CT} - n_{II})!} (\kappa\gamma)^{n_{eh} - n_{CT} - n_{II}} (\gamma(1 - \kappa))^{n_{CT}} (1 - \gamma)^{n_{II}} \quad (D.3)$$

$$\gamma = 1 - f_{II} \quad (D.4)$$

$$\kappa = \frac{f_{CT} + f_{II} - 1}{f_{II} - 1}. \quad (D.5)$$

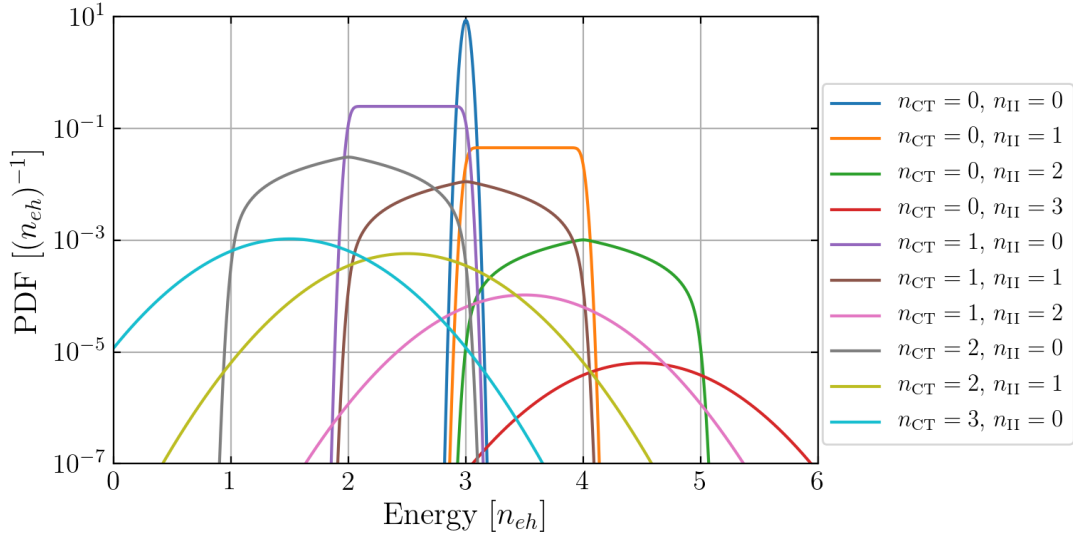


Figure D.1: Example of the charge trapping (CT) and impact ionization (II) probability distribution function (PDF) with $n_{eh} = 3$ and fractional probabilities $f_{CT} = 0.11$, and $f_{II} = 0.02$. Each curve describes the probability distribution for a given number of e^-h^+ pairs that have an occurrence of charge trapping (n_{CT}) and/or impact ionization (n_{II}), following Eqs. D.2 and D.3. This example uses a detector energy resolution of $\sigma_E = 0.03 n_{eh}$.

An example of the charge trapping and impact ionization model is shown in Fig. D.1 with $n_{eh} = 3$, $f_{CT} = 0.11$, and $f_{II} = 0.02$. For the DM search experiment presented in Chapters 4 and 5, a slightly modified version of this model is used to fit to data captured from a laser source to determine the values of f_{CT} and f_{II} . The model used for the laser data is identical to the description above, except the $P_i(n_{eh}|\mu, F)$ term in Eq. D.1 is replaced with a Poisson distribution, i.e.

$$P_i(n_{eh}|\mu, F) \rightarrow P_{\text{Poisson}}(n_{eh}, \lambda), \quad (D.6)$$

where λ is the mean number of photons per laser pulse.

D.2 Model Assumptions

Appendix D.1 states a few assumptions of the described CT and II model. One assumption is that the probability of a CT or II process occurring for a single charge is a flat distribution across the thicknesses of the detector. By assuming a flat distribution, the CT and II model is able to easily determine the shape of the tails on either side of an e^-h^+ -pair peak by using a uniform sum distribution, as seen in Fig. D.1. A more realistic model may start by treating CT and II processes like an absorption process, whereby charges in a detector with infinite thickness would have a 100% probability of having CT or II occur. For such a model, the fractional probabilities f_{CT} and f_{II} can be described by a characteristic length τ_{CT} and τ_{II} for the CT and II process, respectively. For a detector of thickness L , these characteristic lengths are given by:

$$\tau_{\text{CT/II}} = \frac{-L}{\ln(1 - f_{\text{CT/II}})}. \quad (\text{D.7})$$

Treating this like an absorption process, the probability of either CT or II occurring at a location $x = [0, L]$ along the thickness of the detector follows an exponential decay:

$$P^{\text{CT/II}}(x) = \frac{1}{\tau_{\text{CT/II}}} e^{-x/\tau_{\text{CT/II}}}. \quad (\text{D.8})$$

f_{CT} and f_{II} therefore describe the probability of CT or II occurring in isolation for a charge that travels a length L . The cumulative probability for the probability distribution in Eq. D.8 as a function of x is given by:

$$C^{\text{CT/II}}(x) = \left(1 - e^{-x/\tau_{\text{CT/II}}}\right). \quad (\text{D.9})$$

Looking at the CT and II processes in isolation, Eq. D.9 can be rewritten by doing a Taylor expansion on the exponential function:

$$C^{\text{CT/II}}(x) = \left(1 - 1 + \frac{x}{\tau_{\text{CT/II}}} - \left(\frac{x}{\tau_{\text{CT/II}}}\right)^2 + \dots\right). \quad (\text{D.10})$$

Typical measurements for f_{CT} and f_{II} are $\lesssim 0.2$ for a detector with a thickness of 0.4 cm, resulting in $x/\tau_{\text{CT/II}} \lesssim 0.22$ and $(x/\tau_{\text{CT/II}})^2 \ll 1$. The cumulative probability function in Eq. D.10 can reasonably be approximated by:

$$\begin{aligned} C^{\text{CT/II}}(x) &\approx \frac{x}{\tau_{\text{CT/II}}} \\ &= \frac{-\ln(1 - f_{\text{CT/II}}) \cdot x}{L} \\ &\approx \frac{f_{\text{CT/II}} \cdot x}{L}. \end{aligned} \quad (\text{D.11})$$

Therefore for small values of f_{CT} and f_{II} , the cumulative probability can be approximated by a linear function over x with a slope of $f_{\text{CT/II}}/L$. This matches the exact cumulative probability function of a flat probability distribution of $f_{\text{CT/II}}/L$ between $x = 0$ and $x = L$. More realistically, the CT and II processes do not work in isolation. The probability of a charge having CT occur at a location x is the combined probability of CT occurring at x and *not* having II occur before x . The CT probability is then

expressed as:

$$\begin{aligned}
 P^{\text{CT}}(x) &= \frac{1}{\tau_{\text{CT}}} e^{-x/\tau_{\text{CT}}} \cdot (1 - C^{\text{II}}(x)) \\
 &= \frac{1}{\tau_{\text{CT}}} e^{-x/\tau_{\text{CT}}} \cdot e^{-x/\tau_{\text{II}}} \\
 &= \frac{1}{\tau_{\text{CT}}} e^{-x\beta},
 \end{aligned} \tag{D.12}$$

where $\beta = 1/\tau_{\text{CT}} + 1/\tau_{\text{II}}$ combines characteristic lengths of both processes. Equivalently, the II probability is expressed as:

$$P^{\text{II}}(x) = \frac{1}{\tau_{\text{II}}} e^{-x\beta}. \tag{D.13}$$

The cumulative probability function for a charge moving from x to $x + \Delta x$ is found by integrating the probability functions above:

$$\begin{aligned}
 C^{\text{CT/II}}(\Delta x) &= \int_0^{\Delta x} \frac{1}{\tau_{\text{CT/II}}} e^{-x'\beta} dx' \\
 &= \frac{-1}{\beta\tau_{\text{CT/II}}} (e^{-\Delta x\beta} - e^{-0\beta}) \\
 &= \frac{1}{\beta\tau_{\text{CT/II}}} (1 - e^{-\Delta x\beta}).
 \end{aligned} \tag{D.14}$$

For a charge that travels the entire length of the detector, $\Delta x = L$, the cumulative probability for CT or II is given by:

$$C^{\text{CT/II}}(L) = \frac{1}{\beta\tau_{\text{CT/II}}} (1 - e^{-L\beta}). \tag{D.15}$$

Again, for f_{CT} and f_{II} measurements that are $\lesssim 0.2$ for a detector with a thickness of 0.4 cm, the value of $(L\beta)^2$ in the Taylor expansion is $\ll 1$. The cumulative probabilities can still be reasonably approximated by a linear function over Δx distance travelled:

$$C^{\text{CT/II}}(\Delta x) \approx \frac{\Delta x}{\tau_{\text{CT/II}}} \approx \frac{f_{\text{CT/II}} \cdot \Delta x}{L}. \tag{D.16}$$

Therefore as long as the measured values of f_{CT} and f_{II} are relatively small, the probability distribution functions of CT and II are approximately constant over the detector length.

The CT and II model is also assumed to be equally valid for events generated at the surface of the detector as for events generated in the bulk of the detector. For e^-h^+ pairs that are generated at the surface, depending on the sign of the applied voltage bias across the detector, either the electron or hole will propagate the length of the detector, whereas the other charge will effectively travel no distance. In contrast, e^-h^+ pairs in the bulk are presumed to be generated with a uniform distribution across the detector thickness, and have both the electron and the hole travel some amount of distance in the detector. This difference between surface and bulk events is important because the values of f_{CT} and f_{II} are obtained using a laser source, which only generates e^-h^+ pairs at the surface. Other sources of events, including proposed DM candidates, are expected to generate e^-h^+ pairs throughout the detector bulk. In order to apply the CT and II model to the signal of such sources, it must be equally valid for both kinds of events. To verify that f_{CT} and f_{II} is the same for surface and bulk events, consider first the cumulative probability of charge trapping for a surface event, assuming there is no impact ionization.

Because it is a surface event, there is only one charge to consider, and the cumulative probability is just Eq. D.9 with $x = L$:

$$C^{\text{CT}} = \left(1 - e^{-L/\tau_{\text{CT}}}\right). \quad (\text{D.17})$$

Next, consider an e^-h^+ pair created in the bulk of the detector at a distance x away from the detector surface. Because the electron and hole will travel in opposite directions, one charge, say the electron, needs to travel a distance x to reach the surface, and the other charge, say the hole, needs to travel a distance $L - x$. There is a probability that charge trapping will occur for either the electron or hole that depends on the respective distance they each travel. These cumulative probabilities for charge trapping (CT) and no charge trapping (-CT) as a function of x are given by:

$$C_e(x|\text{CT}) = \left(1 - e^{-x/\tau_{\text{CT}, e}}\right) \quad (\text{D.18})$$

$$C_e(x|-\text{CT}) = e^{-x/\tau_{\text{CT}, e}} \quad (\text{D.19})$$

$$C_h(x|\text{CT}) = \left(1 - e^{-(L-x)/\tau_{\text{CT}, h}}\right) \quad (\text{D.20})$$

$$C_h(x|-\text{CT}) = e^{-(L-x)/\tau_{\text{CT}, h}}, \quad (\text{D.21})$$

where $\tau_{\text{CT}, e}$ and $\tau_{\text{CT}, h}$ are the characteristic lengths of charge trapping for electrons and holes, respectively. The probability that CT occurs for the e^-h^+ pair, $C_{eh}(x|\text{CT})$, is the summed probability that CT occurs for either the electron, hole, or both charges. *Assuming that the charge trapping probabilities are the same for electrons and holes*, $\tau_{\text{CT}, e} = \tau_{\text{CT}, h} = \tau_{\text{CT}}$, $C_{eh}(x|\text{CT})$ is given by:

$$\begin{aligned} C_{eh}(x|\text{CT}) &= C_e(x|\text{CT})C_h(x|-\text{CT}) + C_e(x|-\text{CT})C_h(x|\text{CT}) + C_e(x|\text{CT})C_h(x|\text{CT}) \\ &= \left(1 - e^{-x/\tau_{\text{CT}}}\right) e^{-(L-x)/\tau_{\text{CT}}} + e^{-x/\tau_{\text{CT}}} \left(1 - e^{-(L-x)/\tau_{\text{CT}}}\right) \\ &\quad + \left(1 - e^{-x/\tau_{\text{CT}}}\right) \left(1 - e^{-(L-x)/\tau_{\text{CT}}}\right) \\ &= e^{-(L-x)/\tau_{\text{CT}}} - e^{-L/\tau_{\text{CT}}} + e^{-x/\tau_{\text{CT}}} - e^{-L/\tau_{\text{CT}}} \\ &\quad + 1 - e^{-(L-x)/\tau_{\text{CT}}} - e^{-x/\tau_{\text{CT}}} + e^{-L/\tau_{\text{CT}}} \\ &= 1 - e^{-L/\tau_{\text{CT}}}. \end{aligned} \quad (\text{D.22})$$

Not only does Eq. D.22 show that the probability of charge trapping occurring for a single e^-h^+ pair is independent of the initial position of e^-h^+ pair, it is also exactly equal to Eq. D.17, the probability of charge trapping occurring for a single charge generated at the detector surface. The identical argument can be made for the impact ionization probability in isolation. However as previously mentioned, CT and II do not happen in isolation. For an event generated at the surface of the detector, the probability of either CT or II occurring for a single charge travelling a length L is given by Eq. D.15. Consider again an e^-h^+ pair generated in the bulk of the detector where the electron and hole must travel a distance x and $L - x$, respectively, to reach the surface. The cumulative probabilities for CT, II, and no effect

(NE) as a function of x for the electron and hole are given by:

$$C_e(x|\text{CT}) = \frac{1}{\beta_e \tau_{\text{CT}, e}} (1 - e^{-x\beta_e}) \quad (\text{D.23})$$

$$C_e(x|\text{II}) = \frac{1}{\beta_e \tau_{\text{II}, e}} (1 - e^{-x\beta_e}) \quad (\text{D.24})$$

$$C_e(x|\text{NE}) = e^{-x\beta_e} \quad (\text{D.25})$$

$$C_h(x|\text{CT}) = \frac{1}{\beta_h \tau_{\text{CT}, h}} (1 - e^{-(L-x)\beta_h}) \quad (\text{D.26})$$

$$C_h(x|\text{II}) = \frac{1}{\beta_h \tau_{\text{II}, h}} (1 - e^{-(L-x)\beta_h}) \quad (\text{D.27})$$

$$C_h(x|\text{NE}) = e^{-(L-x)\beta_h}. \quad (\text{D.28})$$

As before, the above equations can be used to evaluate the probability of only CT occurring for the e^-h^+ pair as a whole, $C_{eh}(x|\text{CT})$, with the assumptions $\tau_{\text{CT}, e} = \tau_{\text{CT}, h} = \tau_{\text{CT}}$, $\tau_{\text{II}, e} = \tau_{\text{II}, h} = \tau_{\text{II}}$, and $\beta_e = \beta_h = \beta$:

$$\begin{aligned} C_{eh}(x|\text{CT}) &= C_e(x|\text{CT})C_h(x|\text{NE}) + C_e(x|\text{NE})C_h(x|\text{CT}) + C_e(x|\text{CT})C_h(x|\text{CT}) \\ &= \frac{1}{\beta \tau_{\text{CT}}} (1 - e^{-x\beta}) e^{-(L-x)\beta} + e^{-x\beta} \frac{1}{\beta \tau_{\text{CT}}} (1 - e^{-(L-x)\beta}) \\ &\quad + \frac{1}{\beta^2 \tau_{\text{CT}}^2} (1 - e^{-x\beta}) (1 - e^{-(L-x)\beta}) \\ &= \frac{1}{\beta \tau_{\text{CT}}} (e^{-(L-x)\beta} + e^{-x\beta} - 2e^{-L\beta}) \\ &\quad + \frac{1}{\beta^2 \tau_{\text{CT}}^2} (1 - e^{-(L-x)\beta} - e^{-x\beta} + e^{-L\beta}). \end{aligned} \quad (\text{D.29})$$

Similarly, the probability of only II occurring for the e^-h^+ pair as a whole is given by:

$$\begin{aligned} C_{eh}(x|\text{II}) &= C_e(x|\text{II})C_h(x|\text{NE}) + C_e(x|\text{NE})C_h(x|\text{II}) + C_e(x|\text{II})C_h(x|\text{II}) \\ &= \frac{1}{\beta \tau_{\text{II}}} (1 - e^{-x\beta}) e^{-(L-x)\beta} + e^{-x\beta} \frac{1}{\beta \tau_{\text{II}}} (1 - e^{-(L-x)\beta}) \\ &\quad + \frac{1}{\beta^2 \tau_{\text{II}}^2} (1 - e^{-x\beta}) (1 - e^{-(L-x)\beta}) \\ &= \frac{1}{\beta \tau_{\text{II}}} (e^{-(L-x)\beta} + e^{-x\beta} - 2e^{-L\beta}) \\ &\quad + \frac{1}{\beta^2 \tau_{\text{II}}^2} (1 - e^{-(L-x)\beta} - e^{-x\beta} + e^{-L\beta}). \end{aligned} \quad (\text{D.30})$$

Finally, the probability of both CT and II occurring for the e^-h^+ pair is given by:

$$\begin{aligned} C_{eh}(x|\text{CT and II}) &= C_e(x|\text{II})C_h(x|\text{CT}) + C_e(x|\text{CT})C_h(x|\text{II}) \\ &= \frac{2}{\beta^2 \tau_{\text{CT}} \tau_{\text{II}}} (1 - e^{-x\beta}) (1 - e^{-(L-x)\beta}) \\ &= \frac{2}{\beta^2 \tau_{\text{CT}} \tau_{\text{II}}} (1 - e^{-(L-x)\beta} - e^{-x\beta} + e^{-L\beta}). \end{aligned} \quad (\text{D.31})$$

The probability of either CT or II occurring for the single e^-h^+ pair is the sum of Eqs. D.29–D.31:

$$\begin{aligned}
C_{eh}(x|\text{CT or II}) &= C_{eh}(x|\text{CT}) + C_{eh}(x|\text{II}) + C_{eh}(x|\text{CT and II}) \\
&= \frac{1}{\beta\tau_{\text{CT}}} \left(e^{-(L-x)\beta} + e^{-x\beta} - 2e^{-L\beta} \right) + \frac{1}{\beta\tau_{\text{II}}} \left(e^{-(L-x)\beta} + e^{-x\beta} - 2e^{-L\beta} \right) \\
&\quad + \left(\frac{1}{\beta^2\tau_{\text{CT}}^2} + \frac{1}{\beta^2\tau_{\text{II}}^2} + \frac{2}{\beta^2\tau_{\text{CT}}\tau_{\text{II}}} \right) \left(1 - e^{-(L-x)\beta} - e^{-x\beta} + e^{-L\beta} \right) \quad (\text{D.32}) \\
&= \left(\frac{1}{\beta\tau_{\text{CT}}} + \frac{1}{\beta\tau_{\text{II}}} \right) \left(e^{-(L-x)\beta} + e^{-x\beta} - 2e^{-L\beta} \right) \\
&\quad + \left(\frac{1}{\beta\tau_{\text{CT}}} + \frac{1}{\beta\tau_{\text{II}}} \right)^2 \left(1 - e^{-(L-x)\beta} - e^{-x\beta} + e^{-L\beta} \right).
\end{aligned}$$

Noticing that the prefactor terms equate to unity:

$$\begin{aligned}
\frac{1}{\beta\tau_{\text{CT}}} + \frac{1}{\beta\tau_{\text{II}}} &= \frac{\tau_{\text{II}} + \tau_{\text{CT}}}{\beta\tau_{\text{CT}}\tau_{\text{II}}} \\
&= \frac{\tau_{\text{II}} + \tau_{\text{CT}}}{(1/\tau_{\text{CT}} + 1/\tau_{\text{II}})\tau_{\text{CT}}\tau_{\text{II}}} \\
&= \frac{\tau_{\text{II}} + \tau_{\text{CT}}}{\tau_{\text{II}} + \tau_{\text{CT}}} \\
&= 1,
\end{aligned} \quad (\text{D.33})$$

Eq. D.32 can be reduced to:

$$\begin{aligned}
C_{eh}(x|\text{CT or II}) &= \left(e^{-(L-x)\beta} + e^{-x\beta} - 2e^{-L\beta} \right) + \left(1 - e^{-(L-x)\beta} - e^{-x\beta} + e^{-L\beta} \right) \\
&= 1 - e^{-L\beta}.
\end{aligned} \quad (\text{D.34})$$

Equation D.34 demonstrates that the probability of CT or II occurring for a single e^-h^+ pair generated in the detector bulk is independent of its initial position. Moreover, Eq. D.34 is exactly equal to the probability of either CT or II occurring for a single charge generated at the detector surface (see Eq. D.15 together with the unity equation in Eq. D.33).

The expressions above demonstrate that, as long as the individual CT and II probabilities for electrons and holes are equal, the probability of either CT or II occurring for a single e^-h^+ pair does not depend on whether that e^-h^+ pair was generated at the detector surface or in the detector bulk. This is exactly true using the absorption-like analytical expressions for CT and II for all values of f_{CT} and f_{II} . When assuming a flat probability distribution of CT and II across the detector thickness, it is only approximately true in the limit of small values of f_{CT} and f_{II} . Given $f_{\text{CT}} = f_{\text{II}} = 0.2$, the flat probability distribution assumption results in a $\lesssim 3\%$ deviation between the surface and bulk probability of either CT or II occurring for a single e^-h^+ pair. This verification, however, cannot dismiss certain intrinsic differences between surface and bulk events. For instance, it is possible for a single bulk event to undergo both CT and II, yet impossible for a single surface event. But for typically measured values of CT and II of $f_{\text{CT}} = 0.2$ and $f_{\text{II}} = 0.01$, the probability of both CT *and* II occurring for a single bulk event is only $\sim 0.2\%$. Overall as long as the CT and II probabilities remain small and relatively similar for electrons and holes, the model described in Appendix D.1 is equally applicable for surface and bulk events.

Appendix E

Optical Parameters for Si and Ge

As discussed in Sec. 1.5.3, the interaction rate of several DM models depend on the optical parameters of the target material. Such optical parameters include the photoelectric absorption cross section $\sigma_{\text{p.e.}}$ and the complex optical conductivity $\hat{\sigma} = \sigma_1 + i\sigma_2$, where σ_1 and σ_2 represent the real and imaginary parts of the complex optical conductivity, respectively. Furthermore, Appendix B shows that σ_1 is related to $\sigma_{\text{p.e.}}$ by $\sigma_1 = n \cdot \sigma_{\text{p.e.}}$, where n is the index of refraction of the target material. In order to conduct a search experiment for a DM candidate dependent on these optical parameters, the values of the parameters must be known for energies accessible to that experiment. This appendix presents the n , $\sigma_{\text{p.e.}}$, and σ_1 data sourced for Si and Ge, the two target materials used by SuperCDMS experiments. The values of n obtained for Si and Ge are shown in Fig. E.1.

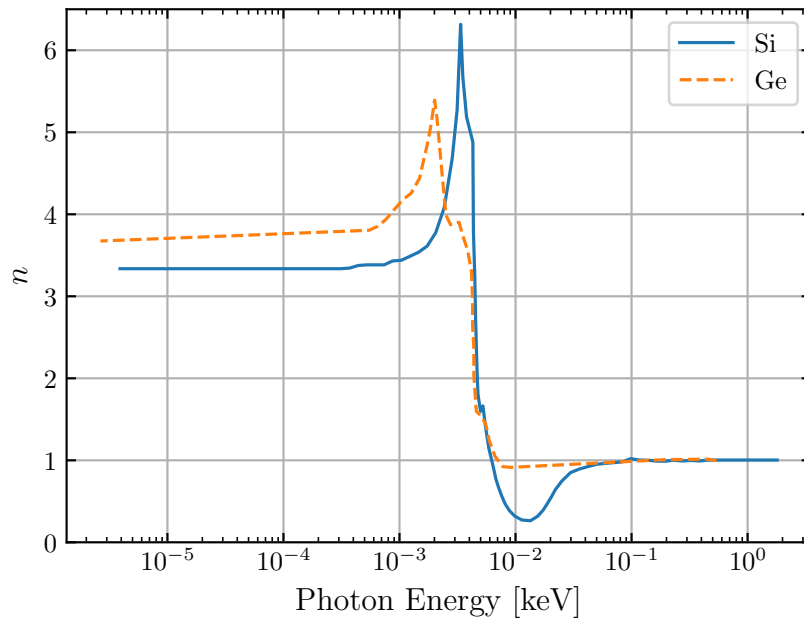


Figure E.1: Index of refraction n for Si (blue curve) and Ge (orange curve). The values of n for Si and Ge are obtained from Ref. [114] and Ref. [188], respectively.

The data for $\sigma_{\text{p.e.}}$ were obtained through a broad and extensive literature search. The various sources from which the $\sigma_{\text{p.e.}}$ data are collected from are listed in Tab. E.1. This list, however, is by no means exhaustive. A large emphasis was placed on collecting data at low energies ($\lesssim 100$ eV) where there are a lot fewer data points and where there are more discrepancies in the data that is available. There exists many additional sources of $\sigma_{\text{p.e.}}$ data at higher energies whose data are consistent with other available data and are therefore redundant. Figure E.2 shows the amalgamation of $\sigma_{\text{p.e.}}$ data collected from the sources listed in Tab. E.1 for photon energies < 20 keV. Section 2.3 discusses a temperature correction applied to these data for Si, as well as the $\sigma_{\text{p.e.}}$ curves used for DM search experiments.

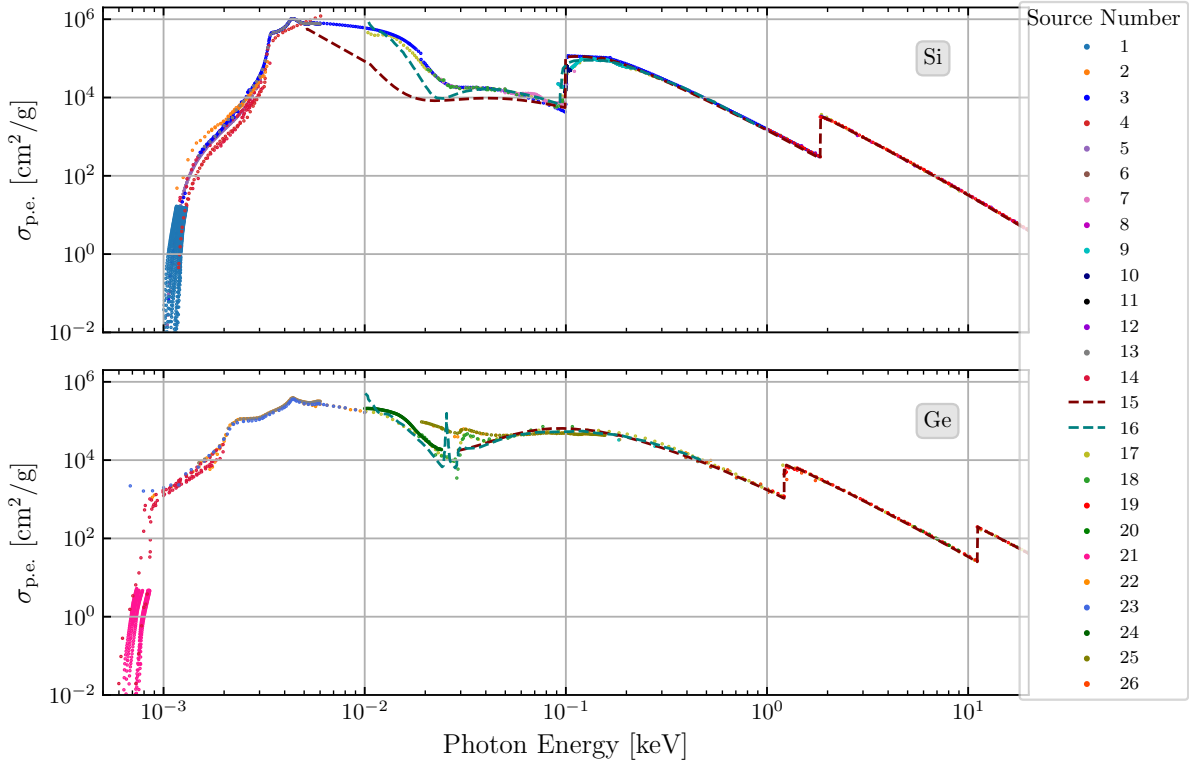


Figure E.2: Amalgamation of the photoelectric absorption cross section $\sigma_{\text{p.e.}}$ data collected from the sources listed in Tab. E.1 for Si (top) and Ge (bottom). The data points correspond to data measured experimentally or semi-empirically, whereas the dashed-curves correspond to theoretical calculations of $\sigma_{\text{p.e.}}$.

The last optical parameter to consider is the imaginary part of the complex conductivity, σ_2 . σ_2 can be interpreted as the delay of the charge carrier response to quick changes in the electric field, and depends on the energy of the incoming photon or possible DM candidate. This parameter is necessary for the in-medium correction applied to the dark photon signal model. Because there is much less literature that provides data for σ_2 as compared to $\sigma_{\text{p.e.}}$, only one set of σ_2 values are used in the analyses presented in Chapters 5 and 6. The absolute values of σ_2 for Si and Ge are shown in the top and bottom plots of Fig. E.3, respectively.

Table E.1: List of references for the photoelectric absorption cross section $\sigma_{\text{p.e.}}$ data obtained for Si and Ge. For each reference, the material, methodology, photon energy range, and temperature of which the data was measured/calculated are also listed. This list does not include the new $\sigma_{\text{p.e.}}$ data that is presented in Chapter 6.

Source No.	Reference (Year)	Material	Method	Energy Range	Temperature
1	Ref. [112] (1958)	Si	Experimental	1–1.3 eV	4.2–415 K
2	Ref. [113] (1975)	Si	Experimental	1–3.3 eV	296 K [†]
3	Ref. [114] (1997)	Si	Experimental	1 eV–1 keV	296 K [†]
4	Ref. [115] (2003)	Si	Experimental	1.5–5 eV	77 K
5	Ref. [116] (2008)	Si	Experimental	< 10 eV	300 K
6	Ref. [117] (1995)	Si	Experimental	< 10 eV	300 K
7	Ref. [118] (1994)	Si	Experimental	25–97 eV	296 K [†]
8	Ref. [189] (1970)	Si	Experimental	69–220 eV	296 K [†]
9	Ref. [190] (1970)	Si	Experimental	90–210 eV	296 K [†]
10	Ref. [191] (1977)	Si	Experimental	98–105 eV	296 K [†]
11	Ref. [192] (1972)	Si	Experimental	99–105 eV	296 K [†]
12	Ref. [193] (1995)	Si	Experimental	1.4–30 keV	296 K [†]
13	Ref. [119] (1983)	Si, Ge	Experimental	1.5–6 eV	296 K [†]
14	Ref. [120] (1955)	Si, Ge	Experimental	< 10 eV	77–300 K
15	Ref. [121] (2005)	Si Ge	Theory Calculation	5 eV–433 keV 30 eV–443 keV	296 K [†]
16	Ref. [122] (1987)	Si Ge	Theory Calculation	10–926 eV 10–487 eV	296 K [†]
17	Ref. [123] (1992)	Si, Ge	Semi-Empirical	10 eV–30 keV	296 K [†]
18	Ref. [124] (1966)	Si, Ge	Experimental	20–120 eV	296 K [†]
19	Ref. [111] (2010)	Si, Ge	Experimental	1 keV–100 GeV	296 K [†]
20	Ref. [194] (1973)	Si, Ge	Theory/Experimental	5–25 keV	296 K [†]
21	Ref. [195] (1957)	Ge	Experimental	< 1 eV	4–291 K
22	Ref. [188] (1997)	Ge	Experimental	1 eV–1 keV	296 K [†]
23	Ref. [196] (1959)	Ge	Experimental	1–10 eV	296 K [†]
24	Ref. [197] (1967)	Ge	Experimental	10–25 eV	296 K [†]
25	Ref. [198] (1970)	Ge	Experimental	15–170 eV	296 K [†]
26	Ref. [199] (1967)	Ge	Experimental	400 eV–1.7 keV	296 K [†]

[†]The temperature that the data is measured at is not explicitly stated in this reference, and is therefore assumed to be room temperature.

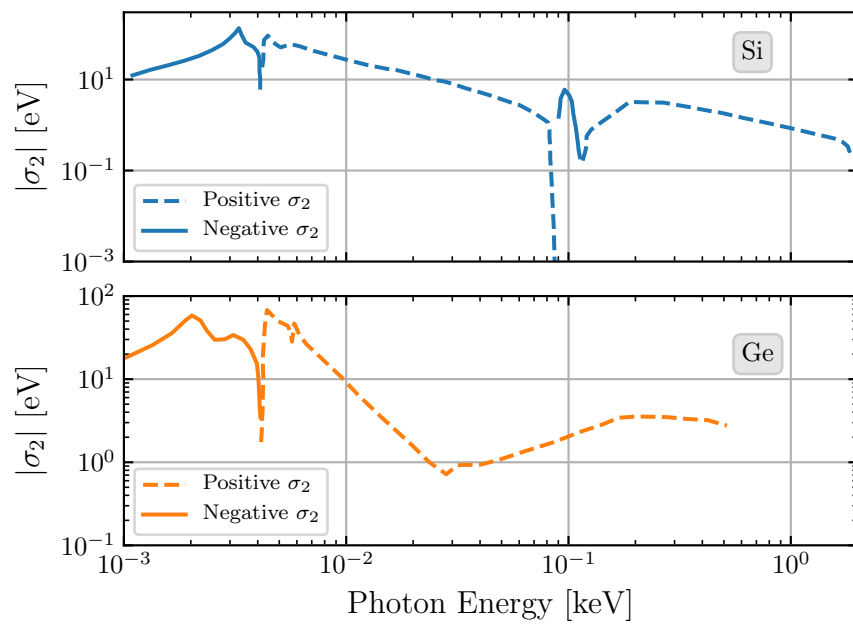


Figure E.3: Imaginary part of the complex optical conductivity $\sigma_2 = \text{Im}(\hat{\sigma})$ for Si (top) and Ge (bottom). The dashed (solid) curve in each plot denote the positive (negative) values of σ_2 . The values of σ_2 are obtained from Ref. [79].

Appendix F

Photon Absorption Model for Si

As discussed in Sec. 2.3.1, electrons within a semiconductor material such as Si can be excited into the conduction band by means of either the direct or indirect absorption of a photon. At energies near the Si band gap, indirect photon absorption becomes the dominant or the only mechanism for electron excitation, leading to a strong temperature dependence in the photoelectric absorption cross section $\sigma_{\text{p.e.}}$. This appendix describes the phenomenological photon absorption model presented by Rajkaran *et. al.* [200] that is used in Chapter 2 to apply a temperature correction to $\sigma_{\text{p.e.}}$ data found in literature, as well as in Chapter 6 as a fit to new $\sigma_{\text{p.e.}}$ measurements.

The total linear absorption coefficient α is the sum of the linear absorption coefficients for direct photon absorption, α_v , and indirect photon absorption, α_n , at temperature T :

$$\alpha(T) = \alpha_v(T) + \alpha_n(T). \quad (\text{F.1})$$

Recall that α is proportional to $\sigma_{\text{p.e.}}$ as $\alpha = \rho \cdot \sigma_{\text{p.e.}}$, where $\rho = 2.33 \text{ g/cm}^3$ is the density of Si. Indirect photon absorption involves either the absorption or emission of a phonon in order to conserve the momentum of the electron. Accounting for the various phonon energies and indirect band gaps, $\alpha_n(T)$ is expressed as:

$$\alpha_n(T) = \sum_{i,j} C_i A_j(T) \left(\frac{(E_\gamma - E_{g,j}(T) + E_{p,i})^2}{e^{E_{p,i}/k_b T} - 1} + p_i \frac{(E_\gamma - E_{g,j}(T) - E_{p,i})^2}{1 - e^{-E_{p,i}/k_b T}} \right), \quad (\text{F.2})$$

where i refers to the various possible phonons with energy E_p that can be emitted or absorbed, j refers to the various temperature-dependent band gap energies $E_g(T)$ that are involved in indirect absorption, E_γ is the energy of the incoming photon, and $k_b = 8.617 \times 10^{-5} \text{ eV/K}$ is the Boltzmann constant. The first term in Eq. F.2 corresponds to indirect absorption via phonon absorption ($E_\gamma \geq E_{g,j}(T) - E_{p,i}$), and the second term corresponds to indirect absorption via phonon emission ($E_\gamma \geq E_{g,j}(T) + E_{p,i}$). The C_i parameter is the electron-phonon coupling constant for the i^{th} phonon, and the $A_j(T)$ parameter is a proportionality constant for the j^{th} indirect band gap. Lastly, the p_i parameter describes a preference of phonon absorption or emission and, following Ref. [200], is set to $p_i = 1$ because its maximum theoretical value in Si is close to unity.

The band gap energies $E_{g,j}(T)$ in Eq. F.2 have a temperature dependence according to:

$$E_{g,j}(T) = E_{g,j}(0) - \frac{\beta T^2}{T + \gamma}, \quad (\text{F.3})$$

where $E_{g,j}(0)$ is the band gap energy at 0K, and $\beta = 7.021 \times 10^{-4}$ eV/K and $\gamma = 1108$ K for Si. The direct absorption contribution to total linear absorption coefficient is given by:

$$\alpha_v(T) = A_d (E_\gamma - E_{gd}(T))^{1/2}, \quad (\text{F.4})$$

where A_d is the proportionality constant for direct absorption, and the direct band gap energy $E_{gd}(T)$ follows the same temperature dependence described by Eq. F.3. For the absorption process in Si, two indirect band gaps at 1.1557 eV and 2.5 eV are considered, along with the direct band gap at 3.2 eV. The various phonon energies correspond to the lattice vibrations possible in Si, those being longitudinal optical (LO), transverse optical (TO), longitudinal acoustic (LA), and transverse acoustic (TA). However the LO and LA lattice vibrations are considered to be subdominant, and therefore only the TO and TA vibrations are used in the model [200]. In Si, the phonon energy and electron-phonon coupling constant for the TO mode are $E_p = 57.73$ meV and $C_{TO} = 4.0$, and for the TA mode are $E_p = 18.27$ meV and $C_{TA} = 5.5$. The values of $A_j(T)$ are determined in Ref. [200] by fitting the model to experimental data, and are found to be independent of temperature; this is in contrast to the analysis presented in Chapter 6, which finds temperature dependence in one of the $A_j(T)$ parameters. Putting this all together, the total linear absorption coefficient can be described as:

$$\alpha(T) = \sum_{i,j=1,2} C_i A_j \left(\frac{(E_\gamma - E_{g,j}(T) + E_{p,i})^2}{e^{E_{p,i}/k_b T} - 1} + \frac{(E_\gamma - E_{g,j}(T) - E_{p,i})^2}{1 - e^{-E_{p,i}/k_b T}} \right) + A_d (E_\gamma - E_{gd}(T))^{1/2}. \quad (\text{F.5})$$

In practice, Eq. F.5 is computed as a piece-wise solution depending on E_γ and the energetically allowed transitions. Using $\alpha_{n,a}^{i,j}$ and $\alpha_{n,e}^{i,j}$ as the coefficients for indirect absorption via phonon absorption and emission, respectively, for the i^{th} phonon and j^{th} band gap, the total indirect absorption coefficient term $\alpha_n^{i,j}$ can be broken into several cases:

$$\alpha_n^{i,j}(T) = \begin{cases} 0 & E_\gamma \leq E_{g,j}(T) - E_{p,i} \rightarrow \text{no indirect absorption;} \\ \alpha_{n,a}^{i,j}(T) & E_{g,j}(T) - E_{p,i} < E_\gamma \leq E_{g,j}(T) + E_{p,i} \rightarrow \text{phonon absorption only;} \\ \alpha_{n,a}^{i,j}(T) + \alpha_{n,e}^{i,j}(T) & E_\gamma > E_{g,j}(T) + E_{p,i} \rightarrow \text{phonon absorption and emission.} \end{cases} \quad (\text{F.6})$$

Considering that $E_{g,1}$ is the lowest band gap energy and $E_{p,2}$ is the highest phonon energy, Eq. F.5 can also be broken down into several cases:

$$\alpha(T) = \begin{cases} 0 & E_\gamma \leq E_{g,1} - E_{p,2} \rightarrow \text{sub-gap absorption (not modelled);} \\ \alpha_n(T) & E_{g,1} - E_{p,2} < E_\gamma \leq E_{gd}(T) \rightarrow \text{indirect absorption only;} \\ \alpha_n(T) + \alpha_v(T) & E_\gamma > E_{gd}(T) \rightarrow \text{direct and indirect absorption.} \end{cases} \quad (\text{F.7})$$

As stated in Ref. [200], this photon absorption model is valid for photon energies between 1.1 and 4 eV. Table F.1 lists all of the parameters used in this model along with their corresponding value taken from

Ref. [200]. Where appropriate, the values determined from the analysis presented in Chapter 6 are also shown.

Table F.1: List of parameters and their corresponding values for the photon absorption model for Si taken from Rajkanan *et. al.* [200] and references therein. For comparison, the parameters that are determined separately from the analysis presented in Chapter 6 are also shown. Note that for the proportionality constant of the first indirect band gap, A_1 , the analysis in Chapter 6 considers a temperature-dependent model instead of a fixed value.

Parameter	Value (Ref. [200])		Description
$E_{g2}(0)$ [eV]	2.5		Second indirect band gap energy at 0 K
$E_{gd}(0)$ [eV]	3.2		Direct band gap energy at 0 K
E_{p1} [meV]	18.27		Energy of the <i>TA</i> phonon
E_{p2} [meV]	57.73		Energy of the <i>TO</i> phonon
C_1	5.5		Electron-phonon coupling constant of the <i>TA</i> phonon
C_2	4.0		Electron-phonon coupling constant of the <i>TO</i> phonon
A_d [$\text{cm}^{-1}\text{eV}^{-1/2}$]	1.052×10^6		Prop. constant for the direct band gap
β [eV K^{-1}]	7.021×10^{-4}		Parameter of the band gap temperature dependence
γ [K]	1108		Parameter of the band gap temperature dependence

Parameter	Value		Description
	Ref. [200]	Chapter 6	
$E_{g1}(0)$ [eV]	1.1557	1.134	First indirect band gap energy at 0 K
A_1 [$\text{cm}^{-1}\text{eV}^{-2}$]	323.1	-	Prop. constant of the first indirect band gap
c_0 [$\text{cm}^{-1}\text{eV}^{-2}$]	-	325	Prop. constant of the first indirect band gap using
c_1 [K^{-1}]	-	1.7×10^{-3}	the model $A_1(T) = c_0 e^{-c_1 T}$
A_2 [$\text{cm}^{-1}\text{eV}^{-2}$]	7.237×10^3	6×10^3	Prop. constant of the second indirect band gap

Acronyms and Abbreviations

e^-h^+ electron-hole pair	31
ADC analog-to-digital converter	67
ADR adiabatic demagnetization refrigerator	59, 61, 65
ALP axion-like particle	22, 24, 40, 62, 123, 152
C.L. confidence level	63, 124, 166
CMB Cosmic Microwave Background	7
CT charge trapping	35, 36, 110, 126, 177, 192
Cz Czochralski	154
DAQ data acquisition	67
DC direct current	53, 67
DM dark matter	ii, 1, 30, 51, 62, 123, 152, 173
DQ data-quality	92, 134
EDF empirical distribution function	134
ER electron-recoil	27, 33
FAA Ferric Ammonium Alum	66
Ge germanium	16, 30, 182
GGG Gadolinium Gallium Garnet	66
GR general relativity	5
HEMT high-electron-mobility transistor	48
HV high voltage	28, 48, 179
HVeV high-voltage eV-scale	ii, 3, 50, 51, 62, 123, 173

II impact ionization.....	35, 36, 110, 126, 177, 192
iZIP interleaved Z-sensitive ionization phonon.....	28, 48
KS Kolmogorov-Smirnov	134
LA longitudinal acoustic.....	204
LDM light dark matter.....	19, 63, 123, 165, 181
LHM lower half-maximum	154
LO longitudinal optical.....	204
MACHO Massive Astrophysical Compact Halo Object.....	26
MC Monte Carlo.....	63, 150, 175
MEMS micro-electro-mechanical system.....	153
MOND modified Newtonian dynamics.....	5
MPA Migdal-photo-absorption	187
NR nuclear-recoil	27, 33
NTL Neganov-Trofimov-Luke	32, 51, 81
OF optimal filter	69
OI optimum interval	63, 123
PCB printed circuit board.....	65, 174
PMT photomultiplier tube	157
PSD power spectral density	69
QET quasiparticle-trap-assisted Electrothermal-feedback TES.....	54, 65
QP quasiparticle.....	54
RQs reduced quantities.....	73
RTD resistance temperature detector.....	68
SD spin-dependent	16
SHM Standard Halo Model.....	11
SI spin-independent.....	16, 183
Si silicon.....	16, 30, 182

SM Standard Model	3
SQUID superconducting quantum interference device.....	51
SuperCDMS Super Cryogenic Dark Matter Search	ii, 3, 27
SUSY Supersymmetry	14
TA transverse acoustic.....	204
TES transition edge sensor	48, 51, 52, 65
TO transverse optical.....	204
TTL transistor-to-transistor logic.....	69
UHM upper half-maximum	154
WIMP Weakly Interacting Massive Particle.....	14, 165, 181
Xe xenon.....	184

Bibliography

- [1] D. W. Amaral, T. Aralis, T. Aramaki, I. J. Arnquist, E. Azadbakht, S. Banik, D. Barker, C. Bathurst, D. A. Bauer, *et al.*, “Constraints on low-mass, relic dark matter candidates from a surface-operated SuperCDMS single-charge sensitive detector,” *Phys. Rev. D*, vol. 102, p. 091101, Nov 2020.
- [2] C. Stanford, M. J. Wilson, B. Cabrera, M. Diamond, N. A. Kurinsky, R. A. Moffatt, F. Ponce, B. von Krosigk, and B. A. Young, “Photoelectric absorption cross section of silicon near the bandgap from room temperature to sub-Kelvin temperature,” *AIP Advances*, vol. 11, no. 2, p. 025120, 2021.
- [3] B. von Krosigk, M. J. Wilson, C. Stanford, B. Cabrera, R. Calkins, D. Jardin, N. A. Kurinsky, F. Ponce, and C.-P. Wu, “Effect on dark matter exclusion limits from new silicon photoelectric absorption measurements,” *Phys. Rev. D*, vol. 104, p. 063002, Sep 2021.
- [4] NASA Hubble Site, “Hubble Deep Field Image Unveils Myriad Galaxies Back to the Beginning of Time.” <https://hubblesite.org/contents/media/images/1996/01/385-Image.html>, 1996. Accessed: 2021.
- [5] G. Bertone and D. Hooper, “History of dark matter,” *Rev. Mod. Phys.*, vol. 90, p. 045002, Oct 2018.
- [6] Centro Ciência Viva do Algarve, “Astronomy in the Middle Ages.” http://www.ccvalg.pt/astronomia/historia/idade_media.htm. Accessed: 2021.
- [7] N. Copernicus, *De Revolutionibus Orbium Caelestium, Libri VI*. Johannes Petreius, 1543.
- [8] G. Galilei, “Sidereus, nuncius magna longeqve admirabilia spectacula pandens, suspiciendaque proponens vniciuque praesertim vero philosophis, atque astronomis.” <https://wellcomecollection.org/works/yedya9rx>, 1610. Accessed: 2021.
- [9] Planck Collaboration, Adam, R., Ade, P. A. R., Aghanim, N., Alves, M. I. R., Arnaud, M., Ashdown, M., Aumont, J., Baccigalupi, C., *et al.*, “Planck 2015 results - X. Diffuse component separation: Foreground maps,” *A&A*, vol. 594, p. A10, 2016.
- [10] S. Ahlen, F. Avignone, R. Brodzinski, A. Drukier, G. Gelmini, and D. Spergel, “Limits on cold dark matter candidates from an ultralow background germanium spectrometer,” *Physics Letters B*, vol. 195, no. 4, pp. 603–608, 1987.

- [11] S. Baum, K. Freese, and C. Kelso, “Dark Matter implications of DAMA/LIBRA-phase2 results,” *Physics Letters B*, vol. 789, pp. 262–269, 2019.
- [12] C. Kelso, D. Hooper, and M. R. Buckley, “Toward a consistent picture for CRESST, CoGeNT, and DAMA,” *Phys. Rev. D*, vol. 85, p. 043515, Feb 2012.
- [13] V. C. Rubin, J. Ford, W. K., and N. Thonnard, “Rotational properties of 21 SC galaxies with a large range of luminosities and radii, from NGC 4605 (R=4kpc) to UGC 2885 (R=122kpc).,” *ApJ*, vol. 238, pp. 471–487, June 1980.
- [14] B. Famaey and S. S. McGaugh, “Modified Newtonian Dynamics (MOND): Observational Phenomenology and Relativistic Extensions,” *Living Reviews in Relativity*, vol. 15, p. 10, Sep 2012.
- [15] N. A. Kurinsky, *The Low-Mass Limit: Dark Matter Detectors with eV-Scale Energy Resolution*. PhD thesis, Stanford U., Phys. Dept., 2018.
- [16] P. Schneider, J. Ehlers, and E. E. Falco, *Gravitational Lenses*. Astronomy and astrophysics library, Berlin: Springer-Verlag, 1992.
- [17] R. Massey, T. Kitching, and J. Richard, “The dark matter of gravitational lensing,” *Reports on Progress in Physics*, vol. 73, p. 086901, Jul 2010.
- [18] D. Clowe, M. Bradač, A. H. Gonzalez, M. Markevitch, S. W. Randall, C. Jones, and D. Zaritsky, “A Direct Empirical Proof of the Existence of Dark Matter,” *The Astrophysical Journal*, vol. 648, pp. L109–L113, Aug 2006.
- [19] M. J. Jee, H. Hoekstra, A. Mahdavi, and A. Babul, “Hubble Space Telescope/Advanced Camera for Surveys Confirmation of the Dark Substructure in A520,” *The Astrophysical Journal*, vol. 783, p. 78, Feb 2014.
- [20] G. Bertone, D. Hooper, and J. Silk, “Particle dark matter: evidence, candidates and constraints,” *Physics Reports*, vol. 405, no. 5, pp. 279–390, 2005.
- [21] C. Wood, “How ancient light reveals the universe’s contents.” <https://www.quantamagazine.org/how-the-cosmic-microwave-background-reveals-the-universes-contents-20200128/>, Jun 2020. Accessed: 2021.
- [22] Planck Collaboration, Ade, P. A. R., Aghanim, N., Arnaud, M., Ashdown, M., Aumont, J., Baccigalupi, C., Banday, A. J., Barreiro, R. B., *et al.*, “Planck 2015 results - XIII. Cosmological parameters,” *A&A*, vol. 594, p. A13, 2016.
- [23] E. D. Nobile, M. Nardecchia, and P. Panci, “Millicharge or decay: a critical take on Minimal Dark Matter,” *Journal of Cosmology and Astroparticle Physics*, vol. 2016, pp. 048–048, apr 2016.
- [24] G. Gentile, P. Salucci, U. Klein, D. Vergani, and P. Kalberla, “The cored distribution of dark matter in spiral galaxies,” *Monthly Notices of the Royal Astronomical Society*, vol. 351, pp. 903–922, 07 2004.
- [25] J. I. Read, “The local dark matter density,” *Journal of Physics G: Nuclear and Particle Physics*, vol. 41, p. 063101, May 2014.

- [26] F. Mayet, A. Green, J. Battat, J. Billard, N. Bozorgnia, G. Gelmini, P. Gondolo, B. Kavanagh, S. Lee, *et al.*, “A review of the discovery reach of directional Dark Matter detection,” *Physics Reports*, vol. 627, pp. 1–49, 2016.
- [27] G. Herrera and A. Ibarra, “Direct detection of non-galactic light dark matter,” *Physics Letters B*, vol. 820, p. 136551, 2021.
- [28] SuperCDMS Collaboration, “Super cryogenic dark matter search.” <https://supercdms.slac.stanford.edu/>. Accessed: 2021.
- [29] EDELWEISS Collaboration, “EDELWEISS: Experiment for direct detection of WIMP dark matter.” <http://edelweiss.in2p3.fr/>. Accessed: 2021.
- [30] CRESST Collaboration, “CRESST - Searching for Dark Matter.” <https://www.cresst.de/>. Accessed: 2021.
- [31] XENON Collaboration, “The XENON Experiment: Enlightening the Dark.” <http://www.xenon1t.org/>. Accessed: 2021.
- [32] DEAP Collaboration, “DEAP-3600: Dark Matter Experiment using Argon Pulseshape discrimination.” <http://deap3600.ca/>. Accessed: 2021.
- [33] B. Bottino *et al.*, “The DarkSide experiment,” *Nuovo Cim. C*, vol. 40, no. 1, p. 52, 2017.
- [34] PandaX Collaboration, “PandaX: Particle and Astrophysical Xenon Experiments.” <https://pandax.sjtu.edu.cn/>. Accessed: 2021.
- [35] D. Akerib, X. Bai, S. Bedikian, E. Bernard, A. Bernstein, A. Bolozdynya, A. Bradley, D. Byram, S. Cahn, *et al.*, “The Large Underground Xenon (LUX) experiment,” *Nuclear Instruments and Methods in Physics Research Section A: Accelerators, Spectrometers, Detectors and Associated Equipment*, vol. 704, pp. 111–126, 2013.
- [36] SENSEI Collaboration, “SENSEI: Sub-electron-noise Skipper-CCD Experimental Instrument.” <https://sensei-skipper.github.io/>. Accessed: 2021.
- [37] N. Castelló-Mor *et al.*, “DAMIC-M experiment: Thick, silicon CCDs to search for light dark matter,” *Nuclear Instruments and Methods in Physics Research Section A: Accelerators, Spectrometers, Detectors and Associated Equipment*, vol. 958, p. 162933, 2020. Proceedings of the Vienna Conference on Instrumentation 2019.
- [38] PICO Collaboration, “PICO Experiment: searching for dark matter with bubble chambers.” <https://www.picoexperiment.com/>. Accessed: 2021.
- [39] E. Daw, A. Dorofeev, J. R. Fox, J. L. Gauvreau, C. Ghag, L. J. Harmon, J. L. Harton, M. Gold, E. R. Lee, *et al.*, “The DRIFT Dark Matter Experiments,” *ArXiv:1110.0222*, 2011.
- [40] A. Berlin, R. T. D’Agnolo, S. A. R. Ellis, C. Nantista, J. Neilson, P. Schuster, S. Tantawi, N. Toro, and K. Zhou, “Axion dark matter detection by superconducting resonant frequency conversion,” *Journal of High Energy Physics*, vol. 2020, p. 88, Jul 2020.

- [41] NASA, “Fermi Gamma-ray Space Telescope.” <https://fermi.gsfc.nasa.gov/>, 2021. Accessed: 2021.
- [42] F. Donato, D. Maurin, P. Brun, T. Delahaye, and P. Salati, “Constraints on WIMP Dark Matter from the High Energy PAMELA \bar{p}/p Data,” *Phys. Rev. Lett.*, vol. 102, p. 071301, Feb 2009.
- [43] M.-Y. Cui, Q. Yuan, Y.-L. S. Tsai, and Y.-Z. Fan, “Possible Dark Matter Annihilation Signal in the AMS-02 Antiproton Data,” *Phys. Rev. Lett.*, vol. 118, p. 191101, May 2017.
- [44] CERN, “The Large Hadron Collider.” <https://home.cern/science/accelerators/large-hadron-collider>, 2021. Accessed: 2021.
- [45] M. Campajola *et al.*, “Dark Sector first results at Belle II,” *Physica Scripta*, vol. 96, p. 084005, may 2021.
- [46] G. Jungman, M. Kamionkowski, and K. Griest, “Supersymmetric dark matter,” *Physics Reports*, vol. 267, no. 5, pp. 195–373, 1996.
- [47] R. W. Schnee, *Introduction to Dark Matter Experiments*, pp. 775–829. World Scientific, 2011.
- [48] L. Bergström, “Dark matter evidence, particle physics candidates and detection methods,” *Annalen der Physik*, vol. 524, no. 9-10, pp. 479–496, 2012.
- [49] J. Lewin and P. Smith, “Review of mathematics, numerical factors, and corrections for dark matter experiments based on elastic nuclear recoil,” *Astroparticle Physics*, vol. 6, no. 1, pp. 87–112, 1996.
- [50] D. G. Cerdeno and A. M. Green, “Direct detection of WIMPs,” *ArXiv:1002.1912*, 2 2010.
- [51] R. Agnese, A. J. Anderson, T. Aralis, T. Aramaki, I. J. Arnquist, W. Baker, D. Balakishiyeva, D. Barker, R. Basu Thakur, *et al.*, “Low-mass dark matter search with CDMSlite,” *Phys. Rev. D*, vol. 97, p. 022002, Jan 2018.
- [52] E. Aprile, J. Aalbers, F. Agostini, M. Alfonsi, L. Althueser, F. D. Amaro, V. C. Antochi, E. Angelino, F. Arneodo, *et al.*, “Light Dark Matter Search with Ionization Signals in XENON1T,” *Phys. Rev. Lett.*, vol. 123, p. 251801, Dec 2019.
- [53] X. Cui, A. Abdukerim, W. Chen, X. Chen, Y. Chen, B. Dong, D. Fang, C. Fu, K. Giboni, *et al.*, “Dark Matter Results from 54-Ton-Day Exposure of PandaX-II Experiment,” *Phys. Rev. Lett.*, vol. 119, p. 181302, Oct 2017.
- [54] L. T. Yang, H. B. Li, Q. Yue, H. Ma, K. J. Kang, Y. J. Li, H. T. Wong, M. Agartioglu, H. P. An, *et al.*, “Search for Light Weakly-Interacting-Massive-Particle Dark Matter by Annual Modulation Analysis with a Point-Contact Germanium Detector at the China Jinping Underground Laboratory,” *Phys. Rev. Lett.*, vol. 123, p. 221301, Nov 2019.
- [55] R. Agnese, T. Aralis, T. Aramaki, I. J. Arnquist, E. Azadbakht, W. Baker, S. Banik, D. Barker, D. A. Bauer, *et al.*, “Search for low-mass dark matter with CDMSlite using a profile likelihood fit,” *Phys. Rev. D*, vol. 99, p. 062001, Mar 2019.

- [56] G. Adhikari, P. Adhikari, E. B. de Souza, N. Carlin, S. Choi, M. Djamel, A. C. Ezeribe, C. H. Ha, I. Hahn, *et al.*, “An experiment to search for dark-matter interactions using sodium iodide detectors,” *Nature*, vol. 564, no. 7734, pp. 83–86, 2018.
- [57] E. Behnke, J. Behnke, S. J. Brice, D. Broemmelsiek, J. I. Collar, A. Conner, P. S. Cooper, M. Crisler, C. E. Dahl, *et al.*, “First dark matter search results from a 4-kg CF₃I bubble chamber operated in a deep underground site,” *Phys. Rev. D*, vol. 86, p. 052001, Sep 2012.
- [58] A. H. Abdelhameed, G. Angloher, P. Bauer, A. Bento, E. Bertoldo, C. Bucci, L. Canonica, A. D’Addabbo, X. Defay, *et al.*, “First results from the CRESST-III low-mass dark matter program,” *Phys. Rev. D*, vol. 100, p. 102002, Nov 2019.
- [59] A. Aguilar-Arevalo, D. Amidei, D. Baxter, G. Canelo, B. A. C. Vergara, A. E. Chavarria, J. C. D’Olivo, J. Estrada, F. Favela-Perez, *et al.*, “Results on Low-Mass Weakly Interacting Massive Particles from an 11 kg d Target Exposure of DAMIC at SNOLAB,” *Phys. Rev. Lett.*, vol. 125, p. 241803, Dec 2020.
- [60] P. Agnes, I. F. M. Albuquerque, T. Alexander, A. K. Alton, G. R. Araujo, M. Ave, H. O. Back, B. Baldin, G. Batignani, *et al.*, “DarkSide-50 532-day dark matter search with low-radioactivity argon,” *Phys. Rev. D*, vol. 98, p. 102006, Nov 2018.
- [61] R. Ajaj, P.-A. Amaudruz, G. R. Araujo, M. Baldwin, M. Batygov, B. Beltran, C. E. Bina, J. Bonatt, M. G. Boulay, *et al.*, “Search for dark matter with a 231-day exposure of liquid argon using DEAP-3600 at SNOLAB,” *Phys. Rev. D*, vol. 100, p. 022004, Jul 2019.
- [62] Q. Arnaud, D. Asner, J.-P. Bard, A. Brossard, B. Cai, M. Chapellier, M. Clark, E. Corcoran, T. Dandl, *et al.*, “First results from the NEWS-G direct dark matter search experiment at the LSM,” *Astroparticle Physics*, vol. 97, pp. 54–62, 2018.
- [63] E. Behnke, M. Besnier, P. Bhattacharjee, X. Dai, M. Das, A. Davour, F. Debris, N. Dhungana, J. Farine, *et al.*, “Final results of the PICASSO dark matter search experiment,” *Astroparticle Physics*, vol. 90, pp. 85–92, 2017.
- [64] C. Amole, M. Ardid, I. J. Arnquist, D. M. Asner, D. Baxter, E. Behnke, M. Bressler, B. Broerman, G. Cao, *et al.*, “Dark matter search results from the complete exposure of the PICO-60 C₃F₈ bubble chamber,” *Phys. Rev. D*, vol. 100, p. 022001, Jul 2019.
- [65] M. Felizardo, T. A. Girard, T. Morlat, A. C. Fernandes, A. R. Ramos, and J. G. Marques, “Recent results from the SIMPLE dark matter search,” *Journal of Physics: Conference Series*, vol. 375, p. 012011, Jul 2012.
- [66] H. B. Li, H. Y. Liao, S. T. Lin, S. K. Liu, L. Singh, M. K. Singh, A. K. Soma, H. T. Wong, Y. C. Wu, *et al.*, “Limits on Spin-Independent Couplings of WIMP Dark Matter with a *p*-Type Point-Contact Germanium Detector,” *Phys. Rev. Lett.*, vol. 110, p. 261301, Jun 2013.
- [67] K. Abe, K. Hiraide, K. Ichimura, Y. Kishimoto, K. Kobayashi, M. Kobayashi, S. Moriyama, M. Nakahata, T. Norita, *et al.*, “A direct dark matter search in XMASS-I,” *Physics Letters B*, vol. 789, pp. 45–53, 2019.

- [68] D. Akimov, H. Araújo, E. Barnes, V. Belov, A. Bewick, A. Burenkov, V. Chepel, A. Currie, L. DeViveiros, *et al.*, “WIMP-nucleon cross-section results from the second science run of ZEPLIN-III,” *Physics Letters B*, vol. 709, no. 1, pp. 14–20, 2012.
- [69] F. Ruppin, J. Billard, E. Figueroa-Feliciano, and L. Strigari, “Complementarity of dark matter detectors in light of the neutrino background,” *Phys. Rev. D*, vol. 90, p. 083510, Oct 2014.
- [70] B. W. Lee and S. Weinberg, “Cosmological Lower Bound on Heavy-Neutrino Masses,” *Phys. Rev. Lett.*, vol. 39, pp. 165–168, Jul 1977.
- [71] R. Essig, M. Fernández-Serra, J. Mardon, A. Soto, T. Volansky, and T.-T. Yu, “Direct detection of sub-GeV dark matter with semiconductor targets,” *J. High Energy Phys.*, vol. 2016, p. 46, 2016.
- [72] M. Battaglieri, A. Belloni, A. Chou, P. Cushman, B. Echenard, R. Essig, J. Estrada, J. L. Feng, B. Flaugher, *et al.*, “US Cosmic Visions: New Ideas in Dark Matter 2017: Community Report,” *ArXiv:1707.04591*, 2017.
- [73] R. Catena, T. Emken, N. A. Spaldin, and W. Tarantino, “Atomic responses to general dark matter-electron interactions,” *Phys. Rev. Research*, vol. 2, p. 033195, Aug 2020.
- [74] R. Catena, T. Emken, M. Matas, N. A. Spaldin, and E. Urdshals, “Crystal responses to general dark matter-electron interactions,” *ArXiv:2105.02233*, 2021.
- [75] R. Essig, J. Mardon, and T. Volansky, “Direct detection of sub-GeV dark matter,” *Phys. Rev. D*, vol. 85, p. 076007, Apr 2012.
- [76] T.-T. Yu *et al.*, “Direct Detection of sub-GeV Dark Matter.” <http://ddlDM.physics.sunysb.edu/dd1DM>, 2019. Accessed: 2019.
- [77] J. Baur, N. Palanque-Delabrouille, C. Yèche, C. Magneville, and M. Viel, “Lyman-alpha forests cool warm dark matter,” *Journal of Cosmology and Astroparticle Physics*, vol. 2016, pp. 012–012, Aug 2016.
- [78] I. M. Bloch, R. Essig, K. Tobioka, T. Volansky, and T.-T. Yu, “Searching for dark absorption with direct detection experiments,” *J. High Energy Phys.*, vol. 2017, p. 1029, 2017.
- [79] Y. Hochberg, T. Lin, and K. M. Zurek, “Absorption of light dark matter in semiconductors,” *Phys. Rev. D*, vol. 95, p. 023013, Jan 2017.
- [80] T. Mannel, “Theory and Phenomenology of CP Violation,” *Nuclear Physics B - Proceedings Supplements*, vol. 167, pp. 170–174, 2007. Proceedings of the 7th International Conference on Hyperons, Charm and Beauty Hadrons.
- [81] R. D. Peccei, *The Strong CP Problem and Axions*, pp. 3–17. Berlin, Heidelberg: Springer Berlin Heidelberg, 2008.
- [82] M. Tanabashi, K. Hagiwara, K. Hikasa, K. Nakamura, Y. Sumino, F. Takahashi, J. Tanaka, K. Agashe, G. Aielli, *et al.*, “Review of Particle Physics,” *Phys. Rev. D*, vol. 98, p. 030001, 2018.
- [83] A. Derevianko, V. A. Dzuba, V. V. Flambaum, and M. Pospelov, “Axio-electric effect,” *Phys. Rev. D*, vol. 82, p. 065006, Sep 2010.

- [84] C. Fu, X. Zhou, X. Chen, Y. Chen, X. Cui, D. Fang, K. Giboni, F. Giuliani, K. Han, *et al.*, “Limits on Axion Couplings from the First 80 Days of Data of the PandaX-II Experiment,” *Phys. Rev. Lett.*, vol. 119, p. 181806, Nov 2017.
- [85] M. Pospelov, A. Ritz, and M. Voloshin, “Bosonic super-WIMPs as keV-scale dark matter,” *Phys. Rev. D*, vol. 78, p. 115012, Dec 2008.
- [86] A. B. Migdal, “Ionization of atoms accompanying α - and β -decay,” *J. Phys. USSR*, vol. 4, p. 449, 1941.
- [87] K. Petraki and R. R. Volkas, “Review of Asymmetric Dark Matter,” *International Journal of Modern Physics A*, vol. 28, no. 19, p. 1330028, 2013.
- [88] D. E. Kaplan, M. A. Luty, and K. M. Zurek, “Asymmetric dark matter,” *Phys. Rev. D*, vol. 79, p. 115016, Jun 2009.
- [89] B. Carr and F. Kühnel, “Primordial Black Holes as Dark Matter: Recent Developments,” *Annual Review of Nuclear and Particle Science*, vol. 70, no. 1, pp. 355–394, 2020.
- [90] K. Jedamzik, “Primordial black hole dark matter and the LIGO/Virgo observations,” *Journal of Cosmology and Astroparticle Physics*, vol. 2020, pp. 022–022, Sep 2020.
- [91] A. Boyarsky, M. Drewes, T. Lasserre, S. Mertens, and O. Ruchayskiy, “Sterile neutrino Dark Matter,” *Progress in Particle and Nuclear Physics*, vol. 104, pp. 1–45, 2019.
- [92] M. D. Campos and W. Rodejohann, “Testing keV sterile neutrino dark matter in future direct detection experiments,” *Phys. Rev. D*, vol. 94, p. 095010, Nov 2016.
- [93] SNOLAB, “About the facilities.” <https://www.snolab.ca/facility/about-the-facilities/>, 2021. Accessed: 2021.
- [94] R. Agnese, A. J. Anderson, T. Aramaki, I. Arnquist, W. Baker, D. Barker, R. Basu Thakur, D. A. Bauer, A. Borgland, *et al.*, “Projected sensitivity of the SuperCDMS SNOLAB experiment,” *Phys. Rev. D*, vol. 95, p. 082002, Apr 2017.
- [95] R. Agnese, A. J. Anderson, M. Asai, D. Balakishiyeva, R. Basu Thakur, D. A. Bauer, J. Beaty, J. Billard, A. Borgland, *et al.*, “Search for Low-Mass Weakly Interacting Massive Particles with SuperCDMS,” *Phys. Rev. Lett.*, vol. 112, p. 241302, Jun 2014.
- [96] D. S. Akerib, H. M. Araújo, X. Bai, A. J. Bailey, J. Balajthy, P. Beltrame, E. P. Bernard, A. Bernstein, T. P. Biesiadzinski, *et al.*, “Improved Limits on Scattering of Weakly Interacting Massive Particles from Reanalysis of 2013 LUX Data,” *Phys. Rev. Lett.*, vol. 116, p. 161301, Apr 2016.
- [97] B. S. Neganov and V. N. Trofimov, “Calorimetric method measuring ionizing radiation,” *Otkryt. Izobret.*, vol. 146, p. 215, 1985.
- [98] P. N. Luke, “Voltage-assisted calorimetric ionization detector,” *J. Applied Phys.*, vol. 64, p. 6858, 1988.

- [99] R. Ren, C. Bathurst, Y. Y. Chang, R. Chen, C. W. Fink, Z. Hong, N. A. Kurinsky, N. Mast, N. Mishra, *et al.*, “Design and characterization of a phonon-mediated cryogenic particle detector with an eV-scale threshold and 100 keV-scale dynamic range,” *Phys. Rev. D*, vol. 104, p. 032010, Aug 2021.
- [100] G. Wang, “Phonon emission in germanium and silicon by electrons and holes in applied electric field at low temperature,” *Journal of Applied Physics*, vol. 107, no. 9, p. 094504, 2010.
- [101] Y. Kahn and T. Lin, “Searches for light dark matter using condensed matter systems,” *ArXiv:2108.03239*, 2021.
- [102] K. Ramanathan and N. Kurinsky, “Ionization yield in silicon for eV-scale electron-recoil processes,” *Phys. Rev. D*, vol. 102, p. 063026, Sep 2020.
- [103] J. Lindhard, V. Nielsen, M. Scharff, and P. V. Thomsen, “Integral Equations Governing Radiation Effects. (Notes on Atomic Collisions, III),” *Kgl. Danske Videnskab., Selskab. Mat. Fys. Medd.*, vol. 33, 1 1963.
- [104] J. Lindhard, M. Scharff, and H. E. Schiøtt, “Range Concepts and Heavy Ion Ranges (Notes on Atomic Collision, II),” *Kgl. Danske Videnskab. Selskab. Mat. Fys. Medd.*, vol. 33, 1 1963.
- [105] J. Lindhard, V. Nielsen, and M. Scharff, “Approximation Method in Classical Scattering by Screened Coulomb Fields,” *Kgl. Danske Videnskab. Selskab. Mat. Fys. Medd.*, vol. 36, 1 1968.
- [106] R. Agnese, T. Aralis, T. Aramaki, I. J. Arnquist, E. Azadbakht, W. Baker, S. Banik, D. Barker, D. A. Bauer, *et al.*, “First Dark Matter Constraints from a SuperCDMS Single-Charge Sensitive Detector,” *Phys. Rev. Lett.*, vol. 121, p. 051301, Aug 2018.
- [107] V. S. Vavilov, “Radiation ionization processes in germanium and silicon crystals,” *Soviet Physics Uspekhi*, vol. 4, pp. 761–769, May 1962.
- [108] A. Owens, G. W. Fraser, and K. J. McCarthy, “On the experimental determination of the Fano factor in Si at soft X-ray wavelengths,” *Nucl. Instrum. Meth. A*, vol. 491, p. 437, 2002.
- [109] F. Ponce, C. Stanford, S. Yellin, W. Page, C. Fink, M. Pyle, B. Sadoulet, B. Serfass, S. L. Watkins, P. L. Brink, *et al.*, “Measuring the impact ionization and charge trapping probabilities in SuperCDMS HVeV phonon sensing detectors,” *Phys. Rev. D*, vol. 101, p. 031101(R), 2020.
- [110] F. Ponce, W. Page, P. L. Brink, B. Cabrera, M. Cherry, C. Fink, N. Kurinsky, R. Partridge, M. Pyle, *et al.*, “Modeling of Impact Ionization and Charge Trapping in SuperCDMS HVeV Detectors,” *Journal of Low Temperature Physics*, vol. 199, pp. 598–605, May 2020.
- [111] M. J. Berger *et al.*, “XCOM: Photon Cross Section Database (version 1.5).” <http://physics.nist.gov/xcom>, 2010. Accessed: 2020.
- [112] G. G. Macfarlane, T. P. McLean, J. E. Quarrington, and V. Roberts, “Fine Structure in the Absorption-Edge Spectrum of Si,” *Phys. Rev.*, vol. 111, pp. 1245–1254, Sep 1958.
- [113] R. Hulthén, “Optical Constants of Epitaxial Silicon in the Region 1 – 3.3 eV,” *Phys. Scr.*, vol. 12, p. 342, 1975.

- [114] D. F. Edwards, “ - Silicon (Si)*,” in *Handbook of Optical Constants of Solids* (E. D. Palik, ed.), pp. 547 – 569, Burlington: Academic Press, 1997.
- [115] S. E. Holland, D. E. Groom, N. P. Palaio, R. J. Stover, and Mingzhi Wei, “Fully depleted, back-illuminated charge-coupled devices fabricated on high-resistivity silicon,” *IEEE Transactions on Electron Devices*, vol. 50, no. 1, pp. 225–238, 2003.
- [116] M. A. Green, “Self-consistent optical parameters of intrinsic silicon at 300K including temperature coefficients,” *Solar Energy Materials and Solar Cells*, vol. 92, no. 11, pp. 1305 – 1310, 2008.
- [117] M. A. Green and M. J. Keevers, “Optical properties of intrinsic silicon at 300 K,” *Progress in Photovoltaics: Research and Applications*, vol. 3, no. 3, pp. 189–192, 1995.
- [118] E. M. Gullikson, P. Denham, S. Mrowka, and J. H. Underwood, “Absolute photoabsorption measurements of Mg, Al, and Si in the soft-x-ray region below the $L_{2,3}$ edges,” *Phys. Rev. B*, vol. 49, pp. 16283–16288, Jun 1994.
- [119] D. E. Aspnes and A. A. Studna, “Dielectric functions and optical parameters of Si, Ge, GaP, GaAs, GaSb, InP, InAs, and InSb from 1.5 to 6.0 eV,” *Phys. Rev. B*, vol. 27, pp. 985–1009, Jan 1983.
- [120] W. C. Dash and R. Newman, “Intrinsic Optical Absorption in Single-Crystal Germanium and Silicon at 77°K and 300°K,” *Phys. Rev.*, vol. 99, p. 1151, 1955.
- [121] C. Chantler, K. Olsen, R. Dragoset, J. Chang, A. Kishore, S. Kotochigova, , and D. Zucker, “X-Ray Form Factor, Attenuation and Scattering Tables (version 2.1),” *NIST Standard Reference Database 66*, 2005.
- [122] G. Doolen and D. A. Liberman, “Calculations of photoabsorption by atoms using a linear response method,” *Physica Scripta*, vol. 36, pp. 77–79, Jul 1987.
- [123] B. Henke, E. Gullikson, and J. Davis, “X-Ray Interactions: Photoabsorption, Scattering, Transmission, and Reflection at $E = 50$ -30,000 eV, $Z = 1$ -92,” *Atomic Data and Nuclear Data Tables*, vol. 54, no. 2, pp. 181 – 342, 1993.
- [124] W. R. Hunter, “Observation of Absorption Edges in the Extreme Ultraviolet by Transmittance Measurements Through Thin Unbacked Metal Films,” in *Optical Properties and Electron Structure of Metals and Alloys* (F. Abelès, ed.), pp. 136–146, North-Holland Publishing Company - Amsterdam, 1966.
- [125] P. Fernandez Garrillo, *Development of highly resolved and photo-modulated Kelvin probe microscopy techniques for the study of photovoltaic systems*. PhD thesis, Université Grenoble Alpes, 09 2018.
- [126] B. O. Seraphin and N. Bottka, “Franz-Keldysh Effect of the Refractive Index in Semiconductors,” *Phys. Rev.*, vol. 139, pp. A560–A565, Jul 1965.
- [127] D. Schroder, R. Thomas, and J. Swartz, “Free Carrier Absorption in Silicon,” *IEEE Journal of Solid-State Circuits*, vol. 13, no. 1, pp. 180–187, 1978.
- [128] C. W. Fink, S. L. Watkins, T. Aramaki, P. L. Brink, S. Ganjam, B. A. Hines, M. E. Huber, N. A. Kurinsky, and R. o. Mahapatra, “Characterizing TES power noise for future single optical-phonon and infrared-photon detectors,” *AIP Advances*, vol. 10, no. 8, p. 085221, 2020.

- [129] C. W. Fink, S. L. Watkins, T. Aramaki, P. L. Brink, J. Camilleri, X. Defay, S. Ganjam, Y. G. Kolomensky, R. Mahapatra, *et al.*, “Performance of a large area photon detector for rare event search applications,” *Applied Physics Letters*, vol. 118, no. 2, p. 022601, 2021.
- [130] I. Alkhatib, D. W. P. Amaral, T. Aralis, T. Aramaki, I. J. Arnquist, I. Atae Langroudy, E. Azadbakht, S. Banik, D. Barker, *et al.*, “Light Dark Matter Search with a High-Resolution Athermal Phonon Detector Operated above Ground,” *Phys. Rev. Lett.*, vol. 127, p. 061801, Aug 2021.
- [131] R. K. Romani, P. L. Brink, B. Cabrera, M. Cherry, T. Howarth, N. Kurinsky, R. A. Moffatt, R. Partridge, F. Ponce, *et al.*, “Thermal detection of single e-h pairs in a biased silicon crystal detector,” *Applied Physics Letters*, vol. 112, no. 4, p. 043501, 2018.
- [132] Z. Hong, R. Ren, N. Kurinsky, E. Figueroa-Feliciano, L. Wills, S. Ganjam, R. Mahapatra, N. Mirabolfathi, B. Nebolsky, *et al.*, “Single electron-hole pair sensitive silicon detector with surface event discrimination,” *Nuclear Instruments and Methods in Physics Research Section A: Accelerators, Spectrometers, Detectors and Associated Equipment*, vol. 963, p. 163757, 2020.
- [133] K. Irwin and G. Hilton, *Transition-Edge Sensors*, pp. 63–150. Berlin, Heidelberg: Springer Berlin Heidelberg, 2005.
- [134] B. A. Hines, K. M. Sundqvist, D. N. Seitz, and M. E. Huber, “Flux-Coupled Direct Feedback in a SQUID Amplifier,” *IEEE Transactions on Applied Superconductivity*, vol. 21, no. 3, pp. 262–266, 2011.
- [135] M. C. Pyle, *Optimizing the design and analysis of cryogenic semiconductor dark matter detectors for maximum sensitivity*. PhD thesis, Stanford University, 1 2012.
- [136] K. D. Irwin, S. W. Nam, B. Cabrera, B. Chugg, and B. A. Young, “A quasiparticle-trap-assisted transition-edge sensor for phonon-mediated particle detection,” *Review of Scientific Instruments*, vol. 66, no. 11, pp. 5322–5326, 1995.
- [137] S. M. Griffin, Y. Hochberg, K. Inzani, N. Kurinsky, T. Lin, and T. C. Yu, “Silicon carbide detectors for sub-GeV dark matter,” *Phys. Rev. D*, vol. 103, p. 075002, Apr 2021.
- [138] J. J. Yen, B. Shank, B. A. Young, B. Cabrera, P. L. Brink, M. Cherry, J. M. Kreikebaum, R. Moffatt, P. Redl, A. Tomada, and E. C. Tortorici, “Measurement of quasiparticle transport in aluminum films using tungsten transition-edge sensors,” *Applied Physics Letters*, vol. 105, no. 16, p. 163504, 2014.
- [139] J. J. Yen, J. M. Kreikebaum, B. A. Young, B. Cabrera, R. Moffatt, P. Redl, B. Shank, P. L. Brink, M. Cherry, and A. Tomada, “Quasiparticle Transport in Thick Aluminum Films Coupled to Tungsten Transition Edge Sensors,” *Journal of Low Temperature Physics*, vol. 184, pp. 30–37, Jul 2016.
- [140] S. B. Kaplan, C. C. Chi, D. N. Langenberg, J. J. Chang, S. Jafarey, and D. J. Scalapino, “Quasiparticle and phonon lifetimes in superconductors,” *Phys. Rev. B*, vol. 14, pp. 4854–4873, Dec 1976.

- [141] T. Guruswamy, D. J. Goldie, and S. Withington, “Nonequilibrium superconducting thin films with sub-gap and pair-breaking photon illumination,” *Superconductor Science and Technology*, vol. 28, p. 054002, apr 2015.
- [142] S. Yellin, “Finding an upper limit in the presence of an unknown background,” *Phys. Rev. D*, vol. 66, p. 032005, 2002.
- [143] S. Yellin, “Extending the optimum interval method,” *ArXiv:0709.2701*, 2007.
- [144] E. Gatti and P. F. Manfredi, “Processing the signals from solid-state detectors in elementary-particle physics,” *Riv. Nuovo Cim.*, vol. 9, p. 1, 1986.
- [145] Z. Hong, R. Ren, N. Kurinsky, E. Figueroa-Feliciano, L. Wills, S. Ganjam, R. Mahapatra, N. Mirabolfathi, B. Nebolsky, H. D. Pinckney, and M. Platt, “Single electron–hole pair sensitive silicon detector with surface event discrimination,” *Nuclear Instruments and Methods in Physics Research Section A: Accelerators, Spectrometers, Detectors and Associated Equipment*, vol. 963, p. 163757, 2020.
- [146] M.-M. Bé, V. Chisté, C. Dulieu, E. Browne, V. Chechev, N. Kuzmenko, R. Helmer, A. Nichols, E. Schönfeld, and R. Dersch, *Table of radionuclides (Vol. 1 - A = 1 to 150)*. Bureau International des Poids et Mesures, 01 2004.
- [147] R. Pincus, *Distribution of the Maximal Gap in a Sample and its Application for Outlier Detection*, pp. 90–91. Dordrecht: Springer Netherlands, 1984.
- [148] T. Aralis, T. Aramaki, I. J. Arnquist, E. Azadbakht, W. Baker, S. Banik, D. Barker, C. Bathurst, D. A. Bauer, *et al.*, “Constraints on dark photons and axionlike particles from the SuperCDMS Soudan experiment,” *Phys. Rev. D*, vol. 101, p. 052008, 2020.
- [149] S. Yellin, “private communication,” 2019.
- [150] A. Makarov and G. Simonova, “Some Properties of Two-Sample Kolmogorov–Smirnov Test in the Case of Contamination of One of the Samples,” *Journal of Mathematical Sciences*, vol. 220, 02 2017.
- [151] A. Aguilar-Arevalo, D. Amidei, D. Baxter, G. Cancelo, B. A. Cervantes Vergara, A. E. Chavarria, E. Darragh-Ford, J. R. T. de Mello Neto, J. C. D’Olivo, *et al.*, “Constraints on Light Dark Matter Particles Interacting with Electrons from DAMIC at SNOLAB,” *Phys. Rev. Lett.*, vol. 123, p. 181802, 2019.
- [152] O. Abramoff, L. Barak, I. M. Bloch, L. Chaplinsky, M. Crisler, Dawa, A. Drlica-Wagner, R. Essig, J. Estrada, *et al.*, “SENSEI: Direct-Detection Constraints on Sub-GeV Dark Matter from a Shallow Underground Run Using a Prototype Skipper CCD,” *Phys. Rev. Lett.*, vol. 122, p. 161801, 2019.
- [153] Q. Arnaud, E. Armengaud, C. Augier, A. Benoît, L. Bergé, J. Billard, A. Broniatowski, P. Camus, A. Cazes, *et al.*, “First Germanium-Based Constraints on Sub-MeV Dark Matter with the EDELWEISS Experiment,” *Phys. Rev. Lett.*, vol. 125, p. 141301, Oct 2020.
- [154] R. Essig, T. Volansky, and T.-T. Yu, “New constraints and prospects for sub-GeV dark matter scattering off electrons in xenon,” *Phys. Rev. D*, vol. 96, p. 043017, 2017.

- [155] R. Essig, A. Manalaysay, J. Mardon, P. Sorensen, and T. Volansky, “First Direct Detection Limits on Sub-GeV Dark Matter from XENON10,” *Phys. Rev. Lett.*, vol. 109, p. 021301, 2012.
- [156] H. An, M. Pospelov, J. Pradler, and A. Ritz, “Direct detection constraints on dark photon dark matter,” *Phys. Lett. B*, vol. 747, p. 331, 2015.
- [157] N. Viaux, M. Catelan, P. B. Stetson, G. G. Raffelt, J. Redondo, A. A. R. Valcarce, and A. Weiss, “Neutrino and Axion Bounds from the Globular Cluster M5 (NGC 5904),” *Phys. Rev. Lett.*, vol. 111, p. 231301, 2013.
- [158] M. M. M. Bertolami, B. E. Melendez, L. G. Althaus, and J. Isern, “Revisiting the axion bounds from the Galactic white dwarf luminosity function,” *J. Cosmol. Astropart. Phys.*, vol. 1410, p. 069, 2014.
- [159] R. A. Moffatt, N. A. Kurinsky, C. Stanford, J. Allen, P. L. Brink, B. Cabrera, M. Cherry, F. Insulla, F. Ponce, K. Sundqvist, S. Yellin, J. J. Yen, and B. A. Young, “Spatial imaging of charge transport in silicon at low temperature,” *Applied Physics Letters*, vol. 114, p. 032104, Jan 2019.
- [160] C. Stanford, R. A. Moffatt, N. A. Kurinsky, P. L. Brink, B. Cabrera, M. Cherry, F. Insulla, M. Kelsey, F. Ponce, *et al.*, “High-field spatial imaging of charge transport in silicon at low temperature,” *AIP Adv.*, vol. 10, p. 025316, 2020.
- [161] B. Shank, D. Q. Nagasawa, J. J. Yen, M. Cherry, and B. A. Young, “Temperature Dependent I–V and Resistance Characterization of SuperCDMS Germanium Crystals,” *Journal of Low Temperature Physics*, vol. 167, no. 3, pp. 202–207, 2012.
- [162] B. Shank, D. Q. Nagasawa, B. Cabrera, M. Cherry, and B. A. Young, “Charge Transport Asymmetry in Cryogenic High Purity Germanium,” *Journal of Low Temperature Physics*, vol. 176, no. 3, pp. 148–154, 2014.
- [163] Thorlabs, “LED Driver for High-Power and Mounted LEDs.” https://www.thorlabs.com/newgrouppage9.cfm?objectgroup_id=9117. Accessed: 2018.
- [164] R. Moffatt, *Two-Dimensional Spatial Imaging of Charge Transport in Germanium Crystals at Cryogenic Temperatures*. PhD thesis, Stanford University, 3 2016.
- [165] V. P. Markevich, M. Vaqueiro-Contreras, J. T. De Guzman, J. Coutinho, P. Santos, I. F. Crowe, M. P. Halsall, I. Hawkins, S. B. Lastovskii, *et al.*, “Boron-Oxygen Complex Responsible for Light-Induced Degradation in Silicon Photovoltaic Cells: A New Insight into the Problem,” *physica status solidi (a)*, vol. 216, no. 17, p. 1900315, 2019.
- [166] J. A. Hornbeck and J. R. Haynes, “Trapping of Minority Carriers in Silicon. I. *P*-Type Silicon,” *Phys. Rev.*, vol. 97, pp. 311–321, Jan 1955.
- [167] M. Crisler, R. Essig, J. Estrada, G. Fernandez, J. Tiffenberg, M. S. Haro, T. Volansky, and T.-T. Yu, “SENSEI: First Direct-Detection Constraints on Sub-GeV Dark Matter from a Surface Run,” *Phys. Rev. Lett.*, vol. 121, p. 061803, Aug 2018.
- [168] Y. Hochberg, Y. Kahn, M. Lisanti, K. M. Zurek, A. G. Grushin, R. Ilan, S. M. Griffin, Z.-F. Liu, S. F. Weber, and J. B. Neaton, “Detection of sub-MeV dark matter with three-dimensional Dirac materials,” *Physical Review D*, vol. 97, Jan 2018.

- [169] S. M. Griffin, K. Inzani, T. Trickle, Z. Zhang, and K. M. Zurek, “Multichannel direct detection of light dark matter: Target comparison,” *Physical Review D*, vol. 101, Mar 2020.
- [170] N. Kurinsky, T. C. Yu, Y. Hochberg, and B. Cabrera, “Diamond detectors for direct detection of sub-GeV dark matter,” *Physical Review D*, vol. 99, Jun 2019.
- [171] S. M. Griffin, Y. Hochberg, K. Inzani, N. Kurinsky, T. Lin, and T. C. Yu, “SiC Detectors for Sub-GeV Dark Matter,” *ArXiv:2008.08560*, 2020.
- [172] C.-P. Liu, C.-P. Wu, H.-C. Chi, and J.-W. Chen, “Model-independent determination of the Migdal effect via photoabsorption,” *Phys. Rev. D*, vol. 102, p. 121303, Dec 2020.
- [173] R. Essig, J. Pradler, M. Sholapurkar, and T.-T. Yu, “Relation between the Migdal Effect and Dark Matter-Electron Scattering in Isolated Atoms and Semiconductors,” *Physical Review Letters*, vol. 124, Jan 2020.
- [174] N. Kurinsky, D. Baxter, Y. Kahn, and G. Krnjaic, “Dark matter interpretation of excesses in multiple direct detection experiments,” *Phys. Rev. D*, vol. 102, p. 015017, Jul 2020.
- [175] A. E. Robinson and É. Michaud, “Comment on A dark matter interpretation of excesses in multiple direct detection experiments [arXiv:2002.06937],” *ArXiv:2002.08893*, 2020.
- [176] N. Kurinsky, D. Baxter, Y. Kahn, G. Krnjaic, and P. Abbamonte, “Reply to Robinson and Michaud, arXiv:2002.08893,” *ArXiv:2003.00101*, 2020.
- [177] A. Trukhin, K. Smits, G. Chikvaidze, T. Dyuzheva, and L. Lityagina, “Luminescence of silicon Dioxide — silica glass, α -quartz and stishovite,” *Open Physics*, vol. 9, no. 4, pp. 1106–1113, 2011.
- [178] T. F. Silva, A. L. Bonini, R. R. Lima, N. L. Maidana, A. A. Malafrente, P. R. Pascholati, V. R. Vanin, and M. N. Martins, “Optical transition radiation used in the diagnostic of low energy and low current electron beams in particle accelerators,” *Review of Scientific Instruments*, vol. 83, no. 9, p. 093301, 2012.
- [179] L. Burmeister, “Charakterisierung von SuperCDMS Hintergrund Spektren in HVeV-Detektor Daten,” Master’s thesis, Universität Hamburg, 8 2021.
- [180] T. Enqvist, A. Mattila, V. Föhr, T. Jämsén, M. Lehtola, J. Narkilahti, J. Joutsenvaara, S. Nurmenniemi, J. Peltoniemi, *et al.*, “Measurements of muon flux in the Pyhäsalmi underground laboratory,” *Nuclear Instruments and Methods in Physics Research Section A: Accelerators, Spectrometers, Detectors and Associated Equipment*, vol. 554, no. 1, pp. 286–290, 2005.
- [181] S. Knapen, T. Lin, and K. M. Zurek, “Light dark matter in superfluid helium: Detection with multi-excitation production,” *Phys. Rev. D*, vol. 95, p. 056019, Mar 2017.
- [182] C. Kouvaris and J. Pradler, “Probing Sub-GeV Dark Matter with Conventional Detectors,” *Phys. Rev. Lett.*, vol. 118, p. 031803, Jan 2017.
- [183] A. Thompson *et al.*, “X-Ray Data Booklet.” Center for X-Ray Optics and Advanced Light Source, Lawrence Berkeley National Laboratory, University of California, Oct. 2009. 1.7 Atomic Scattering Factors.

- [184] R. Essig, “private communication,” 2020.
- [185] M. Ibe, W. Nakano, Y. Shoji, and K. Suzuki, “Migdal effect in dark matter direct detection experiments,” *Journal of High Energy Physics*, vol. 2018, p. 194, Mar 2018.
- [186] D. Baxter, Y. Kahn, and G. Krnjaic, “Electron ionization via dark matter-electron scattering and the Migdal effect,” *Physical Review D*, vol. 101, Apr 2020.
- [187] S. Knapen, J. Kozaczuk, and T. Lin, “The Migdal effect in semiconductors,” *ArXiv:2011.09496*, 2020.
- [188] R. F. Potter, “ - Germanium (Ge),” in *Handbook of Optical Constants of Solids* (E. D. Palik, ed.), pp. 465 – 478, Burlington: Academic Press, 1997.
- [189] C. Gähwiller and F. C. Brown, “Photoabsorption near the $L_{II,III}$ Edge of Silicon and Aluminum,” *Phys. Rev. B*, vol. 2, pp. 1918–1925, 1970.
- [190] C. Gähwiller and F. Brown, “Photoabsorption Near the $L_{II,III}$ Edge of Silicon,” in *Proc. 10th International Conference on the Physics of Semiconductors*, pp. 213–216, U.S. Atomic Energy Commission, Division of Technical Information, 1970.
- [191] F. C. Brown, R. Z. Bachrach, and M. Skibowski, “ $L_{2,3}$ threshold spectra of doped silicon and silicon compounds,” *Phys. Rev. B*, vol. 15, pp. 4781–4788, May 1977.
- [192] F. C. Brown and O. P. Rustgi, “Extreme Ultraviolet Transmission of Crystalline and Amorphous Silicon,” *Phys. Rev. Lett.*, vol. 28, pp. 497–500, Feb 1972.
- [193] W. Da-Chun, L. Ping-An, and Y. Hua, “Measurement of the mass attenuation coefficients for SiH_4 and Si,” *Nuclear Instruments and Methods in Physics Research Section B: Beam Interactions with Materials and Atoms*, vol. 95, no. 2, pp. 161 – 165, 1995.
- [194] G. Hildebrandt, J. D. Stephenson, and H. Wagenfeld, “Normale und anomale Absorption von Röntgen-Strahlen in Germanium und Silicium,” *Zeitschrift für Naturforschung A*, vol. 28, p. 588, 1973.
- [195] G. G. Macfarlane, T. P. McLean, J. E. Quarrington, and V. Roberts, “Fine Structure in the Absorption-Edge Spectrum of Ge,” *Phys. Rev.*, vol. 108, pp. 1377–1383, Dec 1957.
- [196] H. R. Philipp and E. A. Taft, “Optical Constants of Germanium in the Region 1 to 10 eV,” *Phys. Rev.*, vol. 113, pp. 1002–1005, Feb 1959.
- [197] L. Marton and J. Toots, “Optical Properties of Germanium in the Far Ultraviolet,” *Phys. Rev.*, vol. 160, pp. 602–606, Aug 1967.
- [198] M. Cardona, W. Gudat, B. Sonntag, and P. Yu, “Optical Absorption of Semiconductors from 12 eV to 200 eV,” in *Proc. 10th International Conference on the Physics of Semiconductors*, pp. 209–212, U.S. Atomic Energy Commission, Division of Technical Information, 1970.
- [199] O. A. Ersov, I. A. Brytov, and A. P. Lukirskii, “Reflection of X Rays from Certain Substances in the Region 7 to 44 Å,” *Optics and Spectroscopy*, vol. 22, pp. 66–69, 1967.

- [200] K. Rajkanan, R. Singh, and J. Shewchun, "Absorption coefficient of silicon for solar cell calculations," *Solid State Electron.*, vol. 22, p. 793, 1979.